SYNTHESIS AND OPTICAL PROPERTIES OF EUROPIUM AND TERBIUM DOPED CERIUM BASED OXIDES

Thesis submitted to
THE UNIVERSITY OF KERALA
For the award of the degree of

DOCTOR OF PHILOSOPHY

in
PHYSICS

under
THE FACULTY OF SCIENCE

by
ATHIRA K. V. RAJ

Under the Supervision of
Dr. P. PRABHAKAR RAO

Materials Science and Technology Division
CSIR - National Institute for Interdisciplinary Science and Technology (NIIST)
Thiruvananthapuram - 695019
Kerala, India

NOVEMBER 2018

Synthesis and Optical Properties of Europium and Terbium doped Ceria Based Oxides

PhD Thesis in the field of Physics

Author:

Athira K. V. Raj

Materials Science and Technology Division National Institute for Interdisciplinary Science and Technology (NIIST) Thiruvananthapuram - 695019, Kerala, India

Supervising Guide:

Dr. P. Prabhakar Rao

Materials Science and Technology Division National Institute for Interdisciplinary Science and Technology (NIIST) Thiruvananthapuram - 695019, Kerala, India

---

November 2018

DECLARATION

I hereby declare that the PhD thesis entitled "**Synthesis and Optical Properties of Europium and Terbium doped Cerium Based Oxides"** is an independent work carried out by me and it has not been submitted anywhere else for any other degree, diploma, or title.

Athira K. V. Raj

THIRUVANANTHAPURAM

Date: November 7, 2018

सीएसआईआर -राष्ट्रीय अंतर्विषयी विज्ञान तथा प्रौद्योगिकी संस्थान
CSIR-National Institute for Interdisciplinary Science and Technology
(वैज्ञानिक तथा औद्योगिक अनुसंधान परिषद)
(Council of Scientific & Industrial Research)
विज्ञान और प्रौद्योगिकी मंत्रालय,भारत सरकार/ Ministry of Science & Technology Govt. of India
इंडस्ट्रियल एस्टेट पोस्ट Industrial Estate PO, तिरुवनंतपुरम, केरल Thiruvananthapuram,
Kerala -695019, भारत India

Dr. P. Prabhakar Rao
Chief Scientist
Material Science and Technology Division

Tel Ph: +914712515311
Fax: +91-471-2491 712
Email:padala_rao@yahoo.com

07.11.2018

CERTIFICATE

This is to certify that the work embodied in the thesis entitled "**Synthesis and Optical Properties of Europium and Terbium doped Cerium Based Oxides"** has been carried out by **Ms. Athira K. V. Raj** under my supervision and guidance in the Materials Science and Technology Division of National Institute for Interdisciplinary Science and Technology (NIIST), CSIR, Thiruvananthapuram, for the degree of Doctor of Philosophy in Physics under the faculty of Science, The University of Kerala and has not been included in any other thesis submitted for the award of any degree.

THIRUVANANTHAPURAM

Date: November 7, 2018

Dr. P. Prabhakar Rao

(Supervising Guide)

To succeed in your mission, you must have single minded devotion to your goal

A. P. J. Abdul Kalam (1931 - 2015)

ACKNOWLEDGEMENTS

I'm blessed and I thank Bhagavan for everyday
for everything that happens
for me

The work presented in the thesis is the result of my journey of Ph.D which was just like mountaineering accompanied with encouragement, trust, hardwok, frustrations etc. I would like to thank a number of people who have contributed to make my name appears on the cover of this thesis in many different ways.

I would like to start with the person who made the biggest difference in my life by his constant support, inspiration, encouragement, fatherly love & care and thoughtful guidance throughout my research as well as my life, my mentor, ***Dr. P. Prabhakar Rao****. He has been there in front of my eyes from the start of my M.Sc dissertation till date, for his patience, motivating and inspiring every bit of me towards new possibilities in life. He successfully guided me in several difficult situations and I can able to learn a lot from him. His attitude of living simple, making keen observation and converting them into a new possibilities, correlating ideas and understanding the obvious has helped me to come a long way and will always guide me in future. He has taught me another aspect of life, "goodness can never be defied and good humans can never be denied". With a great feel of pleasure I would like to express sincere gratitude to Sir from the bottom of my heart and truly indebted to him throughout my life time.*

No research is possible without infrastructure and resource. For this I wish to extend my gratitude to Dr. A. Ajayghosh, Director CSIR-NIIST and Dr. Gangan Pratap and Dr. Suresh Das former directors of NIIST, for providing the necessary facilities for carrying out the work in the institute. I thank Dr. K. Harikrishna Bhat, Dr. P. Prabhakar Rao, Dr. M. L. P. Reddy and Dr. M. T. Sebastian, present and former Head of Materials Science and Technology Division, for maintaining discipline and other academic facilities in the division from which I was benefitted a lot as a student. I wish to thank scientists and technical staff of NIIST for the help rendered during the course of this research work.

I extend my gratitude to staff in Administrative, Finance, Accounts, Stores, Purchase, Library and IT sections for their help and services.

I acknowledge ICDD, USA and CSIR Network Project SURE for the financial assistance during my research. This work has also been benefitted from DRDO and DST.

I would like to thank Mr. M. R Chandran, Mrs. Lucy Paul, Mr. Shanoj P. S, Mrs Soumya V, Mr. Pruthiviraj N, Mr. M. P Varkey and Mr. Harish Raj for SEM imaging and technical support. I also thank Mrs. Jiji S. G, Department of Optoelectronics, Kerala

University for the help with Raman analysis, Dr. B. M. Reddy, CSIR-IICT, Hyderabad and Dr. Suresh Bapu, CSIR-CECRI, Karaikudi for XPS Analysis .

My acknowledge will never be complete without the special thanks to my lab seniors especially Dr. Mariyam Thomas, Dr. Sameera S and Mrs. Vineetha James who have taught me the lab culture and helping me to understand the hard face of life. I would like to extend my acknowledge to Dr. Linda Francis and Dr. Divya S. My heartful thanks to my fellow labmates, Mrs. Parvathi S Babu, Ms. Suchitra V. G, Mrs. Aswathy B. A and Ms. Ajuthara T. R. "A real friend is one who walks in when the rest of the world walks out", i.e Ms. Sreena T. S. She is always besides me from the last eleven years, during the happy and hard moments to push me and encourage me. I am extremely indebted to her for the nice and strong friendship that I ever had. I would like to thank M.Sc. project students, Ms. Aiswarya K, Mrs. Arathijith P and Shinoj P. My special thanks are due to my roommate Ms. Veena K S and sweet friend Mrs. Swetha P.

With a heart full gratitude and love, I mark my gratefulness to all my teachers, especially from Manarul Huda Higher Secondary School, who taught me the beautiful subject physics that opening my way to research life.

Finally, I acknowledge the people who mean a lot to me, my parents, Acha (Vijayaraj) and Amma (Usha), for showing faith in me and giving me the liberty to choose what I desired. I salute you both of them for the love, care, pain and sacrifice, and you people hardly understood my feelings, supported me in any decisions I made. Let me extend my sincere thanks to my Ammuma (Sarada) who loved me a lot than anybody and prayed for me. I express my thanks to Poovatoor Ammuma, Appechi, Maman, Attaya and cousins for the moral support. The best thing about having a sister was that I always had a friend. Thanks to my sweet sister Kunchi (Aswathi K. V. Raj) for her selfless love, care and quarrels that make my life beautiful. I owe thanks to a very special person, my life partner, Mr. Singuru Ramana for his love, support and understanding during my pursuit of Ph.D degree. You were always keep patience and helped me to keep things perspective. I greatly value his contribution and deeply appreciate his belief in me.

At the end, I would like to thank all those people who were there with me to make this thesis possible and made my research life an unforgettable experience. Thank You All.

"The love for all living thing creatures is the most noble attribute of man"
Charles Darwin

Athira K V Raj

CONTENTS

LIST OF TABLES

LIST OF FIGURES

ABBREVATIONS

ASTM	: American Society for Testing and Materials
CCT	: Correlated Color Temperature
CIE	: Commission Internationale de I' Eclairage
CN	: Coordination Number
CRI	: Color Rendering Index
CT	: Charge Transfer
DIN	: Deutsches Institute fur Normung (German Standards Organisation
ED	: Electric Dipole
EDS	: Energy Dispersive Spectroscopy
FWHM	: Full Width Half Maximum
ISO	: International Organization for Standardisation
JCPDS	: Joint Committee on Powder Diffraction Standards
LED	: Light Emitting Diode
LMCT	: Ligand to Metal Charge Transfer
Ln	: Lanthanide
MD	: Magnetic Dipole
NIR	: Near Infrared
NTSC	: National Television Standards Committee
pc-WLED	: Phosphor Converted White Light Emitting Diode
PL	: Photoluminescence
PMMA	: Poly(Methyl Methacrylate)
PTFE	: Poly–tetrafluoroethylene
QE	: Quantum Efficiency
RE	: Rare Earth
SEM	: Scanning Electron Microscopy
SSL	: Solid State Lighting
TEM	: Transmission Electron Microscopy
UV-vis	: Ultraviolet Visible
XPS	: X-ray Photoelectron Spectroscopy
XRD	: X-ray Diffraction

PREFACE

Cerium oxide (CeO_2) is a well-known functional material with a cubic fluorite structure. It is considered to be one of the most important oxide materials because of its good thermal and chemical stability and special optical properties, e.g. its high refractive index, optical transparency, high dielectric constant and non-toxicity. Because of these characteristics it has wide potential applications: in optical coatings; in electro-optical, microelectronic, and optoelectronic devices etc. Cerium oxide is well known for having large deviations in stoichiometry as a result of the easy reducibility of Ce^{4+} ions to Ce^{3+} ions. The simultaneous reduction of Ce^{4+} to Ce^{3+} results in the releasing of oxygen in a low oxygen environment found uses in three way catalyst (TWC) for its oxygen storage capacity. However such reduction of cerium is deleterious in optical properties. The tetravalent cerium ion (Ce^{4+}) has no 4f electrons and a strong light absorption through charge transfer (CT) from O^{2-} to Ce^{4+} around 370 nm, which makes it a promising optical host material. In this regard the optical properties like photoluminescence and colouring properties of Cerium based compounds are studied by doping with various rare earth elements such as Eu^{3+}, Tb^{3+}, Pr^{3+}etc. However the substitution of such trivalent ions creates oxygen vacancies to compensate for the effective negative charge associated with the trivalent dopant. These oxygen vacancies adversely affect the optical properties of the ceria limiting its applications. In view of this, it is more difficult to achieve a sizeable luminescence and good colouristic characteristics for use in practical applications in the CeO_2 fluorite lattice. The present thesis aims to prepare a CeO_2-based host lattices and manipulating the cerium environment to overcome these limitations in its optical properties.

The thesis comprises of eight chapters, Chapter 1 gives an introduction about the general properties of cerium. It portrays the importance of CeO_2 in the field of red phosphors for white LED applications and also IR reflecting non toxic red and yellow pigments for energy saving applications.

The chapter two focuses on the influence of local structure on the photoluminescence properties of Eu^{3+} doped CeO_2 red phosphors through induced oxygen vacancies by contrasting rare earth (La & Y) substitutions. $Ce_{0.1}Y_{0.8}O_{2-\delta}$:$0.1Eu^{3+}$ phosphor exhibited maximum red emission intensity at 612 nm, which is 8

times higher than that of $Ce_{0.9}O_{2-\delta}$:0.1Eu^{3+} and better than that of commercial Philips red phosphor, whereas La substitution yielded poor emission intensities with higher concentrations. The co-substitution of contrasting rare earth metals with Eu^{3+} allow the understanding of local structure and a smaller ion like Y^{3+} greatly functionalizes CeO_2:Eu^{3+} phosphor.

Chapter three comprises of efforts to produce a new series of red phosphors $A_{1.9}Ce_2O_7$:0.1Eu^{3+} (A = La, Y and Gd) having cerium in the tetravalent lattice site. The present Eu^{3+} doped system gave scope to understand the influence of different rare earths, Ce^{3+} concentration and the Eu^{3+} environment on the photoluminescence properties. The defect Ce^{3+} concentration is dependent on the nature of the A site rare earths and also influenced the photoluminescence properties. Gadolinium based system showed better luminescent properties hence further studies are confined to the $Gd_2Ce_2O_7$ host lattice which has been doped with different concentrations of Eu^{3+} to improve the luminescence properties. Further, the influence of Ca-Nb substitution on the optical properties of $Gd_{1.8-x}Ce_{2-y}O_7$:0.2 Eu^{3+} red phosphors have been investigated to modify the Eu^{3+} chemical environment.

In the fourth chapter, an effort has been made to study the photoluminescent properties of $Y_2Ce_2O_7$:Eu^{3+} red phosphors through modification of the cerium oxidation states and oxygen vacancy ordering. The substitution of Eu^{3+} at the Ce^{4+} site induced a structural transition from a defect fluorite structure to a C-type structure, whereas substitution at the Y^{3+} site showed a biphasic nature of defect fluorite and C-type structures. The structural transition enhanced the Eu^{3+} luminescence as a result of increased oxygen vacancy ordering, a reduction in the Ce^{3+} oxidation states and distortion of the environment and hence further investigations were confined to $Y_2Ce_{2-x}O_7$:xEu^{3+} with respect to the variation of Eu^{3+} concentration. This study suggests that sizeable Eu^{3+} luminescence in a Ce-based lattice can be achieved under blue light excitation, which matches well with the emission of commercial GaN LED (440–470 nm) chips.

Chapter five presents a new class of red pigments: $Ln_2Ce_{2-x}Tb_xO_7$ (Ln = Y, La, Gd and Sm; x = 0, 0.2, 0.4, 0.6, 0.8, and 1.0) with high NIR reflectance as alternatives to the traditional toxic reds. The Tb substitution extends the absorption edge to longer wavelengths by introducing an additional electronic level between the

valence band and conduction band leading to various red colors by fine tuning the band gap from 3.11 eV (ivory white) to 1.87 eV (red). The applicability studies of these pigments in polymer matrix (poly methyl methacrylate), cement slab, asbestos sheet and ceramic glazes exhibited good coloring performance with high near infrared reflectance. These results demonstrate the synthesized pigments as potential near infrared reflective candidates for cool roof and surface coating applications.

In the chapter six, an attempt has been made to tune the colour from yellow to red in Sr_2CeO_4 system by Ba-Tb substitutions. The Ba-Tb substitution extends the absorption edge to longer wavelengths by introducing an additional electronic level between the valence and conduction bands. Consequently, the prepared pigments exhibit various yellow colors (b^* = 70.30) by fine tuning of the band gap from 3.03 (white) to 2.52 eV (reddish-greenish yellow) by Tb substitution. Doping of Ba into Sr_2CeO_4 enhances the red hue (a^* = 33.4) which is higher than commercially available red pigments. The NIR reflectance is also enhanced by Ba-Tb substitution from 87% to 91%. The coloring performance of the synthesized pigments was investigated in the polymer matrix for plastic coloring applications. The exhibition of high NIR reflectance with comparable color properties of these pigments makes them potential candidates as cool colorants to reduce the heat build-up.

The seventh chapter consists of the synthesis of a new series of high near-infrared (NIR) reflecting pigments with colors ranging from yellow to red by tuning the $Bi_2Ce_2O_7$ with rare earth ion substitutions on both A and B sites. A brilliant yellow hue was obtained for $Bi_{1.75}Y_{0.25}Ce_2O_7$ (b^* = 51.4), whereas $Bi_2Ce_{1.50}Tb_{0.50}O_7$ (a^* = 15.0) exhibited a red color. High NIR solar reflectance of 93% and 88% were obtained for $Bi_{0.5}Y_{1.5}Ce_2O_7$ yellow and $Bi_2Ce_{1.50}Tb_{0.50}O_7$ red pigments respectively. The application study of these selected pigments was investigated in the polymer matrix which demonstrates their coloring performance for various potential applications. These results demonstrate the synthesized pigments as potential near infrared reflective candidates for cool roof applications.

Chapter eight summarizes the major findings and conclusions drawn from the work and gives the scope for further studies.

Chapter 1

Introduction on Optical Properties and its Applications

Modern optical materials applied to key optical markets such as mobile and optical communications, security, lasers, sensor, (lighting) phosphors, displays, imaging, optical fibres, pigments, photocatalysts, biomedicine etc to satisfy the demand for enhanced performance. Particularly the research on phosphors and pigments has put on an incredible drive in the past decade due to their intrinsic advantages and wide applications as energy saving products. This chapter portrays on the importance of choosing cerium based oxides in the field of red phosphors for white LED applications and IR reflecting non-toxic yellow and red pigments for energy saving applications. And also emphasis is given to the luminescence properties of Eu^{3+} doped cerium based red phosphors and terbium doped cerium based yellow and red pigments.

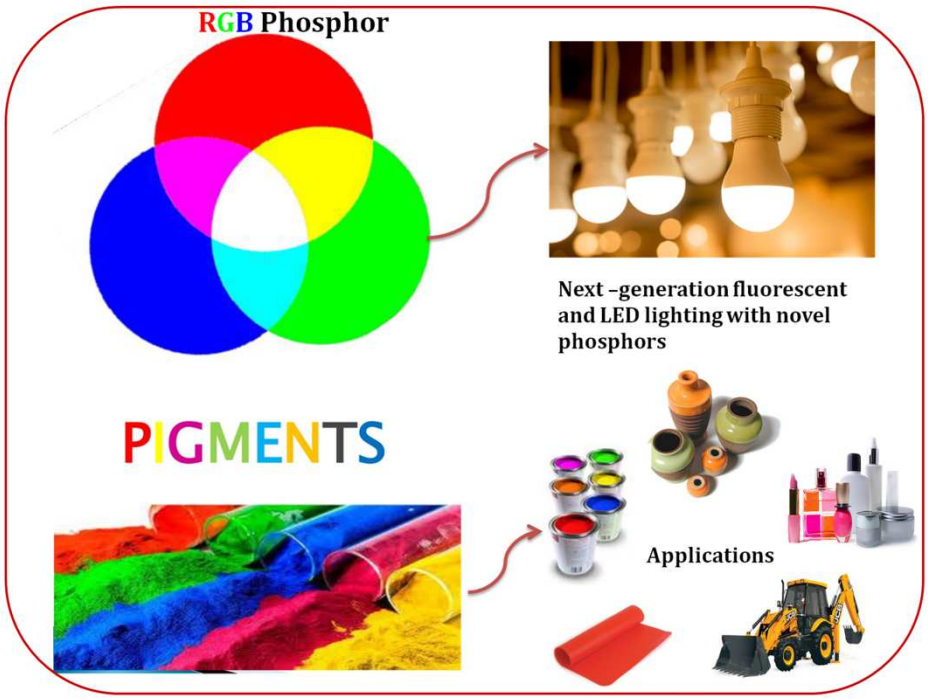

1.1 Introduction on optical properties

The optical properties of a material are defined as how it interacts with electro-magnetic radiation in the visible (light). Interaction of photons with the electronic or crystal structure of a material leads to a number of phenomena. The photons may give their energy to the material (absorption); photons give their energy, but photons of identical energy are immediately emitted by the material (reflection); photons may not interact with the material structure (transmission); or during transmission photons are changes in velocity (refraction) (Fig. 1.1). At any instance of light interaction with a material, the total intensity of the incident light striking a surface is equal to sum of the absorbed, reflected, and transmitted intensities.

$$I = I_A + I_R + I_T \tag{1.1}$$

where the intensity 'I 'is defined as the number of photons impinging on a surface per unit area per unit time.

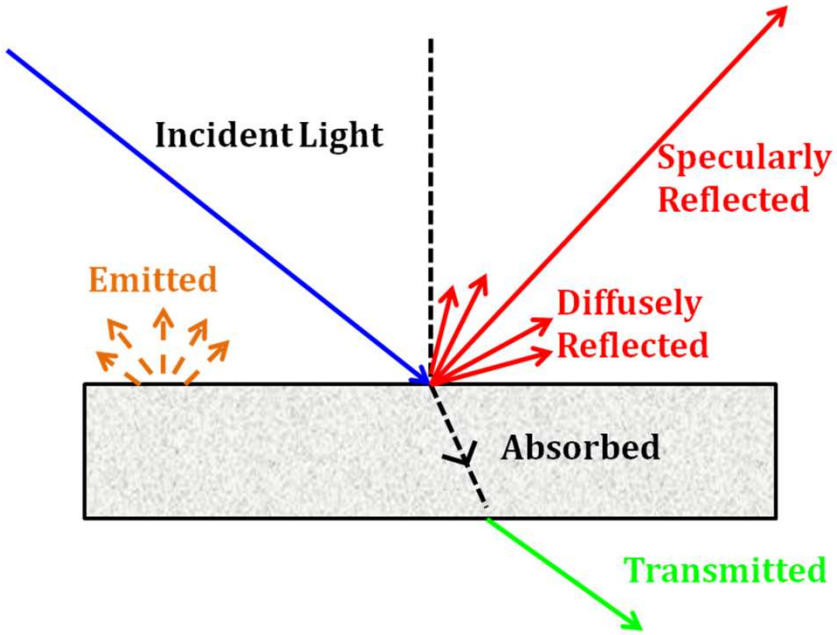

Fig. 1.1 Light can be reflected, absorbed and transmitted.

Materials are classified on the basis of their interaction with visible light into three categories. Materials that are capable of transmitting light with relatively little absorption and reflection are called transparent materials i.e. we can see through them. Translucent materials are those through which light is transmitted diffusely i.e. objects are not clearly distinguishable when viewed through. Those materials

that are impervious to the transmission of visible light are termed as opaque materials. These materials absorb all the energy from the light photons. Metals consist of partially filled high-energy conduction bands. When photons are directed at metals, their energy is used to excite electrons into unoccupied states. Thus metals are opaque to the visible light. Metals are, however, transparent to high end frequencies i.e. x-rays and γ-rays. The absorbed radiation is emitted from the metallic surface in the form of visible light of the same wavelength as reflected light. The reflectivity of metals is about 0.95, while the rest of impinged energy is dissipated as heat. The amount of energy absorbed by metals depends on the electronic structure of each particular metal. Non-metallic materials consist of various energy band structures. Thus, all four optical phenomena such as absorption, reflection, transmission and refraction are important for these materials.

Modern optical materials applied to key optical markets such as mobile and optical communications, security, lasers, sensor, (lighting) phosphors, displays, imaging, optical fibres, pigments, photocatalysis, biomedicine etc to satisfy the demand for enhanced performance. All these find quite many applications in technology for everyday life. Global population growth and urbanization increases the overall demand for lighting products and the corresponding energy consumption by lighting. According to recent studies by US Department of Energy (DOE), about 20% of electricity is used for lighting. Hence considering the rising demand for high – efficiency lighting devices, various scientists all over the world are working to meet this challenge by developing high efficient phosphors for white LED applications. 'Color' of objects has got significant importance in our world. Developing less toxic inorganic pigments for high performance coatings is extremely necessary for coloring applications. Hence, the thesis emphasis on the development of novel red phosphors and inorganic pigments as energy saving products.

1.2 Luminescence

Luminescence is the process where a material absorbs energy and then immediately emits visible or near-visible radiation. It consists of electron excitation and then dropping down to lower energy states. If the emission of radiation occurs within 10^{-8} sec after excitation, the luminescence is called fluorescence. The fluorescence has no change of electron spin and is caused by singlet to singlet or triplet to triplet transition ($S_N \rightarrow S_{N-1 \text{ or } 0}$, $T_N \rightarrow T_{N-1}$; $N \geq 2$). If the emission of radiation

takes longer than 10^{-8} sec, it is known as phosphorescence and it has emission involving spin changes transition ($S_N \rightarrow T_{N-1}$, $T_N \rightarrow S_{N\ or\ 0}$; N ≥2). Fig 1.2 is the Jablonski diagram illustrating the electronic states of a molecule and the transitions between them. Based on the energy source for electron excitation, luminescence process is classified as photo-luminescence, cathode-luminescence, and electro-luminescence. Photoluminescence is the process in which the compound absorbs photons or electromagnetic radiation, and the electrons gets excited to higher electron energy state and then radiates the photons back out, returning to a lower energy state. Ordinarily pure materials do not display the Photoluminescence phenomenon. Special materials called phosphors have the capability of absorbing high-energy radiation and spontaneously emitting lower-energy radiation.

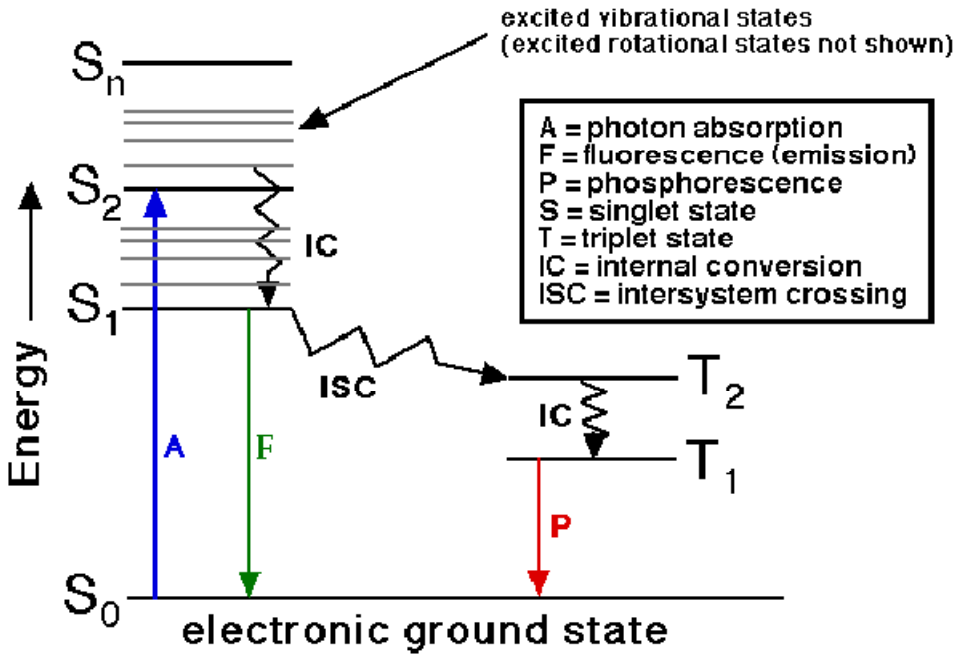

Fig. 1.2 Jablonski diagram illustrating electronic states of a molecule and the transitions.

1.2.1 Phosphors: A basic understanding

Phosphors are luminescent materials capable of emitting light when subjected to external energy source such UV radiation, X-rays, electron bombardment, friction or some other form of excitation (Blasse et al. 1979). Phosphors are one which converts the radiation energy into visible or infrared light

(Feldmann *et al*. 2003). Phosphors are usually made from a suitable host material (H), to which an activator (A), usually a 3d or 4f electron metal, is added. The host materials for phosphors are oxides, nitrides, oxynitrides, sulfides, selenides, halides or silicates etc. Activators are often impurity metal cations acts as luminescent centers, where the electrons radiatively relax and prolong the emission time. Commonly used activators are Mn^{2+}, Sb^{3+}, Ce^{3+}, Eu^{2+}, Tm^{3+}, Er^{3+}, Tb^{3+}, Pr^{3+}, Eu^{3+}, Dy^{3+} etc. If the activator does not absorb the excitation radiation effectively, it is possible to excite the activator by indirect means by energy transfer (ET). In such cases, sensitizers (S) are ions or ionic groups incorporated in the host lattice plays the role, which absorb the energy and subsequently transfer the excitation energy to the activator. The schematic representation of a typical phosphor material and the physical processes involved in the phenomenon of characteristic luminescence are presented in Fig. 1.3.

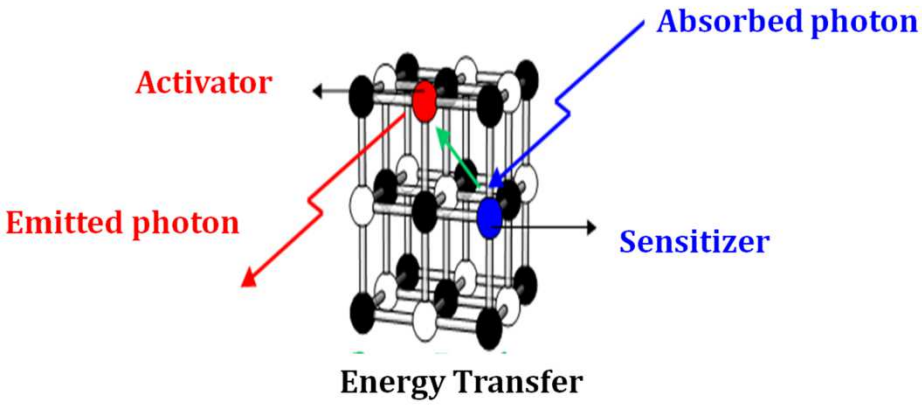

Fig. 1.3 Schematic representation of a typical phosphor material.

The underlying processes that occur within a phosphor material include absorption of energy by the activator ion, radiative relaxation of the excited ions via photon emission and non-radiative relaxation processes via phonon emission or transfer of energy. The amount of relaxation that takes place during the excitation and emission that determines the efficiency of a phosphor. The luminescence of phosphors is determined by the local environment around the activator ions and is sensitive to this crystal field. Generally, lanthanide ions exhibit three types of excitation transitions (Blasse et al. 1989):

(i) 4f - 4f transitions: Most of the phosphors based on rare earth activator ions involve movements of electrons between the different energy levels of the 4f orbitals of the same lanthanide ion.

(ii) 4f - 5d transitions: In 4f - 5d transitions, one of the 4f electrons is excited to a 5d orbital of higher energy. This type of excitation absorption is usually denoted as $4f^n$ - $4f^{n-1}5d$ and is typically observed in Ce^{3+} ions. Unlike 4f - 4f transitions, 4f - 5d transitions are allowed, which results in strong and broad absorption cross-sections.

(iii) charge – transfer state transitions: In the charge-transfer state (CTS) transition, in which 2p electrons from the neighbouring anions (e.g. O^{2-} in oxides) are transferred to a 4f orbital. These transitions result in broad and intense absorptions.

1.2.2 Phosphors: Applications

The use of phosphors by man probably started from more than 2000 years ago when they were used in fireworks to modify the color output, but real phosphor development is a 20^{th} century phenomena starting in the 1940s (Allan Mills et al. 2005). Earlier days the phosphor development has most of the market demands being generated by cathode ray tubes i.e for TVs, PC monitors, test equipments etc and emissive display devices like color projection televisions (Hardy et al. 1965), amplifiers in optical communication (Tick et al. 1995) fluorescent tubes, lasers (Joubert et al. 1999), X-ray detector systems (Ratinen et al. 1972) and scintillators (Blasse et al. 1994). However, from the last 5 years LED phosphors have become very important lighting sources for white as well as colored light must be considered an important market driver in the future. Further, the phosphor research was extended to the other areas like solar cells (Shalav et al. 2007; Richards et al. 2006) and white light emitting LEDs over the last two decades. Hence these phosphor materials are focusing up towards its application as general illumination sources as solid state lighting devices to replace all the existing sources.

1.2.3 Performance requirements of a phosphor

Phosphors play a fundamental role in determining the performance of white LEDs. In fact, all phosphors that show luminescence under excitation cannot be used

in white light applications. There are several prerequisites for selecting a phosphor for different practical applications (Xie *et al*. 2011) and are as follows:

(i) The phosphor must have strong absorption of the emissions from UV (350-410 nm) or blue (440-480 nm) LEDs and the excitation maximum should fall in the range of the pumping LED.

(ii) The performance of WLEDs depend on the position and shape of the emission spectrum i.e the emissions of the developed phosphor in combination with the emissions from other components (LED, other phosphors) must lead to the generation of pure white light with good CRI and CCT.

(iii) The quantum efficiency (QE) is a measure of the ability of a phosphor to convert the absorbed photons into luminescence, and should be as high as possible maximizing the electrical to optical conversion efficiency (less energy loss) of the LED package.

(iv) Phosphors possessing high quantum yield values are idyllic for lighting applications.

(v) High Luminous Efficacy of Radiation.

(vi) The phosphors should have high thermal stability to maintain the brightness and color coordinates of WLEDs.

(vii) The phosphor must possess high chemical stability which should be stable for handling, storage, and usage under the ambient atmosphere and should not chemically react with CO, CO_2, water, air, etc.

(viii) Phosphors should have high CRI and low CCT for warm white emission.

(ix) The phosphors must have a long lifetime (>30000h) under the high excitation desirable in SSL applications.

(x) In the economic aspect, synthesis route should be easy so as to manufacture the phosphor on a large scale.

(xi) The phosphor should be non-toxic, and the fabrication, use, and disposal of the phosphor should be as environmentally benign.

1.2.4 Current status of the red phosphors

Widespread research in the field of developing novel and stable phosphors for pc-WLEDs was carried out by many research groups in order to produce white light. The commercial pc-WLEDs normally use a 450-470 nm blue GaN LED chip

covered by a yellow phosphor, YAG: Ce^{3+}. The $5d^1 \rightarrow 4f^1$ emission of Ce^{3+} in this host exhibits a broad band with maximum intensity at 520 nm. However, they suffer from some weaknesses, such as poor color rendering index and low stability of color temperature. The color rendering index of white LEDs made by blue LED with yellow emitting phosphor method is low due to the deficiency of red light component. These drawbacks make it inappropriate for applications in indoor lighting and full colour displays. To improve the deficiency of the red emission component in WLEDs, extra red emission is required either from other chips or from co-fabricated phosphors. Therefore, numerous efforts have been made to search for new phosphors that can emit suitable red light. Some of the phosphor materials whose emission wavelengths are falling under red upon blue or/and UV excitations are listed in Table 1.1 (Li et al. 2009; Piao et al. 2007; Setlur et al. 2006; Neeraj et al. 2004; Liao et al. 2013; Fu et al. 2007; Luo et al. 2006).

Table 1.1 Some of red phosphors for WLED applications.

Composition	**Excitation peak (nm)**	**Emission Peak (nm)**
$M_2Si_5N_8$(M = Eu, Ba, Sr, Ca) : Eu^{2+}	465	570 - 680 609 - 680 515 - 606
$CaAlSiN_3$: Eu^{2+}	460	634 649
$Lu_2CaMg_2(Si,Ge)_3O_{12}$: Ce^{3+}	470	605
Ln_2MoO_6, AMO_4,(A = Ca, Sr; M = Mo, W): Eu^{3+}	394, 465	615
K_2SiF_6: Mn^{4+}	460	646
$Mg_3Y_2Ge_3O_{12}$: Ce^{3+}	460	604
Y_2O_3, Y_2O_2S : Eu^{3+}	395	612
(Sr, Ca)$AlSiN_3$: Eu^{2+}	455	650

1.2.5 Need for developing new red phosphors

In currently available near UV LEDs method, Y_2O_2S: Eu^{3+}, ZnS : Cu^{2+}, Al^{3+} and $BaMgAl_{10}O_{17}$: Eu^{2+} are used for red, green and blue respectively (Nishida et al. 2003). The currently available red phosphor cannot absorb light efficiently in the UV region and its brightness is about eight times less than that of the available green and blue

phosphors. Most of the major red phosphors available in the markets are sulphide based phosphors. And these sulfides based red phosphors lacks chemical stability and are highly harmful to the environment. Thus novel red phosphor materials that could be effectively excited in the near UV and visible region with good absorption and emission properties, good thermal and chemical stability, minimal thermal quenching, high quantum yield and preferably with low cost should be developed to meet the requirements.

1.2.6 Eu^{3+} activated phosphor

Over the past decade, rare earth-activated inorganic red phosphors have got much attention due to the narrow emission band. The rare earth ions are characterized by their deep lying 4f shells which are not entirely filled. The electrons in the 4f orbitals are shielded by the outer electrons shells, so they give rise to discrete energy levels. Rare earth ions (RE^{3+}) particularly Eu^{3+}, Sm^{3+}, Pr^{3+} and Dy^{3+} are suitable as activators, and are widely used as the activators for red emission. Eu^{3+} ions are considered to be the preferable choice of activators for red luminescence as they exhibit a high lumen equivalent, quantum efficiency, and photostability (Nazarov et al. 2011). In the periodic table, Eu^{3+} lies among the lanthanides, 6 electrons past Xe, which ends period 5 leaving the 5d and the 4f subshells empty, therefore [Xe]4f electronic configuration. They form a number of discrete energy levels owing to the presence of these deep lying 4f shells which is not entirely filled. The energy level diagram of Eu^{3+} ion is shown in Fig. 1.4.

Among the rare earth ions, Eu^{3+} ion has a simple energy level scheme and the transitions are hypersensitive, i.e., they depend strongly on the chemical surroundings. Luminescence originating from electronic transitions between 4f levels is predominantly due to magnetic dipole or electric dipole interactions that offer the possibility of efficient emissions. Electric dipole f – f transitions are parity forbidden; the intensity of these transitions depends strongly on the site symmetry in a host crystal. Magnetic dipole transitions are not affected much by the site symmetry because they are parity allowed. Intense red emissions of trivalent europium (Eu^{3+}) ions are due to the intraconfigurational f-f transitions is of technological importance because it has been widely applied to phosphors for color displays and fluorescent lamps. When the Eu^{3+} ions are surrounded in a site with

inversion symmetry, the $^5D_0 \rightarrow {}^7F_1$ magnetic dipole transition (~ 592 nm) is dominating, while in a site without inversion symmetry the $^5D_0 \rightarrow {}^7F_2$ electric dipole transition (~ 610 - 620 nm) is dominating (Blasse et al. 1979). Actually, both the electric-dipole and the magnetic-dipole transitions appear simultaneously in practical inorganic luminescent materials, although their intensities are different and, in most cases, one of which is much stronger. Therefore the luminous intensity ratio of $^5D_0 \rightarrow {}^7F_2$ to $^5D_0 \rightarrow {}^7F_1$; called as asymmetry ratio gives a measure of the degree of distortion from inversion symmetry of the local environment around the Eu^{3+} ions in the host lattice (Walrand et al. 1996).

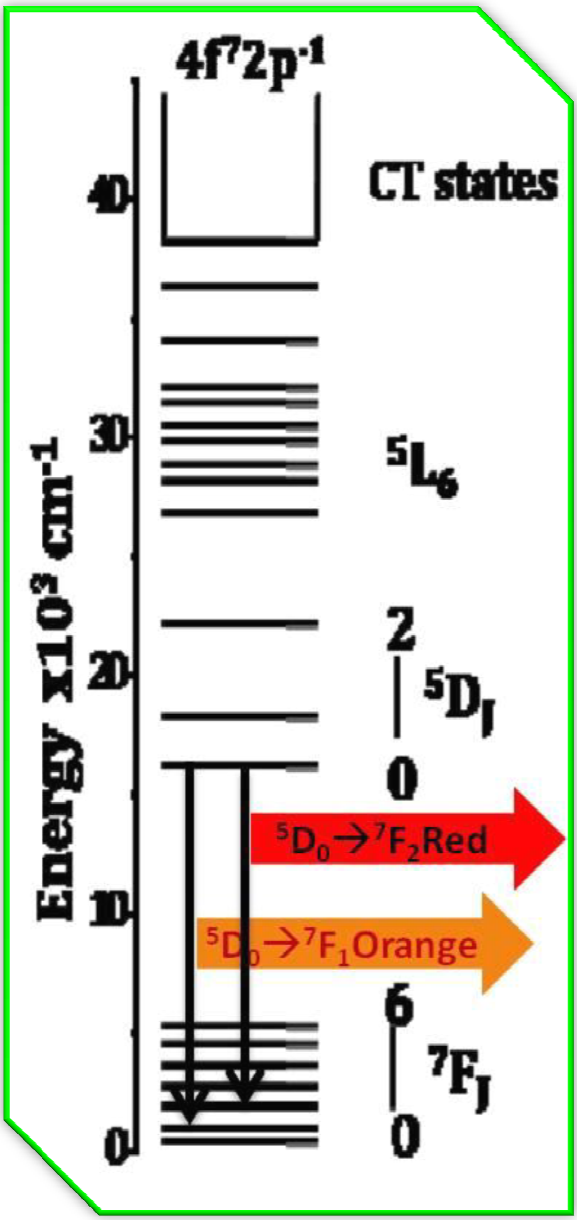

Fig. 1.4 Energy level diagram of Eu^{3+} ion.

Interesting properties of Eu^{3+} in brief:

- Emission wavelengths of Eu^{3+} strongly depend on local structures, coordination numbers, ordering and degree of distortion.
- Magnetic dipole f – f transitions are parity allowed.
- Electric dipole f – f transitions are parity forbidden.
- When Eu^{3+} ion occupies a site with inversion symmetry, ($\Delta J = \pm 1$) the $^5D_0 \rightarrow {}^7F_1$ MD transition (orange) is dominating.
- When Eu^{3+} ion occupy a site without inversion symmetry, ($\Delta J = \pm 2, 4, 6$) the $^5D_0 \rightarrow {}^7F_2$ ED transition (red) is the strongest.
- Asymmetric ratio (red to orange ratio) provides a degree of local distortion and the nature of the doping sites.
- Split in the $^5D_0 \rightarrow {}^7F_0$ transition asses the site occupancy of Eu^{3+}.

1.3 Inorganic Pigments

1.3.1 General properties of Pigments

We only have to open our eyes and look around to observe how important part color plays in our everyday lives. Color influences our moods and emotions and generally enhances the way in which we enjoy our surroundings. Natural colors are all around us. In addition, there is large number of examples of synthetic colors which are the products of the chemical manufacturing industry. They are called pigments. The word pigment is of Latin origin ("pigmentum" means something that colors) and originally denoted a color in the sense of a coloring matter. It is a material which possesses color as the result of selective absorption and reflection of light encounters on it. This process is entirely different from the fluorescence and phosphorescence in which light is emitted. Pigments are generally in powdered form and fine particles are in the range of 0.01-30 microns. They usually have special properties that make them ideal for coloring other materials. These colors commonly serve a purely decorative or aesthetic purpose.

The materials that used for the manufacturing of pigments usually have special properties that make them ideal for coloring other materials. A pigment must have a high tinting strength relative to the materials it colors. It must be stable in solid form at ambient temperatures. For industrial applications, as well as in the arts, permanence and stability are desirable properties. Pigments that are not

permanent are called fugitive. Fugitive pigments fade over time or with exposure to light, while some eventually blacken (Christie et al. 2001).

Coloring materials are usually classified as dyes or pigments (Fig. 1.5). Dyes are chemically bound to a substrate such as a textile whereas pigments require another substance called a binder, to help them adhere to the substrate. No chemical reaction actually takes place between the pigment and the binder. The binder serves only to incorporate the pigment onto the surface of the substrate. Normally, binder and pigment are mixed mechanically and then applied together. A distinction is usually made between a pigment, which is insoluble in its vehicle resulting in a suspension and a dye, which either is itself a liquid or is soluble in its vehicle resulting in a solution. A colorant can act as either a pigment or a dye depending on the vehicle involved. In some cases, a pigment can be manufactured from a dye by precipitating a soluble dye with a metallic salt. The resulting pigment is called a lake pigment.

Fig. 1.5 Images of pigments and dyes.

Pigments appear the colors they are because they selectively reflect and absorb certain wavelengths of visible light. This is the physical basis of color of the pigments. White light is a roughly equal mixture of the entire spectrum of visible light with a wavelength in a range from about 375 or 400nanometers to about 760 or 780 nm. When this light encounters a pigment, parts of the spectrum are absorbed by the pigment. Some other wavelengths or parts of the spectrum are reflected or scattered. Most pigments are charge transfer complexes, like transition

metal compounds, with broad absorption bands that subtract most of the colors of the incident white light. The new reflected light spectrum creates the appearance of a color.

1.3.2 Scientific and Technical Issues

Selection of a pigment for a particular application is determined by cost and by the physical properties and attributes of the pigment itself. For example, a pigment that is used to color glass must have very high heat stability in order to survive the manufacturing process. In artistic paint, heat stability is less important, while light fastness and toxicity are greater concerns.

The following are some of the attributes of pigments that determine their suitability for particular manufacturing processes and applications:

- Light fastness and sensitivity for damage from ultra violet light
- Heat stability
- Toxicity
- Tinting strength
- Staining
- Dispersion
- Opacity or transparency
- Resistance to alkalis and acids
- Reactions and interactions between pigments

Generally, inorganic pigments are able of offering excellent resistance to heat, light, weathering, solvents and chemicals, and they can offer technical advantage over most organic pigments. Inorganic pigments are of high refractive index materials which are capable of giving high opacity while organic pigments are of low refractive index and consequently are transparent (Christie et al. 2001). Inorganic pigments have been linked to high opacity and durability so that they have been mostly used in outdoor applications. In the case of anticorrosive pigments, they aid in corrosion-prevention of metal substrates.

1.3.3 Classification of inorganic pigments

The color of an object is not actually within the object itself. Rather, the color is in the light that shines upon it and is ultimately reflected or transmitted to our eyes. Visible light spectrum consists of a range of frequencies, each of which

corresponds to a specific color. Any visible light that strikes the pigment and becomes reflected or transmitted to our eyes will contribute to the color appearance. So the color is not in the pigment itself, but in the light that strikes it and ultimately reaches our eye. The only role that the pigment plays is that, it might contain atoms capable of selectively absorbing one or more frequencies of the visible light that shine upon it. If the pigment absorbs all the frequency of the visible light falling on it, then it will appear to be black. If the pigment reflects all the frequency of the visible spectrum, it appears to be white. If selective absorption takes place, the pigment appears to be colored. Based on that, inorganic pigments can be classified into different types. The classification given in Table 1.2 follows a system recommended by ISO and DIN (Buxbaum et al. 1997).

Table 1.2 Classification of inorganic pigments.

Type	Definition
White pigments	Nonselective light scattering (examples: titanium dioxide and zinc sulfide pigments, lithopone, zinc white)
Colored pigments	Selective light absorption and also to a large extent by selective light scattering (examples: iron oxide red and yellow, cadmium pigments)
Black pigments	Nonselective light absorption (examples: carbon black pigment, iron oxide black)
Effect pigments	Regular reflection or interference
Luminescent pigments	The capacity to absorb radiation and to emit it as light of a longer wavelength
Fluorescent pigments	The light of longer wavelength is emitted after excitation without a delay (example: silver-doped zinc sulfide)
Phosphorescent pigments	The light of longer wavelength is emitted within several hours after excitation (example: copper-doped zinc sulfide)

1.3.4 Current status of the inorganic yellow and red pigments

Table 1.3 Some of inorganic yellow pigments.

Composition	Definition
Arsenic pigments	Orpiment: Natural monoclinic deep orange-yellow colored arsenic sulfide mineral with formula As_2S_3
Cadmium pigments	Cadmium yellow: Class of pigments that have cadmium as one of the chemical Components
Cobalt pigments	Aureolin: Also called Cobalt Yellow. It is Potassium cobaltinitrite ($K_3Co(NO_2)_6$)
Chromium pigments	Chrome yellow: natural pigment of plumbous chromate ($PbCrO_4$)
Iron pigments	Yellow Ochre: Naturally occurring clay of monohydrated ferric oxide ($Fe_2O_3.H_2O$)
Lead pigments	Naples yellow: Also called antimony yellow can range from reddish yellow pigment to a bright light yellow, and is the chemical compound lead (II) antimonite
Titanium pigments	Titanium yellow: Also called nickel antimony titanium yellow or nickel antimony titanium yellow rutile. It is a yellow pigment with the chemical composition of $NiO.Sb_2O_3.20TiO_2$
Tin pigments	Mosaic gold: Also called bronze powder refers to tin (IV) sulfide as used as a pigment

Yellow is the color the human eye sees when it looks at light within the wavelengths of 570 and 590 nm, the wavelength of light between green and orange. The oldest yellow pigment is yellow ochre, which was amongst the first pigments used by humans. Recent inventions led to the creation of many other yellow including chrome yellow, cadmium yellow, lemon yellow, and cobalt yellow. Yellow is particularly important color in the pigment industry and the consumption of the yellow exceeds that of any other colored pigments. Another important pigment in the commercial industry is the red pigment. Red is the color at the longer-wavelengths end of the spectrum of visible light i.e 620–740 nm. Reds can vary in shade from very light pink to very dark maroon or burgundy; and in hue from the

bright orange-red scarlet or vermilion to the bluish-red crimson. Some of the inorganic red and yellow pigments are listed in Table 1.3 and 1.4.

Table 1.4 Some of inorganic red pigments.

Composition	Definition
Cadmium pigments	Cadmium Red (PR108): cadmium selenide (CdSe)
Iron oxide pigments	Red Ochre (PR102): anhydrous Fe_2O_3, takes its reddish color from the mineral hematite, which is an anhydrous iron oxide
Lead pigments	Red Lead: lead tetroxide, Pb_3O_4, is a bright red or orange crystalline or amorphous pigment
Mercury pigments	Vermilion (PR106): Synthetic and natural pigment: Occurs naturally in mineral cinnabar. Mercuric sulfide (HgS)

1.3.5 Demerits of Currently Used Pigments

- Toxicity due to the presence of heavy metals is the major demerit of Pigments. It may be acute or chronic and is caused by lead, mercury, iron, thallium, cadmium, bismuth, arsenic etc. Pigments containing lead or arsenic have long been recognized as being dangerous. This group includes flake white or Cremnitz white (made of lead carbonate), Naples yellow (made of lead antimoniate pigment), the chrome yellows (made of lead chromate), chrome green (made of mixtures containing lead chromate), cobalt violet (when it contains cobalt arsenate) and greens such as Schweinfurt green, emerald green, Paul Veronese green or Paris green (made of arsenic compounds such as copper acetoarsenite). Since 1975 many reports have called attention to the possible dangerous effects of pigments containing cadmium, chromium, manganese and mercury. These colors include the cadmium reds, cadmium yellows, cadmium orange, viridian and chrome oxide opaque, manganese blue, manganese violet, burnt and raw umber and vermilion (mercuric sulfide).
- The shape and size distribution of pigment particles affects their physical properties, in particular their hue. But, during high temperature calcinations,

particles growth of the pigment will occur. This will affect the properties of pigments. Also, some applications of pigments need fine dispersion.

- × Some pigments may absorb IR radiation, especially from the near infrared (NIR) region. As a result, interior temperature of buildings and automobiles may reach an uncomfortable level during hot weather, which requires the use of air conditioners.

1.3.6 How to Overcome

- ✓ The rare earth elements offer a vast opportunity for developing environmentally secure alternative. Rare earth, because of their unique electronic configuration of partially filled f orbitals, show unusual properties. The color developed depends on the number of unpaired electrons. The pigments derived from rare earths show their characteristic intense color due to charge transfer interactions between a donor and an accepter with the metal ion playing generally the role of an acceptor. Dopants based on rare earth elements in mixed oxide systems offer opportunity to tune in color response through manipulation of energy gaps in conduction band and valance band.
- ✓ Elements are suitably chosen such that the pigment need only low temperature calcination and thus can prevent particle growth.
- ✓ Infrared reflective pigments can be utilized to minimize heat build in objects exposed to sunlight resulting in local energy efficiencies and physical performance enhancement. They will reflect a significant amount of solar radiation away from colored surfaces to keep them cooler. Reflectance is achieved by the physical back scattering of radiation through pigment particles. The reflected radiation comprises not only the visible spectrum of wavelength range 400 to 700 nm, but also the UV (<400 nm) and NIR (700 to 2,500 nm) radiation. Among them, the NIR radiation dominates the overall irradiated solar energy by more than 50 percent, thus called near infrared reflective pigments.

1.3.7 NIR Reflecting Pigments

Earth's average surface temperature is increasing due to effect of greenhouse gases such as carbon dioxide emissions from burning fossil fuels or from deforestation as a result of global warming, which trap heat that would otherwise escape from Earth. 45% of the total solar energy is in the non-visible infrared region.

Heat is a direct consequence of infrared radiation incident on an object. Infrared radiation ranges from 700-2500 nm wavelength. The wavelength ranges from 700-1100 nm produces more heat. These radiations on absorption result in heating up of the surface. A cool roof is one that strongly reflects sunlight and also cools itself by efficiently emitting radiation to its surroundings. This can be achieved by using the solar reflectance property of some pigments called the NIR reflecting pigments (Bendiganavale et al. 2008). These cool coatings lower roof surface temperature which in turn reduces the need for cooling energy in conditioned buildings and makes unconditioned buildings more comfortable. If a builder does not have air conditioning, these cool roofs keep the building cooler and a more constant temperature. A cool roof need not be white. There are many 'cool color' products which use darker-colored pigments that are highly reflective in the near infrared (non-visible) portion of the solar spectrum. The two basic characteristics that determine the "coolness" of a roof are solar reflectance (SR) and thermal emittance (TE). The schematic representation of SR and TE is shown in Fig 1.6.

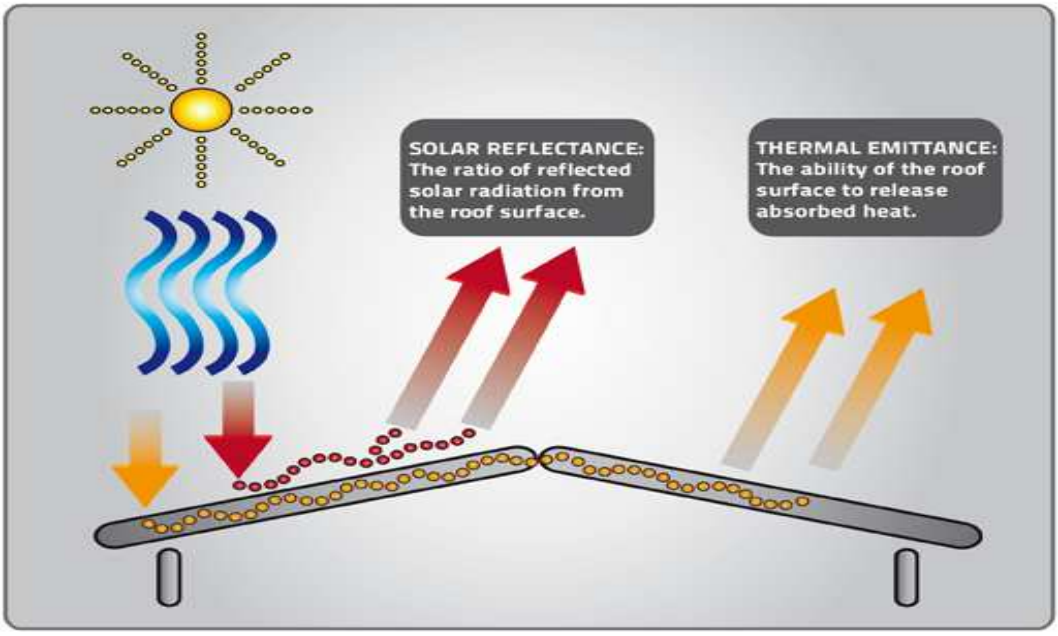

Fig. 1.6 Schematic representation of solar reflectance and thermal emittance (http://www.siplast-international.com/environmentDetail/CoolRoof)

IR reflective pigments are increasingly used for roof and building coatings because of their weatherability. In urban areas, the design of roofs has a major influence in the heat absorption of sunlight. The hot buildings also known as

'Concrete Jungle' radiates heat and warm the air in the surroundings. If there are several such buildings in the vicinity, the combined effect lead to a phenomenon called 'Urban Heat Island effect'.

Infrared reflective pigmentation technology allows to achieving a specific color space in the visible light range while reflecting incident light in the near infrared (NIR) range of the electromagnetic spectrum. The reflection of the light in the NIR reduces the temperature of the coated object by lowering overall energy absorption from terrestrial solar irradiance. When designing an infrared reflective pigment, maximizing solar reflectance and emissivity and minimizing all contamination by infrared absorbing materials is necessary. Contamination must be eliminated from NIR pigments in order to achieve maximum reflective properties. The NIR reflecting pigments are highly stable and chemically inert. They can withstand the chemically aggressive environments and still retain their color. They do not fade in the presence of ozone, acid rain, SO_x, NO_x or other air pollutants common in industrial areas. They even remain color in the presence of strong acids, bases, oxidizing or reducing agents. They do not dissolve when in contact with the solvent. In addition, they are stable at high temperature, thus used for high heat coating.

General benefits of infrared reflective coating are,

- Longer life cycle due to less polymer degradation and thermal expansion due to lower temperature,
- Aesthetically pleasing color,
- Cooler to touch for better handling,
- Improved system durability and less thermal degradation,
- Energy consumption by avoiding air conditioning purposes,
- Lowering roof maintenance costs and extend roof life, avoiding reroofing costs and reducing solid waste
- Lighten community's Urban Heat Island Effect.

Particle size of a pigment is very essential in determining the IR reflective ability of a pigment. The particle size should be more than half of the wavelength of the light to be reflected. Thus for infrared light of 700-1100 nm wavelength, the particle size should be about 0.35-0.55 microns. Thus excessive grinding and dispersion may therefore be counterproductive.

NIR reflective pigment has another major application that, they can be used for camouflage applications (Jeevanandam et al. 2007). The most common colors in the military area are green, brown, black and desert yellow. A very important property of camouflage pigments is that they can merge an object with its surrounding in the visible as well as in infrared light. As the environment has a natural reflection in the infrared light, the camouflage pigments also need to show this reflection. The production of camouflage pigments is very demanding as only a limited number of inorganic pigments show a suitable spectral curve in the IR area.

1.4 Cerium dioxide (CeO_2): An Optical Material

In recent technology, optical materials play a vital role in various fields of science, such as physics, chemistry and materials sciences. In the general sense, optical materials can be defined as materials whose function is to alter or control electromagnetic radiation in the ultraviolet (UV), visible or infrared (IR) spectral regions. At the microscopic level, atoms and their electronic configurations in the material interact with the electromagnetic radiation (photons) to determine its macroscopic optical properties such as transmission and refraction. These optical properties are functions of the wavelength of the incident light, the temperature of the material, the applied pressure on the material, and in certain instances the external electric and magnetic fields applied to the materials. There is a wide range of substances that are useful as optical materials (Sudarsan et al. 2012). Many of optical materials, including metal oxides, ferrites, rare-earth oxides and so on, have been developed. In the choice of a material, the important properties are degree of transparency, refractive index, the uniformity of the material, thermal and chemical stability, hydroscopic nature etc are need to be considered.

Cerium (Ce) belongs to the rare-earth family and its abundance tin (66.5 ppm) is much higher than copper and tin (60 and 2.3 ppm, respectively) (Veronica et al. 2007). Cerium usually has two types of oxides named cerium dioxide (CeO_2) and cerium sesquioxide (Ce_2O_3), but in a larger context, CeO_2 is used as cerium oxide due to higher stability over Ce_2O_3. CeO_2 is a wide bandgap semiconductor ($\sim$ 3.4 eV), which is considered as an important optical material because of its unique properties such as a high refractive index (2.2-2.8), high dc dielectric constant (2.6 $MVcm^{-1}$), optical transparency and non-toxicity etc. The chemical functionalization

of CeO_2 is a well-known method for tuning the band structure and majority carrier type for optical applications (Khan et al. 2014). Its high abundance as well as its excellent optical, physical and chemical properties made this material technologically important with wide applications in various optical sectors, such as optical coatings, in ultraviolet shielding materials, pigments, electro-optical microelectronic and optoelectronic devices, phosphors, electrochromic thin - film application and also in various sectors like auto-exhaust catalyst, low-temperature water-gas shift (WGS) reaction, oxygen sensors, oxygen permeation membrane systems, solid oxide fuel cells, glass-polishing materials, as well as biotechnology, environmental chemistry and medicine (Maksimchuk et al. 2013) (Fig. 1.7).

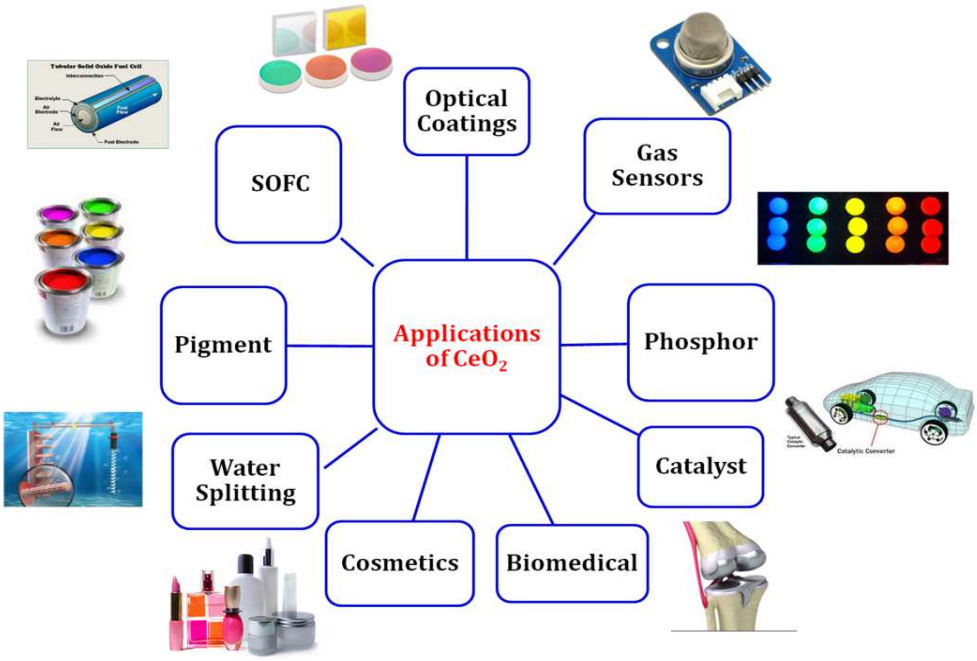

Fig. 1.7 Various application of CeO_2.

1.4.1 Cerium oxide (CeO_2): material properties

1.4.1.1 Electronic configuration

The ground state electronic configuration of the lanthanides are generally expressed of the type $[Xe]4f^n5d^16s^2$ or $[Xe]4f^{n+1}6s^2$, where the increase in n from 0 to 14 corresponds to the change from La (Z = 57) to Lu (Z = 71). Cerium dioxide (CeO_2/ceria) is considered as the most stable oxide form of the cerium. Cerium is the second member and the most reactive element in the lanthanide series. It is electropositive in nature; cerium can exist in dual oxidation states, 3+ and 4+. The

Ce^{4+} oxidation state is generally considered more stable than 3+ due to the stable electronic structure Ce(4+) $[Xe]4f^0$ than the electronic structure Ce(3+) $[Xe]4f^1$.

1.4.1.2 Crystal structure

Cerium dioxide (CeO_2) is known to crystallize in fluorite structure (FCC) with a space group *Fm3m*, so called because it is the same structure as calcium fluoride (CaF_2). It is pale yellow in color due to the charge-transfer transition of O^{2-} -Ce^{4+}. Fig 1.8a shows the two unit cells of CeO_2 crystal, in which the cerium (yellow) ions is coordinated to eight equivalent oxygen (red) anions at the corner of a cube and each anions is tetrahedrally co-ordinated by four cations. This structure can also be viewed as a simple cubic array of oxygen with a cerium in the center of alternate cubes. Cubes formed by array of oxygen ions with cerium ions at alternate body center position of cube is illustrated in Figure 1.8b (Kilbourn et al; Trovarelli et al. 1997). There are obviously diagonal planes of cubes containing no cations which create voids in the planes and these voids are called octahedral holes. These octahedral holes are strongly enhancing the ions mobility through the structural defects.

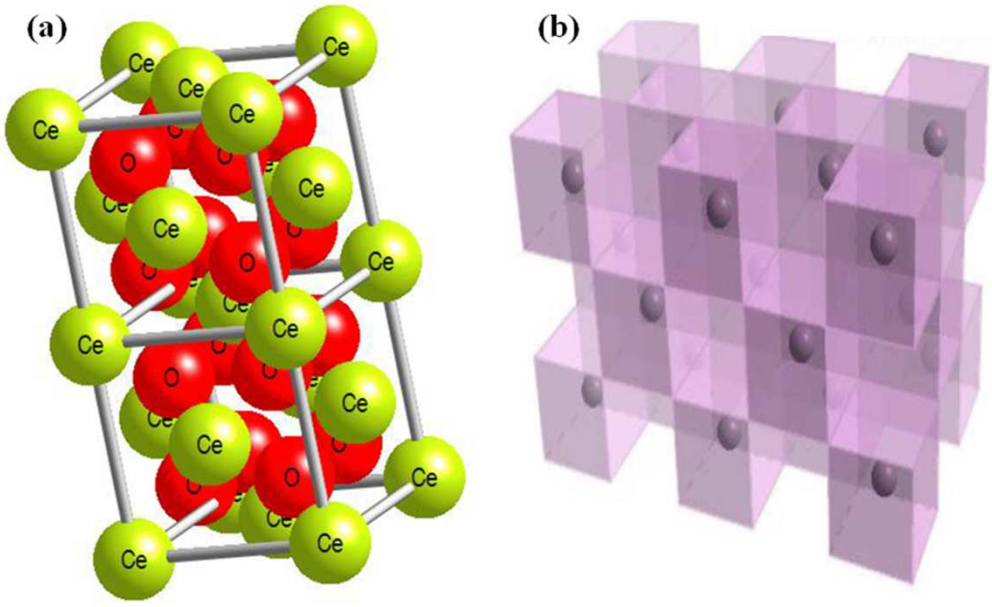

Fig. 1.8 The crystal structure of CeO_2: (a) two unit cells (b) alternate view.

1.4.1.3 Imperfections/defect in CeO_2

Imperfections in a crystal structure can be occurred due to the displacement of atoms from their lattice positions that lead to the breaking of symmetry of a

perfect periodic crystal lattice. There are two different types of defects existing in the CeO_2; intrinsic and extrinsic defects. Intrinsic defects are mainly due to thermal disorderness in the crystal, which can be formed by redox reactions between the solid and surrounding atmosphere. Frenkel and Schottky defects are considered to be more plausible crystalline intrinsic defects. The extrinsic defects are formed by introducing foreign dopant or due to impurities. Frenkel disorder is a result of an atom that is displaced from its lattice site to an interstitial site, forming a defect pair made of vacancy–interstitial and is expressed as

$$Ce_{Ce} + 2O_O \rightleftarrows V_{Ce}^{3+} + V_O^{2-} + CeO_2 \quad (1.1)$$

where V_O^{2-} and V_{Ce}^{3+} are the oxygen and cerium vacancies. The Schottky defect is obtained by removal of cations and anions in formula units to form vacant lattice sites and is given in the following equation:

$$O_O \rightleftarrows O_{int}^{2+} + V_O^{2-} \quad (1.2)$$

The most dominant and stable known defects in ceria is the extrinsic disorder includes defects resulting from oxidation or reduction of lattices and/or the presence of dopants, impurities, etc. in a lattice. A reversible transition in the oxidation state of two cerium ions from Ce^{3+} to Ce^{4+} may generate neutral oxygen vacancies in ceria and the process can be expressed as

$$O^{2-} + 2Ce^{4+} \rightarrow 2Ce^{3+} + \tfrac{1}{2}O_2 \quad (1.4)$$

Thus, a neutral species $\frac{1}{2}O_2$ (g) is formed if an oxygen ion (O^{2-}) leaves the ceria lattice. The two electrons left behind were trapped at two cerium sites, i.e. they become localized at two cerium sites.

1.4.2 Role of defects in the optical properties of CeO_2

However, defects hold different roles in different hosts. For example, they act as the emitting center in systems such as zinc oxide (Fan et al. 2004), while it can act as the PL quenching center in CeO_2 (Babu et al. 2008). As already discussed that, cerium oxide is well known for having large deviations in stoichiometry as a result of the easy reducibility of Ce^{4+} ions to Ce^{3+} ions. The simultaneous reduction of Ce^{4+} to Ce^{3+} results in the releasing of oxygen in a low oxygen environment found uses in three way catalyst (TWC) for its oxygen storage capacity. However such reduction of cerium is deleterious in optical properties. The tetravalent cerium ion (Ce^{4+}) has no 4f electrons and a strong light absorption through charge transfer (CT) from O^{2-} to

Ce^{4+} around 370 nm, which makes it a promising optical host material. In this regard the optical properties like photoluminescence and colouring properties of Cerium based compounds are studied by doping with various rare earth elements such as Eu^{3+}, Tb^{3+}, Pr^{3+} etc. However the substitution of such trivalent ions creates oxygen vacancies to compensate for the effective negative charge associated with the trivalent dopant. In the case of Eu^{3+}-doped cerium oxide red phosphor, the substitution of Eu in the CeO_2 lattice creates oxygen vacancies and the luminescence in Eu^{3+}-doped CeO_2 is mainly limited by the number of oxygen vacancies. These oxygen vacancies act as PL-quenching centres and adversely affect the PL of Eu^{3+} by controlling the radiative route of emission. Similarly, in the case of pigments, the reduction of Ce^{4+} to Ce^{3+} oxidation state decreases the band gap of the material which in turn results in the more absorption in UV-vis wavelength range. These factors decrease the lightness as well the pleasing nature of the pigment. Further, the NIR reflectance properties also adversely affected and it limits the energy saving applications of cerium based oxides. Hence the defects/imperfections adversely affect the optical properties of the ceria limiting its applications. In view of this, it is more difficult to achieve a sizeable luminescence and good colouristic characteristics for use in practical applications in the CeO_2 lattice.

1.4.2.1 How to overcome

Though ceria has its inherent properties such as oxygen vacancy defects and readily available redox nature (Ce^{4+}/Ce^{3+}), it still needs modifications to improve its optical performance for use cerium based oxides in practical applications. We can manipulate the cerium based oxides for distorting and local environment for the reduction in the defects/imperfections formation through

- Doping with different rare earth elements
- Structural transformation
- Ordering in the lattice
- Oxygen vacancy ordering
- Reducing Ce^{3+} concentration
- Band gap tuning by using various elements

Cerium oxide has a fluorite structure with every Ce ion surrounded by eight equatorial oxygen ions in O_h symmetry. The ideal fluorite structure is a simple crystal structure with a general formula AO_2. However, the defect fluorite structure

is anion-deficient with a formula of $AO_{1.75}$. To improve the properties of cubic fluorite ceria, suitable metal elements can be incorporated into it to form a mixed solid ceria–based oxides. The dopant ion selection obviously plays an important role in modifying the chemical and physical properties of the produced mixed oxide. For instance, the concentration of oxygen vacancies that are produced during the doping of ceria depends on the oxidation state of the dopant ion and the mobility of the oxygen vacancy/oxide ion depends on the association energy of the dopant ion with the oxygen vacancy. If the additive is aliovalent cation (M^{2+}/M^{3+}) then the oxygen vacancies can be introduced due to charge compensation mechanism and thus storage and release of oxygen increases. On the other hand, for isovalent cation the oxygen vacancy/oxide ion migration aids from the strain and distortion due to mismatch of the ionic radius of the dopant and Ce–ions in the substituted sample. Figure 1.9 shows schematic presentation of CeO_2 and doped CeO_2.

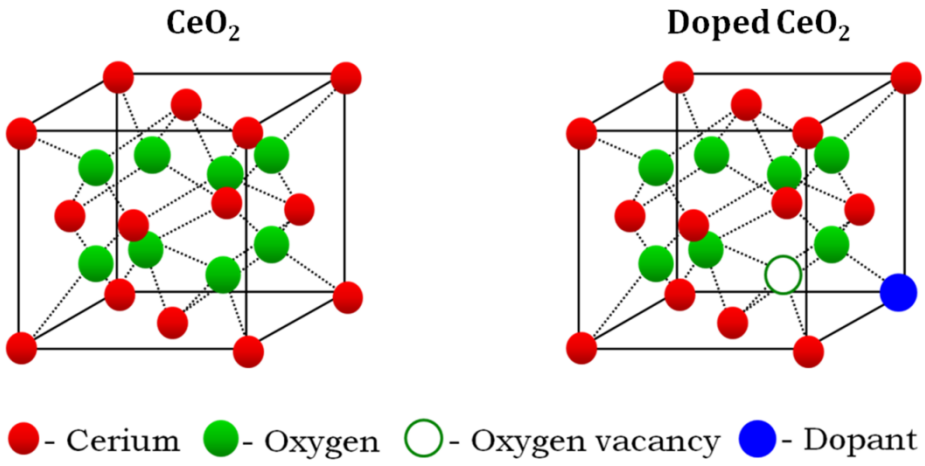

Fig. 1.9 Schematic presentation of CeO_2 and doped CeO_2.

The interesting properties of fluorite (F)-type structure is that it can accept various numbers of oxygen vacancies, from which pyrochlore (P)-type, Orthorhombic and Rare earth C (C)-type structures can be derived, depending on the oxygen content. The cubic C-type structure, A_2O_3 ($AO_{1.5}$), belongs to the space group Ia3 (Z = 16), which can also be recognized as an F-type structure with ordered oxygen vacancies in the anionic sub-lattice (Nishino et al. 2004). This structure may also tolerate excess anions in the presence of tetravalent lanthanides, which promotes the eight-fold coordination of the lanthanide sites. Thus the formation of the C-type phase from a defect fluorite structure incorporates more oxygen into the lattice and increases the oxygen vacancy ordering with the substitution of trivalent lanthanides

for Ce^{4+}. The Crystal structure of cubic Rare earth C-Type phase of Ln^{3+} doped CeO_2 is shown in Fig. 1.10.

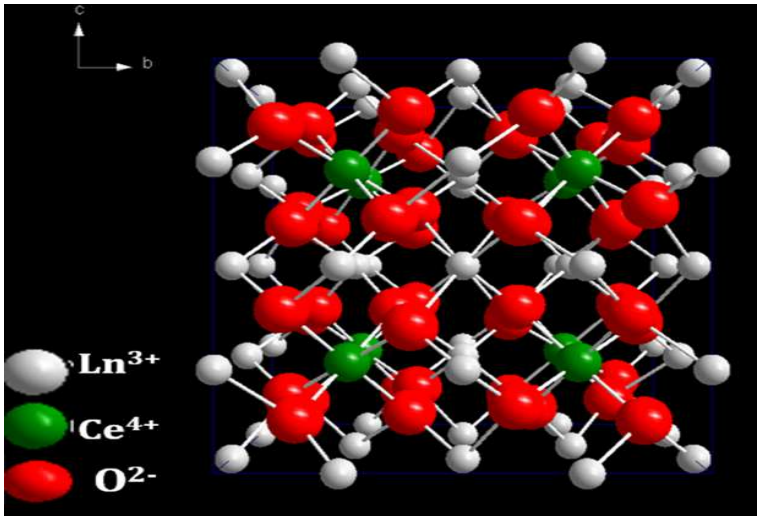

Fig. 1.10 Crystal structure of cubic Rare earth C-Type phase of Ln^{3+} doped CeO_2.

Another crystal structure based on cerium oxide is the orthorhombic, with space group *Pbam* as shown in Fig. 1.11. It can be found that the compound possesses one dimensional chain structure of edge-sharing CeO_6 octahedron, with two terminal oxygen atoms per cerium center, that are isolated from one another by M^{2+} cations (Pieterson et al. 2000).There are two molecules per unit cell. Each cerium atom is coordinated by six oxygen atoms. These octahedrons present two trans-terminal Ce–O1bonds perpendiculars to the plane defined by four equatorial O2 atoms, while the Ce–O1 bonds are about 0.1Å shorter than the Ce–O2 bonds.

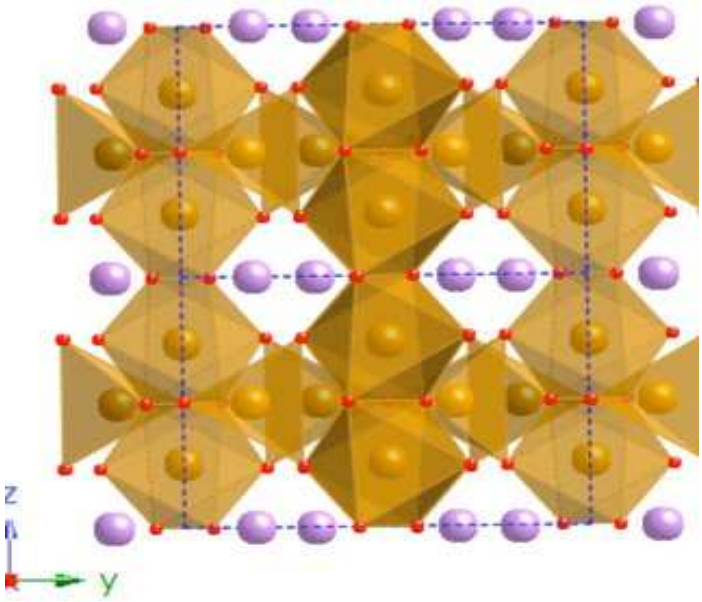

Fig. 1.11 Crystal structure of orthorhombic M_2CeO_4.

1.4.3 Literature review on cerium based red phosphors

Avram et al reported on the homogeneity, structural and luminescence properties of ceria nanoparticles doped with Eu^{3+}. Eu^{3+} in concentration of 1, 5 and 10 wt% was incorporated via wetness impregnation into preformed ceria nanoparticles followed by calcination in air at 1000 °C. A remarkable homogeneity of Eu^{3+}-ceria solid solutions was measured for ceria grown by citrate and micro-emulsion methods using Raman, Diffuse Reflectance in UV–Vis, photoluminescence spectroscopies and X-ray diffraction, even for the Eu^{3+} concentration of 10 wt%. The emission properties of all Eu^{3+} -doped ceria samples were well-characterized by a two main centre model assigned to perturbed and isolated Eu^{3+} centres. These centres correspond to Eu^{3+} located in the nearest (local symmetry lower than cubic and Eu^{3+}-oxygen coordination lower than eight) and next nearest-neighbour positions (cubic local symmetry and eightfold Eu^{3+}-oxygen coordination) to oxygen vacancy, respectively. With increase of Eu^{3+} concentration, both the oxygen vacancy concentration and the relative contribution of the perturbed Eu^{3+} centre to the total emission increase. It was established that the characteristic emission and excitation spectra of the two main Eu^{3+} centres as well as the overall multisite distribution of Eu^{3+} within ceria lattice are intrinsic properties of Eu^{3+}-doped ceria since these do not depend on synthesis route, nanoparticle size and Eu^{3+} concentration (Avram et al 2015).

The luminescence properties of Ln (Eu, Sm, Dy, and Er) doped CeO_2 nanoparticles have been in-depth investigated by low temperature, site selective, time-resolved luminescence spectroscopy by Daniel et al. The measurements sustain a physical model based on two distinct Ln centers which substitute for Ce fluorite sites but differ by the presence of zero vacancy (cubic center) and one vacancy (Ln−vacancy associate) in the first oxygen coordination shell. On the basis of the first reported example of Dy emission in site with inversion symmetry, the use of Dy as a structural probe is re-evaluated. The emission shape and decay of the cubic Ln centers measured before and after high temperature calcination are highly similar, that is, tentatively assigned to a nonrandom distribution of the oxygen vacancies into the ceria lattice. The dependence of the luminescence decays on Ln concentration indicates that the cross-relaxation in Ln−Ln pairs prevails over the subsequently induced oxygen vacancies as nonradiative quenching paths. The

effects of Ln concentration and subsequently induced oxygen vacancies on sensitization of Ln emission can be discriminated by choosing the Er, La codoped CeO_2 as a model system. Finally, it was shown that the Ln luminescence effectively reveals the effects of Zr doping on CeO_2 at the atomic scale, a significant effect being that Zr scavenges the Ln induced oxygen vacancies.

A novel synthesis strategy to prepare CeO_2:Eu^{3+} nanophosphors and its luminescence behaviour was reported by Vimal et al. Different structural characterization techniques such as X-ray diffraction, transmission electron microscope and thermogravimetric analysis revealed that thermal decomposition of oxalate precursor was an effective pathway to produce rare earth oxide nanocrystals. Optical characterizations of the CeO_2:Eu^{3+} were done by UV–Visible absorption, photoluminescence excitation and emission spectra. The presence of structural defects and their role on the band gap and luminescence were discussed on the basis of absorption and emission studies. Luminescence study of the CeO_2:Eu^{3+} ensures that the strong charge transfer band of CeO_2 makes it a suitable host material for efficiently exciting Eu^{3+} ions by subsequent energy transfer. The dependence of luminescence efficiency of the CeO_2:Eu^{3+} with varying concentrations of Eu^{3+} was also studied and discussed. The results show that Eu^{3+}-doped CeO_2 nanophosphor is a potential candidate in ultraviolet-based LEDs (Vimal et al. 2015).

Enhancing the optical emission of cerium oxide nanoparticles is essential for potential biomedical applications. In the present work, Kumar et al reported a simple chemical precipitation technique to synthesize europium-doped cerium oxide nanostructures to enhance the emission properties. Structural and optical properties showed an acute dependence on the concentration of oxygen ion vacancy and trivalent cerium, which, in turn, could be modified by dopant concentration and the annealing temperature. Results from X-ray photoelectron spectroscopy showed an increase in tetravalent cerium concentration to 85% on annealing at 900 °C. The concentration of oxygen ion vacancy increased from 1.7×10^{20} cm^{-3} to 4.1×10^{20} cm^{-3} with the increase in dopant concentration. Maximum emission at room temperature was obtained for 15 mol % Eu-doped ceria, which improved with annealing temperature. The oxygen ion vacancies and trivalent cerium played an important role in modifying the emission properties (Kumar et al. 2009).

Liu et al reported CeO_2:Eu^{3+} phosphor powders with various Eu^{3+} concentrations had synthesized by the solid-state reaction method. XRD analysis showed the formation of pure cubic fluorite phase up to 10 mol% doping concentration of Eu^{3+}. The dependence of PL emission intensity on the Eu^{3+} concentrations shows the different behavior for direct excitation at 467 nm and indirect excitation of CeO_2 host at 373 nm. The nature of this behavior is closely related to the defects and symmetry distortion generated by Eu^{3+} replacing Ce^{4+}. The cause of the concentration quenching is likely to be due to the nonradiative recombination centers created by the Eu^{3+} doping, which hinder the energy transfer from CeO_2 host to Eu^{3+} (Liu et al. 2007).

Wang et al. synthesized the CeO_2 nanocrystals doped and undoped with trivalent lanthanide ions (Eu^{3+}, Sm^{3+}, Tb^{3+}) and discussed their optical properties. The as-prepared CeO_2 and CeO_2:Eu^{3+} (Sm^{3+}, Tb^{3+}) nanocrystals are highly uniform and can be dispersed in hexane to form a transparent colloidal solution. The absorption spectrum of CeO_2:Eu^{3+} nanocrystals exhibit a red shift with respect to that of undoped CeO_2 nanocrystals; i.e., the blocking range for UV is enhanced by doping lanthanide ions in CeO_2 nanocrystals and it showed a remarkable enhanced PL intensity with respect to the CeO_2 nanocrystals due to the increase of oxygen vacancy in the CeO_2 nanocrystals (Wang et al. 2007).

Here a facile electrochemical deposition route was developed for the synthesis of Eu^{3+} ion doped CeO_2 nanobelts by Wang et al. $Ce(OH)_3$ as the intermediate is crucial for the growth of Eu^{3+}-doped CeO_2 nanobelts. TEM results showed that these synthesized nanobelts have a polycrystalline structure. XPS results indicate these obtained deposits are Eu^{3+}-doped CeO_2 with a small quantity of impurity of Ce^{3+} oxidation state. The results of XRD indicate Eu^{3+}-doped CeO_2 nanobelts are well-crystallized and have a cubic structure. It can be clearly observed that the absorption spectrum of Eu^{3+}- doped CeO_2 nanobelts obviously exhibited a red shift and a stronger absorption compared with those of Eu^{3+}-doped CeO_2 nanosheets and CeO_2 nanosheets. The PL spectrum of Eu^{3+}- doped CeO_2 nanobelts shows remarkable enhancement compared with Eu^{3+}-doped CeO_2 nanosheets and CeO_2 nanosheets because of the rapidly increasing oxygen vacancies and their special morphologies. Importantly, this cardinal principle of shape and doping

enhanced optical properties of Eu^{3+}-doped CeO_2 nanobelts is expected to apply to other RE^{3+}-doped CeO_2 systems (Wang et al. 2011).

Octahedral CeO_2:Eu^{3+} nanocrystals, successfully prepared using a simple hydrothermal method, were investigated to determine their photovoltaic properties in DSSCs by Roh et al. The prepared CeO_2:Eu^{3+} nanocrystals were large in size, with mirror like facets that provided excellent light-scattering ability. UV light was converted to visible light via downconversion PL corresponding to the $^5D_0 \rightarrow {}^7F_J$ transitions of trivalent Eu^{3+} ions. By controlling the concentration of Eu^{3+}, the power conversion efficiency of the DSSC with a P25-CeO_2:Eu^{3+} photoanode exhibited the best efficiency of 8.36% at 1 mol % Eu^{3+}, which was an overall 14% enhancement, compared with that of a bare P25 photoanode. This enhanced performance was attributed to the excellent light-scattering and downconversion luminescent properties of CeO_2:Eu^{3+} nanocrystals. With further optimization of CeO_2:Eu^{3+} nanocrystals in DSSCs, it is anticipated that this dual-functional material will provide new opportunities to further enhance light absorption for highperformance DSSCs (Roh et al. 2014).

Min et al. reported CeO_2:Eu^{3+} and CeO_2:Eu^{3+}/Na^+ nanoparticles, were successfully prepared via a spray pyrolysis process. Luminescence properties, morphology and particle size were systematically studied with varying the Eu^{3+} concentration, introducing ethylene glycol, and codoping monovalent Na+ ion. A strong excitation observed around 365 nm is attributed to the charge transfer from O^{2-} to Ce^{4+}. In CeO_2:Eu^{3+}, Eu^{3+} ions are mainly located in sites with inversion symmetry. As a result, the strong emission peak at 593 nm due to the $^5D_0 \rightarrow {}^7F_1$ transition of Eu^{3+} was observed in a whole range of Eu^{3+} concentration. The local symmetry of Eu^{3+}, however, was lowered with increasing the Eu^{3+} concentration due to the lattice distortion as well as the formation of oxygen vacancies, which led to increase the peak at 612 nm due to the $^5D_0 \rightarrow {}^7F_2$ transition of Eu^{3+}. When the Eu^{3+} content was over 4%, the concentration quenching of the emission intensity was identified to occur through the dipole-dipole interaction. Introducing EG to the spray solution was found to an effective way to prepare CeO_2:Eu nanoparticles of smaller than 80 nm, but the emission intensity was largely lowered due to the reduction of particle size. This lowered emission intensity of CeO_2:Eu^{3+} nanoparticles prepared using EG could be enhanced about 16.5 times higher via codoping Na^+ with Eu^{3+} in

CeO_2 matrix, which was attributed to the charge compensation as well as the increase of crystallite size. According to the dot mapping of elements, the Ce, Eu, Na and O components were confirmed to have a uniform distribution throughout the nanoparticles without any phase separation. The use of EG and co-dopant Na^+ was experimentally identified to be a good way to synthesize high luminescent CeO_2:Eu^+ /Na^+ nanoparticles of less than 200 nm via the spray pyrolysis (Min et al. 2016).

Sorbello et al. developed monodispersed spheroidal sub-microparticles obeying the general formula $Ce_{0.95-x}Gd_xEu_{0.05}O_{1.975-x/2}$, with $0 \leq x \leq 0.95$, were obtained by the urea method coupled with a high temperature oxidative annealing. Samples with $0.57 \leq x \leq 0.95$ exhibit a c-type structure while a *Fm3m*-type structure was found for $0 \leq x \leq 0.19$. For both ternary families, the partial substitution of host cations dramatically decreases the efficiency of the ligand to metal charge transfer (LMCT) based emission, with respect to their binary end members. The present Eu(III) based phosphors offer the possibility to be used as bio-probes given their ability to be excited at non-harmful radiation ranges. For both structures, the binary Ce(IV)–Gd(III) host improved emission with respect to $Gd_{0.95}Eu_{0.05}O_{1.5}$ and $Ce_{0.95}Eu_{0.05}O_{1.975}$ hosts, achieving an optimum value for the sample $Ce_{0.23}Gd_{0.71}Eu_{0.05}O_{1.6}$ with a *Ia3* structure (Sorbello et al. 2014).

For the first time, Eu-doped nanoceria have been achieved by the SCS approach and their photoluminescence and X-ray luminescence properties had been reported by Shi et al. The samples can emit typical red luminescence by adjusting the excitation wavelength and the Eu^{3+} concentration. At low Eu^{3+} concentrations, the sample can be effectively excited with 360 nm. With the increase of the Eu^{3+} concentration, the dominant excitation wavelength is changed to 466 nm, and the quenching concentration of Eu^{3+} is increased to 16 mol%. Under the excitation of X-ray, the samples can also display strong red luminescence through optimizing the Eu doping concentration. Consequently, the CeO_2:Eu phosphor nanopowders may be potential candidates for the use of solid state lighting and radiation detection (Shi et al. 2012).

1.4.4 Literature review on cerium based inorganic pigments

Ln–CeO_2 (Ln = Pr, Tb, Eu) and M–CeO_2 solid solutions (reference samples with M = Cr or In, as transition and main group elements, respectively) had been

prepared by ceramic and coprecipitation routes by Garcia et al. in 2001. The resulting coloured materials were checked as potential pigments for porcelainised stoneware. The colouring mechanism in this system based on the introduction of an additional electronic level of energy in cerianite forbidden band, arising from unpaired 4f electrons of lanthanide ions. The red ceramic pigments obtained were found to be interesting alternatives for the coloration of porcelainised stoneware bodies. In addition, they present a much lower toxicity than classical cadmium sulfoselenide or chromium–$LnAlO_3$ based red pigments, because both the chromophoric agent (praseodymium and europium ions) and ceramic matrix (cerianite) contain lanthanide elements.

Tesitelova et al 2017 was successfully synthesized novel environment-friendly yellow mixed oxide inorganic pigment from Bi_2O_3–ZnO–CeO_2 system with the composition 23 mol% Bi_2O_3, 15 mol% ZnO and 62 mol% CeO_2 by a conventional solid-state reaction method. Comprehensive analyses were carried out to characterize the develop pigment powder including simultaneous TG–DTA thermal analysis, colour properties and particle size distribution. The results demonstrated that the optimum calcination for pigment synthesis was located at a range 800–950°C. The colour of the studied mixed oxide pigment is connected with the calcination condition. The substitution of Zn^{2+} changes the colour from orange to yellow. The colour of the obtained samples was dependent on the calcination condition and the particle size distribution. The most saturated yellow hue was obtained at the calcination temperature of 950°C for 2 h in a furnace of pure air and after its application into organic binder in mass tone. The value C of this sample was approx. 65. The mixed oxide pigments were also evaluated from the standpoint of their particle size distribution. $Bi_2Ce_2O_7$ is considered to be a non-toxic compound, and the other component (Zn^{2+} ions) is also the safe element. Therefore, the present mixed oxide could be an attractive candidate as a novel environment-friendly inorganic yellow pigment.

In the present study, $Ce_{0.36}Si_{0.31-z}Bi_{0.33}Al_zO_{2-(0.33+z)/2}$ solid solutions were successfully synthesized by Wendusu et at. to enhance the thermal stability as well as the yellow hue of the $Ce_{0.36}Si_{0.31}Bi_{0.33}O_{1.835}$ pigment, which was previously reported them. The thermal stability of the pigments depended on the amount of Al^{3+}, and the $Ce_{0.35}Si_{0.24}Bi_{0.32}Al_{0.09}O_{1.795}$ pigment maintained its cubic fluorite

structure in a single phase form up to 1173 K. Furthermore, the yellow hue was also enhanced by both the optimum Al^{3+} doping and heating temperature resulting in the highest yellowness value being obtained for $Ce_{0.35}Si_{0.24}Bi_{0.32}Al_{0.09}O_{1.795}$ calcined at 1123 K. The $L^*a^*b^*$ color coordinate values of this sample were L^* = 74.5, a^* = +11.6, and b^* = +75.1, where the b^* value corresponding to the yellowness was greater than that of the commercial praseodymium yellow (b^* = +70.3). Since the present pigment composed of only nontoxic elements (Ce, Si, Bi, Al, and O), it could be an effective alternative to the conventional toxic pigments.

New inorganic pigments having the general formula $Ce_{1-(x+y)}Zr_xTa_yO2+\delta$ (x ranges from 0.15 to 0.2 and y ranges from 0 to 0.05) displaying colors ranging from white to yellow have been synthesized by a traditional solid-state route, as viable alternatives to lead, cadmium and chromium based yellow toxic inorganic colorants were prepared by Vishnu et al. 2009. The products were characterized by X-ray powder diffraction, UV–vis diffuse reflectance spectroscopy and CIE-$L^*a^*b^*$ 1976 color scales. The coloring mechanism is based on the strong absorptions of the pigments in the visible region under 500 nm, which could originate from the additional energy level between O2p valence band and the Ce4f conduction band by forming a hybrid orbital of Ta5d and O2p. The band gap of these colorants gently changes from 3.0 to 2.34 eV with increasing doping of tantalum. The developed pigments are found to be thermally and chemically stable and also do not contain toxic metals. Thus, the present pigments may find potential alternative to the classical toxic yellow inorganic pigments for various surface coating applications.

Ceramic pigments, CeO_2. α-Fe_2O_3 and CeO_2. α-Pr_6O_{11} systems, were synthesized by Olegario et al. 2013 through the solid state reaction at 1300 C/3 h and modified solgel method at 1300 °C/3 h. The presence of secondary phases was observed in pigments of the CeO_2. α-Fe_2O_3 system, for the CeO_2. α-Pr_6O_{11} system, single phase pigments were obtained both in the synthesis through the solid state reaction and the modified solgel. The addition of dopants (Fe^{3+} or $Pr^{3+/4+}$) in the CeO_2 lattice caused distortions in the lattice, reducing the band gap value and allowing energy absorption within the visible region. The shades obtained were light-brown to reddish-orange for the CeO_2. α-Fe_2O_3 system and shades of light brown to earth-brown for the CeO_2. α-Pr_6O_{11} system, which is promising to the use

as pigments in substitution to those containing toxic pigments, once the oxides under study present low toxicity.

Ecological red pigments $Ce_{0.95}Pr_{0.05-x}M_xO_2$ (M = Mn, Si) have been synthesized by Kumari et al. 2012 through conventional solid-state route and characterized by X-ray diffractometer, scanning electron microscope and UV–vis spectroscopy. Mn^{4+}/Si^{4+} were incorporated into the CeO_2–PrO_2 system to tune the color properties of the pigments by shifting the optical absorption edge. Si^{4+} substitution blue shifts the absorption edge of Pr-doped ceria and shows bright reddish brown color. Mn^{4+} substitution stabilizes the absorption edge and exhibits dark brown hue. The coloring mechanism is based on the shift of charge transfer band of CeO_2 to higher wavelength by co-substitution of Pr^{4+} and tetravalent metal ions in ceria. Si co-doped pigments possess smaller particles and hence exhibit more lightness compared to Mn co-doped samples. The reddish brown pigments exhibit very good coloring performance in polymer matrix. These $Ce_{0.95}Pr_{0.05-x}M_xO_2$ (M = Mn, Si) pigments have potential to be used as ecological red pigments for coloration of plastics.

Chen et al. 2018 had successfully developed a series of non-toxic cool pigments $La_2Ce_{2-x}W_{0.5x}Fe_{0.5x}O_{7+\delta}$ (x = 0.1, 0.3, 0.5, 0.7, 0.9) by the Pechini route. The W^{6+} and Fe^{3+} co-doped $La_2Ce_2O_7$ yellow-orange pigments contributed to high NIR solar reflectance. The higher calcination temperature improved the color performance as well as reduced their NIR reflectance slightly. The typical pigment $La_2Ce_{1.7}W_{0.15}Fe_{0.15}O_{7+\delta}$ (calcined at 1150°C) was coated on a galvanized sheet and showed a good yellow color (L^* = 67.98, a^* = 16.75, b^* = 50.10). In addition, the coating possessed high NIR solar reflectance of 71.01% which is agreed with the Chinese architectural standard. The synthesized $La_2Ce_{1.3}W_{0.35}Fe_{0.35}O_{7+\delta}$ were chemically stable survived under adverse environmental conditions. The developed non-toxic and sustainable yellow-orange pigment can be used as energy-saving coatings in building facade and automotive coating for reducing the interior temperature.

The environmentally friendly pigments based on Pr^{4+} and Tb^{4+} doped $La_2Ce_2O_7$ inorganic pigments have been synthesized for the first time by Huang et al. via a Sol-Gel method. The pigments of $La_2Ce_{2-x}Pr_xO_7$ and $La_2Ce_{2-x}Tb_xO_7$ (x = 0, 0.01, 0.05, 0.1, 0.2, 0.3, 0.4, 0.5) were of a disordered defect fluorite type structure, the

two types of pigments exhibited a color evolution from light yellow, soft orange to dark orange, which can be attributed to the incorporation of suitable chromophore metal ions (Pr^{4+} or Tb^{4+}) in the $La_2Ce_2O_7$ crystal, and the charge transfer band of O_{2p}-Ce_{4f} shift to the longer wavelength. Furthermore, the Pr doped pigment possessed an outstanding NIR solar reflectance over 72.47% in the range of 700-2500 nm, and the value of Tb doped pigments was 87.41%, which was pretty high with the dark orange color (L^* = 51.35, a^* = 15.94, b^* = 17.57). The pigments also showed the high NIR solar reflectance in their coatings on the galvanized sheet (>55.64% for Pr-doped pigments and >57.8% for Tb-doped pigments), which can be used as "cool pigments" applied in the building roofing and facade materials. Moreover, the pigments are chemically stable towards the acid/alkali testing. As a result, the Pr^{4+} and Tb^{4+} doped $La_2Ce_2O_7$ compounds with high NIR solar reflectance would be non-toxic, environment-friendly, chemically stable pigments for coating applications.

In the presented work, Zhao et al. 2013 had prepared a novel yellow pigments $Y_2Ce_{2-x}Fe_xO_{7+\delta}$ (x = 0.00, 0.05, 0.10, 0.15) with high NIR reflectance. The doping of Fe^{3+} ions changes the color of pigments from ivory white to light yellow, which is attributed to the charge transfer transitions between O2p and Fe3d. Moreover, the powder samples possess very high NIR reflectance (>80.6%), and when used as building roofing materials, the pigmented coatings showing the solar reflectance (>65.3%) much higher than early reports. In addition, the indoor air temperature difference of building coatings made by these pigments and standard pigments for roofs can arrive at 3.5 °C, so these pigments could be well serve as "cool pigments" used for building roofing materials.

The main aim of the work was carried out by Sulcova et al. 2008 was to synthesize inorganic pigments based on the perovskite structure of strontium stannate doped by terbium cations, and to find out whether additional substitution of tin ions by ions of cerium or titanium can affect its colour properties and extend their applicability in ceramic industry for colouring of glazes. The pigments were synthesized by the common ceramic method, i.e., solid state reaction, upgraded by an activation of the precursors by mechano-chemical treatment. The particle size d50 of all pigments was between 2-3 μm. Strontium stannate pigments doped by terbium are characterised by intensive yellow colour hue; they are thermally very stable, but in application into a ceramic glaze their colour becomes not interesting.

Substitution of Sn (IV) ions by Ce (IV) ions has a positive effect on the colour properties. The increasing content of cerium causes the formation of pigments with the increased amount of yellow colour hue; the pigments are thermally stable to the temperature of 1200°C, and they are applicable into a ceramic glaze. In the ceramic glaze, they form yellow-orange glossy surfaces without any defects. The pigment $SrSn_{0.4}Ce_{0.2}Tb_{0.4}O_3$ can be recommended for colouring of organic binders and ceramic glazes, especially, for colouring of the decorative, lead containing high temperature glazes. Substitution of SnIV ions by ions of Ti IV was effective only in application into an organic binder. In this application the samples provide brighter yellow hues, but in application into the ceramic glaze, the yellow colour hue is lost and the applications become white.

1.5 Objectives of the present work

From the literature review, the fundamental understanding of the distribution and local structure of trivalent rare earth dopants and their role with respect to ionic radius, rare-earth concentration, oxygen vacancies and Ce^{3+} concentrations and how these factors control optical properties of ceria based phosphors and pigments are still lacking. The primary aim of this research work is to decipher the correlation between these factors in the optical properties and to develop novel and potential red phosphor and inorganic red and yellow pigment candidates to be used as energy saving products. Our objective also includes correlating various aspects like structural variation with respect to the rare earth substitutions, morphology and photoluminescence/coloring/reflectance properties of developed ceria based oxides. Focus will be given to the methods for improving the red luminescence and coloring value in CeO_2 based host structures through compositional, structural, Ce^{3+} concentration variation and thereby ordering the oxygen vacancy and reducing the defects/imperfections in the system and also optimizing the doping concentration.

Chapter 2

Influence of local structure on photoluminescence properties of Eu^{3+} doped CeO_2red phosphors through induced oxygen vacancies by contrasting rare earth substitutions

The influence of contrasting rare earth substitutions (Y and La) on the $Ce_{0.9-x}RE_xO_{2-\delta}$:0.1$Eu^{3+}$ system was investigated on the local structure and associated photoluminescence properties. These substitutions have a distinct effect on local structure, absorption, luminescence and lifetimes. The smaller Y^{3+} ion substitution enables the ordering of oxygen vacancies in a lattice, inhibiting the defect formation of Ce^{3+} oxidation states while the larger La^{3+} ion substitution liberates oxygen vacancies, allowing defect formation. Consequently, the concentration of Ce^{3+} is dependent on the ionic radius of the metal ions and it has a bearing on the band gap and luminescence properties of the system. The co-substitution of contrasting rare earth metals with Eu^{3+} allow the understanding of local structure and a smaller ion like Y^{3+} greatly functionalizes CeO_2:Eu^{3+} phosphor.

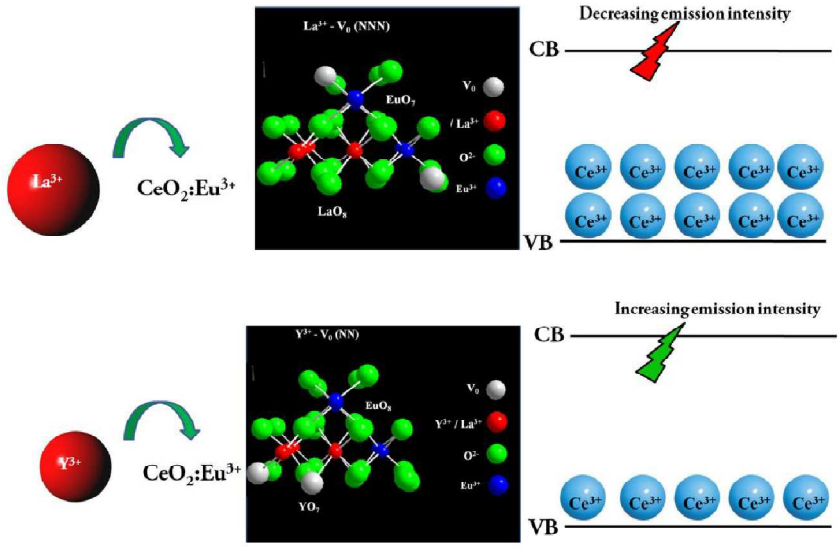

Athira et. al. ***Phys. Chem. Chem. Phys.,*** *19,* ***2017,*** *20110-20120.*

2.1 Introduction

Rare earth oxides are known to be very promising fluorescent materials due to their excellent physiochemical and optical properties (Yuan et al. 2009). The applicability of RE oxides can be tuned based on their physical and chemical characteristics resulting from 4f electronic shells. Among several rare earth oxides, CeO_2 is established as an efficient host material having a fluorite structure that has a structural tendency to substitute other activator ions, allowing a higher concentration of mobile oxygen vacancies to be incorporated into the material. It has been the focus of intense research due to its various applications in diverse areas including as solid oxide fuel cell electrolyte, a catalyst in the three-way automobile exhaust system, in oxygen storage capacitors, UV blocker and filters, efficient polishing agent for glasses, hybrid solar cells, high refractive index materials, coatings for corrosion protection of metals and alloys, cosmetics, ceramics, medicine phosphors, and as a catalyst in three-way automobile exhaust system. Cerium is one of the most important constituent in several new-generation phosphors in tricolor lamps (Tiseanu et al. 2011; Ji et al. 2008; Alammar et al. 2015; Yabe et al. 2003). The reason for extensive use of ceria in all these applications is because of the generation and migration of oxygen vacancies. Although ceria has been widely studied under prominent conditions, it becomes inefficient with time and many innate properties are affected (Reddy et al. 2010; Masui et al. 1998; Balducci et al. 2000). Hence, ceria is combined with other metal ions to make solid solutions with improved properties.

Undoped ceria has relatively small oxygen vacancy formation energy due to the capability of cerium to change oxidation state from (formally) +4 to (formally) +3 valence state. Doping ceria with aliovalent cations such as trivalent lanthanide (Ln^{3+}) ions leads to the generation of oxygen vacancies, which induces high mobility of the lattice oxygen and positively influences the thermal stability and the surface area compared to the pure oxide, and these doped ceria are found to be an important material in view of its potential applications including as solid electrolyte for use in oxygen concentration cells, in solid oxide fuel cells (Chavan et al. 2005), in controlling the air-to-fuel ratio in automobile exhaust (Logothetis et al. 1976), and phosphors (Balestrieri et al. 2015). Rare earth ion-doped ceria has been considered as potential material for many biomedical applications (Cho et al. 2012) due to its non-toxicity and excellent biocompatibility. A number of reports have appeared in

literature on rare earth oxide doping in CeO_2 during the last few decades, such as Sm_2O_3 (Wu et al. 2014), Eu_2O_3 (Primus et al. 2014), Dy_2O_3 (Horlait et al. 2011), Er_2O_3 (Avram et al. 2015), Y_2O_3 (Fan et al. 2011), Gd_2O_3 (Artini et al. 2015), La_2O_3 (Ridwan et al. 2015), Sc_2O_3 (Rahaman et al. 1995), Nd_2O_3 (Hagiwara et al. 2009), Ho_2O_3 (Carvalho et al. 2015), Tb_4O_7 (Guo et al. 2010), Pr_6O_{11} (Ahn et al. 2012) and Yb_2O_3 (Ou et al. 2006). Among the trivalent lanthanide (Ln^{3+}) ions, europium (Eu^{3+}) introduces luminescence properties in addition to being an effective probe for the local structure of ceria (Bunzil et al. 1989). However, few investigations have been carried out on the photoluminescent properties of Eu^{3+}-doped CeO_2 and these properties are dependent on the synthesis method, symmetry diversity (cubic to lower symmetries), dopant concentration, thermal treatment, Ce^{3+} concentration and oxygen vacancy content in the lattice (Avram et al. 2014; Srinivasan et al. 2011; Fujihara et al. 2004; Liu et al. 2007). When Eu^{3+} substitutes Ce^{4+} cubic sites with O_h symmetry, local environment around Eu^{3+} structure is affected by lattice strain owing to the size mismatch between Ce^{4+} and Eu^{3+} and the trapping effect of oxygen vacancies by Eu^{3+} due to charge compensation effect. Generally, the site preference of oxygen vacancies as nearest-neighbour (NN) or next-nearest-neighbor (NNN) to the dopant ion is determined by the strength and nature of their interaction, both of which are dependent on dopant ion size: lanthanides with ionic radii greater than Gd favour the interaction with the oxygen vacancy in the NNN mode, while those smaller than Gd favour that in the NN mode (Nakayama et al. 2009; Nolan et al. 2011). The luminescence properties and mechanisms in CeO_2 should strongly affect the way the lanthanides interact with defects. The bulkier lanthanides repel the oxygen vacancy from the NN position and thus eight-fold coordinated Eu^{3+} may preserve O_h symmetry of Ce^{4+} sites. In O_h symmetry, only pure electronic transitions of magnetic dipole (MD) are allowed, while electric dipole transitions are forbidden. However, the emission spectra can be more complex, since even small crystal field distortions of O_h symmetry induced by strain or distance charge compensation defect can lead to the relaxation of the transition rules. In this case, for sevenfold coordinated lanthanide, both magnetic and electric dipole transitions are allowed.

However, rare-earth co-doping in europium doped ceria is not widely reported, but (Sorbello et al. 2014) studied Ce(IV)–Gd(III)– Eu(III) oxide phosphors with respect to structural variation. The fundamental understanding of the

distribution and local structure of trivalent rare earth dopants and their role with respect to ionic radius, rare-earth concentration, oxygen vacancies and Ce^{3+} concentrations and how these factors control photoluminescence properties of europium doped ceria phosphors is still lacking. To decipher the correlation between these factors, we investigate the contrasting rare earth co-doped ceria with the general formula $Ce_{0.9-x}RE_xO_{2-\delta}:0.1Eu^{3+}$ (RE = Y and La; x = 0, 0.20, 0.40, 0.60, 0.80, and 0.90) via a conventional solid-state reaction method to probe the influence of the structure on luminescence properties. The structure, morphology, photoluminescence properties and electronic structure of the developed phosphors are characterized by powder X-ray diffraction, FT-Raman spectroscopy, transmission electron microscopy, scanning electron microscopy with energy dispersive spectrometry, X-ray photoelectron spectroscopy, UV-visible absorption, and photoluminescence and lifetime measurements.

2. 2 Experimental

2.2.1 Materials and Methods

Cerate based red phosphors $Ce_{0.9-x}RE_xO_{2-\delta}:0.1Eu^{3+}$ (RE = Y and La; x = 0, 0.20, 0.40, 0.60, 0.80, and 0.90) were synthesized by a conventional solid-state reaction technique. CeO_2, Eu_2O_3, Y_2O_3 and La_2O_3 from Sigma-Aldrich, Steinheim, Germany with 99.99% purity were used as the starting materials and the precursor oxides were in the form of fine powders. These precursors were taken in the required stoichiometric ratios and mixed thoroughly in an agate mortar using acetone as the mixing medium until a fine slurry was obtained. The slurry was dried by placing it in an air oven at a temperature of 100°C. The mixing and drying was repeated thrice to obtain a homogenous mixture. The homogeneous mixture was then calcined on a sintered alumina plate in an air atmosphere electrical furnace at 1500°C for 18 h with intermittent grinding. The temperature of the furnace was programmed with an initial heating rate of 10°C/min up to 900°C, followed by a heating rate of 5°C/ min to attain the desired temperature.

2.2.2 Characterization

The crystalline structure, phase purity and lattice parameter of the samples were examined by recording X-ray diffraction patterns using a PANalytical X'Pert Pro diffractometer having Ni filtered CuK_α radiation with X-ray tube operating at 40

kV, 30mA and 2θ varied from 10 to 90° in 0.016° steps. The Raman spectra of the powdered samples were acquired using an integrated micro-Raman system of a Labram HR 800 spectrometer (Horiba Scientific) using a 784 nm helium-neon laser with a spatial resolution of 2 mm. XPS for the selected samples was recorded on a Multilab 2000 (Thermofisher Scientific, U.K.) X-ray photoelectron spectrometer fitted with a twin anode X-ray source using Mg K_α radiation (1253.6 eV). For recording the desired spectra, the powdered samples were pressed onto a conducting carbon tape pasted with indium coated stainless steel stubs. The sample stubs were initially kept in the preparatory chamber overnight at 10^{-9} mbar to desorb any volatile species and then introduced into the analysis chamber at 9.8 x 10^{-10} mbar to record the spectra. High-resolution spectra averaged over five scans with a dwell time of 100 ms in steps of 0.02 eV were obtained for the samples at pass energy of 20 eV in the constant analyzer energy mode. To overcome the charging problem, a charge neutralizer of 2 eV was applied, and the binding energy (BE) of the C 1s core level (BE = 284.6 eV) of adventitious hydrocarbon was used as the standard. Experimental data were curve fitted with a Gaussian and Lorentzian mix product function after subtracting the Shirley background. The size and morphology of the powder particles were obtained by a scanning electron microscope (JEOL, JSM-5600LV) operated at 15 kV. The X-ray microchemical analysis and elemental mapping of the samples were carried out using Silicon Drift Detector-X-MaxN attached with a Carl Zeiss EVO18 SEM. The absorption characteristics of the synthesized samples were studied in the wavelength range 200–800 nm using a Shimadzu, UV-3600 UV-vis spectrophotometer using barium sulphate as the reference. Photoluminescence excitation and emission spectra of the prepared samples were obtained using a Spex- Fluorolog DM3000F spectrofluorometer with a 450 W xenon flash lamp as the excitation source. Luminescence lifetime of the phosphors was recorded by a phosphorimeter attached to Fluorolog®3 spectrofluorometer. All measurements were carried out at room temperature.

2.3 Results and discussion

2.3.1 Powder X-ray diffraction studies

Figs. 2.1 and 2.2 present the powder XRD patterns of the samples, $Ce_{0.9-x}RE_xO_{2-\delta}$:*0.1*$Eu^{3+}$ (RE = Y and La; x = 0, 0.2, 0.4, 0.6, 0.8 and 0.9) with different

concentrations of yttrium and lanthanum. With regard to yttrium doped samples, the occurrence of two different yet related cubic cells was observed. XRD patternsindicate a cubic fluorite type (*Fm3m* Space group) of crystallization for $x \leq 0.4$ samples and for $x \geq 0.6$ it crystallizes in a cubic C-type (*Ia3* space group) lattice. The fluorite to C-type phase transition is more evidently seen in the powder diffraction pattern by the appearance of characteristic superstructure reflections from the *hkl* planes 211, 411, 332, 134 etc. The cell parameters and crystallite size of the prepared samples are given in Table 2.1 and it can be seen that the cell parameter contracts slightly for low doping concentration i.e in the F-type region while shrinks strongly for further high doping i.e in the C-type region. The large deviations in the calculated cell parameters from Vegard's law (i.e decrease in the lattice parameter as compared to that of $Ce_{0.9}O_{2-\delta}$:*0.1*Eu^{3+}, even though the ionic size of Y^{3+}(r = 0.102 nm for CN= VIII) ion is larger than that of Ce^{4+} (r = 0. 097 nm for CN= VIII)) and it may be noted that the aliovalent substitution results in the incorporation of considerable oxygen-ion vacancy in the lattice, which causes lattice contraction. This observation is in good agreement with the earlier studies (Nakamura et al. 2010; Coduri et al. 2013; Chavan et al. 2005; Chavan et al. 2004).

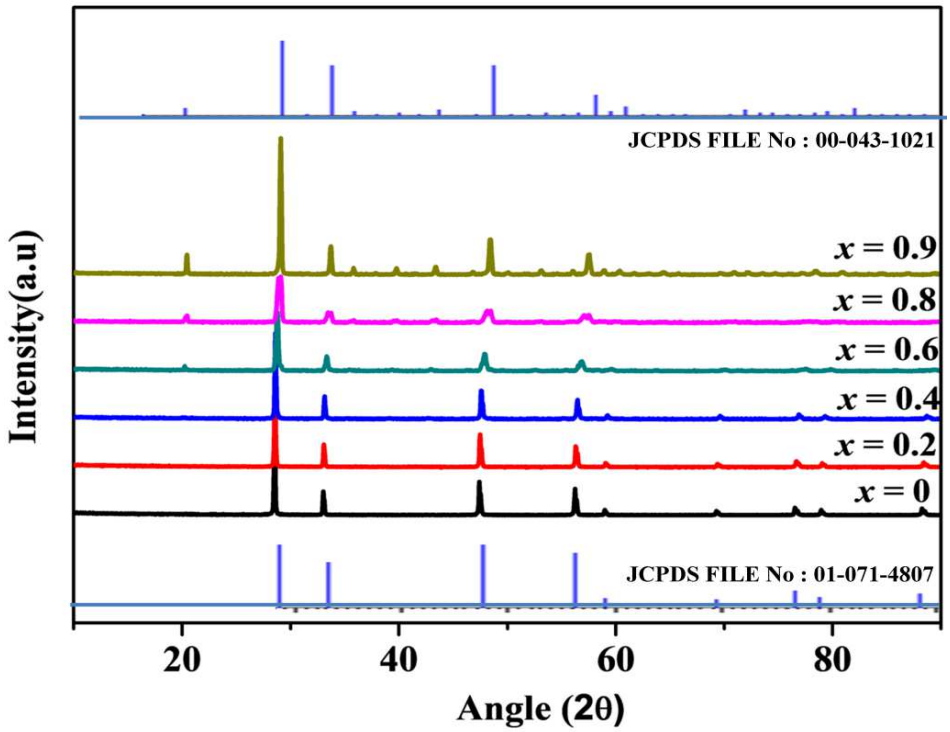

Fig. 2.1 Powder X-ray diffraction patterns of $Ce_{0.9-x}Y_xO_{2-\delta}$:0.1$Eu^{3+}$ (x = 0, 0.2, 0.4, 0.6, 0.8, and 0.90) red phosphors.

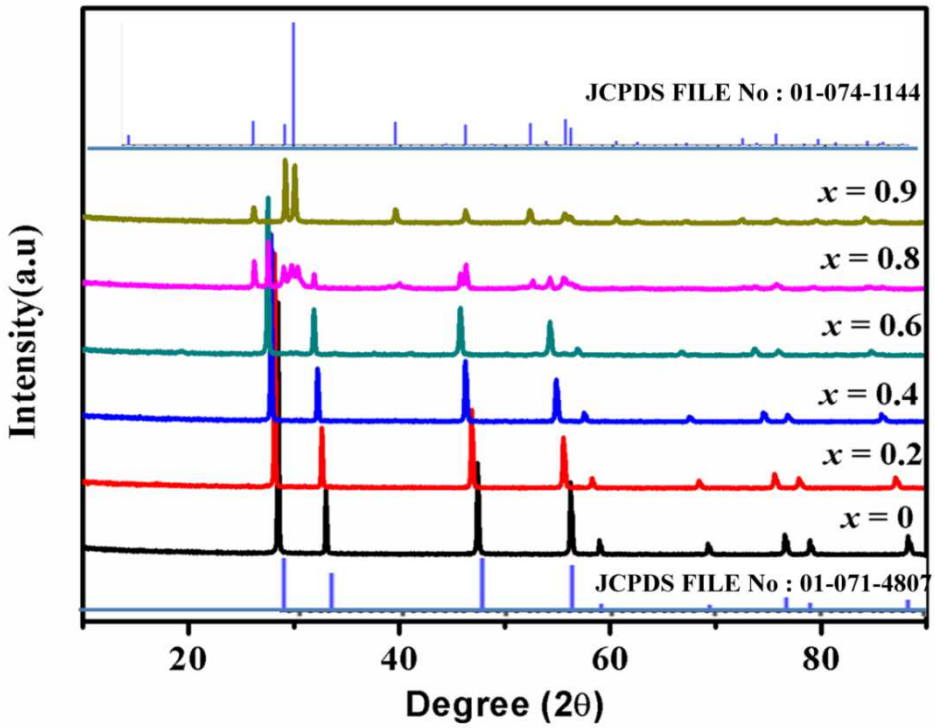

Fig. 2.2 Powder X-ray diffraction patterns of $Ce_{0.9-x}La_xO_{2-\delta}:0.1Eu^{3+}$ (x = 0, 0.2, 0.4, 0.6, 0.8, and 0.90) red phosphors.

Table 2.1 The variation of the lattice parameter and the crystallite size of the as-prepared $Ce_{0.9-x}RE_xO_{2-\delta}:0.1Eu^{3+}$ where RE = Y and La; x = 0, 0.2, 0.4, 0.6, 0.8 and 0.9 red phosphors.

x	Lattice Parameter (Å)		Crystallite Size (nm)	
	RE = Y	RE = La	RE = Y	RE = La
0	5.4212 (7)	5.4212 (7)	63.83	63.83
0.20	5.4144 (4)	5.4795 (2)	63.83	63.76
0.40	5.4006 (6)	5.5452 (4)	63.85	63.74
0.60	5.3684 (6)	5.6024 (5)	42.60	50.95
0.80	5.3499 (8)	5.6029 (7)	51.10	63.70
0.90	5.3122 (6)	5.6035 (4)	63.92	63.80

The detailed analysis of the XRD patterns of ceria-lanthanum samples reveals that for compositions upto x = 0.4, the patterns are similar in nature and match well with the sole presence of the standard fluorite-type cubic phase of CeO_2 according to JCPDS File No. 01-071-4807, and beyond this level of doping, the patterns could be attributed to hexagonal-type phase according to JCPDS File No. 01-074-1144. From the XRD patterns, it could be noted that doping with La^{3+} leads to shifting of diffraction peak to the lower angle side and the peak broadens with low intensity for higher doping. The ionic radius of La^{3+} (r = 0.116 nm for CN = 8) is larger than Ce^{4+} (r = 0.097 nm for CN = 8); hence, lattice expansion is expected due to the incorporation of La^{3+} in CeO_2 lattice and is listed in Table 2.1. Earlier reports on lanthanide doped ceria reveal that the doping lanthanides left to Gd on the periodic table act as a generator of oxygen vacancies with positive association of energy and lanthanides right to Gd behave as a scavenger of oxygen vacancies with negative association of energy. In other words, a bigger ion like La repels the oxygen vacancy in the nearest neighbor (NN) site and allows the formation of cubic O_h symmetry. The substitution of smaller ions like Y trap the oxygen vacancy in the nearest neighbor, losing its symmetry. The studies on molecular dynamics established that the size of an oxygen vacancy is smaller than that of an oxygen ion (Marrocchelli et al. 2013). The variation of lattice parameters in the present systems suggests that the smaller ionic size difference between Y and Ce is overshadowed by the contraction of the lattice due to oxygen vacancies.

2.3.2 Raman spectroscopic studies

Raman spectroscopic studies were performed on all the samples and the Raman spectra are shown in Fig. 2.3. Cerium oxide has a cubic fluorite structure and O_h^5 symmetry (*Fm3m* space group). The presence of RE^{3+} in CeO_2 lattice leads to deformation of the structure and can be detected by Raman analysis. The Raman spectra of $Ce_{0.9-x}RE_xO_{2-\delta}$:*0.1*$Eu^{3+}$ (RE = Y and La; x = 0 and 0.2) show a typical mode at 465 cm^{-1} that is assigned to the symmetric mode of the O atoms around each Ce^{4+}, i.e. the single allowed Raman mode with an F_{2g} symmetry in metal oxides and a fluorite structure (Patil et al. 2006; Weber et al. 1993). The Raman spectra of $Ce_{0.9-x}Y_xO_{2-\delta}$:*0.1*$Eu^{3+}$, where x = 0.8 and 0.9, show the typical modes observed for rare earth C-type oxides. The Raman modes predicted for an ideal C-type structure are

4Ag + 4Eg + 14Fg, where Ag is the Raman active symmetric stretching vibration, Fg is the Raman active triply degenerate symmetric stretching vibration, and Eg is the Raman active symmetric doubly degenerate bending vibration. The characteristic Raman modes of C-type structure are observed more prominently at 130, 163, 196, 330, 380, 433, 470, 491, and 590 cm^{-1} wavenumbers. These modes are in agreement with the reported literature for rare earth C-type phase (Shukla et al. 2015; Zhang et al. 2011; Dilawar et al. 2008; Abrashev et al. 2014; Laversenne et al. 2001; Repelin et al. 1995). $Ce_{0.9-x}Y_xO_{2-\delta}$:*0.1*$Eu^{3+}$ (*x* = 0.4 and 0.6) shows broad peaks around 256, 383, 490 and 613 cm^{-1}, implying that the sample is not completely in either C-type or defect fluorite-type structure, although the XRD analysis of $Ce_{0.9-x}Y_xO_{2-\delta}$:*0.1*$Eu^{3+}$ indicates defect fluorite-type structure for *x* = 0.4 and rare earth C-type structure for x = 0.6.

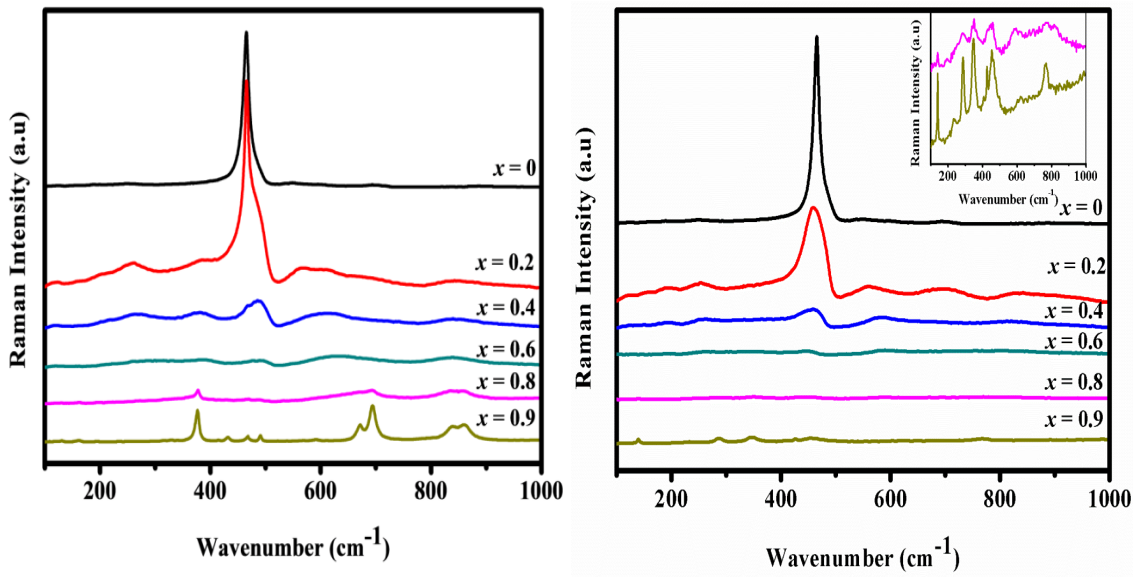

Fig. 2.3 Raman spectra of a) $Ce_{0.9-x}Y_xO_{2-\delta}$:0.1$Eu^{3+}$ b) $Ce_{0.9-x}La_xO_{2-\delta}$:0.1$Eu^{3+}$ where (*x* = 0, 0.2, 0.4, 0.6, 0.8, and 0.90) red phosphors (Inset figure shows the enlarged view of Raman spectra for *x* = 0.8 and 0.9).

$Ce_{0.9-x}La_xO_{2-\delta}$:*0.1*$Eu^{3+}$ (x = 0.4 and 0.6) exhibits broad peaks around 195, 267, 350, 462, 592 and 805 cm^{-1}, indicating the mixed modes of fluorite- and hexagonal-type structures. The Raman spectra of $Ce_{0.9-x}La_xO_{2-\delta}$:*0.1*$Eu^{3+}$, where x = 0.8 and 0.9, show the typical modes observed for hexagonal La_2O_3 and the characteristic Raman modes are observed more prominently at 198, 283, 341, 452 and 767 cm^{-1} wavenumbers (Jianlan et al. 2015; Denning et al. 1972).

With the increase in Ln^{3+} concentration upto x = 0.6, the Y^{3+} Raman spectra show a small positive frequency shift, i.e. towards higher energy, while La^{3+} spectra show a negative frequency shift, i.e. towards lower energy, in the F_{2g} Raman mode. These effects agree well with the evolution of lattice contraction and expansion as observed in XRD analysis. Further broadening, asymmetric nature and appearance of a new mode at 570 cm^{-1} are more predominantly observed in Y-based Raman spectra. These are the signatures of oxygen vacancy dominance in the lattice. Thus, the Raman analysis corroborates the structural analysis carried out by XRD and confirms the presence of oxygen vacancies predominantly in the Y systems (McBride et al. 1994).

2.3.3 X-ray photoelectron spectroscopy studies

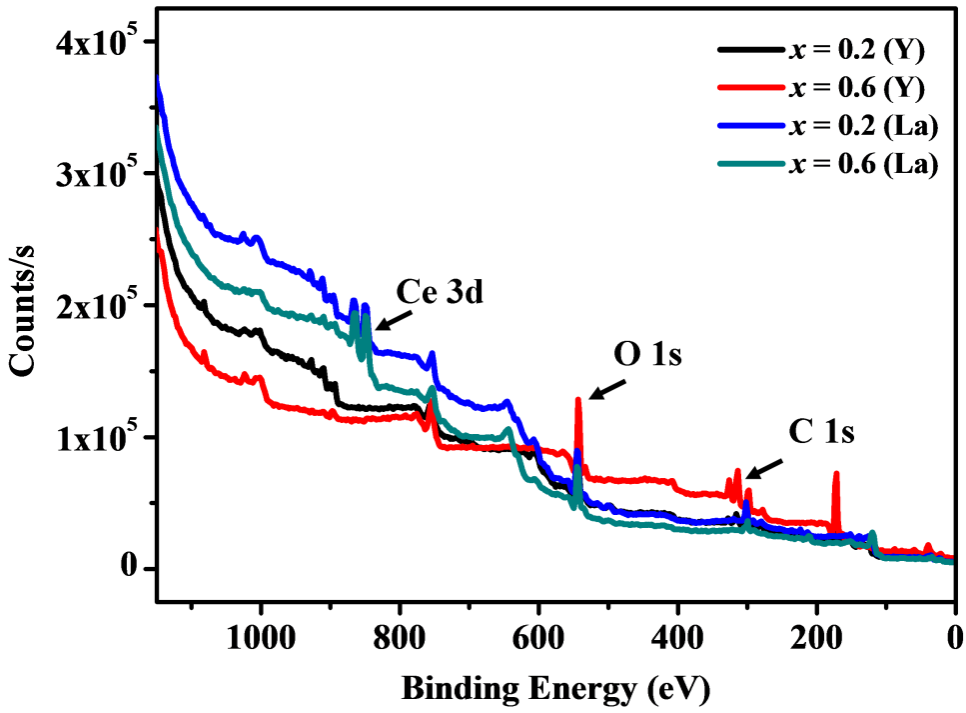

Fig. 2.4 XPS survey spectra of $Ce_{0.9-x}RE_xO_{2-\delta}$:0.1$Eu^{3+}$RE = Y and La where ($x$ = 0.2 and 0.6) red phosphors.

In order to provide further insights into valence states on the addition of rare earth ions in europium doped ceria lattice, the selected samples, $Ce_{0.9-x}RE_xO_{2-\delta}$:*0.1*$Eu^{3+}$ (RE = Y and La; x = 0.2 and 0.6), were analyzed by means of XPS. The recorded XPS spectra were charge-corrected with respect to an adventitious C 1s

signal at 284.6 eV. A wide survey scan X-ray photoelectron spectrum is shown in Fig. 2.4. A series of peaks from Ce 3d, C 1s and O 1s are clearly observed. The carbon content is high, which is typical of adventitious carbon arising from atmospheric exposure. No other significant contamination is detected. The Ce 3d XPS patterns of $Ce_{0.9-x}RE_xO_{2-\delta}$:*0.1*$Eu^{3+}$, where RE = Y and La and x = 0.2 and 0.6 samples are shown in Fig. 2.5. The broad Ce 3d photoelectron peaks are deconvoluted for accurate assignment and allow an inference of the composition of different chemical states present in the samples. The XPS pattern of Ce $3d_{5/2}$ is composed of two structures of Ce_2O_3 and three structures of CeO_2. In this way, a mixed valence sample can contain ten peaks altogether for overlapping Ce $3d_{5/2}$ and Ce $3d_{3/2}$ spin–orbit bands. These peaks are usually described by nomenclature developed by Burroughs (Burroughs et al. 1976). v_0, v, v', $v''$and $v'''$are attributed to the Ce $3d_{5/2}$ ionization, while u_0, u, u', u'' and u''' Ce $3d_{3/2}$ ionization. The bands labelled v, v'', v''', u, u'' and u''' belong to Ce^{4+} ions, and the bands labelled v_0, v', u_0, and u' are assigned to Ce^{3+} ions (Romeo et al. 1993; Borchert et al. 2005). It is clear that Ce^{4+} and Ce^{3+} coexist on the surface of all the samples, and the major valency of cerium is 4+ oxidation, because the relative concentration of Ce^{3+} and Ce^{4+} are in relative proportion to the intensity of corresponding peaks. The peak areas of Ce^{3+} were used to calculate the relative amount of Ce^{3+} concentration in the lattice (Sharma et al. 2015). From the analysis of XPS spectra, it was found that the concentration of Ce^{3+} is relatively less for Y^{3+} substitution compared to that for La^{3+} and the values are listed in Table 2.2.

Table 2.2 Defect Concentration (Ce^{3+} concentration) values of $Ce_{0.9-x}RE_xO_{2-\delta}$:*0.1*$Eu^{3+}$ where RE = Y and La; x = 0.2 and 0.6 red phosphors calculated from the XPS analysis.

	[Ce^{3+}] (%)	
	RE = Y	RE = La
0.20	28.50	27.52
0.60	7.47	18.49

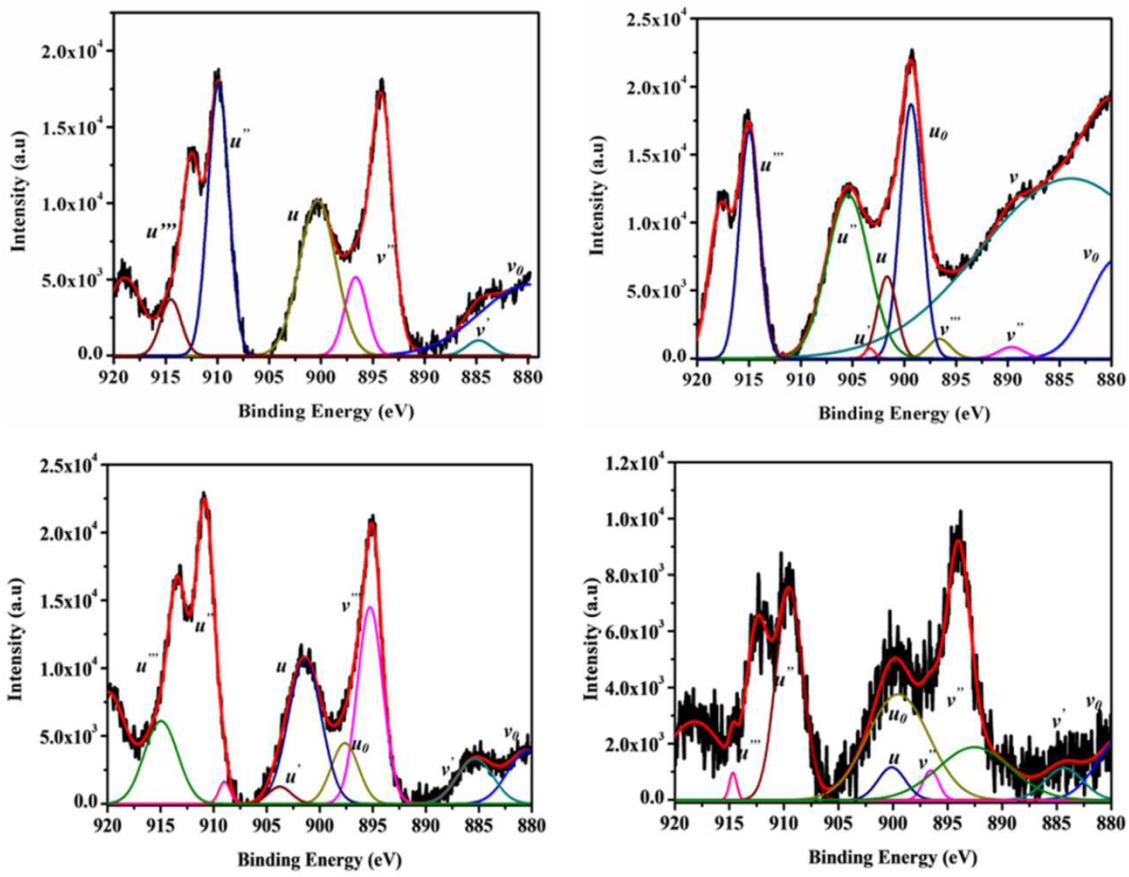

Fig 2.5 XPS spectrum of Ce (3d) for the $Ce_{0.9-x}RE_xO_{2-\delta}:0.1Eu^{3+}$ RE = Y and La where (x = 0.2 and 0.6)red phosphors was deconvoluted to give the individual spin-orbit doublet of $3d_{3/2}$ and $3d_{5/2}$, and the sum of the deconvoluted peaks was used to produce the fit to the actual data.

2.3.4 Morphological studies

Fig. 2.6 and 2.7 show the typical SEM micrographs of all Eu^{3+}-doped $Ce_{0.9-x}RE_xO_{2-\delta}:0.1Eu^{3+}$ (RE = Y and La; x = 0.2, 0.4, 0.6, 0.8 and 0.9) samples. The overall morphologies of all the samples are more or less similar. The powder particles appear to be highly crystalline and are slightly agglomerated. The particles are in the scale of 1–5 μm in size. The chemical composition of typical $Ce_{0.9}O_{2-\delta}:0.1Eu^{3+}$, $Ce_{0.1}Y_{0.8}O_{2-\delta}:0.1Eu^{3+}$ and $Ce_{0.3}La_{0.6}O_{2-\delta}:0.1Eu^{3+}$ phosphors checked using energy dispersive spectrometer attached with SEM is shown in Fig. 2.8 and identifies the presence of all expected elements. Elemental X-ray dot mapping analysis of typical $Ce_{0.1}Y_{0.8}O_{2-\delta}:0.1Eu^{3+}$ and $Ce_{0.3}La_{0.6}O_{2-\delta}:0.1Eu^{3+}$ red phosphor is shown in Fig. 2.9. This reveals that all the elements are uniformly distributed in the sample.

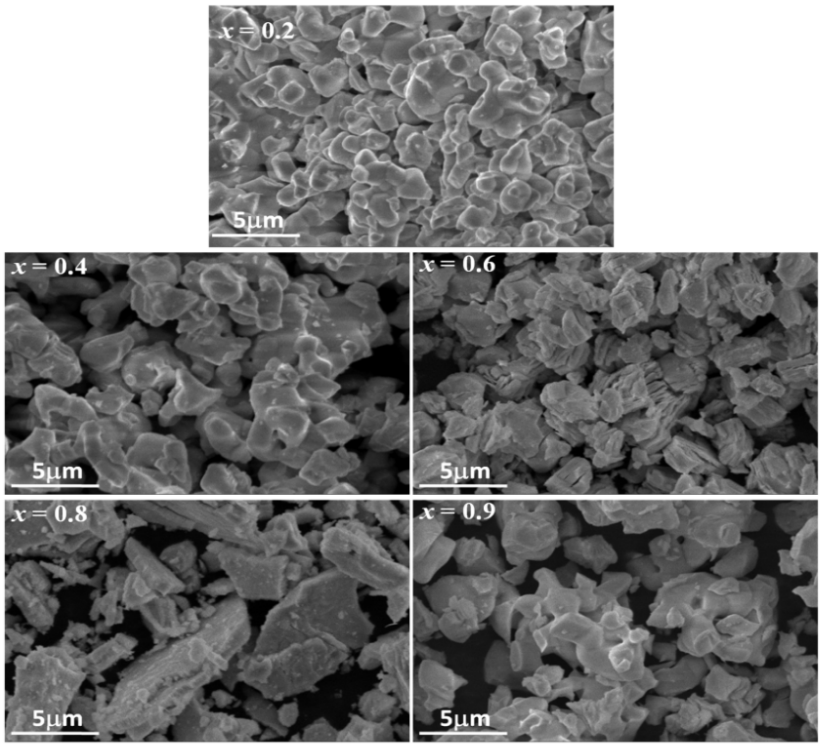

Fig. 2.6 Typical SEM photographs of $Ce_{0.9-x}Y_xO_{2-\delta}:0.1Eu^{3+}$ (x = 0.2, 0.4, 0.6, 0.8, and 0.90) red phosphors.

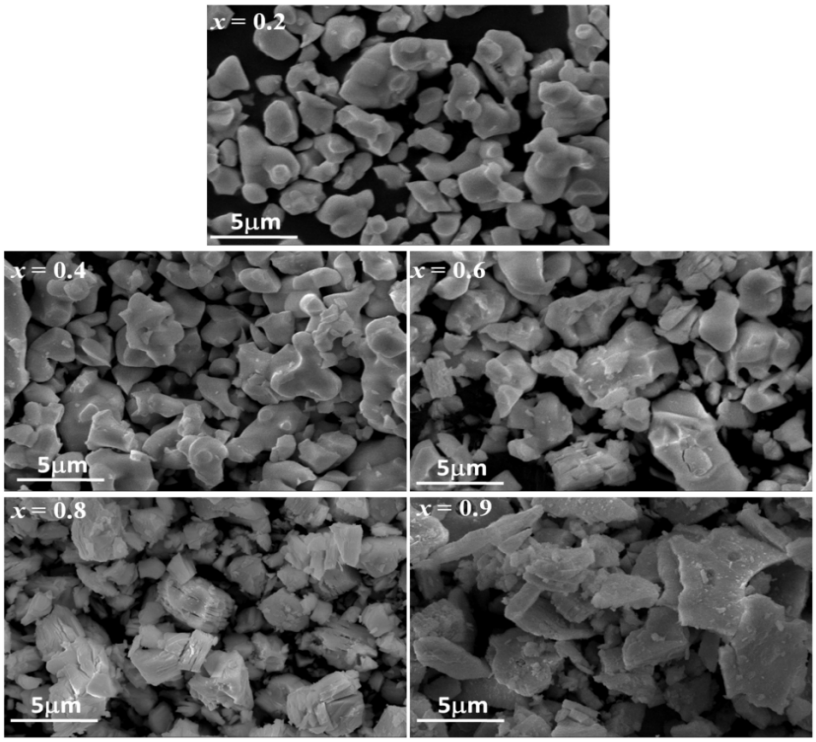

Fig. 2.7 Typical SEM photographs of $Ce_{0.9-x}La_xO_{2-\delta}:0.1Eu^{3+}$ (x = 0.2, 0.4, 0.6, 0.8, and 0.90) red phosphors.

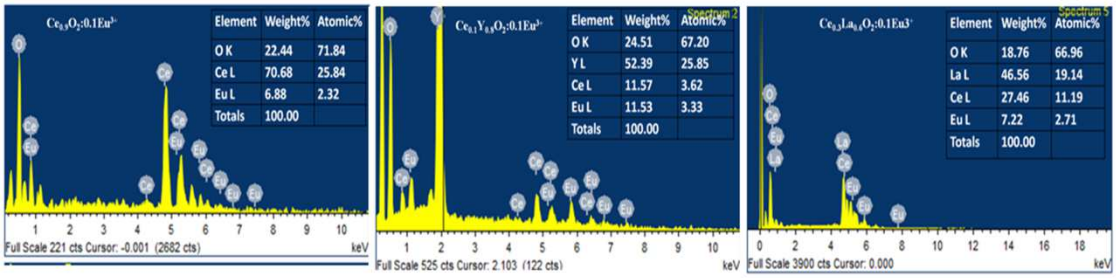

Fig. 2.8 EDS spectra of $Ce_{0.9}O_{2-\delta}:0.1Eu^{3+}$, $Ce_{0.1}Y_{0.8}O_{2-\delta}:0.1Eu^{3+}$ and $Ce_{0.3}La_{0.6}O_{2-\delta}:0.1Eu^{3+}$ red phosphors which identifies the presence of all expected elements.

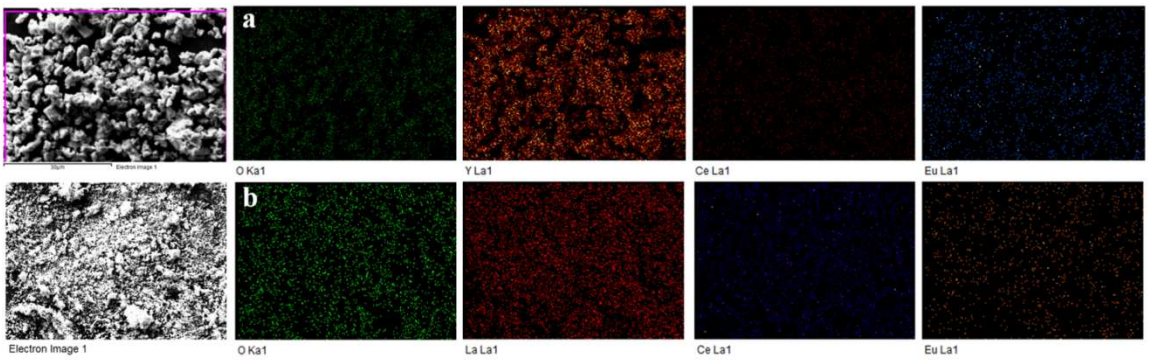

Fig. 2.9 Elemental mapping of typical a) $Ce_{0.1}Y_{0.8}O_{2-\delta}:0.1Eu^{3+}$ and b) $Ce_{0.3}La_{0.6}O_{2-\delta}:0.1Eu^{3+}$ red phosphor. This confirms that all the elements are uniformly distributed in the lattice.

2.3.5 Absorption studies

UV-visible absorption spectroscopy is more useful to investigate metal oxides to obtain information on surface coordination and different oxidation states of metal ions and defect sites in materials (Guo et al. 2011; Reddy et al. 2008). Therefore, in order to understand the doping effects on optical absorption and band gap of the as-synthesized samples, UV-visible absorption spectroscopy measurements were conducted for $Ce_{0.9-x}RE_xO_{2-\delta}:0.1Eu^{3+}$ (RE = Y and La; x = 0, 0.2, 0.4, 0.6, 0.8 and 0.9) red phosphors and the results are shown in Fig. 2.10. As can be noted from this figure, the major UV-vis absorption peaks of the synthesized samples occur at about 255, 288 and 355 nm. The maxima at 255 nm corresponds to O^{2-} to Ce^{3+} charge transfer transitions, whereas the absorption maxima at 288 and 355 nm can be

assigned to O^{2-} to Ce^{4+} charge transfer and interband transitions, respectively (Reddy et al. 2008). The band gap energy was calculated from the absorption spectra using Shapiro's method by extrapolating the onset of absorption edge to the wavelength axis and is given in Table 2.3.

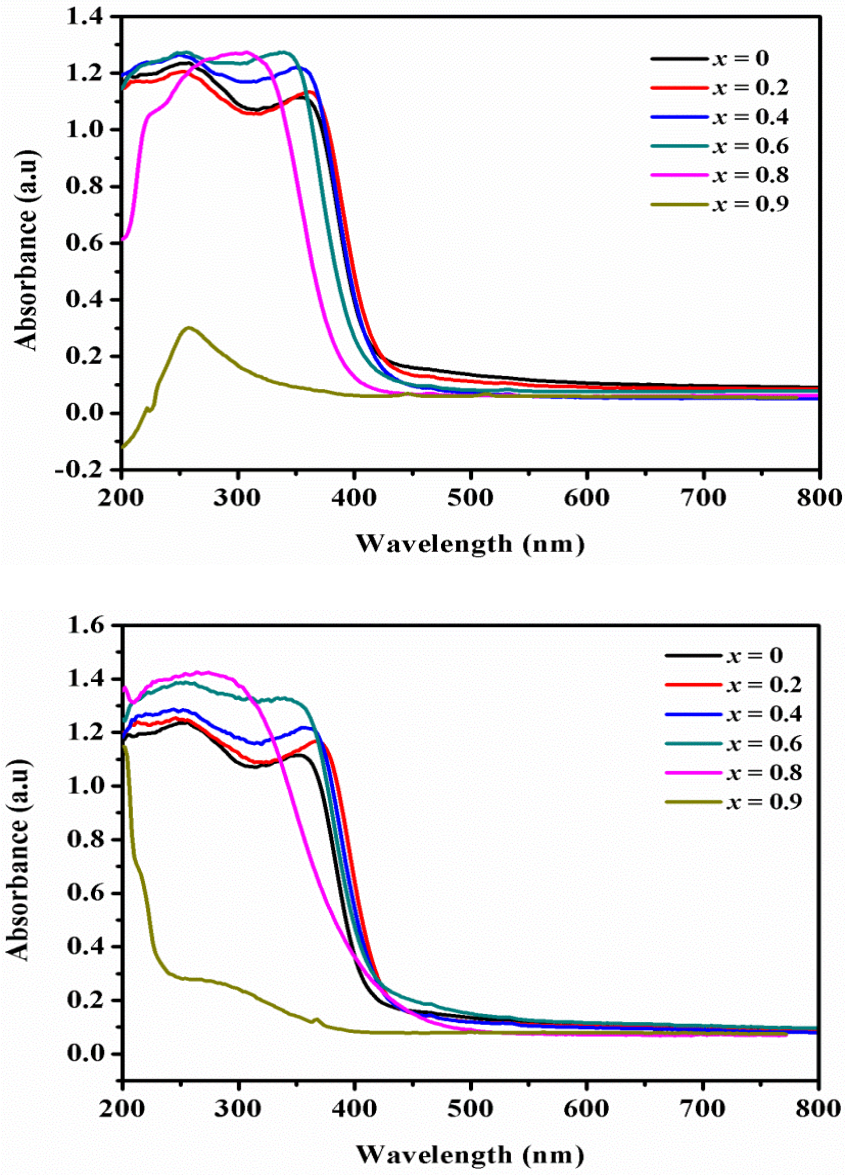

Fig. 2.10 UV-vis absorption spectra of a) $Ce_{0.9-x}Y_xO_{2-\delta}:0.1Eu^{3+}$ b) $Ce_{0.9-x}La_xO_{2-\delta}:0.1Eu^{3+}$ where (x = 0, 0.2, 0.4, 0.6, 0.8, and 0.90) red phosphors.

It can be noted from the spectra that the absorption edge shows a contrasting variation with RE substitution. An increase in band gap energy and absorbance band edge shifts towards the shorter wavelength (blue shift) is demonstrated in the case

of $Ce_{0.9-x}Y_xO_{2-\delta}:0.1Eu^{3+}$ (x = 0, 0.2, 0.4, 0.6, 0.8 and 0.9), whereas a decrease in band gap energy accompanied with a red shift in the absorption edge is observed in the case of $Ce_{0.9-x}La_xO_{2-\delta}:0.1Eu^{3+}$ (x = 0, 0.2, 0.4, 0.6, 0.8 and 0.9). Though both substituent ions are trivalent, their influence on creation of oxygen vacancies is distinct, resulting from oxygen vacancies and variation in valence state of Ce^{4+} ions and Ce^{3+} ions (Athira et al. 2014; Thorat et al. 2014; Wang et al. 2011; Yashima et al. 2010; Wang et al. 2007). This contrasting absorption behaviour can be explained as follows: dopant ionic radii vary from La^{3+}, which is much larger than Ce^{4+}, to Y^{3+}, which is close to Ce^{3+}. Earlier literature indicates that defect association energy is a strong function of ionic radii of the rare earth dopant (Nakayama et al. 2009). Here the smaller Y^{3+} has a stronger association with oxygen vacancy, which leads to the ordering of the vacancies in a lattice. In other words, Y^{3+} being a smaller ion tends to exhibit lower co-ordination by trapping an oxygen vacancy. This situation hinders the hopping/mobility of oxygen in the lattice. On the other hand, the larger ion La^{3+} exhibits the perfect VIII co-ordination of the fluorite structure and repels oxygen vacancies. As reported, oxygen vacancy ordering is strongly dependent on dopant ionic radius. As a result, the liberated oxygen vacancy allows the enhancement of defect formation converting Ce^{4+} to Ce^{3+} compared to bound oxygen vacancy (as in the case of Y^{3+}). The results suggest that oxygen vacancy ordering in the lattice has an important role in defect formation. The above assessment agrees with the XPS analysis as Ce^{3+} concentration increases with La^{3+} dopant compared to Y^{3+} (Table 2.2). In addition, the above conclusion is well evidenced in the absorption spectra (Fig. 2.10). Absorption due to charge transition O^{2-}–Ce^{3+}, O^{2-}–Ce^{4+} have contrasting variations with RE substitutions. The absorption due to O^{2-}–Ce^{4+} increases with Y^{3+} substitution, whereas that due to O^{2-}–Ce^{3+} increases with La^{3+} concentration. Thus, it can be concluded that the larger ion La^{3+} creates more defects in the lattice compared to Y^{3+}. This results in the red shift of the absorption edge in the case of La^{3+} and blue shift in the case of Y^{3+}.

2.3.6 Photoluminescence studies

In order to study local site symmetry and its effect on luminescence behavior of symmetry-sensitive Eu^{3+} ions, detailed photoluminescence studies were performed. Photoluminescence is closely related to surface states, oxygen vacancies,

defects and stoichiometry of any semiconductor material (Khan et al. 2014) and it is an effective method to determine the optical properties of materials and defect chemistry associated with those properties (Thorat et al. 2014). The excitation spectra are collected by measuring emission intensity at a fixed wavelength of 612 nm and are shown in Fig. 2.11.

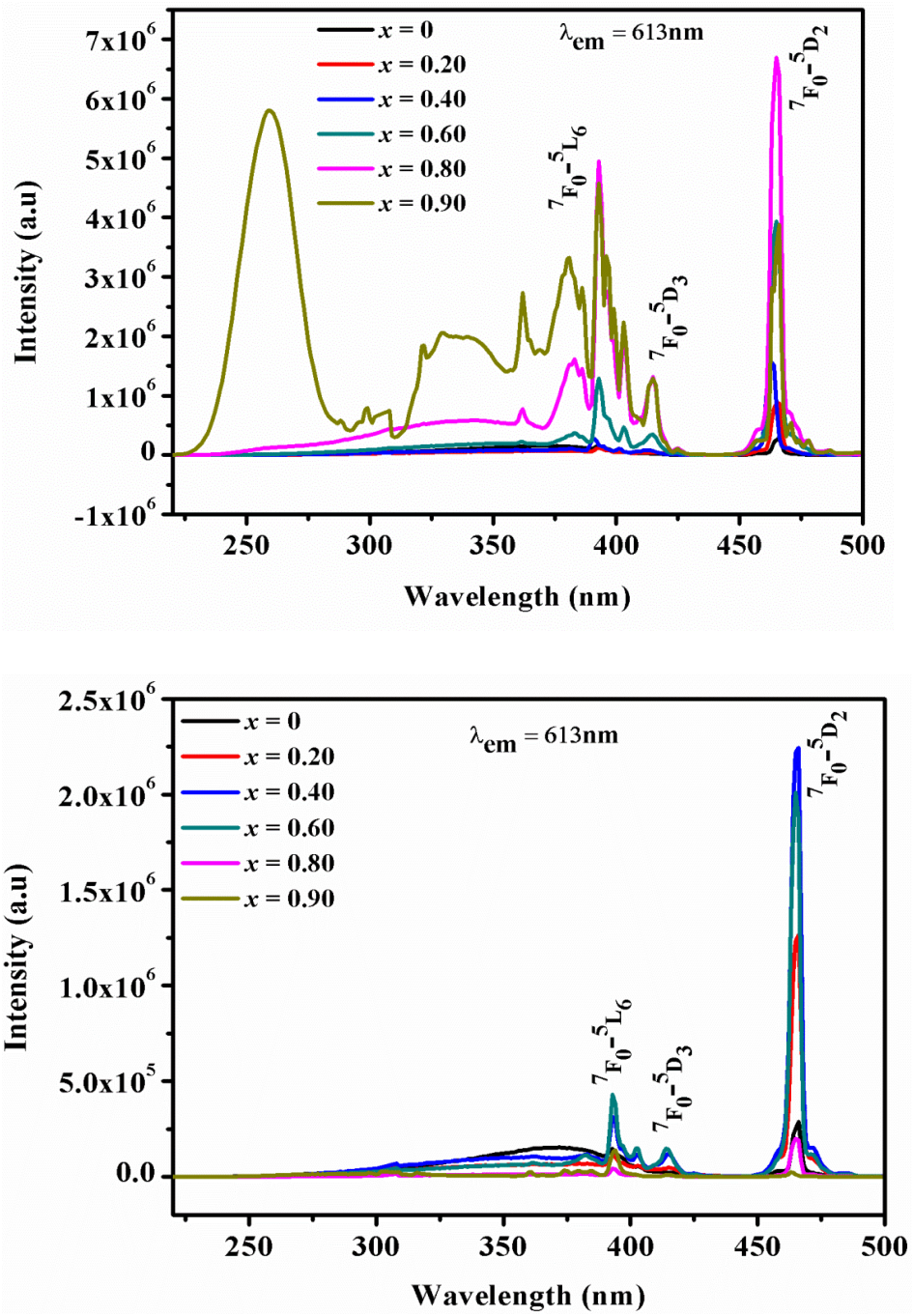

Fig. 2.11 Excitation spectra with emission at 613 nm for a) $Ce_{0.9-x}Y_xO_{2-\delta}:0.1Eu^{3+}$ b) $Ce_{0.9-x}La_xO_{2-\delta}:0.1Eu^{3+}$ where (x = 0, 0.2, 0.4, 0.6, 0.8, and 0.90) red phosphors

The spectra show a gradual shift of LMCT of O^{2-} – Ce^{4+} to the O^{2-}–Eu^{3+} with the incorporation of RE into CeO_2 matrix. The excitation spectra include a weak broad band region centered at 370 nm, which originates from the charge transfer (CT) transitions between O^{2-} and Ce^{4+} ions of the CeO_2 host and some sharp peaks at 380, 394, and 413 nm and a well-defined peak at 466 nm (except for x = 0.9), which can be assigned to the intraconfigurational 4f–4f transitions of Eu^{3+} in the CeO_2 lattice: $^7F_0$ to $^5L_7$, $^5L_6$, $^5D_3$ and $^5D_2$, respectively. The excitation broad band enhances and shifts from 370 nm ($Ce_{0.9}O_{2-\delta}$:0.1Eu^{3+}) to 261 nm ($Ce_{0.9-x}RE_xO_{2-\delta}$:0.1$Eu^{3+}$) (RE = Y and La; x = 0.9). In addition, with the increase in RE doping concentration, the excitation lines at 393 and 466 nm become stronger, especially at 466 nm ($^7F_0$–$^5D_2$), which rather agrees with the emission of commercial GaN light emitting diode (440–470 nm) chips. Therefore, a red phosphor with high efficiency excited with blue light can be achieved by adjusting RE concentrations. It is also observed that the intensity of intra $4f^6$ transition bands of Eu^{3+} becomes greatly stronger with increase in Y^{3+} content to a maximum of 80 mol%, beyond which the intensity decreases. But in the case of La substituted samples, this intensity increases upto a maximum of 60 mol% of La^{3+} concentration.

To understand the host lattice influence on emission, the ceria matrix is excited at the ligand to metal charge transfer (LMCT) bands at 370 nm (Fig. 2.12). It is observed that on LMCT excitation, the emission intensity of the prepared samples is low as compared to direct dopant (Eu^{3+}) excitation. This is mainly due to inefficient energy transfer from the host to the Eu^{3+} energy levels. The previous reports also indicate that the ligand metal charge transfer band excitations yield poor emission intensities in the ternary systems of ceria with respect to its binary systems (Sorbello et al. 2014). The emission spectra of the prepared samples, $Ce_{0.9-x}RE_xO_{2-\delta}$:0.1$Eu^{3+}$ (RE = Y and La; x = 0, 0.2, 0.4, 0.6, 0.8 and 0.9) under excitation at 466 nm are shown in Fig. 2.13. The emission spectra exhibit a series of peaks, which correspond to transitions from the excited $^5D_0$ level to the ^7F_J (J = 0, 1, 2, 3 and 4) levels of Eu^{3+} $4f^6$ configuration (Sreena et al. 2016). However, the relative emission intensities are rather dependent upon the concentration and type of rare earth substituents. Among emission lines, peak intensity at 612 nm ($^5D_0$–$^7F_2$) is predominantly intense, which is mainly due to the forbidden electric dipole

transition of Eu^{3+}. This also proves the lower symmetry of Eu^{3+} compared to O_h inversion symmetry of the fluorite lattice.

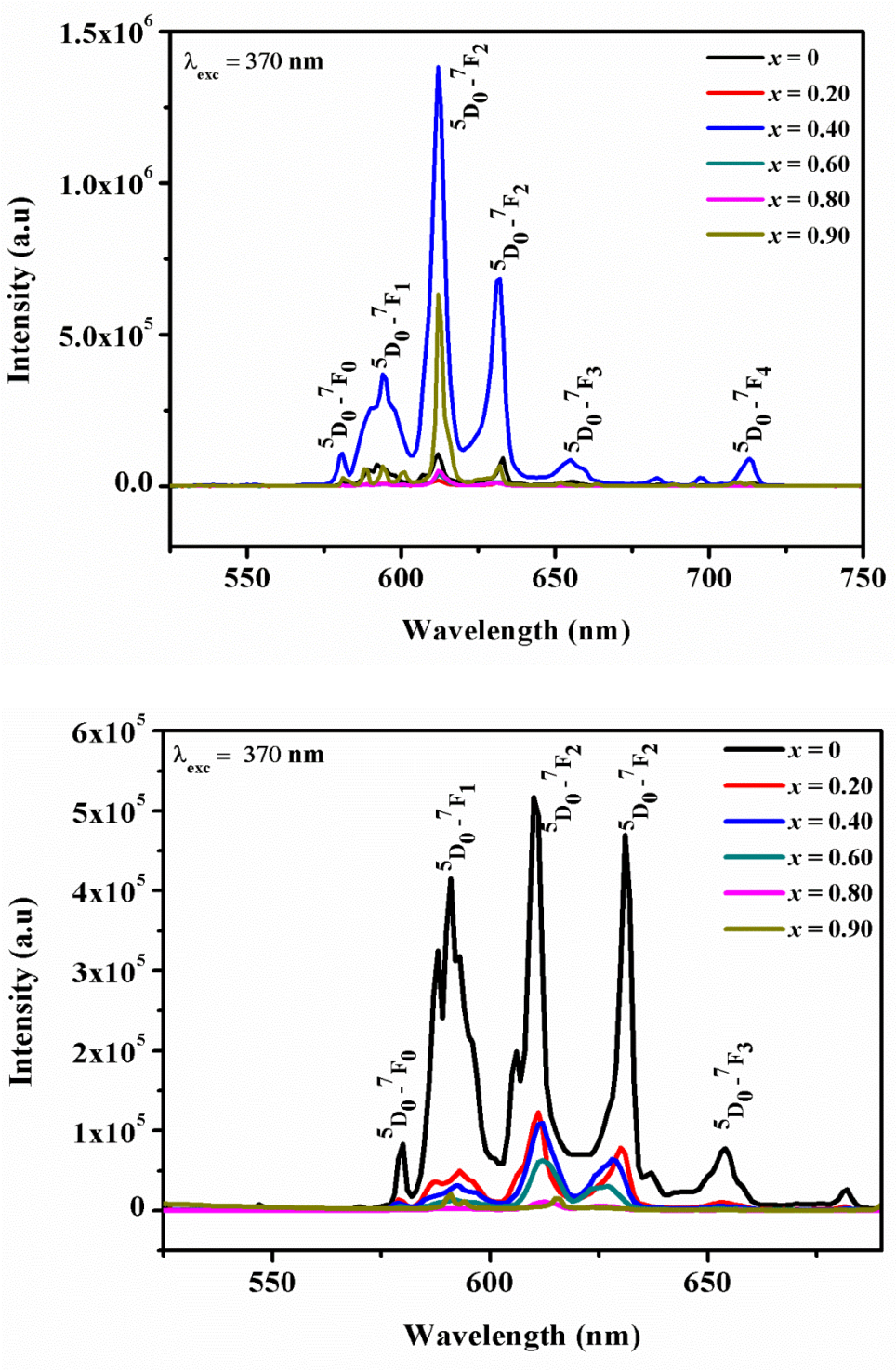

Fig 2.12 Emission spectra a) $Ce_{0.9-x}Y_xO_{2-\delta}$:$0.1Eu^{3+}$b) $Ce_{0.9-x}La_xO_{2-\delta}$:$0.1Eu^{3+}$ where (x = 0, 0.2, 0.4, 0.6, 0.8, and 0.90) red phosphors excited at 370 nm.

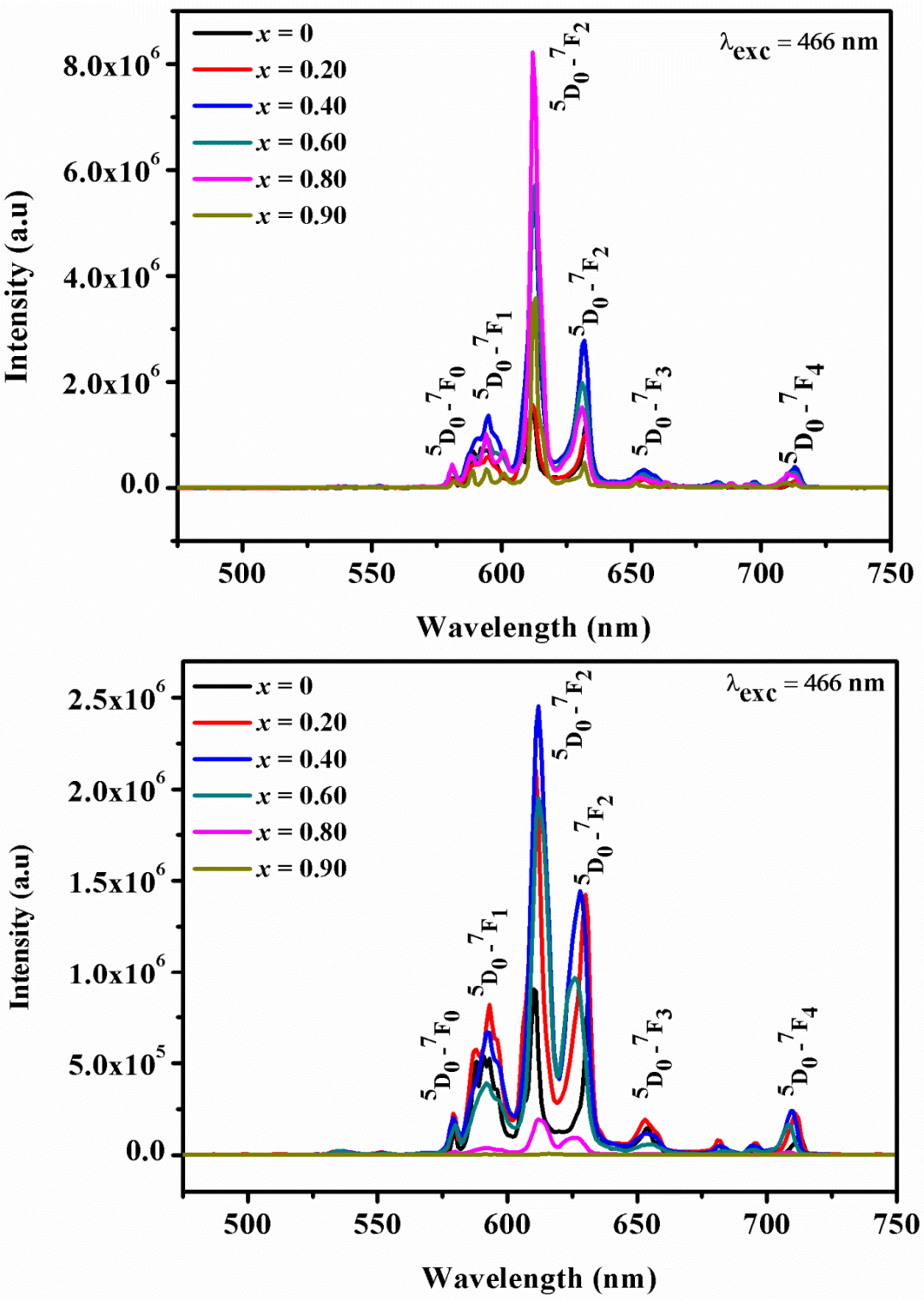

Fig 2.13 Emission spectra a) $Ce_{0.9-x}Y_xO_{2-\delta}$:0.1$Eu^{3+}$b) $Ce_{0.9-x}La_xO_{2-\delta}$:0.1$Eu^{3+}$ where (x = 0, 0.2, 0.4, 0.6, 0.8, and 0.90) red phosphors excited at 466 nm.

However, the extent of symmetry lowering is dependent on the RE in the ceria. The emission intensity of Eu^{3+} is very critical to its location in the lattice and the type of environment around Eu^{3+}. When Ce^{4+} is replaced with RE^{3+} along with Eu^{3+}, the symmetry is lowered or increased depending on the ionic size of the RE^{3+}

substituted. The environmental change around Eu^{3+} in the system affects the luminescence property, which can be assessed by the asymmetric ratio (R). This is expressed as the ratio of transition $^5D_0$–$^7F_2$ to $^5D_0$–$^7F_1$. The calculated R values are listed in Table 2.3. It is found that R values are higher for the La system in the lower concentration range (x = 0.2 and 0.4) and higher for the Y system in the higher concentration range. These variations appear to be associated with the variation in the local environment around Eu^{3+}. Eu^{3+} co-doped with contrasting rare earth ions in ceria probes indirectly affect the local environment of the activator.

Table 2.3 The asymmetric ratio, FWHM of the $^5D_0$-$^7F_2$ transition at 612 nm red emission and the band gap energy of the as-prepared $Ce_{0.9-x}RE_xO_{2-\delta}$:*0.1*$Eu^{3+}$ where RE = Y and La; *x* = 0, 0.2, 0.4, 0.6, 0.8 and 0.9 red phosphors under 466 nm excitation.

	Asymmetric Ratio		FWHM (nm)		Band Gap Energy(E_g) (eV)	
x	RE = Y	RE = La	RE = Y	RE = La	RE = Y	RE = La
0	2.00		3.54		2.92	
0.20	2.59	3.13	5.67	5.45	2.95	2.83
0.40	4.05	4.27	4.77	7.05	2.99	2.84
0.60	5.89	5.76	4.68	7.00	3.07	2.89
0.80	7.79	4.03	4.13	6.94	3.14	2.91
0.90	7.42	1.20	2.50	1.40	3.11	3.00

As discussed earlier, when a larger ion like La is co-doped, it exhibits perfect eight co-ordination and repels NN oxygen vacancies. In such a situation, a relatively smaller ion like Eu^{3+} is forced to exhibit lesser co-ordination and trap oxygen vacancies, resulting in the loss of O_h inversion symmetry. Consequently, forced electric dipole transitions occur, dominantly enhancing the R values. In the case of the Y system, Eu^{3+} being a relatively larger ion maintains the perfect co-ordination of the fluorite lattice, retaining O_h inversion symmetry. Thus, Eu^{3+} emissions due to electric dipole transitions are relatively less dominant, reducing the R values. These

assumptions are concurrent with the obtained R values (Table 2.3). The variation in the emission intensity at $^5D_0$–$^7F_2$ transition with increase in rare earth concentrations is shown in Fig. 2.14. It is clear that emission intensity varies divergently with rare earth concentrations. $Ce_{0.8}Y_{0.1}O_{2-\delta}$:0.1$Eu^{3+}$ phosphor exhibited maximum emission intensity (8 times higher than that of $Ce_{0.9}O_2$:0.1Eu^{3+} and better than commercial red phosphor), whereas La substitution yielded poor emission intensities with higher concentrations.

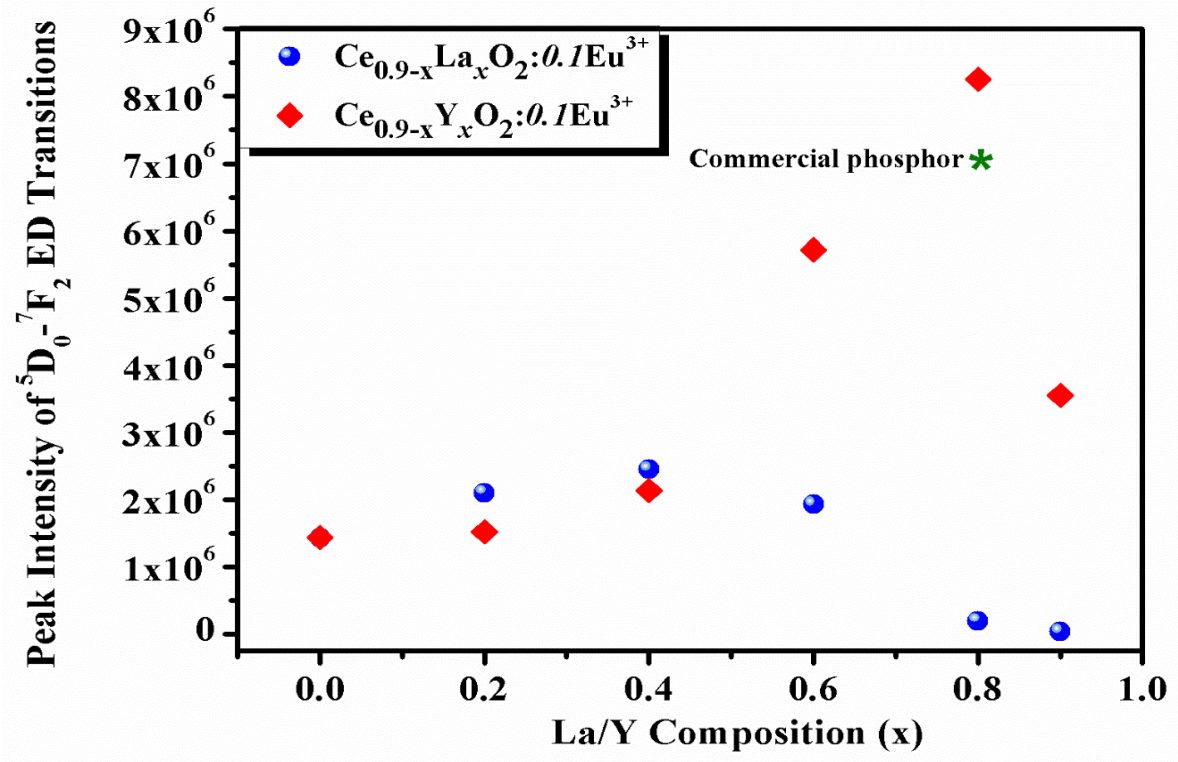

Fig. 2.14 Peak intensities of 612 nm electric dipole transition of $Ce_{0.9-x}RE_xO_{2-\delta}$:0.1$Eu^{3+}$where ($x$ = 0, 0.2, 0.4, 0.6, 0.8, and 0.90) red phosphors under 466 nm excitation.

These contrasting variations in emission intensities can be explained as follows. With increase in the rare earth concentrations (x > 0.4), three significant phenomena are observed: (i) phase transformation from fluorite to the corresponding parent oxide structure, (ii) contrasting lattice and band gap variations and (iii) relatively higher Ce^{3+} concentration in the La system. The structural transformation is driven by oxygen vacancies created by rare earth substitutions. As reported earlier, the smaller ions have a strong association of

oxygen vacancies and vacancy-Ce^{4+} for large dopant cations (Nakayama et al. 2009; Khan et al. 2014; Wei et al. 2009). In other words, Y^{3+} dopant traps oxygen vacancies at the NN site strongly, while La^{3+} dopant repels oxygen vacancies at the NN site (Fig. 2.15). Based on this, Y_{Ce} and $V_O^{\cdot\cdot}$ ordering is exhibited with an increase in Y^{3+} substitutions. Such ordering is also associated with nano-domain formation in the lattice. This kind of ordering and domain formation leads to uniform distribution of Eu^{3+} in the lattice. Further, it prevents defect formation of Ce^{3+} in the lattice. These factors contribute immensely in enhancing Eu^{3+} luminescence in the Y system. On the other hand, La^{3+} substitution leads to more defect formation as the resulting Ce^{4+} and $V_O^{\cdot\cdot}$ ordering facilitate the reduction of Ce^{4+} to Ce^{3+} that acts as a luminescent quenching centre. As a result, La^{3+} substitutions increase Ce^{3+} concentrations compared to Y^{3+} substitutions. This variation in Ce^{3+} concentration is also supported by the XPS analysis results.

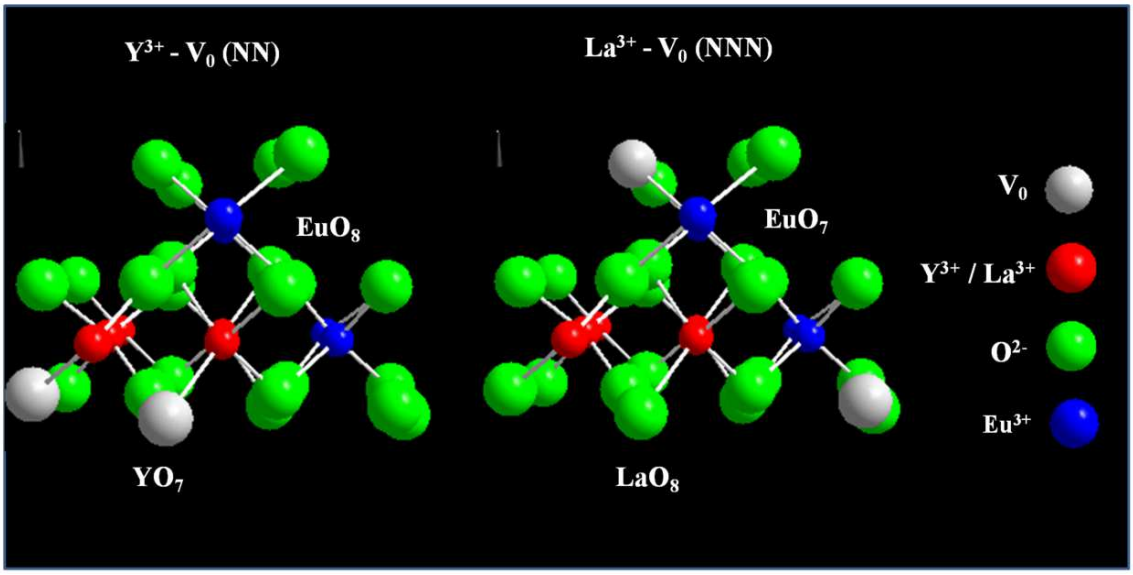

Fig. 2.15 Schematic representation of La^{3+}/ Y^{3+} co-ordination in the Ceria system.

To further explore energy migration, luminescence decay curves of the prepared samples were measured (Fig. 2.16). The decay curves were recorded for Eu^{3+} transition at 612 nm emission with 466 nm excitation wavelength and then the luminescence lifetimes of the phosphors were studied. The lifetime data of $^5D_0$–$^7F_2$ (612 nm) transitions of Eu^{3+} in various (Y and La) concentrations (Table 2.4) were very well fitted to a single exponential function as $I(t) = A \exp(-t/\tau)$ where I is the luminescence intensity at time t, τ is the decay time and A is a constant. As Y^{3+}

content increases, the mean lifetime increases steadily upto x = 0.8 with excitation, while it decreases with increase in La^{3+} content. It is due to the result of the partition of more Eu^{3+} in an ordered and uniform distribution in the Y system compared to that in the La system. The efficiency of the phosphors was calculated from lifetime values, is listed in Table 2.4.

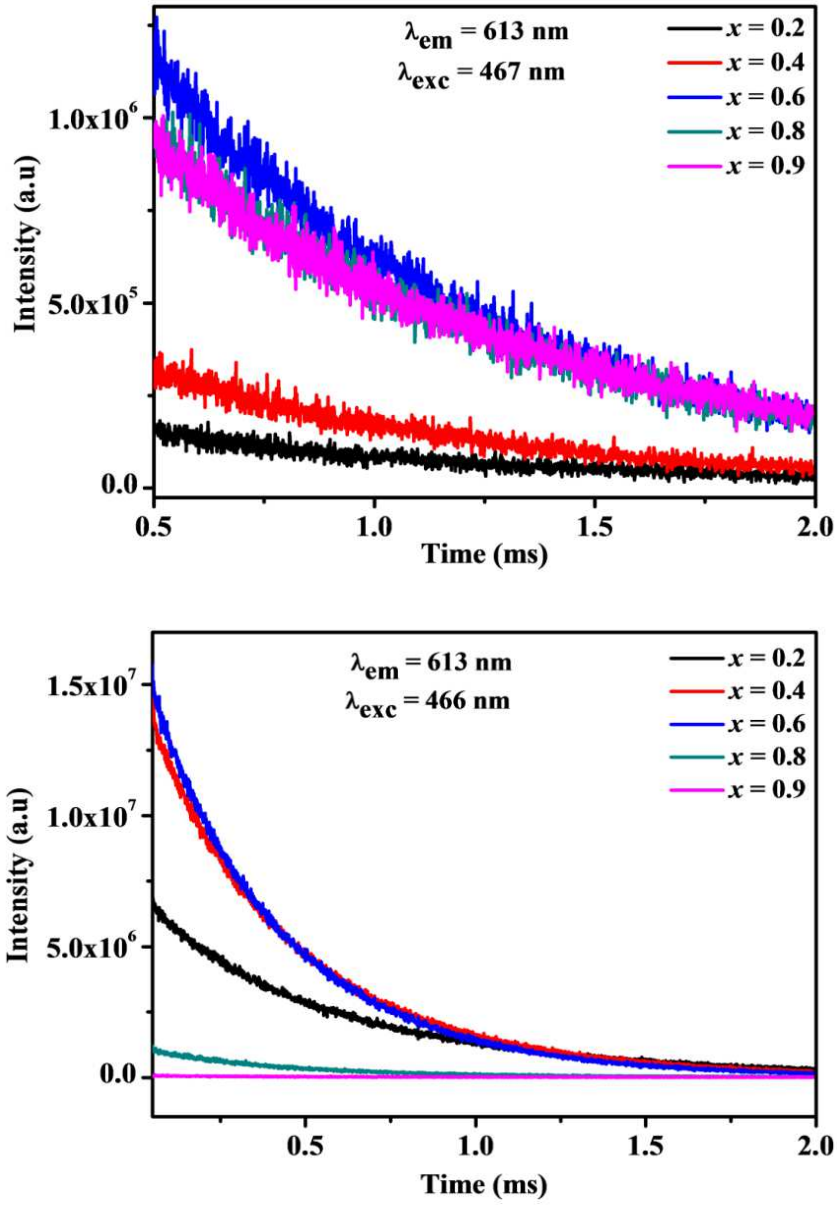

Fig. 2.16 Lifetime decay curves of $^5D_0$-$^7F_2$ transition of Eu^{3+} (wavelength 613 nm) in a) $Ce_{0.9-x}Y_xO_{2-\delta}$:0.1$Eu^{3+}$b) $Ce_{0.9-x}La_xO_{2-\delta}$:0.1$Eu^{3+}$ where (x = 0, 0.2, 0.4, 0.6, 0.8, and 0.90) red phosphors excited at 466 nm.

Table 2.4 Lifetimes, Quantum efficiency and color coordinates of $Ce_{0.9-x}RE_xO_{2-\delta}$:*0.1*$Eu^{3+}$ where RE = Y and La; *x* = 0, 0.2, 0.4, 0.6, 0.8 and 0.9 red phosphors.

x	Lifetime (τ) (ms)		Quantum Efficiency (η)(%)		Color Coordinates	
	Y	La	Y	La	Y	La
0.20	0.607	0.543	9.1	8.9	(0.64, 0.35)	(0.64, 0.36)
0.40	0.688	0.423	13.0	9.1	(0.65, 0.34)	(0.67, 0.32)
0.60	0.743	0.389	16.7	9.8	(0.65, 0.34)	(0.67, 0.32)
0.80	0.808	0.396	21.2	7.9	(0.65, 0.34)	(0.67, 0.32)
0.90	0.801	0.355	26.7	2.3	(0.65, 0.34)	(0.67, 0.32)

The quantum of Ce^{3+} defect formation plays a key role in deciding the photoluminescence properties in the present system. The assessment of absorption edge associated with band gap variation and XPS analysis points out that the amount of defect formation is governed by the size of ionic radii of the rare earth substituted. Based on this, a schematic representation of band gap variation is shown in Fig. 2.17. As explained earlier, the smaller Y^{3+} induces ordering of oxygen vacancies in the lattice, inhibiting defect formation of Ce^{3+} oxidation states, while the larger La^{3+} liberates oxygen vacancies, facilitating defect formation. Unlike other systems, here Ce^{3+} acts as a PL quenching center. In PL studies, it has been observed that host excitations (370 nm) exhibit only Eu^{3+}-poor emission intensities, indicating ineffective energy transfer from the host. Though this energy lies higher than Eu^{3+} excitation levels, the excited energy quenches non-radiatively without transferring to Eu^{3+} $^5D_0$ manifold. Further, it is seen that no emissions related to Ce^{3+} (5d–4f) are detected in the spectra. The presence of high concentration of Ce^{3+} may result in concentration quenching. The above results indicate that Eu^{3+} luminescence is not aided by defect formation. Ce^{3+} ions have $4f^1$ electrons and these states are positioned above the valence band (O 2p). The existence of defects introduced between the O 2p states and Ce 4f states and the quantum of defects is dependent on

the ionic radii of the rare earth. The variation in band gap for contrasting lanthanides in the system fits very well with the Ce^{3+} concentration. Further, it has been reported that cluster formation of the dopant cations and oxygen vacancies increases with rare earth concentration (Avram et al. 2015). The ordering of oxygen vacancies associated with cluster formation helps in trapping excited energy levels, resulting in an increase in the lifetime of the $^5D_0$ levels. The variation in lifetime is evident, confirming the above process (Table 2.4). The Y substituted phosphors of the $^5D_0$ levels show higher lifetime than the La substituted ones. The increased lifetime is also reflected in the assessment of quantum efficiency of the system. Assuming that only radiative and non radiative processes are essentially involved in the depopulation of $^5D_0$ states of Eu^{3+} ion, the quantum efficiency (η) can be expressed as;

$$\eta = A_{rad} / (A_{rad} + A_{nrad}) \quad (2.1)$$

where A_{rad} and A_{nrad} are the radiative and non-radiative transition probabilities respectively. The emission intensity (I) can be calculated as the integral intensity S of $^5D_0$-$^7F_{0-4}$ emission curves as;

$$I_{i-j} = \hbar\omega_{i-j} A_{i-j} N_i \sim S_{i-j} \quad (2.2)$$

where i and j are the initial level ($^5D_0$) and the final levels ($^7F_{0-4}$), respectively; $\hbar\omega_{i-j}$ is the transition energy, A_{i-j} is the Einstein's coefficient of spontaneous emission, and Ni is the population of the $^5D_0$ emitting level. The experimental coefficients of spontaneous emission were then calculated according to the equation;

$$A_{0j} = A_{01} (I_{0j}/ I_{01}) (\nu_{01}/ \nu_{0j}) \quad (2.3)$$

where ν_{01} and ν_{0j} are the energy baricenters of the $^5D_0$-$^7F_1$ and $^5D_0$-^7F_j energy levels determined from the emission peak of Eu^{3+} ion. A_{01} is the Einstein's coefficient of spontaneous emission between $^5D_0$ and $^7F_1$ energy levels. In vacuum, the average refractive index (n) is 1.506 and $(A_{0-1})_{vac} = 14.64s^{-1}$ is considered. Then the value of A_{0-1} was expressed as,

$$A_{0-1} = n^3(A_{0-1})_{vac} \sim 50s^{-1} \quad (2.4)$$

The life time (τ) of the $^5D_0$ states, A_{rad} and A_{nrad} are related as;

$$A_{tot} = 1/\tau = A_{rad} + A_{nrad} \quad (2.5)$$

On the basis of the emission spectra and lifetimes of the $^5D_0$ emitting level, the quantum efficiency (η) of the Eu^{3+} ion excited state can be determined using the equations 2.1-2.5. The quantum efficiency increases with Y substitution, while it decreases with La substitution. Overall, defect formation plays a significant role in photoluminescence properties. The study reveals that a smaller ion like Y can greatly functionalise the Ce–Eu system with improvements in emission intensities and quantum efficiency than those of the binary system.

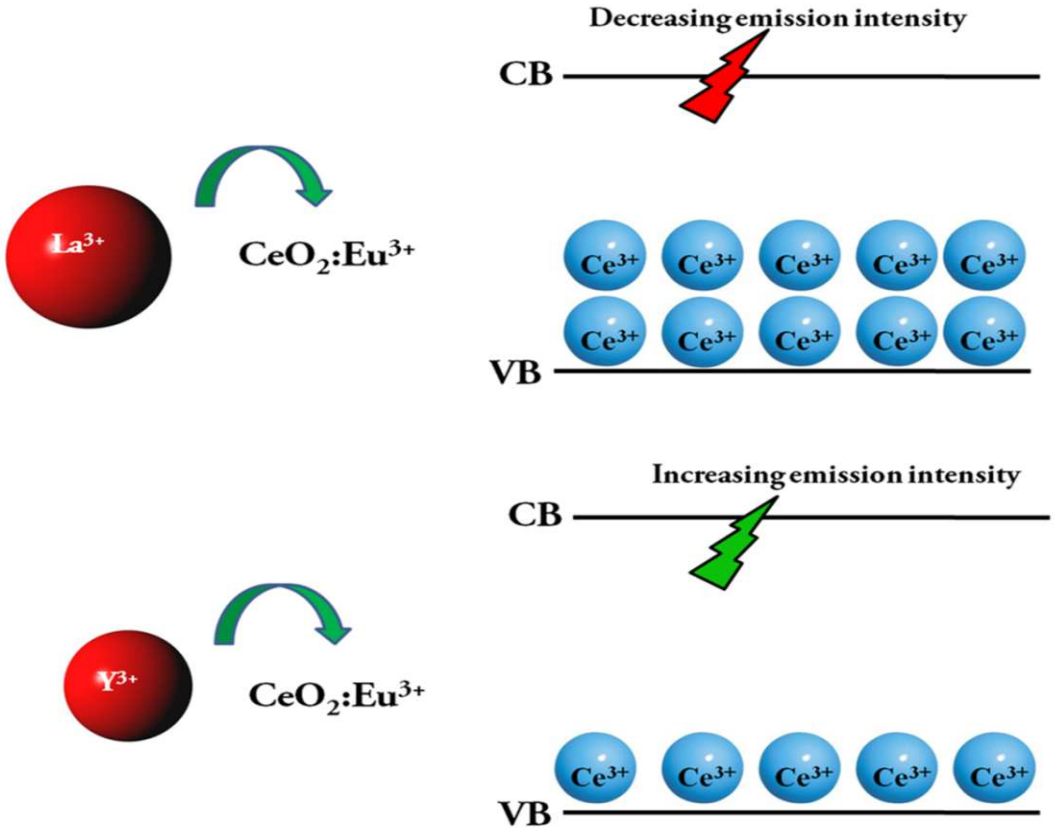

Fig. 2.17 Schematic representation of band gap variation in La^{3+}/ Y^{3+} co-substituted ceria system.

The chromaticity coordinates *x* and *y* values of the Commission Internationale L'Eclairage (CIE) for $Ce_{0.9-x}RE_xO_{2-\delta}$:*0.1*$Eu^{3+}$ (RE = Y and La; *x* = 0.2, 0.4, 0.6, 0.8 and 0.9) red phosphors are determined and listed in Table 2.4. From the table, it can be seen that the coordinates of phosphors with higher RE^{3+} doping concentrations exhibit values very close to the standard red phosphor coordinates

(x = 0.670, y = 0.330) from NTSC (National Television Standards Committee), indicating the purity of our phosphors.

2.4 Conclusions

A family series of red phosphor materials, $Ce_{0.9-x}RE_xO_{2-\delta}$:*0.1*$Eu^{3+}$ (RE = Y and La; x = 0, 0.2, 0.4, 0.6, 0.8 and 0.9), was prepared by a conventional solid-state route. The substitution of contrasting rare earth ions in ceria elucidated the influence of local environment of Eu^{3+} ions on its photoluminescence behavior. The defect formation of Ce^{3+} concentration was found to be a function of ionic radii of rare earths. Ce^{3+} acted as a luminescent quenching center, leading to less efficient luminescence in the system. The smaller ion Y^{3+} substitution in the system inhibited defect formation, resulting in strong luminescence with more efficiency, while the bigger ion La^{3+} substitution yielded poor luminescence due to increased defect formation. $Ce_{0.1}Y_{0.8}O_{2-\delta}$:*0.1*$Eu^{3+}$ phosphor exhibited stronger red luminescence at 612 nm under 466 nm excitation than its binary structures (eight times more than $Ce_{0.9}O_{2-\delta}$:*0.1*Eu^{3+}) and better than commercial red phosphor. The above results demonstrated that the co-substitution of contrasting rare earths with Eu^{3+} would allow the understanding of local structure and a smaller ion like Y^{3+} greatly functionalized $CeO_2:Eu^{3+}$ phosphor.

Chapter 3

Synthesis and photoluminescence properties of Eu^{3+} doped $A_2Ce_2O_7$ (A = La, Y and Gd) red phosphors

Novel defect fluorite type narrow red emitting phosphors $A_2Ce_2O_7:0.1Eu^{3+}$ (A = Y, La, Gd), $Gd_{2-x}Ce_2O_7:xEu^{3+}$ (x = 0.05, 0.10, 0.15 and 0.20) and $Gd_{1.8-x}Ca_xCe_{2-x}Nb_xO_7:0.2Eu^{3+}$ (x = 0.25, 0.50, 0.75 and 1.0) were synthesized for the first time through the conventional solid state method. Studies revealed that the gadolinium sample exhibit enhanced red emission of Eu^{3+} (612nm) under the excitation of blue light (467 nm) that correspond to the popular emission lines of blue LED and improvements in terms of the asymmetric ratio and quantum efficiency. The effect of variation Eu^{3+} in the luminescence intensity in $Gd_{2-x}Ce_2O_7$ system was studied detail in this chapter. The ordering of cations in the lattice, reduction of Ce^{3+} concentration and oxygen vacancy ordering influences the better luminescence properties in the gadolinium based samples.

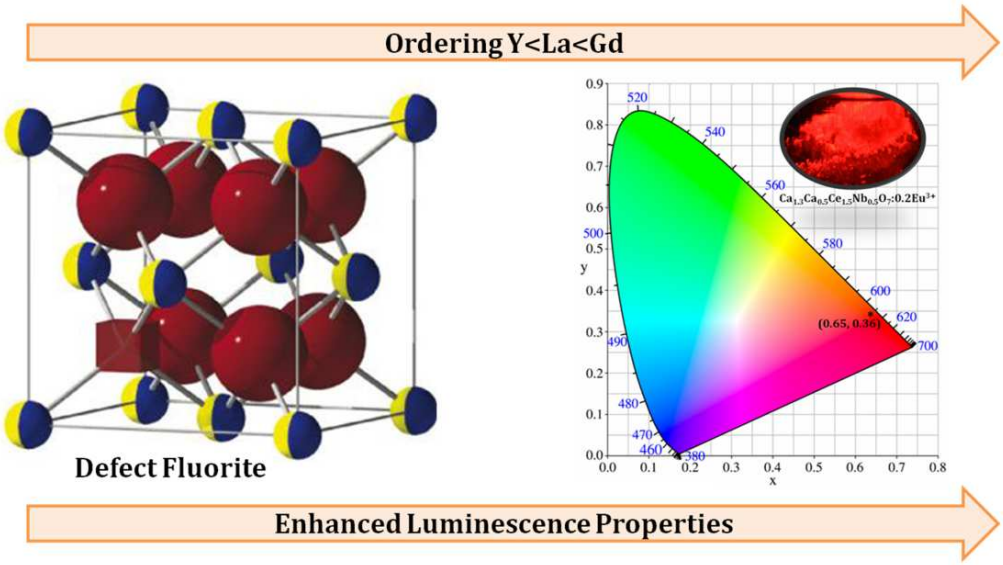

3.1 Introduction

The choice of the host lattice, crystallographic structure of the host lattice and nature of the activator ion plays a vital role in the luminescence properties of various phosphor materials for WLED applications (Dutta et al. 2013). Ternary type oxides having the general formula $A_2B_2O_7$ (A, B = Metals) have attracted great attention in recent years due to their excellent physical and chemical properties (Malathi et al. 2017; Cao et al. 2018; Liao et al. 2017; Culubrk et al. 2014). These oxides are mainly crystallizes in cubic structure with a variety of possible substitutions at the A and B sites (A = Rare earths; B = Ce, Sn, Zr, Ti, etc). Depending upon the radii of A and B site cations, these ternary oxides crystallize pyrochlore-type structure or defect fluorite-type structure (Subramanian et al. 1983). Rare earth containing $A_2B_2O_7$ oxides are excellent refractory materials exhibit interesting fluorescent and phosphorescent behavior and hence it is proposed as potential luminescent host materials for lighting applications. A_2O_3-CeO_2 (A = Rare earths) oxides have fascinated due to their remarkable electrical, catalytic, optical and mechanical properties (Hongsong et al. 2012). Most of the rare earth cerium oxides have been explored that potential candidate material for thermal barrier coating systems, oxide ionic conductivity, photocatalyst etc (Kalland et al. 2016). However, the luminescence properties of $A_2Ce_2O_7$ oxides were reported less. Furthermore, CeO_2 is a well known functional material that absorbs light in the near UV-visible region and also abundant in nature, nontoxic and inexpensive (Hongsong et al. 2015).

It is also reported that the $A_2Ce_2O_7$ oxides (A = La, Nd, Sm, Eu, Gd, Y and Yb) crystallizes either in C-type (*Ia3*) or F-type (*Fm3m*) structure based on the cation radii and co-ordination number (Chavan et al. 2005). The higher ionic size of cation will attribute to higher coordination number which tends to F-type phase and the lower ionic size of cation will attribute to lower coordination number which tends to C-type phase respectively. Moreover, cerium based oxide in F-type structure with the deficiency of anions makes possible substitution of wide range of cations in A-site leading to several compositions with diverse properties. Hongsong et al., recently reported the photo catalytic properties of F-tpye $Ln_2Ce_2O_7$ (Ln = La and Gd) oxides (Hongsong et al. 2015). The introduction of rare earth ion Eu^{3+}, the most

widely used activator for red luminescence to the host oxide can be used as a superior structural probe (Shi et al. 2017) and is considered as a suitable dopant for enhancing the emission in ceria based oxides. However, the literatures shows that by doping Eu^{3+} in ceria systems may increase the trivalent state of Ce and defect concentration which adversely affect the luminescence properties (Kumar et al. 2009). In this paper, we made an attempt to enhance the luminescence properties of cerium based system by reducing the reduction of Ce^{4+} and defect concentration. Therefore, we selected the F-type cerium based oxides having the general formula $A_2Ce_2O_7$ (A = La, Y and Gd).

Shi et. al. developed Eu^{3+} activated $Y_2Ce_2O_7$ nano phosphors through solution combustion synthesis which shown that the doping of Eu^{3+} in Ce^{4+} site is not sufficient for the improvement of photoluminescence within the F-type structure (Shi et al. 2015). Our group prepared Eu^{3+} doped $Y_2Ce_2O_7$ red phosphors by conventional solid state reaction method, in which the luminescence intensity was effectively enhanced and comparable with the commercial red phosphor (Athira et al. 2014). However, these oxides crystallize in C-type structure in spite of having F-type structure of CeO_2. In the present study, our prime interest is to prepared cerium oxide based host lattice which enhance the luminescence emission intensity without altering the F-type crystal structure of CeO_2. Hence, Eu^{3+} was substituted in the $La^{3+}/Y^{3+}/Gd^{3+}$ site of $A_2Ce_2O_7$ (A = La, Y and Gd) oxides and studied the distribution and pholuminescence properties of Eu^{3+}. The Eu^{3+} doping concentration was fixed at x = 0.10 (10 mol%) in all prepared samples. The structure, electronic structure, morphology and photoluminescence properties of the synthesized phosphors were characterized by powder X-ray diffraction, X-ray photoelectron spectroscopy, scanning electron microscopy with energy dispersive spectrometry, UV-visible absorption, photoluminescence and lifetime measurements. Further, the effect of Eu^{3+} concentration in the luminescence intensity of $Gd_2Ce_2O_7$ host lattice was also studied.

Incorporation of cations with different valency and electronegativity to the crystal lattice can cause distortion and modification in polarizability of chemical environment of Eu^{3+}, which can change the photoluminescent properties (Mahesh et al. 2013; Du et al. 2011). Further, we tried to enhance the f-f transition intensity of

$Gd_{1.8}Ce_2O_7$:0.2Eu^{3+} phosphors by incorporating Ca-Nb ions: Ca^{2+} ions to the Gd^{3+} site and Nb^{5+} ions to the Ce^{4+} site. The substitution of cerium ions by lower niobium ions found to have influence on the concentration quenching.

3.2 Experimental

3.2.1 Materials and Methods

The cerate based red phosphors: $A_{1.9}Ce_2O_7$:0.1Eu^{3+} (A = La, Y and Gd), $Gd_{2-x}Ce_2O_7$:*x*Eu^{3+} (*x* = 0.05, 0.10, 0.15 and 0.20) and $Gd_{1.8-x}Ca_xCe_{2-x}Nb_xO_7$:0.2$Eu^{3+}$ (*x* = 0.25, 0.50, 0.75 and 1.0) were synthesized by the conventional solid-state reaction technique. La_2O_3, Y_2O_3, Gd_2O_3, CeO_2, Eu_2O_3, $CaCO_3$ and Nb_2O_5 from Sigma–Aldrich, Steinhheim, Germany with 99.99% were used as the starting materials and the precursor oxides are fine powders.These precursors were taken in the required stoichiometric ratios and mixed thoroughly in an agate mortar using acetone as the mixing medium until fine slurry was obtained. The slurry was dried by placing it in an air oven at a temperature of 100°C. The mixing and drying was repeated thrice to obtain a homogenous mixture. The homogeneous mixture was then calcined on a sintered alumina plate in an air atmosphere electrical furnace at 1200 – 1300°C for 6 h. In order to ensure the completion of the reaction, the calcinations were repeated twice at 1400°C for 12 h with intermittent grinding. $Gd_{1.8-x}Ca_xCe_{2-x}Nb_xO_7$:*0.20*$Eu^{3+}$ (*x* = 0.025, 0.05, 0.075 and 0.10) were calcined at 1500°C for 6 h. The temperature of the furnace is programmed with an initial heating rate of 10°C/min up to 900°C followed by a heating rate of 5°C/min to attain the desired temperatures.

3.2.2 Characterization

The crystalline structure, the phase purity and the lattice parameter of the samples were examined by recording X-ray diffraction patterns using a PANalytical X'Pert Pro diffractometer having Ni filtered CuK_α radiation with X-ray tube operating at 45 kV, 30mA and 2θ varied from 10 to 90° in 0.016° steps. The Raman spectra of the powder samples were acquired using an integrated micro-Raman system using a 633 nm helium-neon laser with a spatial resolution of 2μm to obtain the structure of the powdered samples. X-ray photoelectron spectroscopy (XPS) experiments were carried out on a PHI 5000 VersaProbe II instrument equipped with dual aluminum–magnesium anodes with Mg K_α radiation (1253.6 eV) operated at 5 kV and 15 mA

with a pass energy of 80 eV and an increment of 0.1 eV. The samples were degassed out for several hours in an XPS chamber to minimize air contamination to the sample surface. To overcome the charging problem, a charge neutralizer of 2 eV was applied, and the binding energy (BE) of the C1s core level (BE = 284.6 eV) of adventitious hydrocarbon was used as a standard. The XPS spectra were fitted with a nonlinear square method with the convolution of Lorentzian and Gaussian functions after a polynomial background was subtracted from the raw spectra. The recorded XPS spectra were charge corrected with respect to an adventitious C 1s signal at 284.6 eV. The size and morphology of the powder particles were done by a scanning electron microscope (JEOL, JSM-5600LV) operated at 15kV. The X-ray microchemical analysis and elemental mapping of the samples were carried out using Silicon Drift Detector–X-Max^N attached with a Carl Zeiss EVO SEM. The absorption characteristics of the synthesized samples were studied in the wavelength range 200-800 nm by a Shimadzu, UV-3600 UV-Vis spectrophotometer using barium sulphate as a reference. The photoluminescence excitation and emission spectra of the prepared samples were obtained using a Spex-Fluorolog DM3000F spectrofluorimeter with a 450W xenon flash lamp as the exciting source. Luminescence life time of the phosphors was recorded by the phosphorimeter attached to Fluorolog®3 spectrofluorimeter. All the measurements were carried out at room temperature.

3.3 Results and discussion

3.3.1 Effect of Eu^{3+} doping on the $A_2Ce_2O_7$ (A = La, Y and Gd) red phosphors

3.3.1.1 Powder X-Ray diffraction studies

Powder X-ray diffraction patterns of $A_{1.9}Ce_2O_7$:$0.1Eu^{3+}$ (A = La, Y and Gd) are shown in Fig. 3.1. The sharp and intense peaks of the XRD patterns indicate the crystalline nature of the samples. No traces of impurity peaks were detected indicating that the Eu^{3+} ions have been effectively incorporated into the host lattices. All the samples are matched well with a cubic fluorite structure having the space group *Fm3m* (JCPDS File no. 01-071-4807). For the detailed structural studies, Rietveld refinements of the above three samples were carried out using X′pert High Score Plus software. A pseudo Voigt profile function was used to fit the XRD pattern.

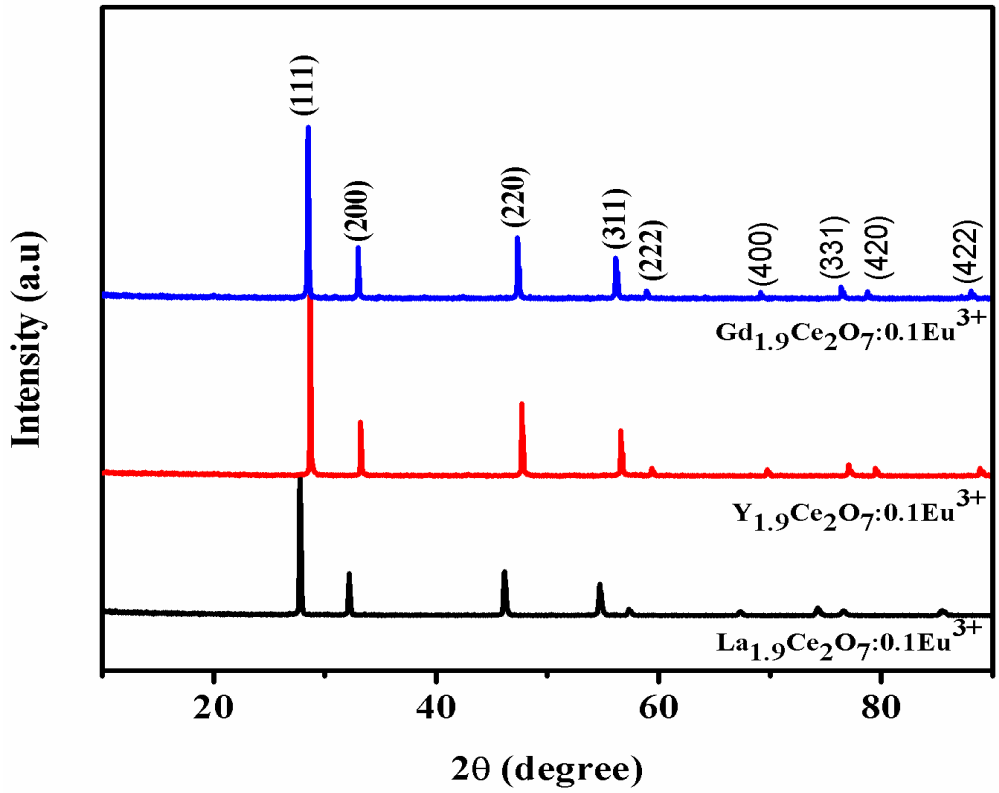

Fig. 3.1 Powder XRD patterns of $A_{1.9}Ce_2O_7$:0.1Eu^{3+} (A = La, Y and Gd) phosphors.

Table 1. Refined parameters obtained from the Rietveld analysis of the $A_{1.9}Ce_2O_7$:0.1Eu^{3+} (A = La, Y and Gd) phosphors

Sample	$La_{1.9}Ce_2O_7$:0.1Eu^{3+}	$Y_{1.9}Ce_2O_7$:0.1Eu^{3+}	$Gd_{1.9}Ce_2O_7$:0.1Eu^{3+}
Crystal Structure	Cubic	Cubic	Cubic
Space group	*Fm3m*	*Fm3m*	*Fm3m*
Lattice parameter (Å)	5.5631(6)	5.3892(8)	5.4322(8)
Flat background	19.4033	40.6865	67.7403
Coefficient 1	-24.5296	-23.7072	-19.4510
Coefficient 2	24.5933	24.6245	24.4076
Scale factor	0.000091	0.000151	0.000080
Caglioti parameters			
U	0.23	0.024	0.014
V	-0.04	-0.003	-0.004
W	0.008	0.0045	0.0044
Residual parameters			
R_{exp} (%)	14.31	11.88	10.43
R_p (%)	14.20	13.00	9.59
R_{wp} (%)	18.99	17.24	12.23
GOF	1.37	1.79	0.90
A-O_{8c} (Å)	2.409	2.334	2.352
Crystallite size (nm)	71	123	124

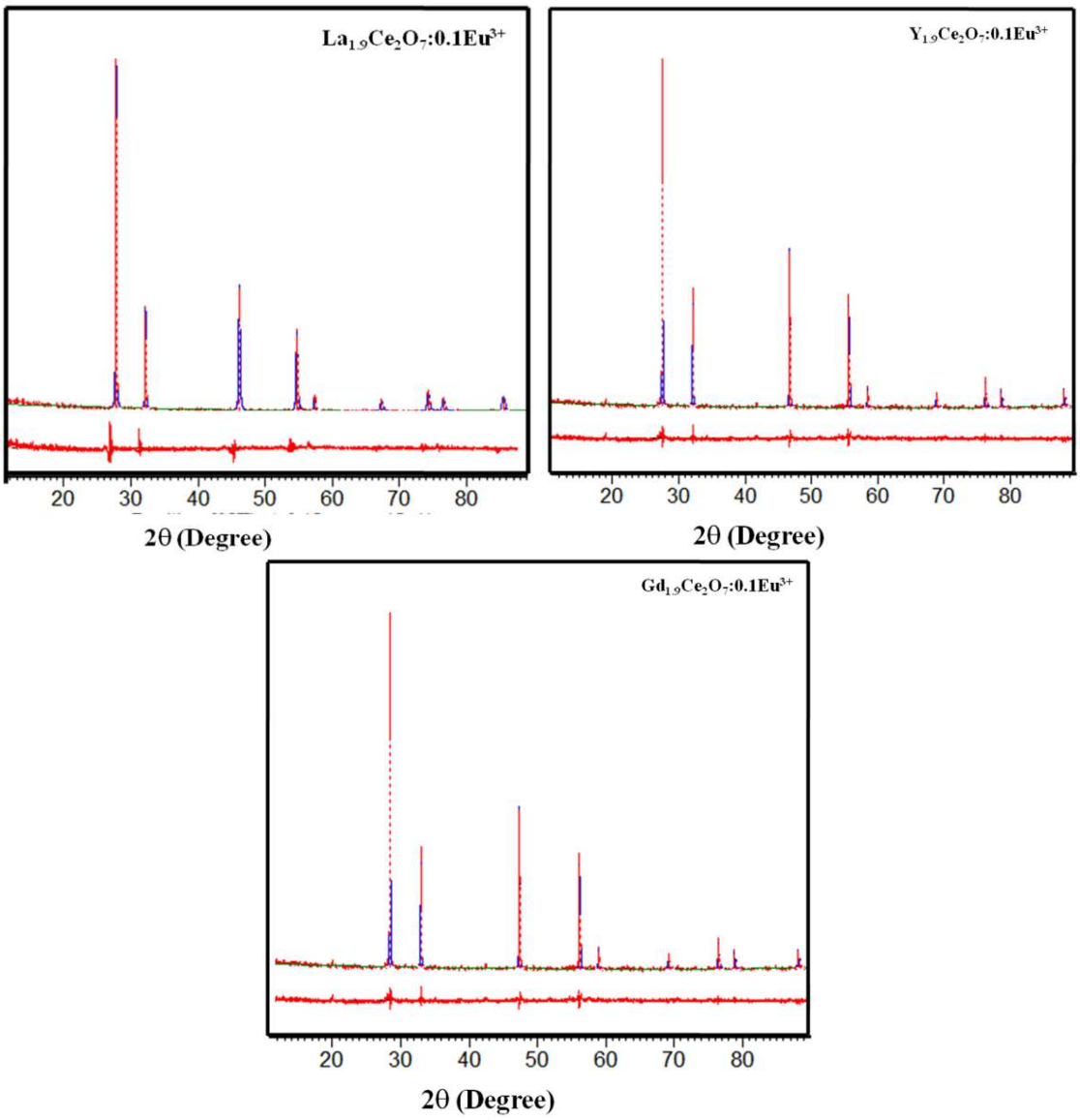

Fig. 3.2 The observed, calculated and difference powder diffraction profiles of $A_2Ce_2O_7$:0.1Eu^{3+} (A = La, Y and Gd) phosphors obtained from Rietveld refinement.

The observed, calculated and difference powder diffraction profiles of $A_{1.9}Ce_2O_7$:0.1Eu^{3+} (A = La, Y and Gd) are given in the Fig. 3.2. The refined parameters obtained from the Rietveld analysis of all the samples are listed in Table 3.1. The refined R values suggest that the refinement is in good agreement with the space group in all respects. Comparing the ionic radii in Co-ordination VIII of La^{3+} (1.160 Å)/ Y^{3+} (1.019 Å)/ Gd^{3+} (1.053 Å) and Ce^{4+} (0.97 Å), Eu^{3+} (1.066 Å) had expected to occupy more in (Gd^{3+}/La^{3+}/Y^{3+}) sites based on its ionic size and charge neutrality. The lattice parameter is also in accordance with the ionic radii ie. Y^{3+} < Gd^{3+} < La^{3+}

and the average crystallite size can be estimated from the Scherrer equation are listed in Table.3.1.

3.3.1.2 Raman spectroscopic studies

Further confirmation of the structures of the $A_{1.9}Ce_2O_7$:0.1Eu^{3+} (A = La, Y and Gd) samples was carried out by Raman spectroscopy. Fig. 3.3 shows the Raman spectra of the samples and it clearly revealed the fluorite structure of the samples having the typical Raman mode with an F_{2g} symmetry at 467 cm^{-1} (Athira et al. 2017).

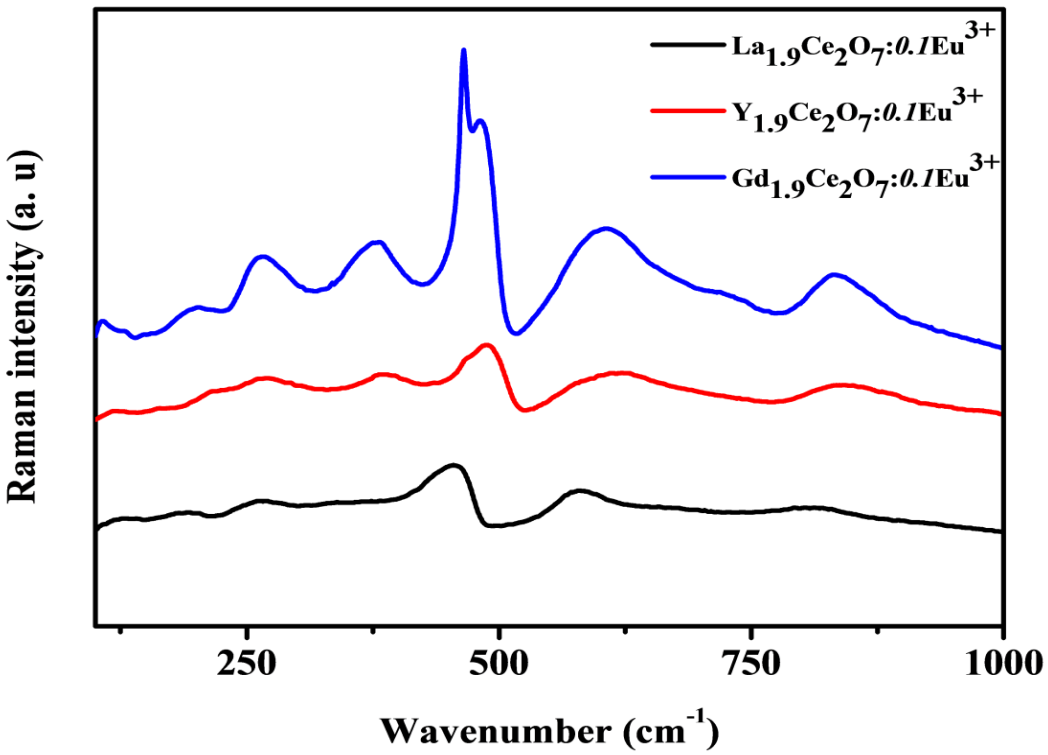

Fig. 3.3 Raman spectra of $A_2Ce_2O_7$:0.1Eu^{3+} (A = La, Y and Gd) red phosphors.

3.3.1.3 Morphological studies

Typical scanning electron micrographs of the three samples $A_{1.9}Ce_2O_7$:0.1Eu^{3+} (A = La, Y and Gd) are given in Fig. 3.4. All the three samples were slightly agglomerated and the particle sizes are in the range 1-3 μm. The chemical composition of the three phosphors were recorded using EDS is shown in Fig. 3.5 and identified the presence of all expected elements. Elemental X-ray dot mapping of the samples were also carried out to study the uniform distributed of elements in the sample and the results are given in Fig. 3.6.

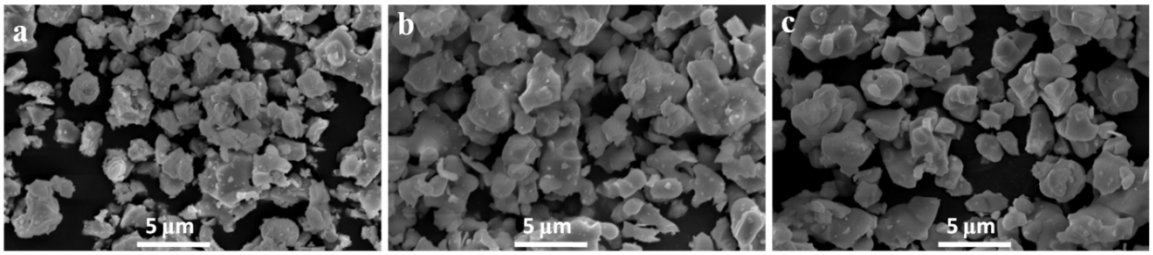

Fig. 3.4 Scanning electron micrographs of $A_{1.9}Ce_2O_7$:0.1Eu^{3+} A = La (a), Y (b) and Gd (c) red phosphors.

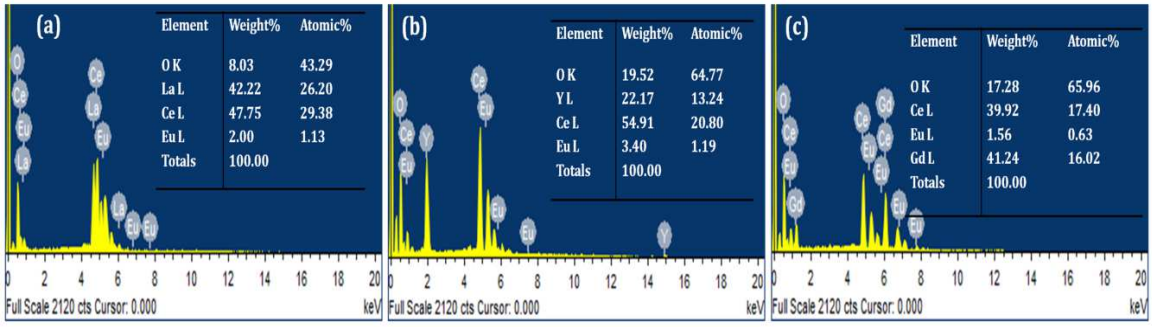

Fig. 3.5 EDS of $A_{1.9}Ce_2O_7$:0.1Eu^{3+} A = La (a), Y (b) and Gd (c) red phosphors.

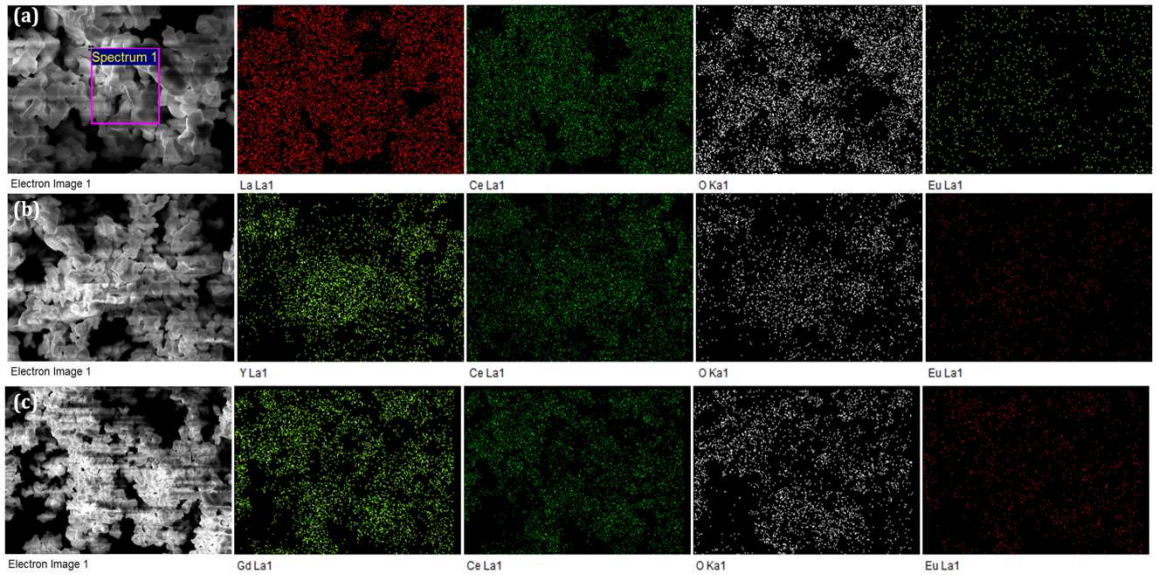

Fig. 3.6 Elemental X-ray dot mapping of $A_{1.9}Ce_2O_7$:0.1Eu^{3+} A = La (a), Y (b) and Gd (c) red phosphors.

3.3.1.4 Absorption studies

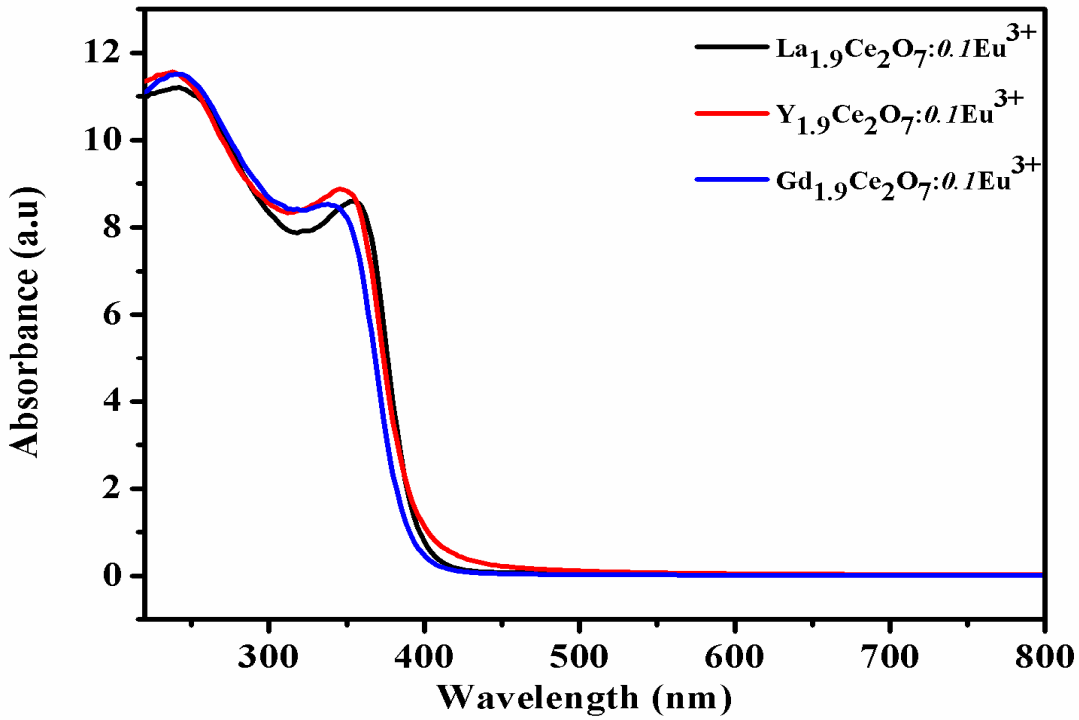

Fig. 3.7 UV/vis absorption spectra of $A_{1.9}Ce_2O_7$:0.1Eu^{3+} (A = La, Y and Gd) red phosphors.

The UV/vis absorption spectra of the $A_{1.9}Ce_2O_7$:0.1Eu^{3+} (A = La, Y and Gd) phosphors are given in Fig. 3.7. All the samples have a strong absorption bands in the UV region due to the charge transfer transition from O^{2-} (2p) to Ce^{3+} (4f) orbitals, O^{2-} (2p) to Ce^{4+} (4f) orbitals in $A_2Ce_2O_7$. The band gap was calculated from the absorption spectra using Shapiro's method by extrapolating the onset of absorption to the wavelength axis and the estimated band gap energies are given in Table 3.2. The absorption spectra of $Y_{1.9}Ce_2O_7$:0.1Eu^{3+} phosphor exhibited a red shift and $Gd_{1.9}Ce_2O_7$:0.1Eu^{3+} phosphor exhibited a blue compared with that of $La_{1.9}Ce_2O_7$:0.1Eu^{3+} phosphors. From our previous studies (Athira et al. 2014; Athira et al. 2017), it is because of that there co-existed a small amount of Ce^{3+} on the surface of $A_2Ce_2O_7$ samples and the fraction of Ce^{3+} ions increased with Eu^{3+} doping. As discussed in XRD analysis because of the matching ionic size of Eu^{3+} and Gd^{3+}, the doping of Eu^{3+} ions in the $Gd_2Ce_2O_7$, results in the decrease of the Ce^{3+} concentration by inhibiting the replacement of Ce^{4+} by trivalent Eu^{3+}. Hence the blue shifting occurs in the absorption spectrum because of the decrease in Ce^{3+} concentration.

The larger the Ce^{3+} concentration may cause the red shift in $Y_{1.9}Ce_2O_7:0.1Eu^{3+}$ and $La_{1.9}Ce_2O_7:0.1Eu^{3+}$.

Table 3.2 Band gap energy and Ce^{3+} concentration, of the $A_{1.9}Ce_2O_7:0.1Eu^{3+}$ (A = La, Y and Gd) phosphors

Composition	Band gap energy (E_g) (eV)	[Ce^{3+}] (%)
$La_{1.9}Ce_2O_7:0.1Eu^{3+}$	3.04	16.5
$Y_{1.9}Ce_2O_7:0.1Eu^{3+}$	3.00	17.1
$Gd_{1.9}Ce_2O_7:0.1Eu^{3+}$	3.08	14.3

3.3.1.5 X-ray photoelectron spectroscopy studies

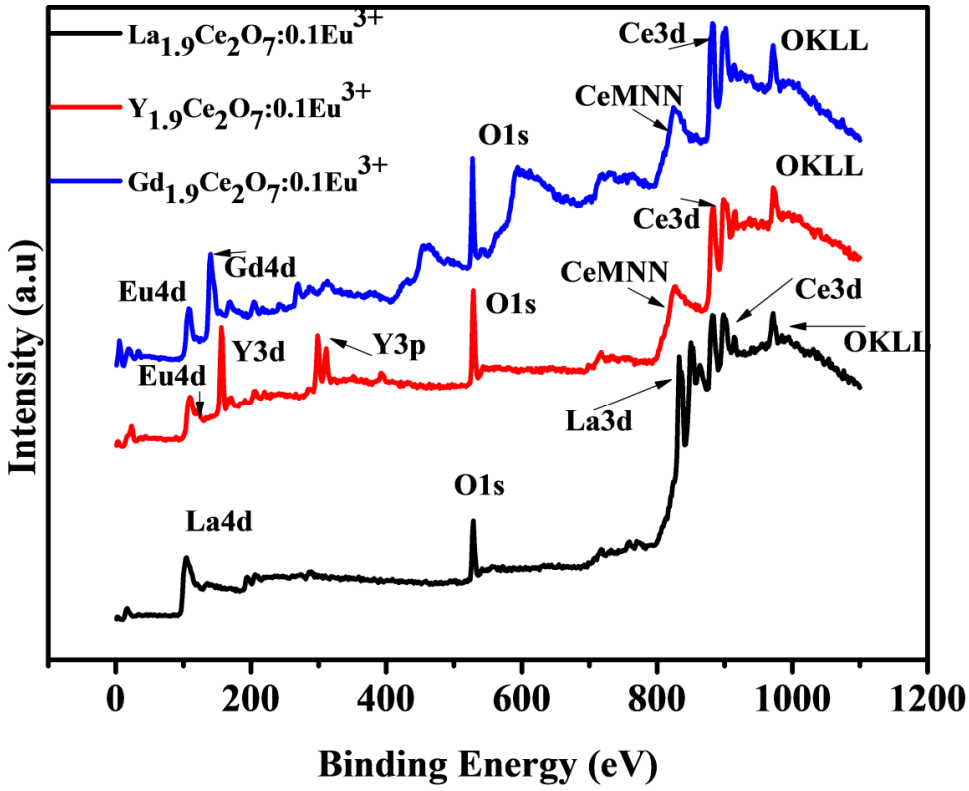

Fig. 3.8 Survey scan X-ray photoelectron spectrum of $A_{1.9}Ce_2O_7:0.1Eu^{3+}$ (A = La, Y and Gd) phosphors

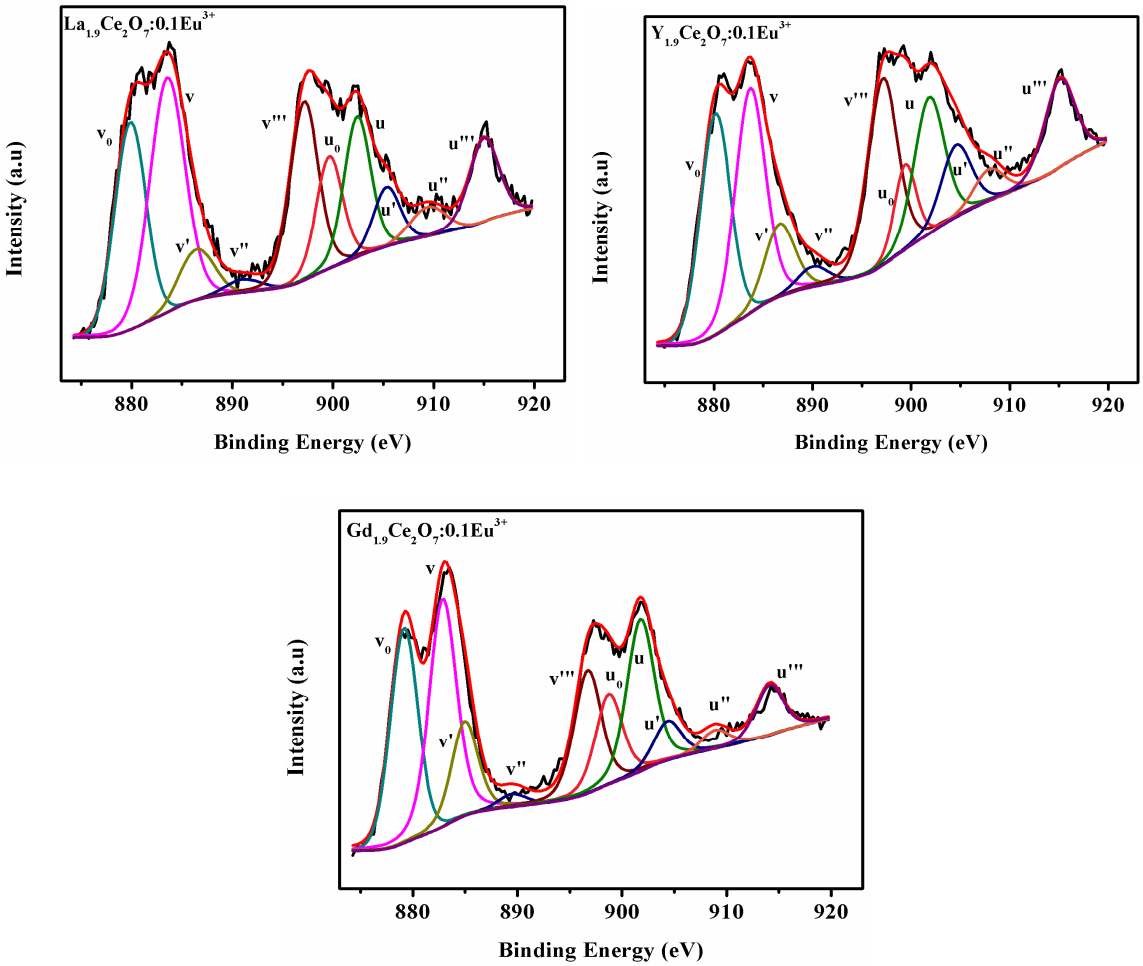

Fig. 3.9 Deconvoluted XPS spectra of Ce (3d) for $A_{1.9}Ce_2O_7$:0.1Eu^{3+} (A = La, Y and Gd) red phosphors.

X-ray photoelectron spectroscopy is a renowned technique to explore the surface chemical composition, the oxidation states of the constituent elements present in the sample. The presence of Ce^{3+} ions can be confirmed by XPS analysis. A wide survey scan X-ray photoelectron spectrum of $A_{1.9}Ce_2O_7$:0.1Eu^{3+} (A = La, Y and Gd) phosphors is shown in Fig. 3.8. The Ce 3d XPS spectrum of the samples is shown in Fig. 3.9. It can be seen that the Ce 3d electron core level XPS spectra are composed of 10 peaks related to five different spin–orbit doublets due to two multiplets 3/2 and 5/2 along with 3+ and 4+ oxidation states of Ce (Ramana et al. 2016). The multiplicity of these states arises from different Ce 4f level occupancies in the final state. According to this result, tetravalent Ce^{4+} and trivalent Ce^{3+} species are considered to coexist on the surface of all the samples ie. v/u, v"/u", and v"'/u"' are attributed to tetravalent Ce^{4+}; v/u and v"/u" that are due to a mixture of $3d^9 4f^2 O2p^4$

and $3d^94f^1O2p^5$ configurations, and v'''/u''' is a $3d^94f^0O2p^6$ final state, while, v_0/u_0 and v'/u' are attributed to trivalent Ce^{3+}, are due to $3d^94f^1O2p^6$ and $3d^94f^2O2p^5$ final state (Burroughs et al. 1976). To evaluate the Ce^{3+} concentration, we measured the surface relative molar ratio of $Ce^{3+}/Ce^{3+} + Ce^{4+}$ from the peak areas of Ce^{3+} and Ce^{4+} in Ce 3d spectrum and the values are listed in Table 3.2. Thus, it was found that the Ce^{4+} concentration was more in $Gd_{1.9}Ce_2O_7$:$0.1Eu^{3+}$ phosphor and comparatively less in $Y_{1.9}Ce_2O_7$:$0.1Eu^{3+}$ phosphors which is in good agreement with the shifting of absorption edge in the Uv-vis absorption spectra.

3.3.1.6 Photoluminescence studies

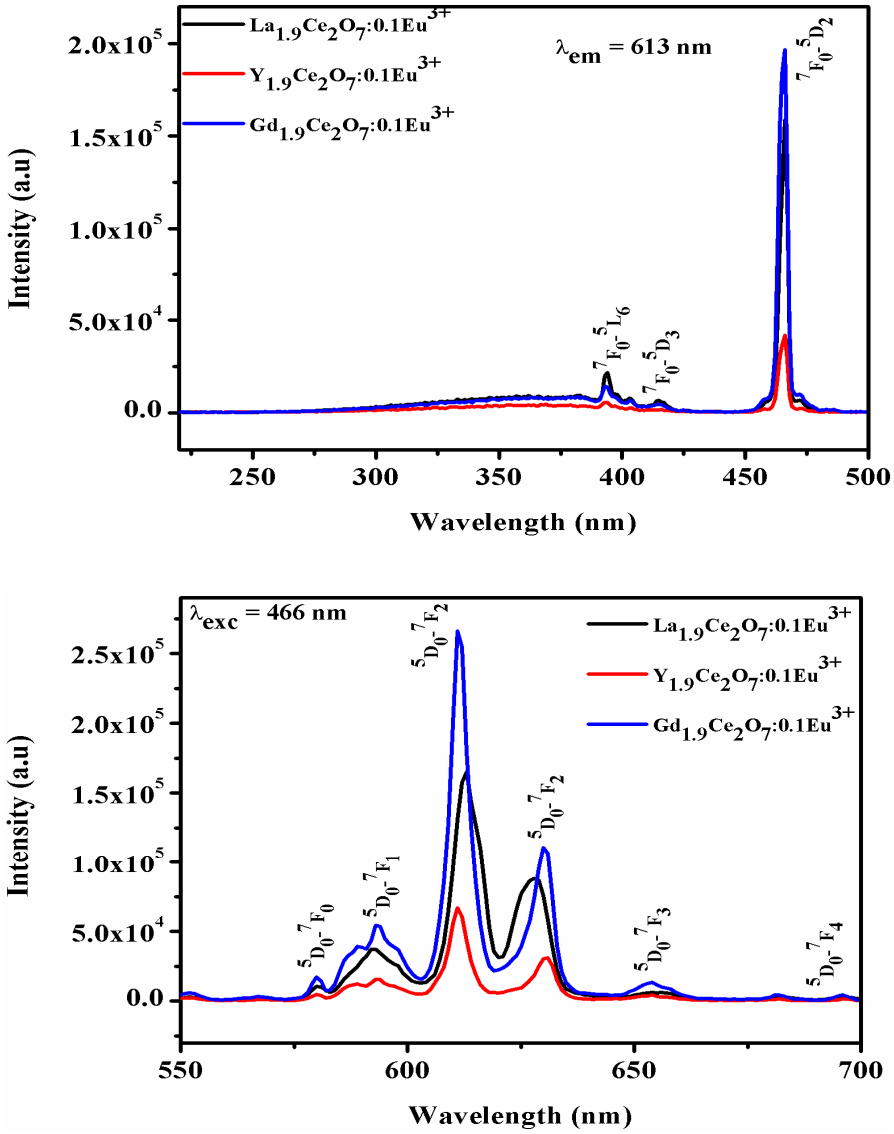

Fig. 3.10 Excitation and Emission spectra of $A_{1.9}Ce_2O_7$:$0.1Eu^{3+}$ (A = La, Y and Gd) red phosphors

Photoluminescence properties of all the three samples were carried out and the excitation and emission spectra of three typical samples are given in Fig. 3.10. The excitation spectra were recorded by monitoring the peak intensity at 612 nm and the spectrum include weak a broad charge transfer (CT) band of Ce^{4+} - O^{2-} from 280 to 380 nm followed by a series of sharp peaks due to intra-$4f^6$ transitions of Eu^{3+} in the lattice. Of these peaks, the most intense peak at 394 and 466 nm are assigned to $^7F_0 \rightarrow {}^5L_6$ and $^7F_0 \rightarrow {}^5D_2$ transitions respectively (Linda et al. 2014) are of particular interest as these correspond to the emission wavelengths of near UV and blue light LEDs.

From the excitation spectra of the three samples, the Eu^{3+} f-f transition at 466 nm is more intense in the order of Gd>La>Y based phosphors. Upon 466 nm excitation, the major emission peaks from characteristics Eu^{3+} transitions are observed at 580 nm ($^5D_0$-$^7F_0$), 593 nm ($^5D_0$-$^7F_1$), 612 and 630 nm ($^5D_0$-$^7F_2$), 654 nm ($^5D_0$-$^7F_3$) and 682, 696 and 711 nm ($^5D_0$-$^7F_4$) respectively. In the emission spectra, it can be seen that for all the three phosphors, the strongest emission is the same at 612 nm the hypersensitive $^5D_0$-$^7F_2$ electric dipole transition dominates over the magnetic dipole transition indicating the non-centrosymmetric site of Eu^{3+} ions in the lattice (Blasse et al. 1979). It can be inferred that the doping ions (Eu^{3+}) occupy the same site in the $La_2Ce_2O_7$, $Y_2Ce_2O_7$ and $Gd_2Ce_2O_7$ which belongs to the CeO_2 fluorite-type structure, resulting in the $^5D_0$-$^7F_2$ emission of Eu^{3+} ions being more prominent and showing red emission. It is clear from the spectra that the Gd based phosphors shows the maximum emission intensity, which is more than 1.8 times that of La based phosphors. This may be due the similarity in the electronic configuration and due to the matching ionic radius of gadolinium and europium ions. The asymmetric ratio (ratio of ED and MD transitions) gives information about the site occupancy of Eu^{3+} ions in the $La^{3+}/Y^{3+}/Gd^{3+}$ sites. The better asymmetric ratio (Table 3.2) of the gadolinite sample shows a better occupancy of Eu^{3+} ions in more non-centrosymmetric sites in comparison with the lanthanide sample. The full width at half maximum (*fwhm*) of the emission band should be as small as possible to achieve high luminous output. From the Table 3.3, it is clear that the *fwhm* of $Gd_{1.9}Ce_2O_7$:$0.1Eu^{3+}$ sample had small compared to the other two samples.

The decay for $^5D_0$-$^7F_2$ transition (612 nm) of $A_{1.9}Ce_2O_7$:0.1Eu^{3+} (A = La, Y and Gd) under near UV excitation are shown in Fig. 3.11. The decay curves can be fitted well with a single exponential function given as; $I = A \exp(-x/\tau)$ where I, τ and A are the intensity, decay time and fitting parameter respectively. The lifetime values are listed in Table 3.2. The decay lifetime (τ) are proportional to the transition probability ie. a heavier distortion of the crystallographic sites usually denotes a higher transition probability of Eu^{3+} ions (Linda et al. 2014). Thus a higher lifetime of the gadolinite sample confirms a more uniform distribution of Eu^{3+} ions in the lattice. On the basis of the emission spectra and life times of the $^5D_0$ emitting level, the quantum efficiency (η) of the Eu^{3+} ion excited state was determined (Table 3.2). Gadolinite sample shows high efficiency compared to other systems. Thus the substitution of Eu^{3+} at gadolinium site favour better environment for the luminescent ions there by showing higher emission intensity, lifetime values and quantum efficiency.

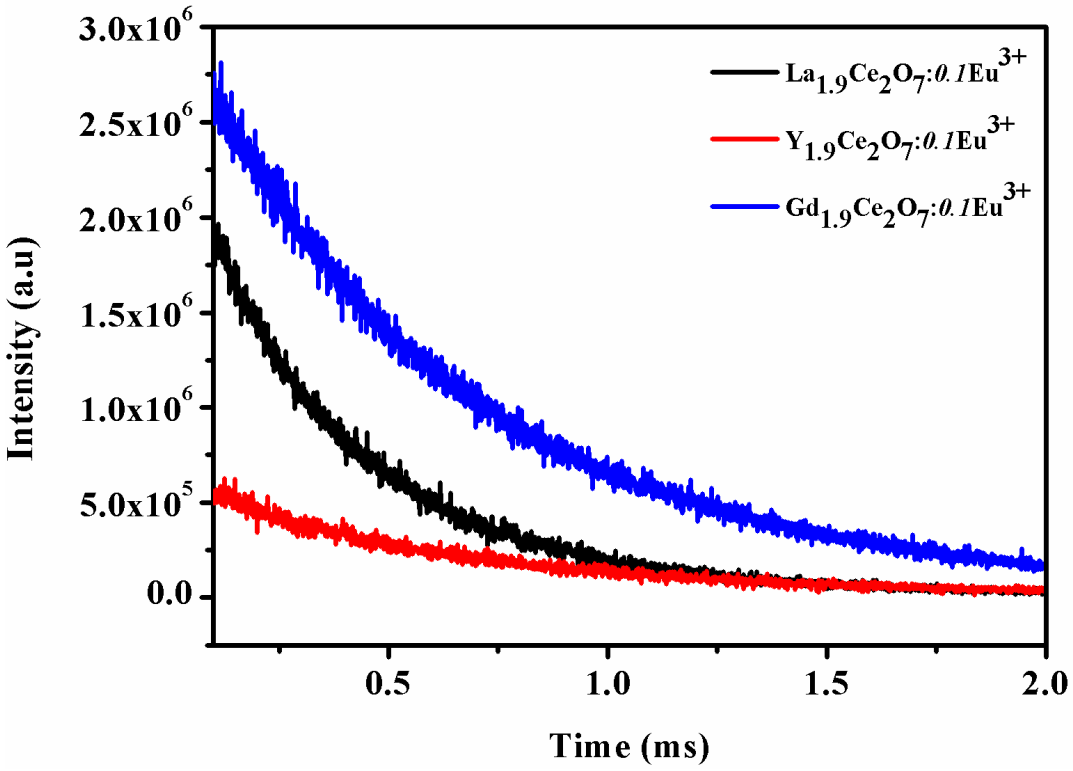

Fig. 3.11 Decay curves of Eu^{3+} emission at 612 nm in $A_{1.9}Ce_2O_7$:0.1Eu^{3+} (A = La, Y and Gd) red phosphors under 466 nm excitation.

Table 3.3 FWHM of the $^5D_0$-$^7F_2$ transition at 613 nm red emission, Asymmetric ration, life time and quantum efficiency of the $A_{1.9}Ce_2O_7$:$0.1Eu^{3+}$ (A = La, Y and Gd) phosphors

Composition	FWHM (nm)	Asymmetric ratio	Lifetime (τ) (ms)	Quantum efficiency (η) (%)
$La_{1.9}Ce_2O_7$:$0.1Eu^{3+}$	8.01	3.72	0.604	10.03
$Y_{1.9}Ce_2O_7$:$0.1Eu^{3+}$	6.24	3.52	0.598	6.78
$Gd_{1.9}Ce_2O_7$:$0.1Eu^{3+}$	5.25	3.84	0.613	11.32

Luminescence is mainly attributed to the crystallographic structure including the co-ordination of the activator and its surroundings, and the ordering of the activator in the lattice (Linda et al. 2016). The present Eu^{3+} doped $A_2Ce_2O_7$ (A = La, Y and Gd) system gave scope to understand the influence of different rare earths, Ce^{3+} concentration and the Eu^{3+} environment on the photoluminescence properties. The degree of ordering of cations is Y < La < Gd, which aids the uniform distribution of Eu^{3+} ions and prevent the further cluster formation of Eu^{3+}- Eu^{3+} in the lattice. This is further characterise by the $^5D_0$ life time and the values follows the same trend of ordering of the lattice. This allows more partition of Eu^{3+} ions in the lattice avoiding the cross relaxation between the Eu^{3+} ions enhancing the luminescence. Since the gadolinium based system showed better luminescent properties we confined our studies to $Gd_2Ce_2O_7$ system and tried to improve the luminescence properties.

3.3.2 Effect of Eu^{3+} doping on the $Gd_2Ce_2O_7$ host lattice

3.3.2.1 Powder X-Ray diffraction studies

Powder X-ray diffraction patterns of $Gd_{2-x}Ce_2O_7$: xEu^{3+} (x = 0.05, 0.10, 0.15 and 0.20) given in Fig. 3.12 reveal the crystallinity and phase purity of all the samples and are in good agreement with the cubic fluorite structure having the space group *Fm3m* (JCPDS File no. 01-071-4807). No impurity peaks were seen upon increasing the doping concentration of Eu^{3+}, which indicating the effective substitution of Eu^{3+} in the host lattice. Furthermore, the peaks are shifted towards left upon doping. This is ascribed to the expansion of the lattice as larger Eu^{3+} ions

(1.066 Å, CN = 8) occupy more and more into the smaller Gd^{3+} (1.053 Å, CN = 8) sites in the $Gd_2Ce_2O_7$ compound. The shift of XRD peaks are shown in the inset of Fig. 3.12.

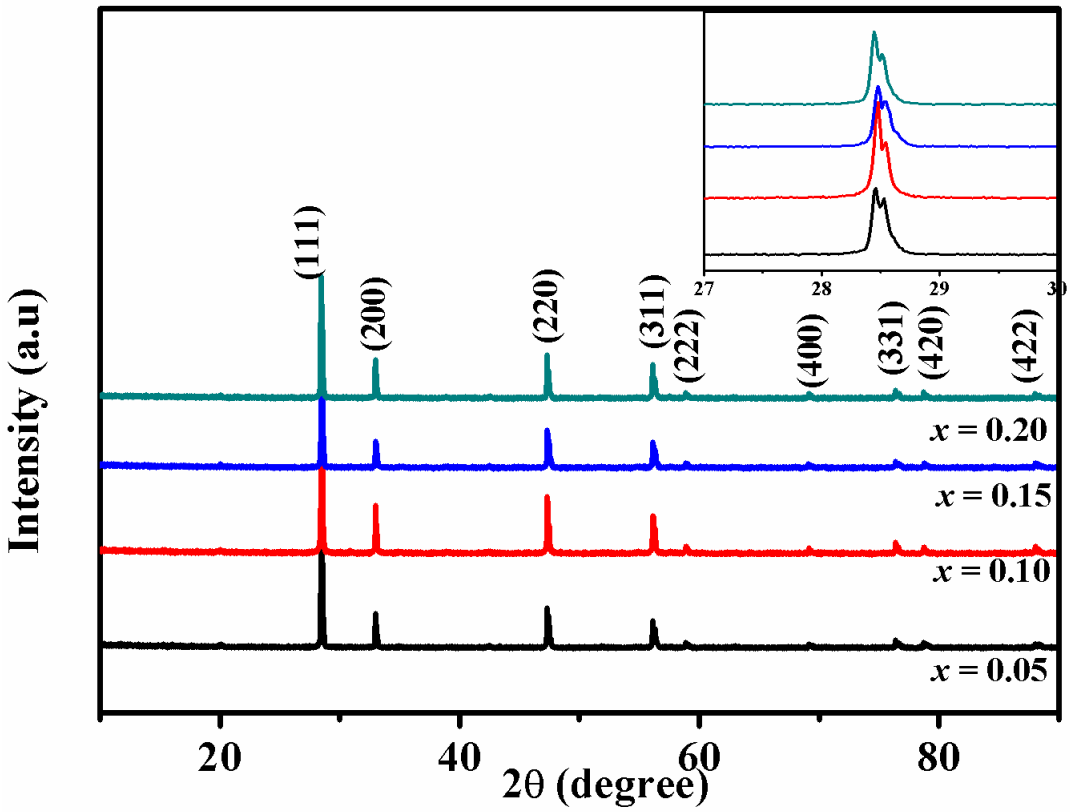

Fig. 3.12 Powder X-ray diffraction patterns of $Gd_{2-x}Ce_2O_7$: xEu^{3+} (x = 0.05, 0.10, 0.15 and 0.20) red phosphors. The inset shows the expanded view of the peak around 2θ 27-30°.

3.3.2.2 Raman spectroscopic studies

Raman spectra of the $Gd_{2-x}Ce_2O_7$: xEu^{3+} (x = 0.05, 0.15 and 0.20) red phosphors were also taken in the wavenumber ranging from 100 to 1000 cm^{-1} and shown in Fig. 3.13. The features of the spectra are similar with some variation in the intensity and *fwhm*. The Raman mode (F_{2g}) at 467 cm^{-1} which is a signature of the cubic fluorite type structure gets decreases as the Eu^{3+} substitution increases.

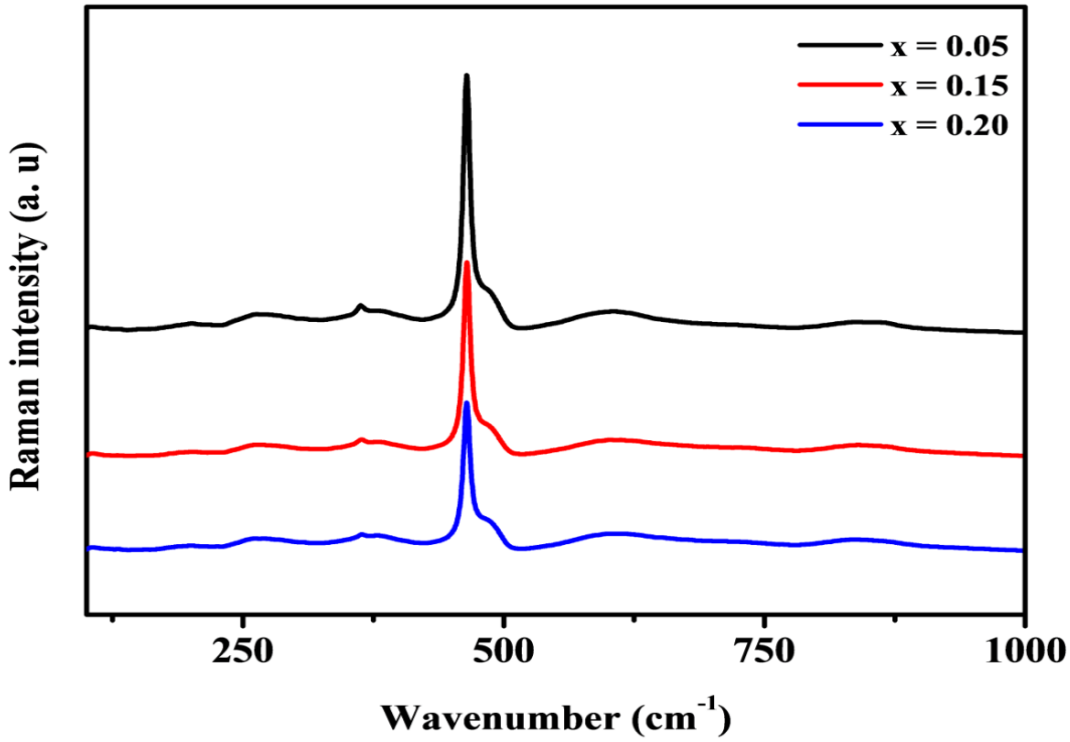

Fig. 3.13 Raman spectra of $Gd_{2-x}Ce_2O_7$: xEu^{3+} (x = 0.05, 0.15 and 0.20) red phosphors.

3.3.2.3 Morphological studies

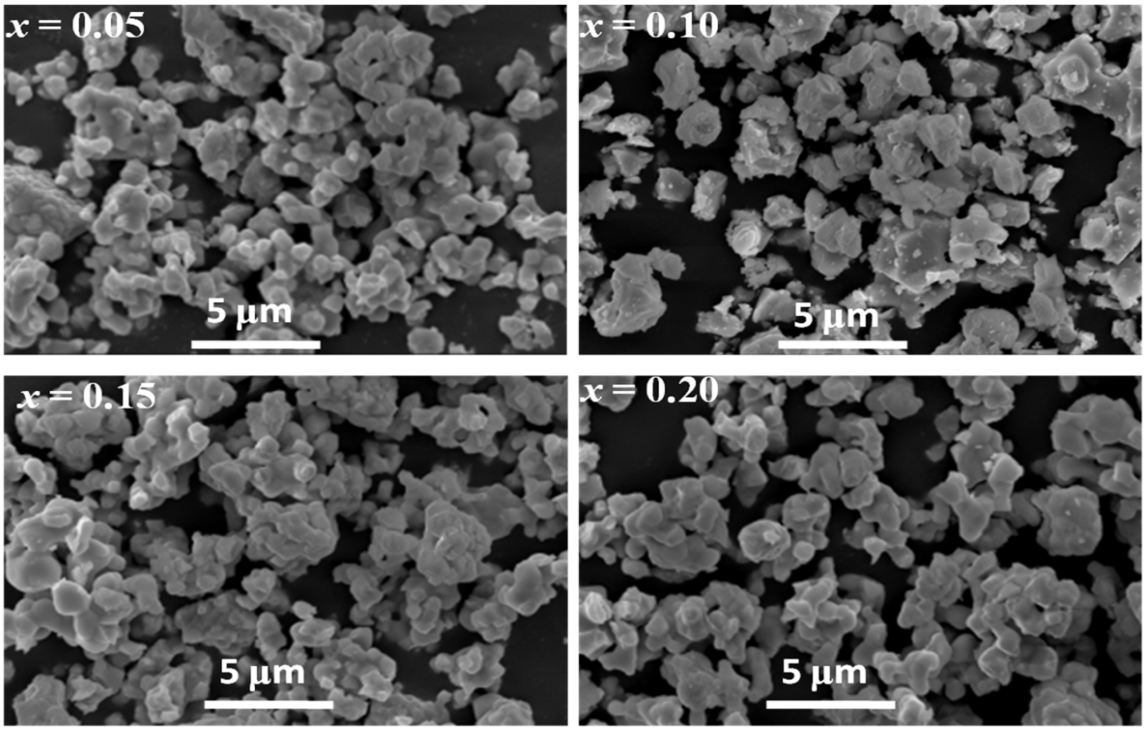

Fig. 3.14 Typical SEM photographs of $Gd_{2-x}Ce_2O_7$: xEu^{3+} (x = 0.05, 0.10, 0.15 and 0.20) red phosphors.

The typical SEM photographs of $Gd_{2-x}Ce_2O_7$: xEu^{3+} (x = 0.05, 0.15 and 0.20) red phosphors are shown in Fig. 3.14. The morphology of all the samples is more or less similar which are highly crystalline and slightly agglomerated particles in the range 1-3 µm. The energy dispersive X-ray spectroscopy measurements are shown in Fig. 3.15 which confirms the presence of the Gd, Ce, Eu and O in the typical $Gd_{2-x}Ce_2O_7$: xEu^{3+}; x = (a) 0.05 and (b) 0.20 phosphor and the obtained chemical composition were close to the theoretical stoichiometry. Fig. 3.16 shows the elemental mapping analysis of typical $Gd_{1.8}Ce_2O_7$:$0.2Eu^{3+}$ red phosphor and it confirms that all elements are uniformly distributed in the sample.

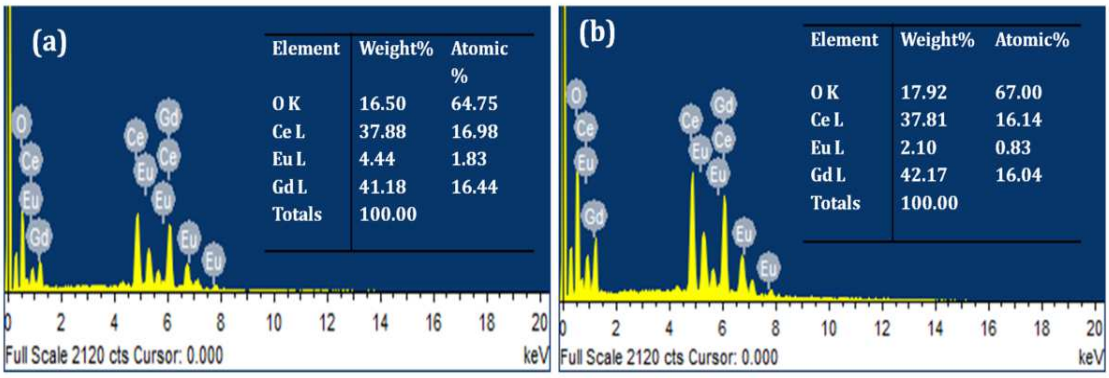

Fig. 3.15 EDS of $Gd_{2-x}Ce_2O_7$: xEu^{3+}; x = (a) 0.05 and (b) 0.20 red phosphors.

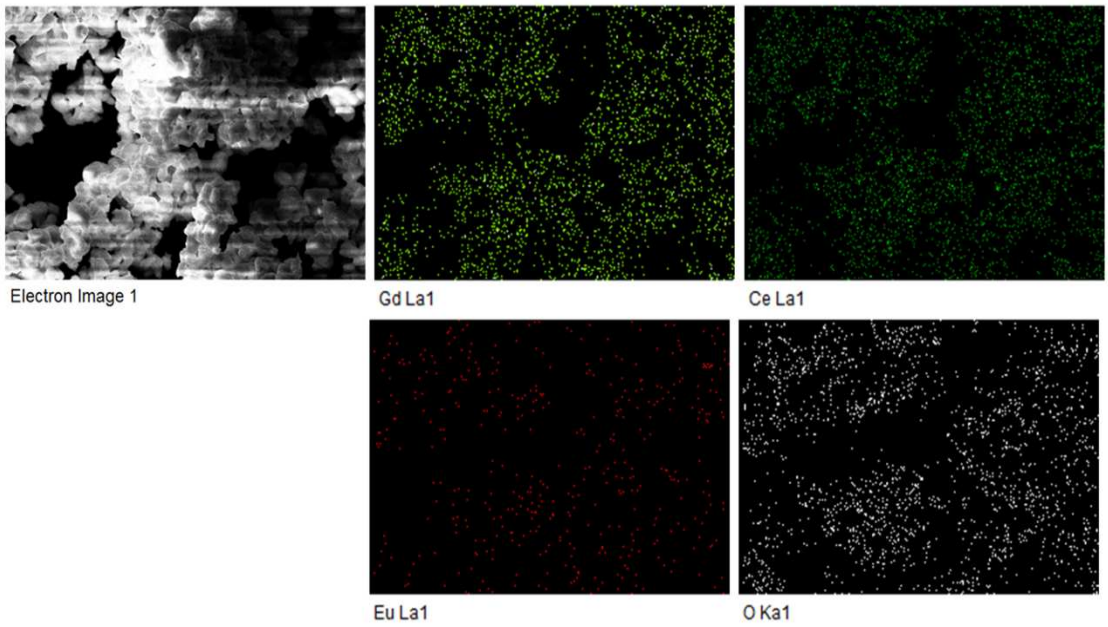

Fig. 3.16 Elemental dot mapping of $Gd_{1.8}Ce_2O_7$: *0.2*Eu^{3+} red phosphors.

3.3.2.4 Absorption studies

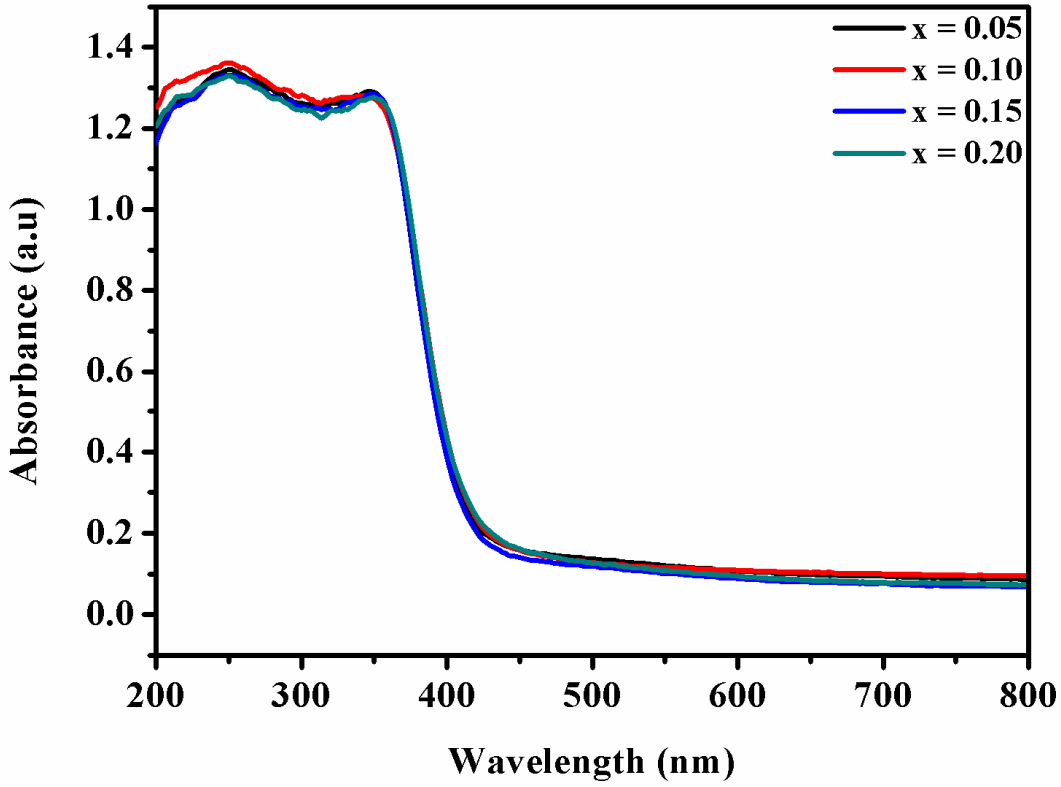

Fig. 3.17 UV-vis absorption spectra of $Gd_{2-x}Ce_2O_7$: xEu^{3+} (x = 0.05, 0.10, 0.15 and 0.20) red phosphors.

The correlation between the band gap energies and the doping of the samples were studied by using UV-vis absorption spectroscopy. Fig. 3.17 shows the UV-vis absorption spectra of $Gd_{2-x}Ce_2O_7$: xEu^{3+} (x = 0.05, 0.10, 0.15 and 0.20) red phosphors. Eu^{3+} doped $Gd_2Ce_2O_7$ samples exhibit stronger absorption bands in the UV range. Furthermore, the onset of absorption spectra exhibited a blue shift compared to the lower dopant sample. The blue shift in the band gap energy (E_g) is correlated to the decrease of Ce^{3+} content which is distributing either at the $Gd_2Ce_2O_7$ grain boundaries forming amorphous Ce_2O_3 or around the oxygen vacancies sites in the lattice. The oxygen vacancy concentration is closely linked to the ease with which the cerium can change the oxidation states (Jiang et al. 2012). This is partially due to the similar energy of the 4f and 5d electronic states and the low potential energy barrier to electron density distribution between them (Lawrence et al. 2011). Due to the change from Ce^{4+} to Ce^{3+} ions in Eu^{3+} doped $Gd_{2-x}Ce_2O_7$, the charge transfer gap between O (2p) and Ce (4f) bonds increased, which led to the blue shift of

absorption spectra. The decrease of Ce^{3+} concentration in the lattice will eliminate some localized states within the band gap due to the corresponding decrease of vacancies (defects) content. Thus the blue shift in the absorption spectra is due to the Ce^{3+} content decrease.

Table 3.4 Band gap energy and Ce^{3+} concentration of the $Gd_{2-x}Ce_2O_7$:xEu^{3+} (x = 0.05, 0.15 and 0.20) phosphors.

Composition	Band gap energy (E_g) (eV)	[Ce^{3+}] (%)
x = 0.05	2.93	15.45
x = 0.15	3.09	14.0
x = 0.20	2.97	12.11

3.3.2.5 X-ray photoelectron spectroscopy studies

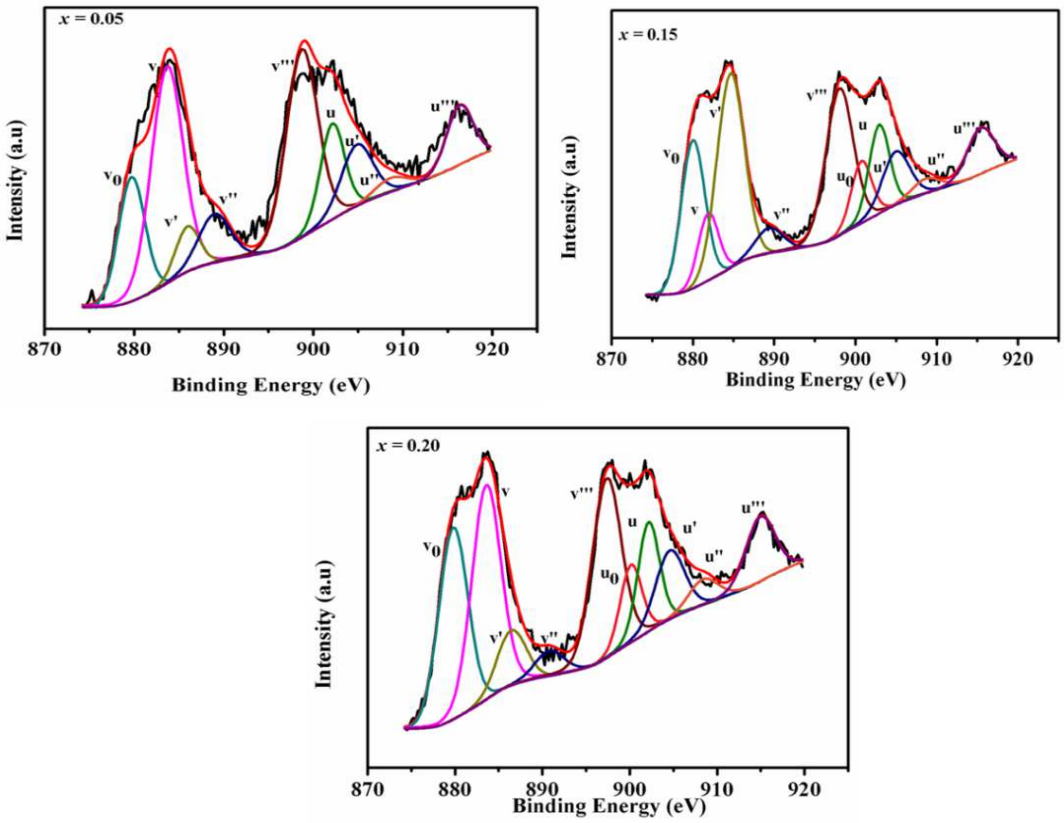

Fig. 3.18 Deconvoluted XPS spectra of Ce (3d) for $Gd_{2-x}Ce_2O_7$: xEu^{3+} (x = 0.05, 0.15 and 0.20) red phosphors.

The quantitative analysis of Ce^{3+} concentration was carried out by using XPS analysis. Fig. 3.18 shows the deconvoluted XPS spectra of Ce (3d) of $Gd_{2-x}Ce_2O_7$: xEu^{3+} (x = 0.05, 0.15 and 0.20) red phosphors. By fitting the curves and then calculating the area of the fitted peaks, we concluded that the Ce^{3+} concentration decreases with increase in Eu^{3+} ions in the $Gd_{2-x}Ce_2O_7$ phosphor and the values are listed in Table 3.4. This assessment of Ce^{3+} oxidation from the absorption spectra is in good agreement with the XPS results.

3.3.2.6 Photoluminescence studies

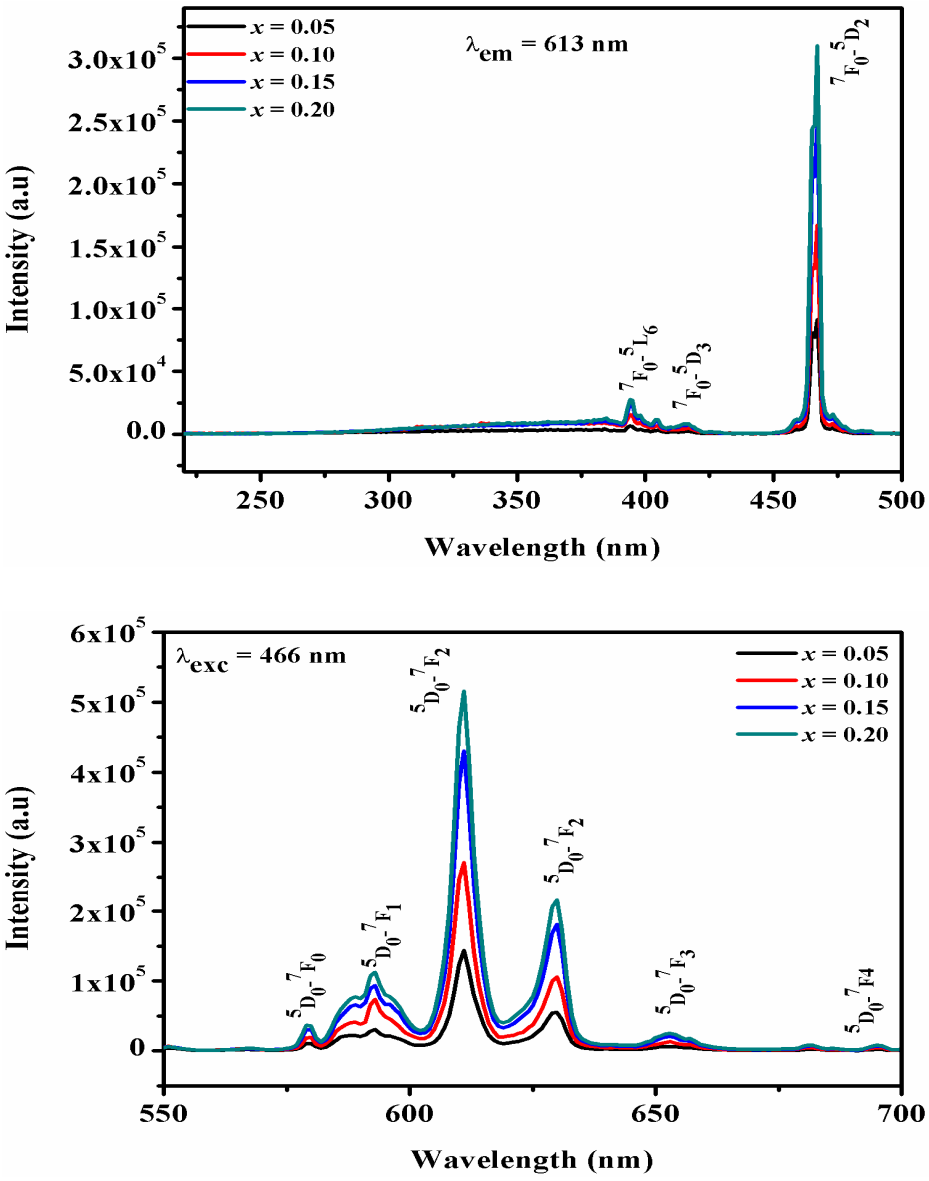

Fig. 3.19 Excitation and Emission spectra of $Gd_{2-x}Ce_2O_7$: xEu^{3+} (x = 0.05, 0.10, 0.15 and 0.20) red phosphors

The critical influence of the activator concentration on the luminescence intensity was studied by recording the excitation and emission spectra (Fig. 3.19). One of the remarkable changes in the excitation spectra is the enhanced f-f transition intensity. Unlike the usual Eu^{3+} doped red phosphor materials the charge transfer band (CTB) is broader and is overlapped with the peak at 394 nm. This broadening of the CTB may be the reason for the intense excitation peak at 467 nm. There is a slight increase in the intensity of the broad peak with increasing doping concentration. The line shape of emission spectra does not change with Eu^{3+} ion concentrations. This implies that europium occupies a single crystallographic site in the lattice. The phosphors show enhanced red emission intensities with increase in doping concentration. The variation of emission intensities with Eu^{3+} concentration does not create any concentration quenching. The enhanced electric dipole transition intensity arises from the symmetry distortion of Eu^{3+} in the lattice.

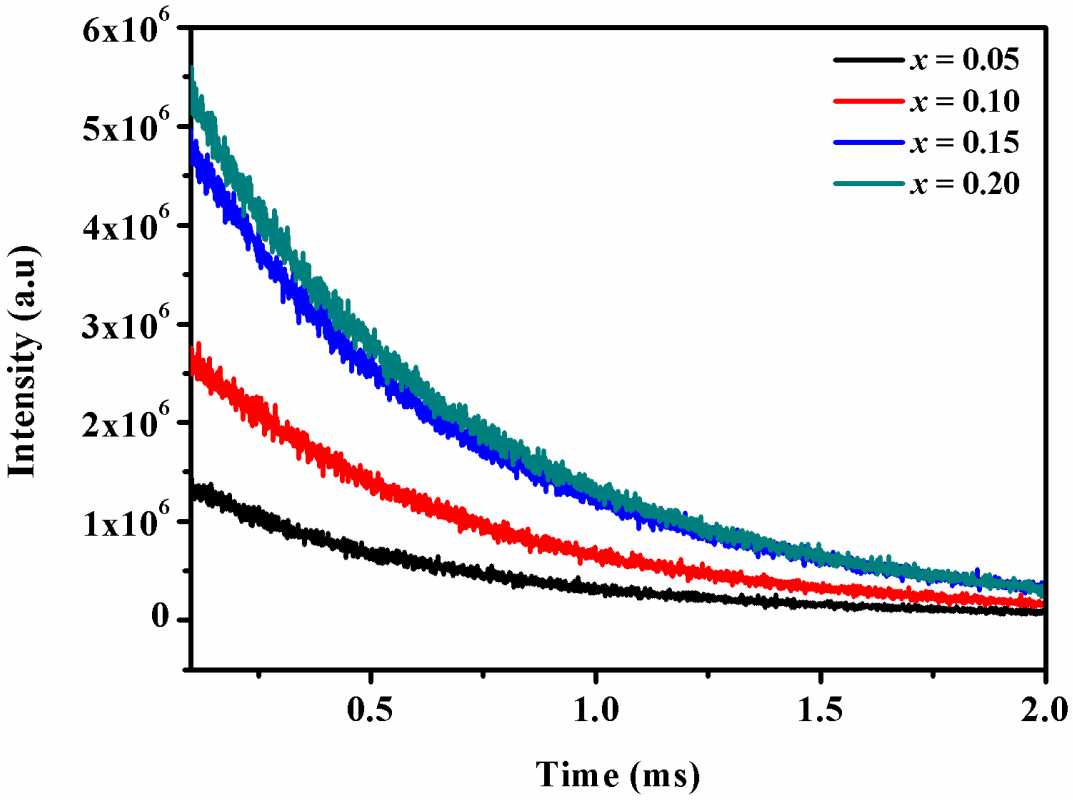

Fig. 3.20 Decay curves of Eu^{3+} emission at 612 nm in $Gd_{2-x}Ce_2O_7$: xEu^{3+} (x = 0.05, 0.10, 0.15 and 0.20) red phosphors under 466 nm excitation.

Table 3.5 FWHM of the $^5D_0$-$^7F_2$ transition at 613 nm red emission, Asymmetric ration, life time and quantum efficiency of the $Gd_{2-x}Ce_2O_7$:xEu^{3+} (x = 0.05, 0.15 and 0.20) phosphors.

Composition	FWHM (nm)	Asymmetric ratio	Lifetime (τ) (ms)	Quantum efficiency (η) (%)
x = 0.05	5.27	3.63	0.582	6.54
x = 0.15	5.38	4.53	0.615	12.33
x = 0.20	5.40	4.56	0.619	13.90

The substitution of higher ionic Eu^{3+} in the Gd^{3+} site increases the degree of ordering of cations in the lattice which helps for the uniform distribution of Eu^{3+} ions and further prevents the cluster formation of Eu^{3+} - Eu^{3+} in the lattice. This allows more partition of Eu^{3+} ions in the lattice avoiding the cross relaxation between the Eu^{3+} ions which results in the enhancement of luminescence without any concentration quenching. The most sensitive parameter used for understanding the symmetry around the Eu^{3+} is the asymmetric ratio (R) and the variation of R with Eu^{3+} ion concentration is tabulated in Table 3.5.The R values increases with increase in Eu^{3+} ion which confirms the more distortion in the Eu^{3+} environment that gives stronger photoluminescence emission. The decay curves of all the samples are given in Fig. 3.20 and the life time values are listed in Table 3.5. It can be seen that the life time values obtained from the decay curves increases monotonically with activator concentration. The quantum efficiency was calculated from the lifetime values and increases with increase in Eu^{3+} ion concentration.

3.3.3 Influence of Ca-Nb substitution on the optical properties of Eu^{3+} doped $Gd_{1.8-x}Ce_{2-y}O_7$:0.2 Eu^{3+} red phosphors

3.3.3.1 Powder X-Ray diffraction studies

As Eu^{3+} emission spectra can reflect any symmetry or covalent changes within the structure, an attempt has been made to modify the luminescence characteristics of $Gd_{1.8}Ce_2O_7$:$0.2Eu^{3+}$ phosphors by introducing various amounts of Ca^{2+} ions in the Gd^{3+} site and Nb^{5+} ions in the Ce^{4+} site without altering the cubic

fluorite crystal structure of the compound. Fig. 3.21 shows the XRD patterns of $Gd_{1.8-x}Ca_xCe_{2-y}Nb_yO_7$:0.2 Eu^{3+} (*x*, *y* = 0.25, 0.50, 0.75 and 1.0) red phosphors. XRD patterns can be matched well to the JCPDS File no. 01-071-4807 corresponding to the cubic fluorite structure having the space group *Fm3m*. There are no traces of extra peaks from impurities in the pattern. To understand the extend of modification of the lattice with Ca-Nb substitution, Rietveild analysis was carried out and Fig. 3.22 shows the typical best fit including observed, calculated, the difference diffraction profiles, and the Bragg positions for $Gd_{1.3}Ca_{0.5}Ce_{1.5}Nb_{1.5}O_7$:0.2$Eu^{3+}$. The lattice parameter, average crystallite size and bond distance of the all the samples are listed in the Table 3.6. As the refinement yielded, Ca^{2+} is expected to occupy Gd^{3+} site and Nb^{5+} in Ce^{4+} site based on its matching ionic size and charge neutrality. Lattice parameter and bond distance decrease with the increase of Ca-Nb substitution as expected which further confirms the effective substitution of Ca-Nb into the lattice.

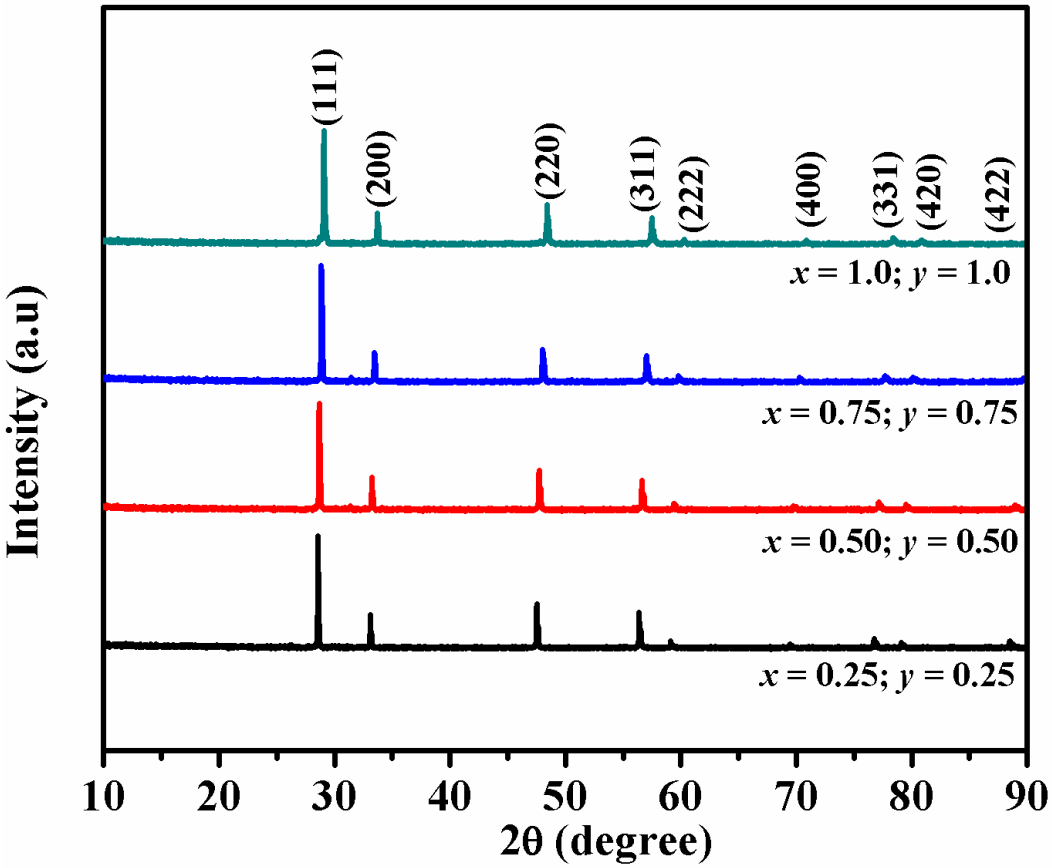

Fig. 3.21 Powder X-ray diffraction patterns of $Gd_{1.8-x}Ca_xCe_{2-y}Nb_yO_7$: *0.2*$Eu^{3+}$ (*x*, *y* = 0.25, 0.50, 0.75 and 1.0) red phosphors.

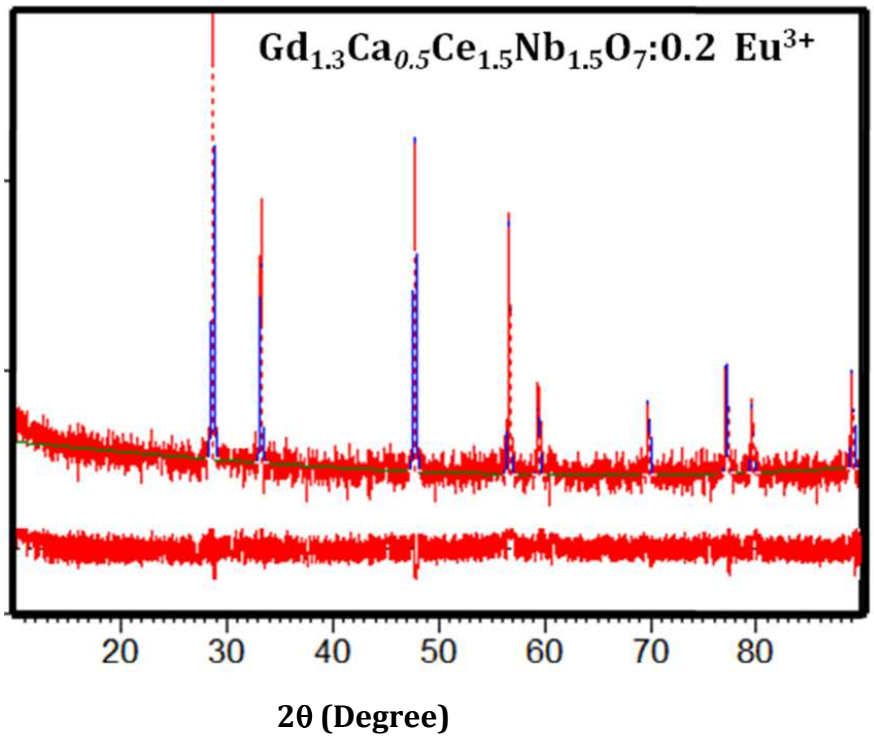

Fig. 3.22 The observed, calculated and difference powder diffraction profiles of $Gd_{1.3}Ca_{0.5}Ce_{1.5}Nb_{0.5}O_7$:0.2 Eu^{3+} phosphor obtained from Rietveld refinement.

Table 3.6 Lattice parameter, average crystallite size and bond distance of the $Gd_{1.8-x}Ca_xCe_{2-y}Nb_yO_7$: *0.2*$Eu^{3+}$ (*x, y* = 0.25, 0.50, 0.75 and 1.0) red phosphors.

Composition	Lattice Parameter (Å)	Average Crystallite Size (nm)	A-O_{8c} (Å)
x, y = 0.25	5.4086 (7)	101.63	2.342
x, y = 0.50	5.3881 (9)	101.65	2.332
x, y = 0.75	5.3534 (8)	101.70	2.317
x, y = 1.0	5.3147 (5)	101.40	2.301

3.3.3.2 Raman spectroscopic studies

Raman spectra of the typical $Gd_{1.3}Ca_{0.5}Ce_{1.5}Nb_{0.5}O_7$:0.2$Eu^{3+}$ phosphor is shown in Fig. 3.23. It exhibits sharp peaks around 467, 600 and 770 cm^{-1} indicating the F_{2g}

mode of the cubic fluorite type structure, oxygen vacancy mode and stretching vibrations of Nb-O (Jehng et al. 1991) respectively.

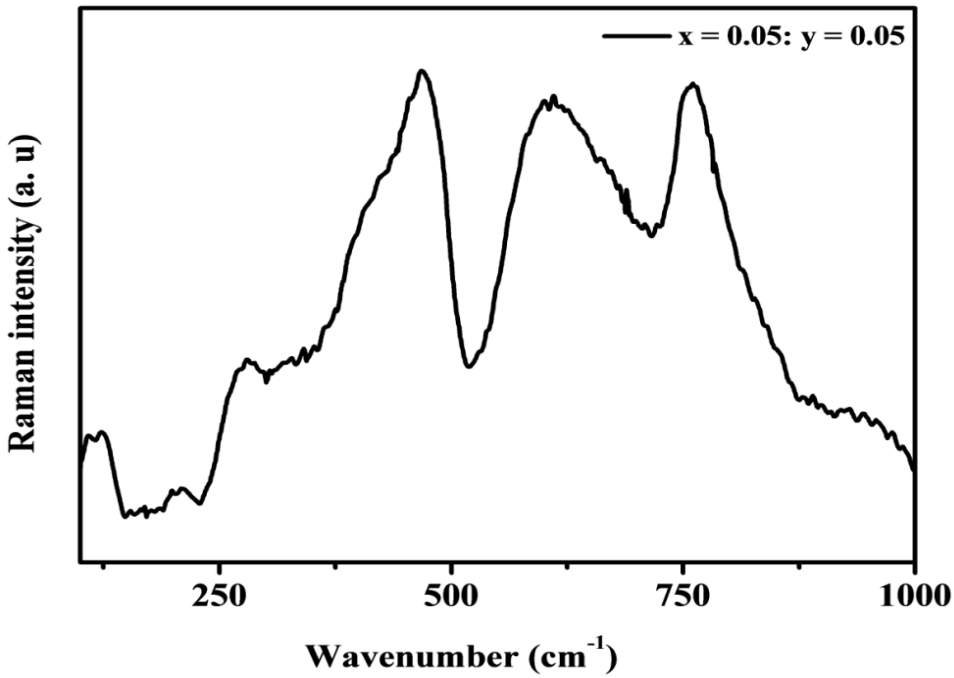

Fig. 3.23 Raman spectra of $Gd_{1.3}Ca_{0.5}Ce_{1.5}Nb_{1.5}O_7$:0.2$Eu^{3+}$ red phosphors.

3.3.3.3 Morphological studies

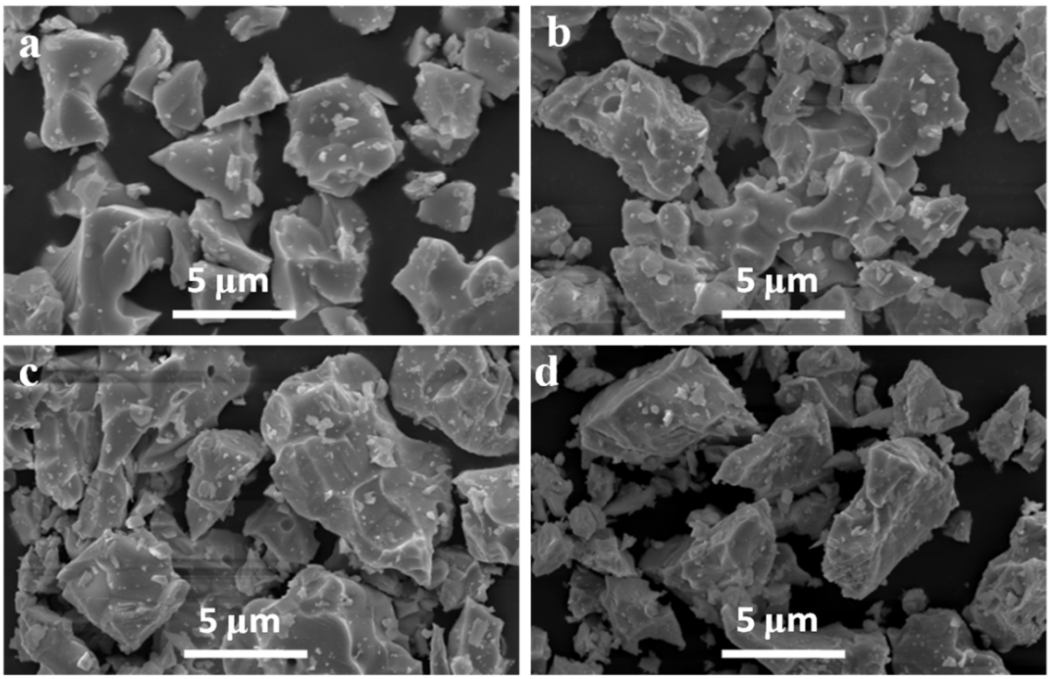

Fig. 3.24 Scanning electron micrographs of $Gd_{1.8-x}Ca_xCe_{2-y}Nb_yO_7$: *0.2*$Eu^{3+}$ (*x, y* = 0.25, 0.50, 0.75 and 1.0) red phosphors.

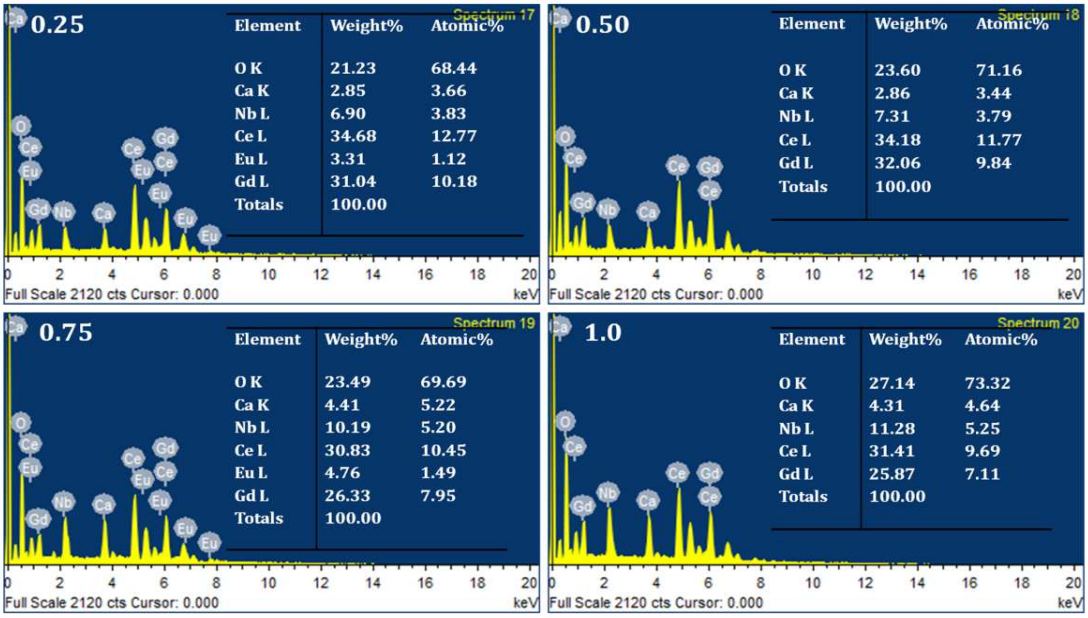

Fig. 3.25 EDS of $Gd_{1.8-x}Ca_xCe_{2-y}Nb_yO_7$: *0.2*$Eu^{3+}$ (*x, y* = 0.25, 0.50, 0.75 and 1.0) red phosphors.

Fig. 3.24 shows the typical SEM micrographs of the $Gd_{1.8-x}Ca_xCe_{2-y}Nb_yO_7$:0.2 Eu^{3+} (*x, y* = 0.25, 0.50, 0.75 and 1.0) red phosphors. The particles are slightly agglomerated with a size range of 1–5 μm. The Ca-Nb substitution made vivid changes in the particle size (increases) and morphology. Fig. 3.25 and 3.26 shows the EDS and elemental mapping analysis of $Gd_{1.8-x}Ca_xCe_{2-y}Nb_yO_7$: *0.2*$Eu^{3+}$ (*x, y* = 0.25, 0.50, 0.75 and 1.0) and typical $Gd_{1.3}Ca_{0.5}Ce_{1.5}Nb_{0.5}O_7$:0.2$Eu^{3+}$ red phosphor respectively and it confirms that all elements are uniformly distributed in the sample.

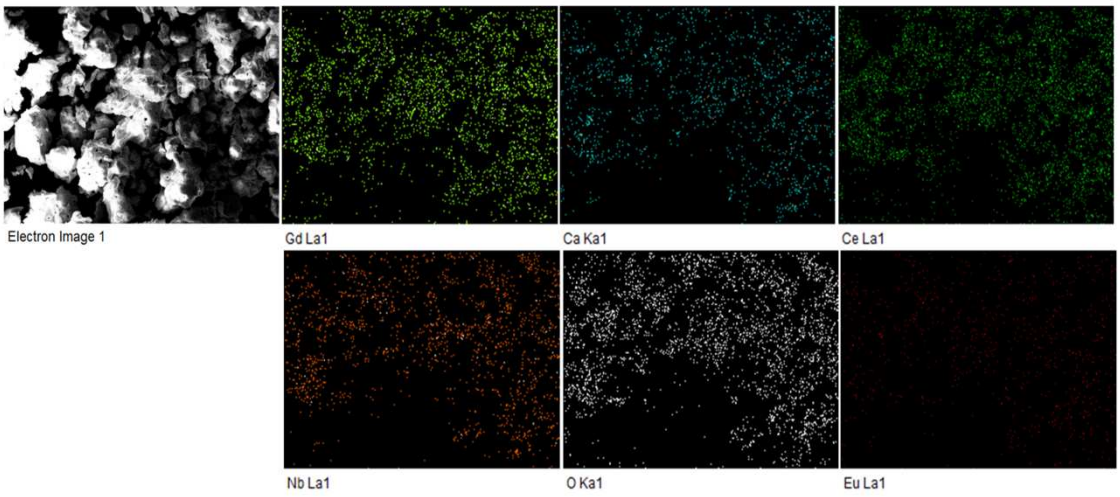

Fig. 3.26 Elemental dot mapping of $Gd_{1.30}Ca_{0.50}Ce_{1.50}Nb_{0.50}O_7$: *0.2*$Eu^{3+}$ red phosphors.

3.3.3.4 Absorption studies

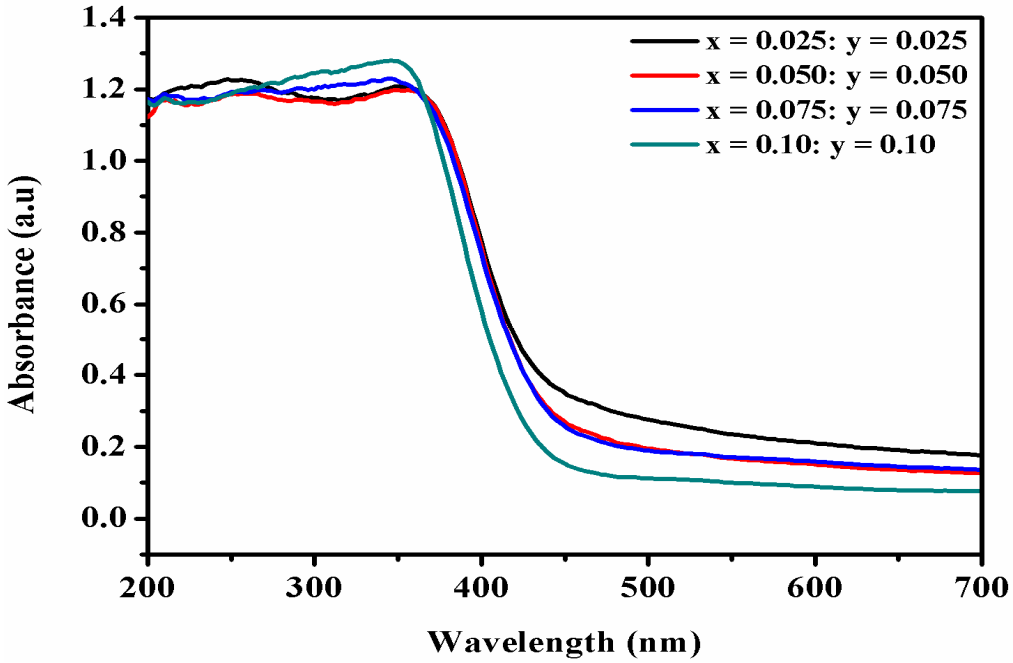

Fig. 3.27 UV-vis absorption spectra of $Gd_{2-x}Ca_xCe_{2-y}Nb_yO_7$: xEu^{3+} (x, y = 0.25, 0.50, 0.75 and 1.0) red phosphors.

Fig. 3.27 presents the UV-Visible absorption spectra of the samples. All the samples exhibited good absorption in the UV region with maxima at 242, and 340 nm which corresponds to the charge transfer transitions of O^{2-} - Ce^{3+} and O^{2-} - Ce^{4+} respectively. In addition, the absorbance due to the charge transfer transitions of O^{2-} - Ce^{4+} enhances by the Ca-Nb substation. And also the absorption edge is blue shifted towards the shorter wavelength as the Ca-Nb substitution increases. These results confirm the dominant of Ce^{4+} oxidation in the system which is consistent with the observation in XPS spectra.

3.3.3.5 X-ray photoelectron spectroscopy studies

The survey scan spectra of the $Gd_{2-x}Ca_xCe_{2-y}Nb_yO_7$: xEu^{3+} (x, y = 0.25, 0.50, 0.75 and 1.0) red phosphor synthesized is shown in Fig. 3.28, which clearly confirms the presence of Gd, Ca, Ce, Nb, O, and Eu from their corresponding binding energies. The XPS spectra of Ce (3d) for the samples are given in Fig. 3.29. When Ca-Nb was substituted into $Gd_{1.8}Ce_2O_7$:$0.2Eu^{3+}$, the Ce 3 d XPS shows that the peaks of Ce^{4+} 3d3/2 and Ce^{4+} 3d5/2 becomes stronger indicating the decrease of Ce^{3+}

concentration in the sample with respect to the increase in dopant (Ca-Nb) concentration.

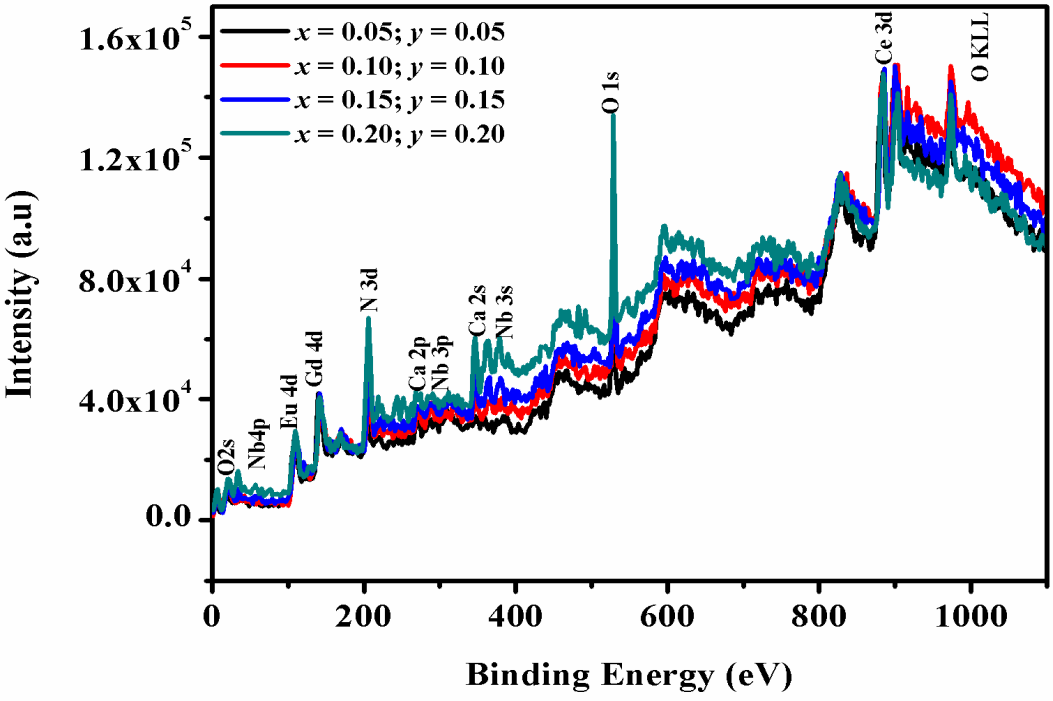

Fig. 3.28 Survey scan X-ray photoelectron spectrum of $Gd_{2-x}Ca_xCe_{2-y}Nb_yO_7$: xEu^{3+} (x, y = 0.25, 0.50, 0.75 and 1.0) red phosphor

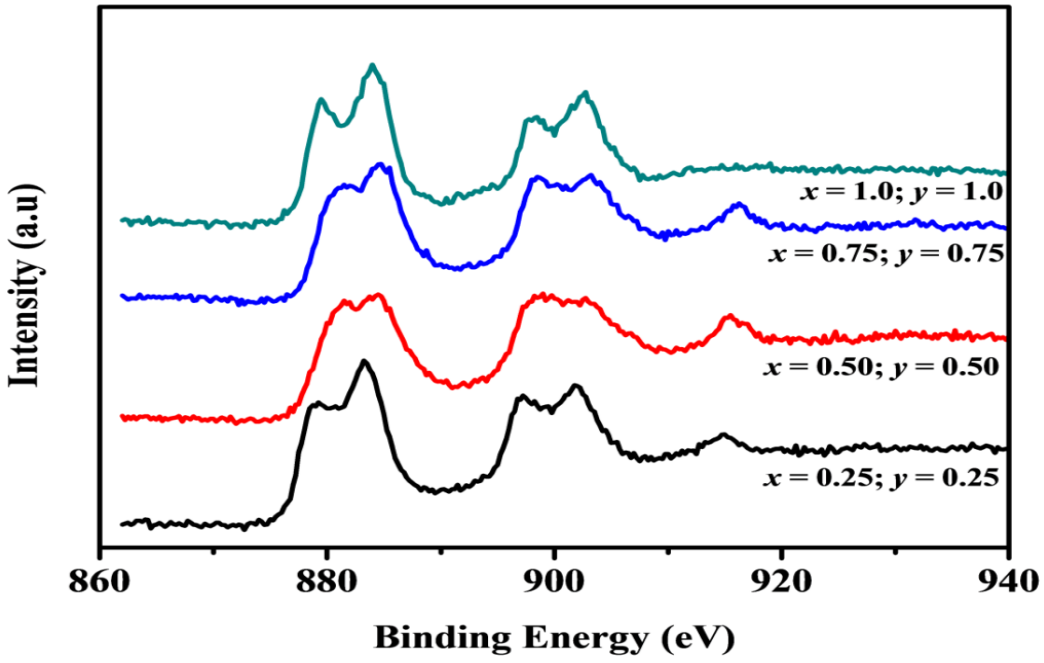

Fig. 3.29 XPS spectra of Ce (3d) for $Gd_{2-x}Ca_xCe_{2-y}Nb_yO_7$: xEu^{3+} (x, y = 0.25, 0.50, 0.75 and 1.0) red phosphors.

3.3.3.6 Photoluminescence studies

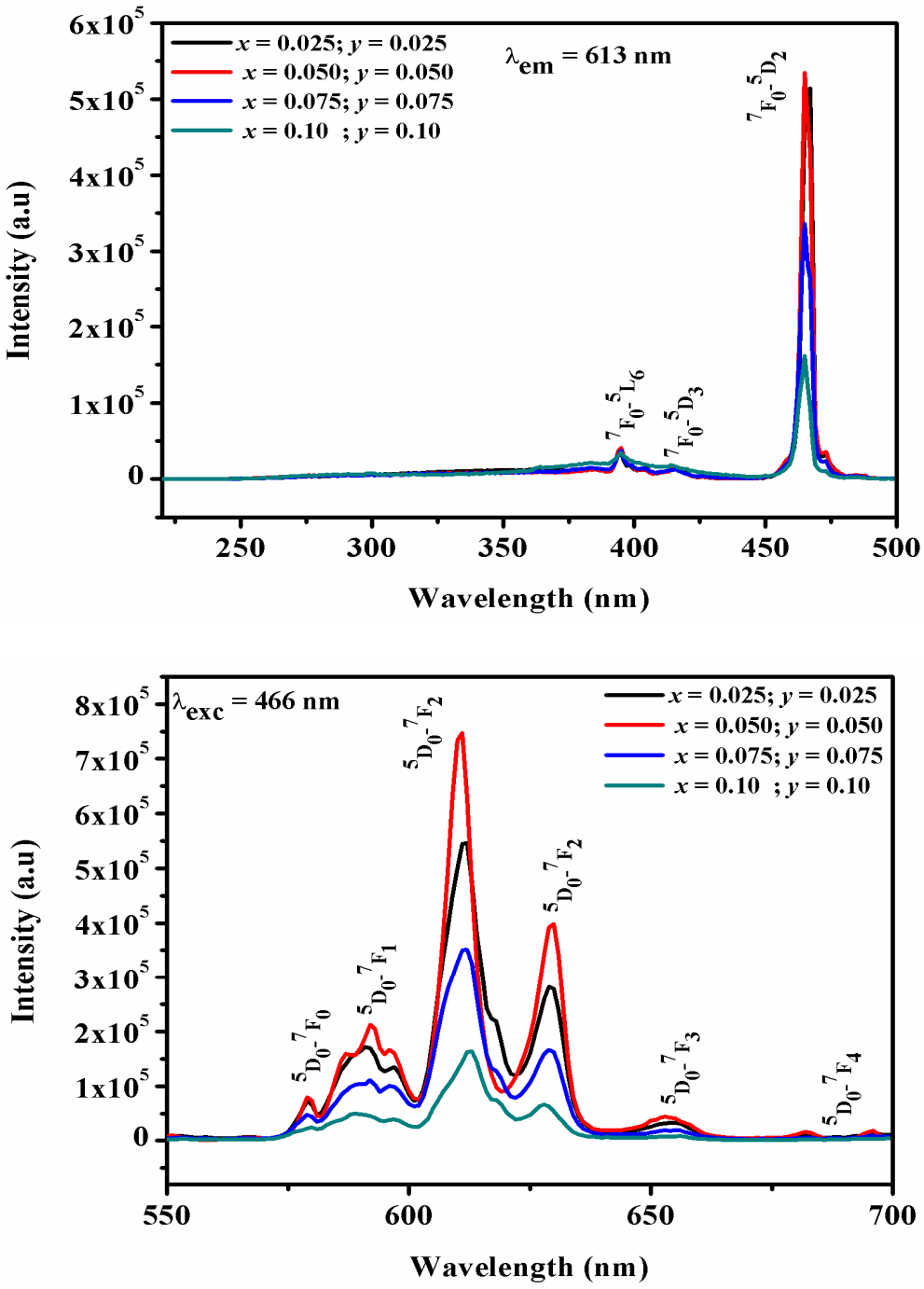

Fig. 3.30 Photoluminescence a) excitation spectra for an emission of 613 nm and b)emission spectra under 466 nm excitation of $Gd_{2-x}Ca_xCe_{2-y}Nb_yO_7$: xEu^{3+} (x, y = 0.25, 0.50, 0.75 and 1.0) red phosphors.

The excitation and emission spectra of $Gd_{2-x}Ca_xCe_{2-y}Nb_yO_7$: xEu^{3+} (x, y = 0.25, 0.50, 0.75 and 1.0) red phosphors is shown in Fig. 3.30. An increase in the Ca-Nb

concentration doesn't change the shape and peak positions of the excitation and emission spectra but the peak intensities changes. At low concentration ranges i.e upto *x, y* = 0.50, the luminescence intensity gradually increases with Ca-Nb substitution. Further increase in Ca-Nb substitution leads to the decrease in luminescence intensity. The asymmetric ratio of Ca-Nb substituted phosphors (Table 3.7) are low compared to the $Gd_{2-x}Ce_2O_7$:xEu^{3+} phosphors as given in Table 3.5. Incorporation of cations with different valency and electronegativity to the cystal lattice distorts the Eu^{3+} ions present in the lattice which increases the lattice symmetry. This is reflected in the emission spectrum of the $Gd_{2-x}Ca_xCe_{2-y}Nb_yO_7$: xEu^{3+} (*x, y* = 0.25 and 0.50) phosphors. By further increase in Ca-Nb substitution, the energy transfer process between the coupled excited Eu^{3+} ions resulting in the turn down of luminescence intensity (Krupa et al. 2005).

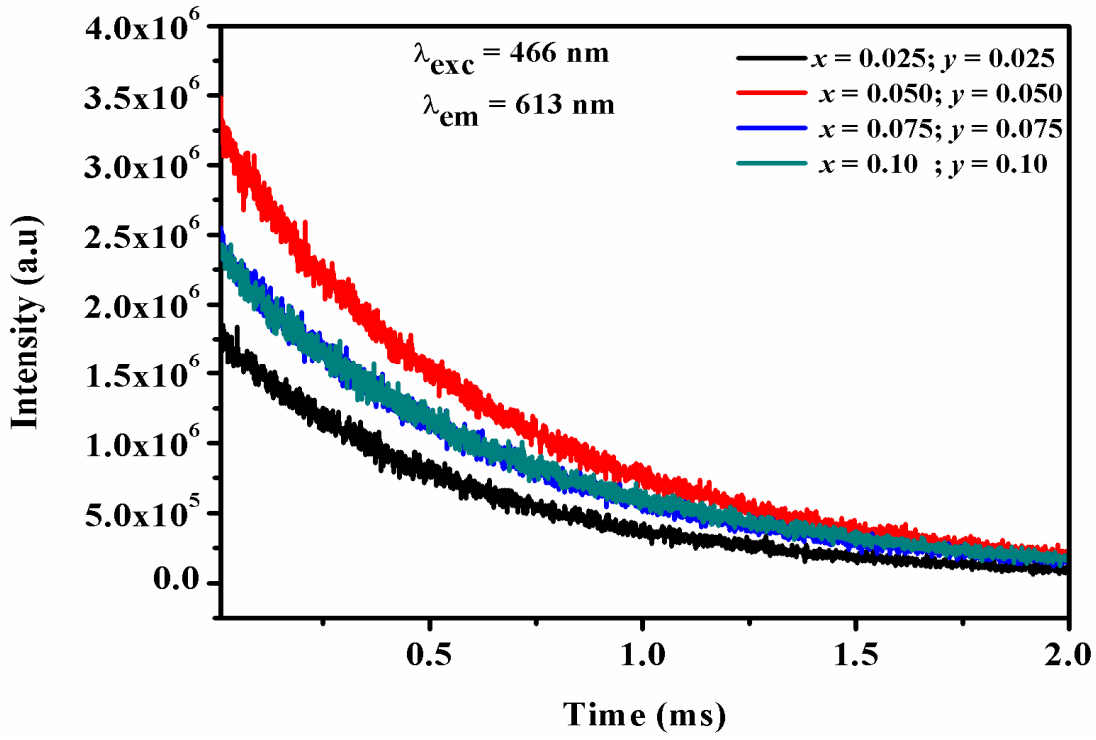

Fig. 3.31 Decay curves of Eu^{3+} emission at 613 nm in $Gd_{2-x}Ca_xCe_{2-y}Nb_yO_7$: xEu^{3+} (*x, y* = 0.25, 0.50, 0.75 and 1.0) red phosphors under 466 nm excitation.

The photoluminescence decay curves of the samples also reveal the dependence of the activator concentration on photoluminescence properties and the decay time could provide vital information of the concentration quenching in the energy transfer process. The fluorescence decay lifetime measurements for Eu^{3+}

emission λ_{exc} = 466 nm, λ_{em} = 613 nm) with increasing Ca-Nb substitution is shown in Fig. 3.31. The decay curves can be well fitted using a first order exponential function as given by, I = Aexp(-t/τ), where I is the intensity at time t, A is the fitting parameter and τ is decay lifetime. It can be seen that the lifetime values obtained from the decay curves increases monotonically. On the basis of the emission spectra and lifetimes of the $^5D_0$ emitting level, the quantum efficiency (η) of the Eu^{3+} ion excited state can be determined and the values are listed in Table 3.7. These values are comparable with the reported Eu^{3+} doped red phosphors.

Table 3.7 Band gap energy, FWHM of the $^5D_0$-$^7F_2$ transition at 613 nm red emission, Asymmetric ration, life time and quantum efficiency of the $Gd_{1.8-x}Ca_xCe_{2-y}Nb_yO_7$: *0.2*$Eu^{3+}$ (*x, y* = 0.25, 0.50, 0.75 and 1.0) red phosphors.

	Band gap energy (E_g) (eV)	FWHM (nm)	Asymmetric ratio	Lifetime (τ) (ms)	Quantum efficiency (η) (%)	Color Coordinates (x y)
x, y = 0.25	2.68	6.7	3.22	0.607	13.78	0.64, 0.34
x, y = 0.50	2.71	8.1	3.41	0.645	14.37	0.65, 0.36
x, y = 0.75	2.73	9.0	3.19	0.651	11.98	0.66, 0.36
x, y = 1.0	2.74	9.3	3.18	0.682	9.76	0.66, 0.36

The color of light can be described by chromaticity coordinates on a Commission International d'Eclairage (CIE) chromaticity diagram. The CIE chromaticity coordinates were calculated using the CIE color calculator software to understand the actual emission color of the developed phosphor. Fig. 3.32 exhibits the CIE chromaticity co-ordinates and the luminescence digital photograph of the $Gd_{1.3}Ca_{0.5}Ce_{1.5}Nb_{0.5}O_7$:0.2 Eu^{3+} red phosphor under the 466 nm excitation. The CIE colour co-ordinates of all the $Gd_{2-x}Ca_xCe_{2-y}Nb_yO_7$: xEu^{3+} (*x, y* = 0.25, 0.50, 0.75 and 1.0) red phosphors were calculated using the software CIE Calculator and were found to be close to the NTSC standard values for a potential red phosphors as enlisted in the Table 3.7. The color coordinates are very close to the standard coordinates (0.67, 0.33) form National Television Standard Committee (NTSC), signifying the high color purity of the as prepared phosphors.

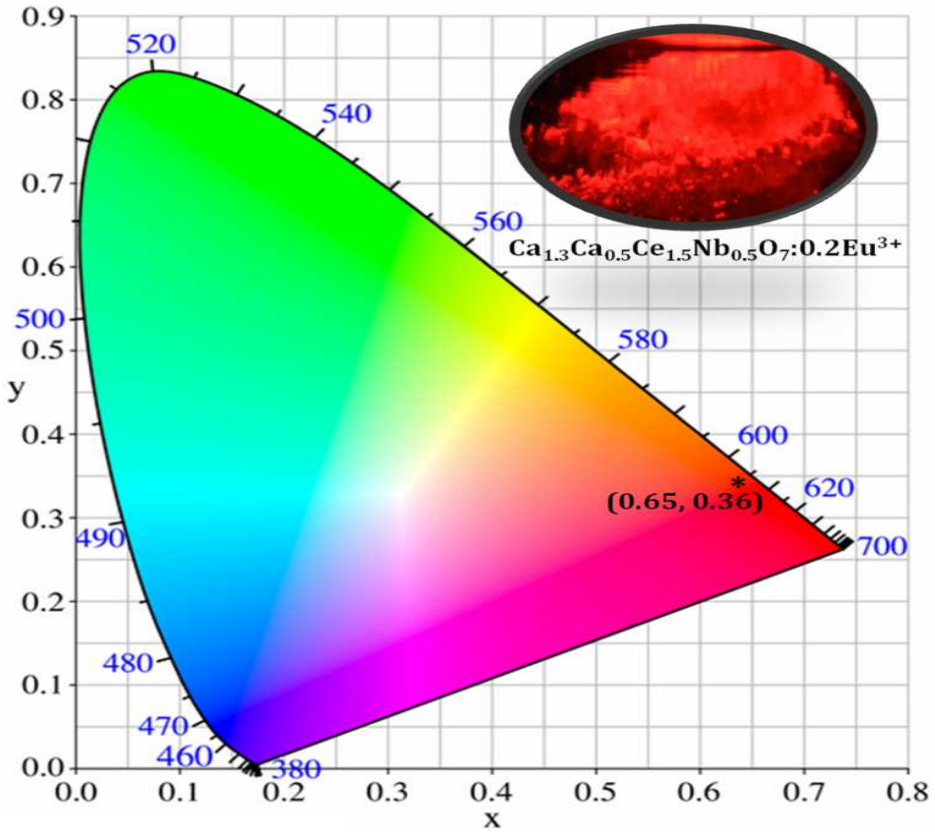

Fig. 3.32 The CIE chromaticity coordinate diagram of the $Gd_{1.3}Ca_{0.5}Ce_{1.5}Nb_{0.5}O_7:0.2Eu^{3+}$ red phosphor. The inset shows the digital photograph of the $Gd_{1.3}Ca_{0.5}Ce_{1.5}Nb_{0.5}O_7:0.2Eu^{3+}$ phosphor under the 466nm excitation.

3.4 Conclusions

A new series of cerium based red phosphor materials: $A_{1.9}Ce_2O_7$:*0.1*Eu^{3+} (A = La, Y and Gd) were prepared by the conventional solid state route. Studies revealed that the gadolinium sample showed better luminescence properties in terms of f-f emission intensity, the asymmetric ratio and quantum efficiency. It was found that the degree of ordering in the crystal lattice as well as the Ce^{3+} oxidation states plays crucial roles in the luminescence properties of Eu^{3+} doped cerium based oxides. The effect of variation Eu^{3+} in the luminescence intensity in $Gd_{2-x}Ce_2O_7$ system was studied detail and the doping concentration was optimised. By substituting Ca-Nb as a network modifier ion in the place of Gd and Ce in $Gd_{1.8}Ce_2O_7$:$0.2Eu^{3+}$ enhanced the red luminescence. Further substitution of different ionic size – Ca-Nb substitution reduces the resonance energy transfer between excited Eu^{3+} ions and leads to the concentration quenching. The above results indicate that the $A_2Ce_2O_7$ (A = La, Y and Gd) system offers a lot of possibilities to manipulate the photoluminescence properties by which nicely fitting in with the widely applied UV and blue LED chips.

Chapter 4

Remarkable changes in the photoluminescent properties of $Y_2Ce_2O_7:Eu^{3+}$ red phosphors through modification of the cerium oxidation states and oxygen vacancy ordering

The influence of the substitution of Eu^{3+} at the isovalent and aliovalent site of $Y_2Ce_2O_7$ on the photoluminescent properties was studied. The substitution of Eu^{3+} at the Ce^{4+} site induces a structural transition from a defect fluorite to a C-type structure, which increases the oxygen vacancy ordering and the distortion of the Eu^{3+} environment, and decreases the formation of Ce^{3+} states. In contrast, isovalent substitution at the Y^{3+} site exhibit the biphasic nature of defect fluorite and a C-type structure, thereby increasing the number of Ce^{3+} oxidation states. These modifications resulted in remarkable changes in the photoluminescent properties of $Y_2Ce_{1.9}O_7:0.1Eu^{3+}$ red phosphors. The cation ordering linked to the oxygen vacancy ordering led to the uniform distribution of Eu^{3+} ions in the $Y_2Ce_{2-x}O_7:xEu^{3+}$ lattice, thus allowing higher doping concentrations without quenching. Our results demonstrate that significant improvements in the photoluminescence properties can be achieved by the structural alteration of a fluorite CeO_2 to a C-type lattice.

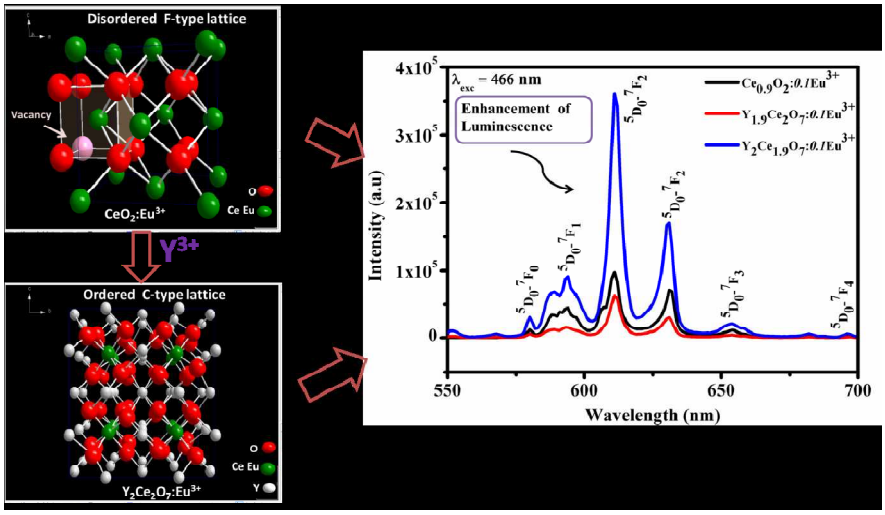

Athira et al. ***Phys. Chem. Chem. Phys.,*** *16,* ***2014,*** *23699-23710.*

4.1 Introduction

In the last two decades, oxide phosphors doped with ions of the rare earth elements (REEs) have attracted much attention as a result of their distinctive optical properties, such as a long fluorescent lifetime, large Stokes shift, and a combination of high luminescence efficiency and good photochemical stability (Alexander et al. 2009; Som et al. 2014). These characteristics make them potentially applicable in a variety of areas such as fluorescent lamps, field emission displays and as biological labels. The oxide phosphors possess higher chemical and thermal stability than commonly used sulfide phosphors (e.g. $ZnS:Cu^{+},Al^{3+}$ and $Y_2O_2S:Eu^{3+}$). This advantage makes these materials more chemically stable under high vacuum and electron excitation. There is therefore much interest in searching for new high-performance oxide phosphors (Liu et al. 2007).

Cerium oxide (CeO_2) is a well-known functional material (Guoa et al. 2008) with a cubic fluorite structure. It is considered to be one of the most important oxide materials because of its good thermal and chemical stability (Wu et al. 1991; Lee et al. 2003) and special optical properties (Barreca et al. 2003; Bhosale et al. 2010; Gnanam et al. 2002; Patsalas et al. 2003), e.g. its high refractive index, optical transparency, high dielectric constant and non-toxicity (Netterfield et al. 1985). It has potential in the following applications: in optical coatings; in electro-optical, microelectronic, and optoelectronic devices; as an ion-conducting layer electrolyte in solid oxide fuel cells (Zhang et al. 2002; Nakayama et al. 2009; Lim et al. 2014); in oxygen gas sensors (Zhang et al. 2005); as a support in automotive catalysts (Imagawa et al. 2011); and in ultraviolet shielding materials (Maksimchuk et al. 2013). The tetravalent cerium ion (Ce^{4+}) has no 4f electrons, which makes it a promising photoluminescence (PL) host material (Fujihara et al. 2004). CeO_2 phosphors doped with Eu^{3+} ions have attracted much attention as a result of strong light absorption through charge transfer (CT) from O^{2-} to Ce^{4+} around 370 nm (Wang et al. 2007). If energy transfer is achieved from the CT states of CeO_2 to the doped REE ions, intense characteristic emissions are observed. The matching ionic radius of Eu^{3+} and Ce^{4+} favors the extensive solubility of Eu within the CeO_2 lattice. Several investigations have been reported on the PL properties of Eu^{3+}-doped cerium oxide (Yu et al. 2012; Sriniasan et al. 2011; Kumar et al. 2009; Kunimi et al. 2012; Shi et al. 2012; Wang et al. 2011).

CeO_2 is well known for having large deviations in stoichiometry as a result of the easy reducibility of Ce^{4+} ions to Ce^{3+} ions. The substitution of Eu in the CeO_2 lattice creates oxygen vacancies to compensate for the effective negative charge associated with the trivalent dopant. The luminescence in Eu^{3+}-doped CeO_2 is mainly limited by the number of oxygen vacancies. These oxygen vacancies act as PL-quenching centers and adversely affect the PL of Eu^{3+} by controlling the radiative route of emission. In view of this, it is more difficult to achieve a sizeable luminescence for use in practical applications in the CeO_2 fluorite lattice. Our prime interest here was to prepare a CeO_2-based host lattice to overcome these limitations in luminescence.

Cerium oxide has a fluorite structure with every Ce ion surrounded by eight equatorial oxygen ions in O_h symmetry. The ideal fluorite structure is a simple crystal structure with a general formula AO_2. However, the defect fluorite structure is anion-deficient with a formula of $AO_{1.75}$ (Radhakrishnan et al. 2009). A fluorite (F)-type structure can accept various numbers of oxygen vacancies, from which pyrochlore (P)-type and rare earth C (C)-type structures can be derived, depending on the oxygen content. The P-type structure has a general formula $A_2B_2O_7$, which belongs to the *Fd3m* space group (Z = 8). The cubic C-type structure, A_2O_3 ($AO_{1.5}$), belongs to the space group *Ia3* (Z = 16), which can also be recognized as an F-type structure with ordered oxygen vacancies in the anionic sub-lattice (Nishino et al. 2004). This structure may also tolerate excess anions in the presence of tetravalent lanthanides, which promotes the eight-fold coordination of the lanthanide sites (Rossell et al. 1977). Thus the formation of the C-type phase from a defect fluorite structure incorporates more oxygen into the lattice and increases the oxygen vacancy ordering (Higawara et al. 2009) with the substitution of Eu^{3+} for Ce^{4+}. We therefore made an attempt to enhance the red emission of CeO_2:Eu^{3+} by choosing CeO_2 in a C-type structure.

Although many soft chemical routes (such as the sol–gel process, the hydrolysis-assisted co-precipitation method, chemical precipitation, solid-state reaction, solution combustion synthesis (Vinod et al. 2014), a non-hydrolytic solution route, a spin-on/pyrolysis technique and electrochemical deposition) have been reported for the preparation of Eu^{3+}-doped cerium oxide phosphors, these techniques have mainly been focused on the preparation of nanophosphors. The

synthesis method and the heat treatment of phosphors have a direct influence on the luminescence properties as a result of changes in the crystallite size, particle size, crystallinity, surface texture and shape of the particles. This work focused on the modifications of the crystalline structure and cerium oxidation states that occurred with the substitution of Eu^{3+} at isovalent and aliovalent sites and the influence of this substitution on the PL properties. The influence of this particular aspect was studied by the solid-state reaction method. In this context, we synthesized a cerium oxide based host with the general formula $Y_2Ce_2O_7$. Eu^{3+} was substituted in both sites via a conventional solid-state reaction to give the compositions $Y_{1.9}Ce_2O_7$:$0.1Eu^{3+}$ and $Y_2Ce_{1.9}O_7$:$0.1Eu^{3+}$ in order to probe the influence of substitutions on the structure and luminescence properties. The structure, morphology, PL properties and electronic structure of the developed phosphors were characterized by powder X-ray diffraction (XRD), FT Raman spectroscopy, transmission electron microscopy (TEM), scanning electron microscopy (SEM) with energy-dispersive spectrometry (EDS), X-ray photoelectron spectroscopy (XPS), UV-visible absorption spectroscopy, and PL and lifetime measurements. It was observed that the substitution of Eu^{3+} at the Ce^{4+} site induced a structural transition and decreased the oxidation states of Ce^{3+}. The developed phosphors $Y_2Ce_{1.9}O_7$:$0.1Eu^{3+}$ showed enhanced red emission of Eu^{3+} (612 nm) under excitation with blue light (466 nm) compared with the emission of $Y_{1.9}Ce_2O_7$:$0.1Eu^{3+}$.

To understand the effect of the Eu^{3+} concentration, the PL properties of the as-prepared $Y_2Ce_{2-x}O_7$:xEu^{3+} (x = 0.05, 0.10, 0.15, 0.20, 0.25 and 0.50) were also studied in detail. By increasing the Eu^{3+} concentration the intra-$4f^6$ transition bands of Eu^{3+} at 466 nm ($^7F_0$–$^5D_2$ transition in the blue region) is more dominant than the other transition bands, which matches well with the emission of commercial GaN LED (440–470 nm) chips. The ordering of oxygen vacancies, increased distortion of Eu^{3+} at the Ce^{4+} site and changes in the next neighbor of Eu^{3+} are some of the other factors that enhanced the luminescence.

4.2 Experimental

4.2.1 Materials and Methods

The red phosphors based on yttrium cerate [$Y_{1.9}Ce_2O_7$:$0.1Eu^{3+}$, $Y_2Ce_{1.9}O_7$:$0.1Eu^{3+}$ and $Y_2Ce_{2-x}O_7$:xEu^{3+} (x = 0.05, 0.10, 0.15, 0.20, 0.25 and 0.50)] were

synthesized by a conventional solid state reaction technique. Fine powders of Y_2O_3, CeO_2 and Eu_2O_3 (Sigma–Aldrich, Steinheim, Germany) of 99.99% purity were used as the starting materials. These precursors were taken in the required stoichiometric ratios of Y: Ce: Eu (1.9: 2: 0.1, 2: 1.9: 0.1 and 2: 2-*x*: *x*) and mixed thoroughly in an agate mortar using acetone as the mixing medium until a fine slurry was obtained. The slurry was dried by placing in an air oven at a temperature of 100 °C. The mixing and drying were repeated three times to obtain a homogenous mixture. The homogeneous mixture was then calcined on a sintered alumina plate in an air atmosphere electrical furnace at 1400°C for 15 h. To ensure the completion of the reaction, the calcinations were repeated twice at 1500°C for 6 h with intermittent grinding. The temperature of the furnace was programmed with an initial heating rate of 10 °C min^{-1} to 900°C followed by a heating rate of 5°C min^{-1} to attain the desired temperatures.

4.2.2 Characterization

The crystalline structure, phase purity and lattice parameters of the samples were examined by recording XRD patterns using a PANalytical X'Pert Pro diffractometer with Ni filtered CuK_α radiation with the X-ray tube operating at 40 kV and 30 mA; 2θ varied from 10 to 90° in 0.016° steps. The Raman spectra of the powder samples were acquired using an integrated micro-Raman system of a Labram HR 800 spectrometer (Horiba Scientific) using a 633 nm helium–neon laser with a spatial resolution of 2 mm to obtain the structure of the powdered samples. XPS experiments were carried out on a KRATOS-AXIS 165 instrument equipped with dual aluminum–magnesium anodes with Mg K_α radiation (1253.6 eV) operated at 5 kV and 15 mA with a pass energy of 80 eV and an increment of 0.1 eV. The samples were degassed for several hours in an XPS chamber to minimize air contamination to the sample surface. To overcome the charging problem, a charge neutralizer of 2 eV was applied and the binding energy of the C1s core level (284.6 eV) of adventitious hydrocarbons was used as a standard. The XPS spectra were fitted by a nonlinear square method with the convolution of Lorentzian and Gaussian functions after a polynomial background was subtracted from the raw spectra.

Selected-area electron diffraction (SAED) patterns and high resolution electron microscopy of the samples were obtained using a TECNAI $30G^2$ S-TWIN

transmission electron microscope (FEI, The Netherlands) operating at 300 kV. The size and morphology of the powder particles were obtained using a scanning electron microscope (JEOL, JSM-5600LV) operated at 15 kV. X-ray microchemical analysis and elemental mapping of the samples were carried out using a silicon drift detector- X-Max^N attached to a Carl Zeiss EVO scanning electron microscope. The absorption characteristics of the synthesized samples were studied in the wavelength range 200–800 nm by a Shimadzu UV-3600 UV-visible spectrophotometer using barium sulfate as a reference. The PL excitation and emission spectra of the prepared samples were obtained using a Spex-Fluorolog DM3000F spectrofluorimeter with a 450 W xenon flash lamp as the exciting source. The luminescence lifetime of the phosphors was recorded by a phosphorimeter attached to a Fluorolog3 spectrofluorimeter. All the measurements were carried out at room temperature.

4.3 Results and discussion

4.3.1 Effect of Eu^{3+} doping on the A and B sites of yttrium cerate ($Y_2Ce_2O_7$) red phosphors

4.3.1.1 Powder X-ray diffraction studies

A careful analysis of the XRD patterns was carried out to determine whether Eu^{3+} doping of the A and B sites of $Y_2Ce_2O_7$ had any effect on the structure of the lattice as well as on the crystallite size; Fig. 4.1 shows the corresponding diffraction patterns. None of the samples had a pyrochlore (P)-type structure because the typical super-lattice peaks at $2\theta \sim 141$, 271, 361 and 501 corresponding to the pyrochlore lattice were absent, despite the fact that the stoichiometry of the compounds had a P-type composition. The diffraction pattern of the Eu^{3+} doping at the B-site (Ce^{4+}) shows several extra weak diffraction peaks other than those of the cubic fluorite (F) type phase; in contrast, these super-lattice peaks were absent for the doped A-site (Y^{3+}) and in the host pattern (inset, Fig. 4.1). As the diffraction lines of the $Y_2Ce_{1.9}O_7$:0.1Eu^{3+} samples were successfully indexed on a basis of the REE C-type phase in accordance with the powder diffraction file (no. 01-074-7393), $Y_2Ce_{1.9}O_7$:0.1Eu^{3+} can be recognized as a non-stoichiometric C-type compound containing excess oxygen (Nishino et al. 2004).

There is no significant peak shift for the Y^{3+} substitution on Eu^{3+} doping at the A and B sites of $Y_2Ce_2O_7$, while the peak for the Ce^{4+}-substituted site shifts to a lower angle with reference to the host $Y_2Ce_2O_7$ (inset, Fig. 4.1). These shifts in peak position are in accordance with the differences in ionic radii of Y^{3+} (0.1019 nm), Ce^{4+} (0.097 nm) and Eu^{3+} (0.1066 nm) in eight-fold coordination and are further evidence of the predicted substitution of Eu^{3+} at the A and B sites. The lattice constant of $Y_2Ce_{1.9}O_7$:$0.1Eu^{3+}$ was calculated to be 10.7764 Å, whereas that of $Y_{1.9}Ce_2O_7$:$0.1Eu^{3+}$ in the typical defect fluorite-type structure was 5.3859 Å. The ionic radius of Ce^{4+} is much smaller than that of Eu^{3+} and is close to that of the Y^{3+} ion. A larger lattice constant was observed for $Y_2Ce_{1.9}O_7$:$0.1Eu^{3+}$, which may be ascribed to the excess oxygen in the C-type structure in addition to the higher cation substitution.

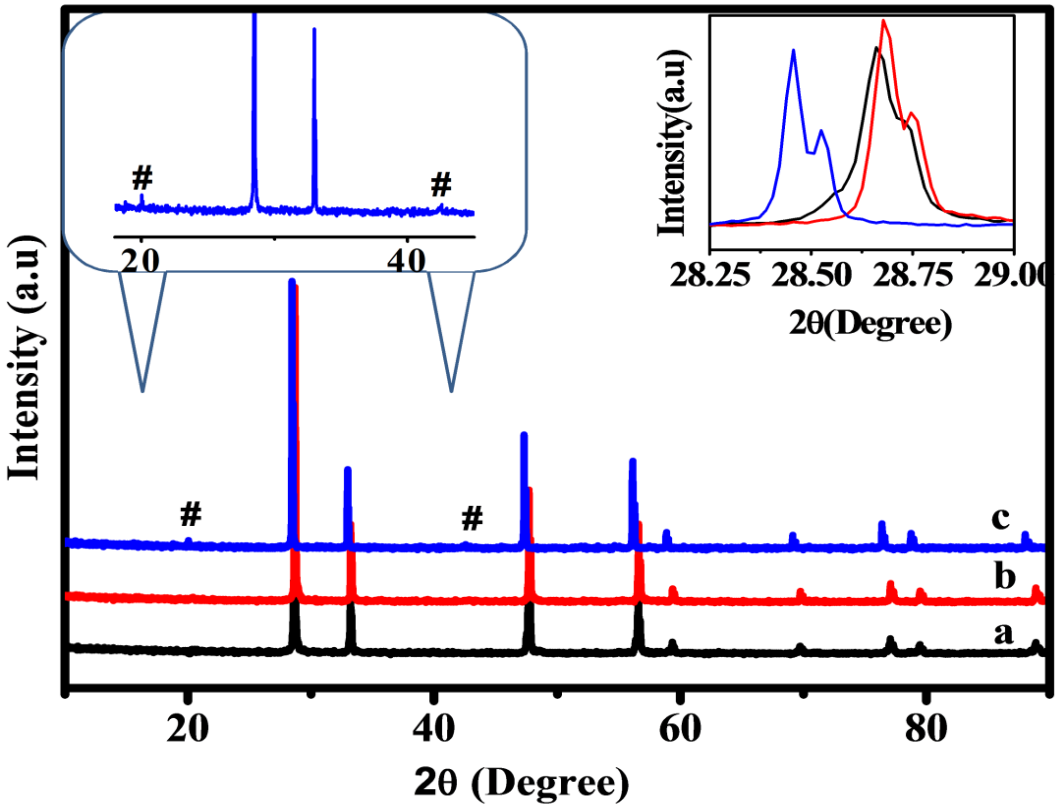

Fig. 4.1 Powder XRD patterns of $Y_2Ce_2O_7$, $Y_{1.9}Ce_2O_7$:*0.1*Eu^{3+} and $Y_2Ce_{1.9}O_7$:*0.1*Eu^{3+} phosphors. For $Y_2Ce_{1.9}O_7$:*0.1*Eu^{3+}additional cubic C-type peaks (denoted by #) appear in the XRD pattern. The inset Fig. shows the expanded XRD of the peak around 2θ 28-29°.

The average crystallite size can be estimated from the Scherrer formula:

$$D_{hkl} = k\lambda/\beta \cos(\theta) \qquad (4.1)$$

where λ is the X-ray wavelength (0.154056 nm), β is the fullwidth half-maximum (FWHM) (in radians), θ is the diffraction angle, k is a constant (0.89) and D_{hkl} represents the size along the (hkl) direction. The crystallite sizes obtained show a marked difference between $Y_{1.9}Ce_2O_7$:$0.1Eu^{3+}$ (123 nm) and $Y_2Ce_{1.9}O_7$:$0.1Eu^{3+}$ (135 nm), which also hints at a structural transition. From the XRD analysis, it is clear that the doping of higher ionic radii Eu^{3+} ions at the Ce^{4+} site induces a structural transition from a defect fluorite structure to a C-type structure.

4.3.1.2 Raman spectroscopic studies

Further structural investigation of the prepared samples was carried out by Raman spectroscopy. As XRD is more sensitive to disorder in the cation sub-lattice than the anion sub-lattice, the X-ray scattering power of oxygen is much less than that for the cations. Raman spectroscopy, however, is more sensitive to metal–oxygen vibration modes than metal–metal vibration modes. Hence Raman scattering is an excellent, non-destructive and rapid analysis technique for investigating the phonon structure of materials; (Glerup et al. 2001) have reported that Raman spectroscopy is an excellent tool with which to analyze the extent of disorder in different phases. Raman spectroscopic information provides an explicit way of distinguishing between a C-type material, a defect fluorite material, and a so-called pyrochlore with a radius ratio close to that of pyrochlore and a defect fluorite border. According to factor group analysis (Keramidas et al. 1973), the Raman spectra of a pyrochlore structure have six Raman active modes ($G = A_{1g} + E_g + 4F_{2g}$), whereas the only Raman active mode of the fluorite-type structure is F_{2g}. Fig. 4.2 shows the Raman spectra for the $Y_2Ce_2O_7$, $Y_{1.9}Ce_2O_7$:$0.1Eu^{3+}$ and $Y_2Ce_{1.9}O_7$:$0.1Eu^{3+}$ samples. It has been reported (Devaiah et al. 2012) that pure $Ce_{0.9}O_2$:$0.1Eu^{3+}$ shows an intense band at 466 cm^{-1} that is assigned to the symmetric mode of the O atoms around each Ce^{4+}, i.e. the single allowed Raman mode with an F_{2g} symmetry in metal oxides with a fluorite structure. The Raman spectra of the host $Y_2Ce_2O_7$ showed a distinct band with a wavenumber of 468 cm^{-1}, which was assigned to the F_{2g} mode due to the symmetrical stretching of the metal oxygen vibrational mode in eight-fold coordination (Nakajima et al. 1994; Kosacki et al. 2002). On Eu^{3+} doping, the F_{2g} mode at 468 cm^{-1} is vanishingly small in the Raman spectrum for substitution at the Y^{3+} site and completely disappears in the spectrum of the Ce^{4+} substituted site. The

characteristic Raman modes of the C-type structure are observed more prominently than the Y^{3+} site substituted samples at 262, 385, 490 and 580 cm^{-1}. Similar Raman modes have been reported (Ikuma et al. 2005; Mandal et al. 2007) for C-type structure compounds. The distinct mode around 490 cm^{-1} was assigned to the T_{2g} mode of the REE C-type structure. Thus the substitution of ions with a higher ionic radius, such as Eu^{3+} at the Ce^{4+} site induces a structural transition from the defect fluorite-type structure to the C-type structure. This result agrees with the XRD analysis. The $Y_{1.9}Ce_2O_7$:0.1Eu^{3+} sample shows broad humps at 262, 385, 490 and 580 cm^{-1}, implying that the sample is not completely in either the C-type or defect fluorite-type structure, although the XRD analysis of $Y_{1.9}Ce_2O_7$:0.1Eu^{3+} indicated the formation of the defect fluorite type structure. Raman analysis suggests the formation of a biphasic C-type and defect fluorite structure.

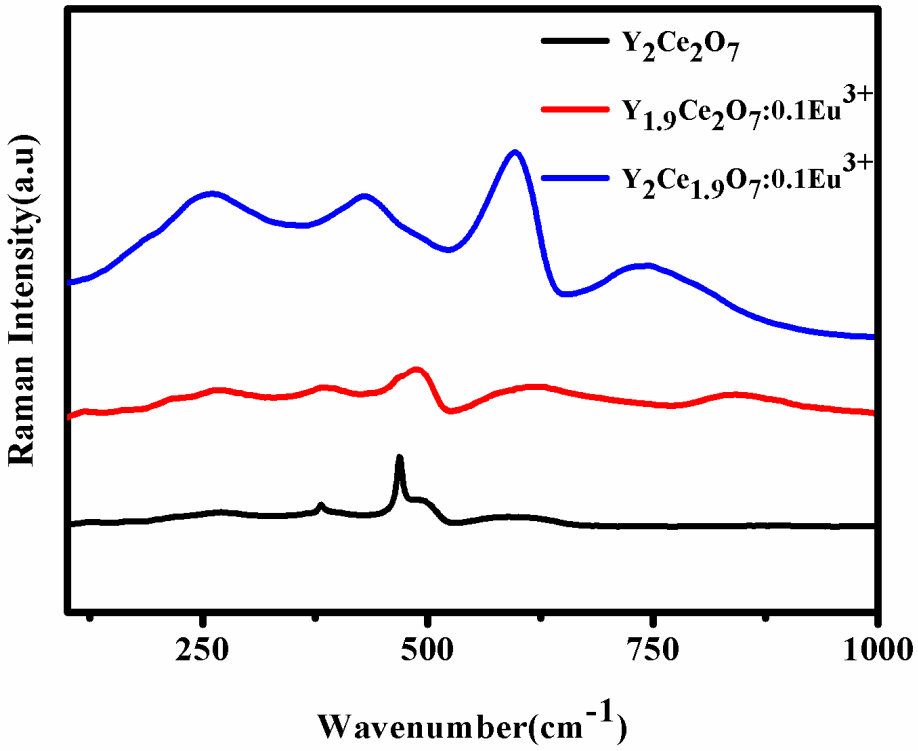

Fig. 4.2 Raman spectra of $Y_2Ce_2O_7$, $Y_{1.9}Ce_2O_7$:*0.1*Eu^{3+} and $Y_2Ce_{1.9}O_7$:*0.1*Eu^{3+} phosphors.

4.3.1.3 X-ray photoelectron spectroscopy studies

To understand the changes in the valency chemistry and BE of the Ce, XPS analysis was carried out. The recorded XPS spectra were charge-corrected with

respect to the C (1s) peak at 284.723 eV. The XPS Ce $3d_{5/2}$ and $3d_{3/2}$ doublets are commonly denoted u and v and are found in the energy range 880–920 eV (Francis et al. 2001; Beche et al. 2008; Normand et al. 1988). Fig. 4.3 shows the XPS spectra for Ce 3d of $Y_2Ce_2O_7$, $Y_{1.9}Ce_2O_7$:0.1Eu^{3+} and $Y_2Ce_{1.9}O_7$:0.1Eu^{3+} phosphors, including the fitted curve and the corresponding deconvoluted peaks. The spectrum was deconvoluted to give the individual spin–orbit doublet of $3d_{3/2}$ and $3d_{5/2}$ and the sum of the deconvoluted peaks was used to produce the fit of the actual data. The deconvoluted Ce (3d) spectrum is relatively complex due to the presence of Ce in 3+ and 4+ oxidation states in addition to multiple d-splitting. If the Gaussian function is used to model the peaks, there are three parameters for each peak, i.e. the energy, the FWHM and the area. The XPS results indicate that Ce is in a mixed valence state of 3+ (885.50 and 904.07 ± 0.7 eV, denoted as v' and u' respectively) and 4+ (882.70, 888.96, 898.20, 901.30, 907 and 916.7 ± 0.7 eV, denoted as v, v'', v''', u, u'' and u''') (Kumar et al. 2009). The v and v'' peaks are attributed to the bonding and antibonding states arising from the multielectron configuration of $3d^94f^2$(O $2p^4$) and $3d^94f^1$(O $2p^5$) Ce^{4+}, and the v'''peak to a $3d^94f^0$(O $2p^6$) Ce^{4+} final state (Larsson et al. 1988; Shyu et al. 1988; Ho et al. 2005). The v' peak corresponds to the $3d^94f^1$(O $2p^6$) Ce^{3+} final state. The same explanation holds true for the series of u structures of the $3d_{3/2}$ level. However, one pair (denoted u_0 and v_0) is hardly observed because it is a shoulder on the Ce^{4+} 3d spectrum. The integrated area under the curve of each deconvoluted peak was used to calculate the concentration of Ce^{3+} ions and is given as:

$$[Ce^{3+}] = \frac{A_{v'} + A_{u'}}{\sum A_i} \qquad (4.2)$$

where $\sum A_i$ is the total integrated area.

Bao (Bao et al. 2008) reported that the major difference in the Ce 3d XPS features between Ce(IV) oxide and Ce(III) oxide is that the Ce 3d XPS spectrum from Ce(IV) oxide consists of three pairs of spin– orbit doublets, whereas that from Ce(III) oxide consists of only two pairs of spin–orbit doublets. The Ce XPS spectrum clearly shows three pairs of spin–orbit doublets, which suggests that Ce(IV) dominates in our system. It was also found that the concentration of Ce^{3+} was greater in $Y_{1.9}Ce_2O_7$:0.1Eu^{3+} (17.1%) than in the host $Y_2Ce_2O_7$ (14.1%) and in $Y_2Ce_{1.9}O_7$:0.1Eu^{3+}

(13.1%). The variation in Ce^{3+} states is also visible in the absorbance spectra and its influence on the luminescence properties is discussed later.

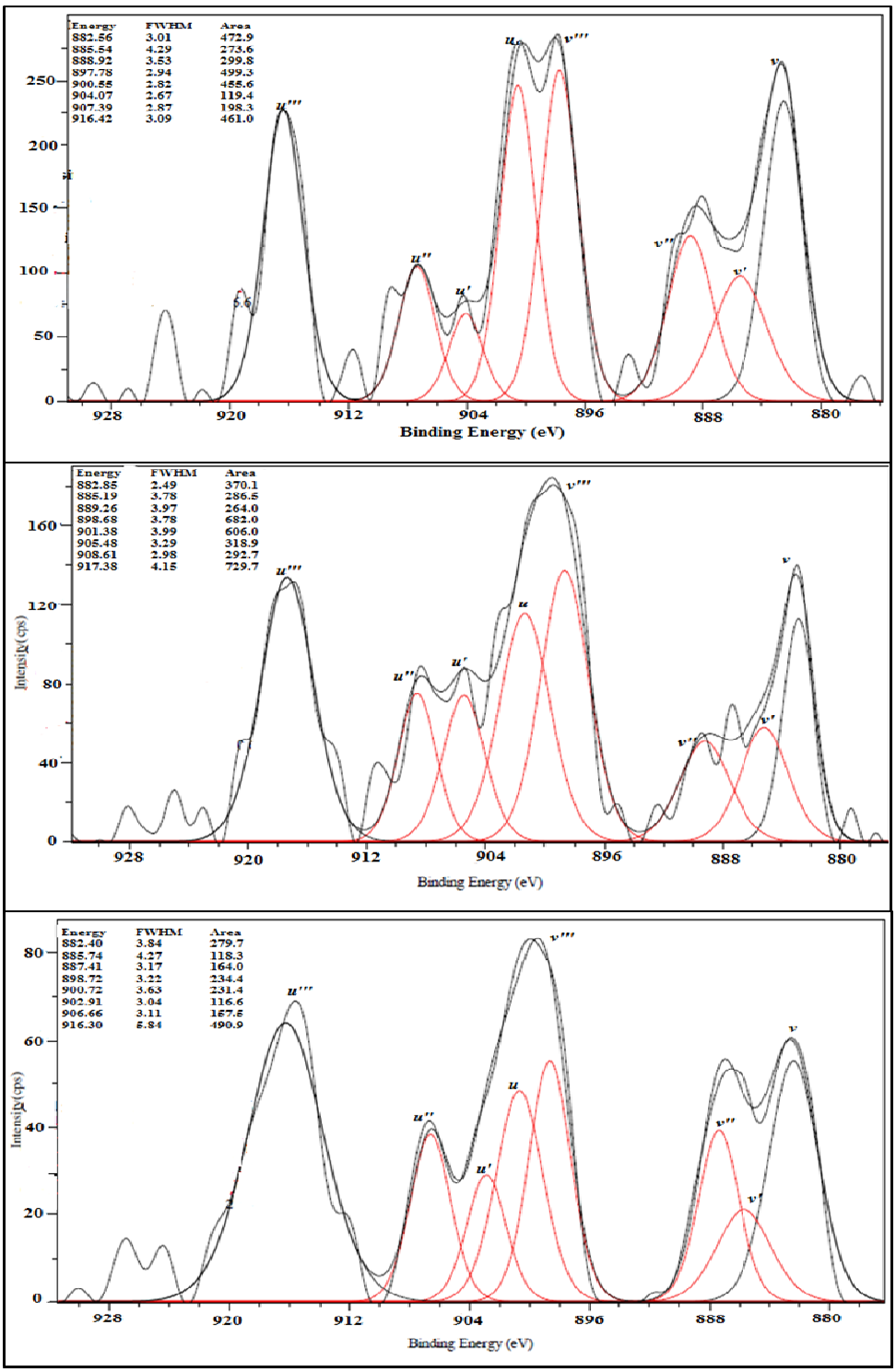

Fig. 4.3 XPS spectrum of Ce(3d) for the $Y_2Ce_2O_7$,$Y_{1.9}Ce_2O_7$:*0.1*Eu^{3+} and $Y_2Ce_{1.9}O_7$:*0.1*Eu^{3+} phosphors was deconvoluted to give the individual spin-orbit doublet of $3d_{3/2}$ and $3d_{5/2}$, and the sum of the deconvoluted peaks was used to produce the fit to the actual data.

4.3.1.4 Morphological studies

Fig. 4.4 shows the scanning electron micrographs of the as-prepared samples synthesized using the solid-state reaction route. The microstructure shows an increasing trend in particle size for the Ce^{4+} -substituted structure compared with the Y^{3+}-substituted structure and the host. The increase in crystallite size on the structural transition from the defect fluorite to C-type structure observed in the XRD analysis is evident in the microstructure. The particles are slightly agglomerated with size in the range 1–3 μm.

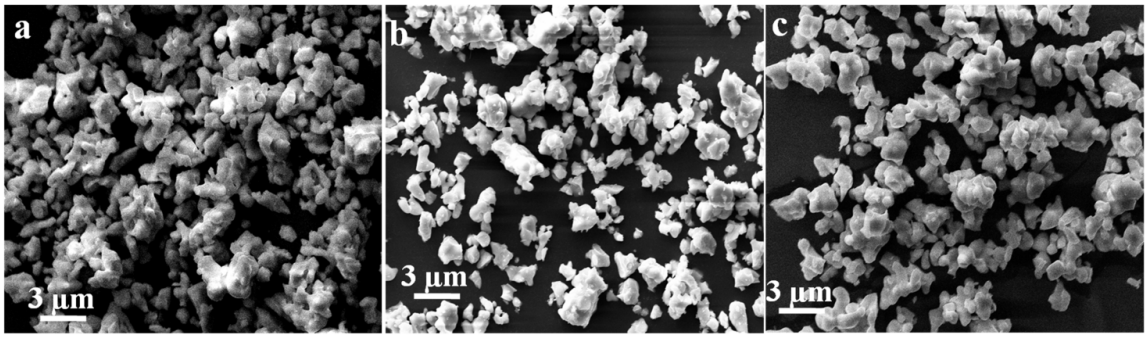

Fig. 4.4 Typical SEM photographs of a) $Y_2Ce_2O_7$, b) $Y_{1.9}Ce_2O_7$:*0.1*Eu^{3+} and c) $Y_2Ce_{1.9}O_7$:*0.1*Eu^{3+} phosphors. The particles are slightly agglomerated and there is a broad distribution of particle size with an average size of 1-3 μm.

4.3.1.5 Absorption studies

Fig. 4.5 shows the UV-visible absorption spectra of $Y_2Ce_2O_7$, $Y_{1.9}Ce_2O_7$:0.1Eu^{3+} and $Y_2Ce_{1.9}O_7$:0.1Eu^{3+}. There is a strong absorption band below 400 nm in the spectra, with maxima at 242, 302 and 340 nm; these are mainly attributed to the CT transitions O^{2-}–Ce^{3+}, O^{2-}–Ce^{4+} and inter-band transfer, respectively (Reddy et al. 2010). In addition, the absorbance due to the charge transition O^{2-}–Ce^{3+} for $Y_{1.9}Ce_2O_7$:0.1Eu^{3+} is relatively greater than that for the host and the Ce^{4+}-substituted structure. This observation also shows the variation in the Ce^{3+} states with the change in Eu^{3+} site substitution. The absorption spectra of $Y_{1.9}Ce_2O_7$:0.1Eu^{3+} phosphors showed a red shift compared with that of the host $Y_2Ce_2O_7$, whereas $Y_2Ce_{1.9}O_7$:0.1Eu^{3+} showed a blue shift. This shift in the absorption band is because some Ce^{3+} always coexists in the structure and the valence change may have some

additional contribution to the absorption spectra (Chen et al. 2007). When Eu^{3+} is doped into the B (Ce)-site of $Y_2Ce_2O_7$, the Ce^{3+} ions may be replaced by Eu^{3+} ions and the change from Ce^{4+} to Ce^{3+} decreases as a result of the structural transition from the defect fluorite structure to the C-type structure, resulting in a blue shift. Although Eu^{3+} was doped into the A (Y)-site of $Y_2Ce_2O_7$, the Ce^{3+} ions in the lattice were retained and caused an increase in the Ce^{3+} ions in the lattice as a result of defect formation in the oxygen-deficient fluorite structure, which increases the change from Ce^{4+} to Ce^{3+} ions and is seen as a red shift in the absorption spectrum. This assessment of the Ce^{3+} oxidation state from the absorption spectra is in good agreement with the XPS results.

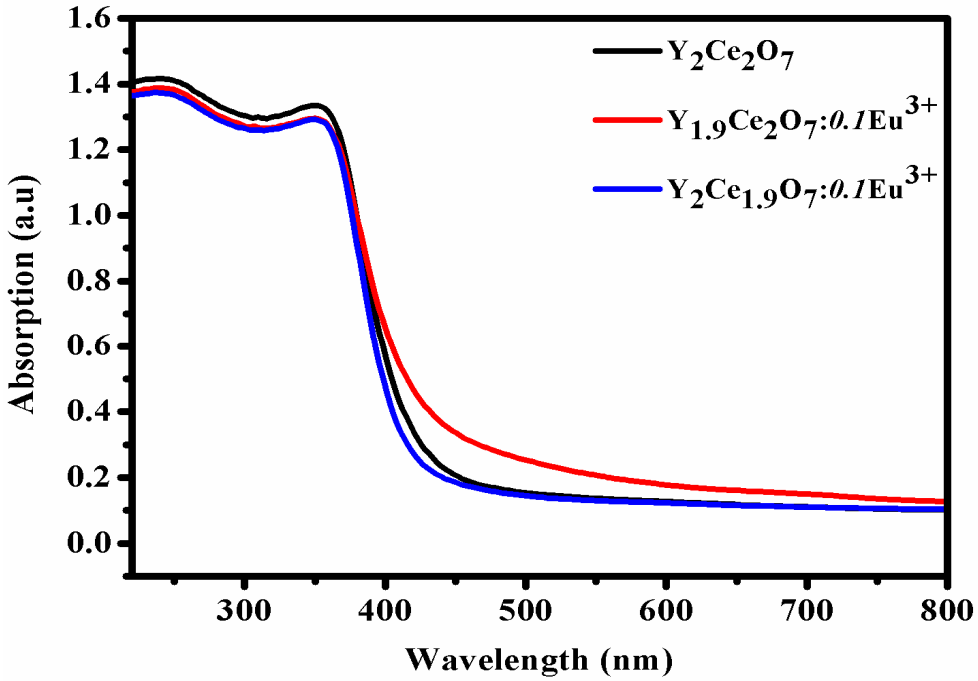

Fig. 4.5 UV-vis absorption spectra of $Y_2Ce_2O_7$, $Y_{1.9}Ce_2O_7$:*0.1*Eu^{3+} and $Y_2Ce_{1.9}O_7$:*0.1*Eu^{3+} phosphors.

4.3.1.6 Photoluminescence studies

The luminescent properties were investigated by recording the PL spectra of $Ce_{0.9}O_2$:$0.1Eu^{3+}$, $Y_{1.9}Ce_2O_7$:$0.1Eu^{3+}$ and $Y_2Ce_{1.9}O_7$:$0.1Eu^{3+}$ phosphors at room temperature under identical instrumental conditions. The excitation spectra were measured by monitoring the peak intensity at 612 nm. Fig. 4.6 shows the excitation spectra, which include a weak broad band region from 280 to 389 nm and some sharp peaks at 380, 394, 414 and 466 nm. These are assigned to the intra-$4f^6$

transition absorptions of Eu^{3+} in the host lattice: $^7F_0$ to $^5G_{2-4}$ and $^5L_7$, $^5L_6$, $^5D_3$ and $^5D_2$, respectively (Mariyam et al. 2009; Som et al. 2014; Wang et al. 2014; Dai et al. 2012). As the O^{2-}–Eu^{3+} CT states lie in a much shorter wavelength region around 250–300 nm (Yu et al. 2002; Blasse et al. 1966) and CeO_2 has a band gap around 3.4 eV (about 370 nm) (Emeline et al. 2000), the broad band in the UV region of the excitation spectra should be attributed to the CT transition of the Ce^{4+}–O^{2-} group. From the excitation spectra, it was found that for the $Y_2Ce_{1.9}O_7$:0.1Eu^{3+} samples, the intra-$4f^6$ transitions of Eu^{3+}, especially that at 466 nm, are more dominant than in the $Ce_{0.9}O_2$:0.1Eu^{3+} and $Y_{1.9}Ce_2O_7$:0.1Eu^{3+} samples.

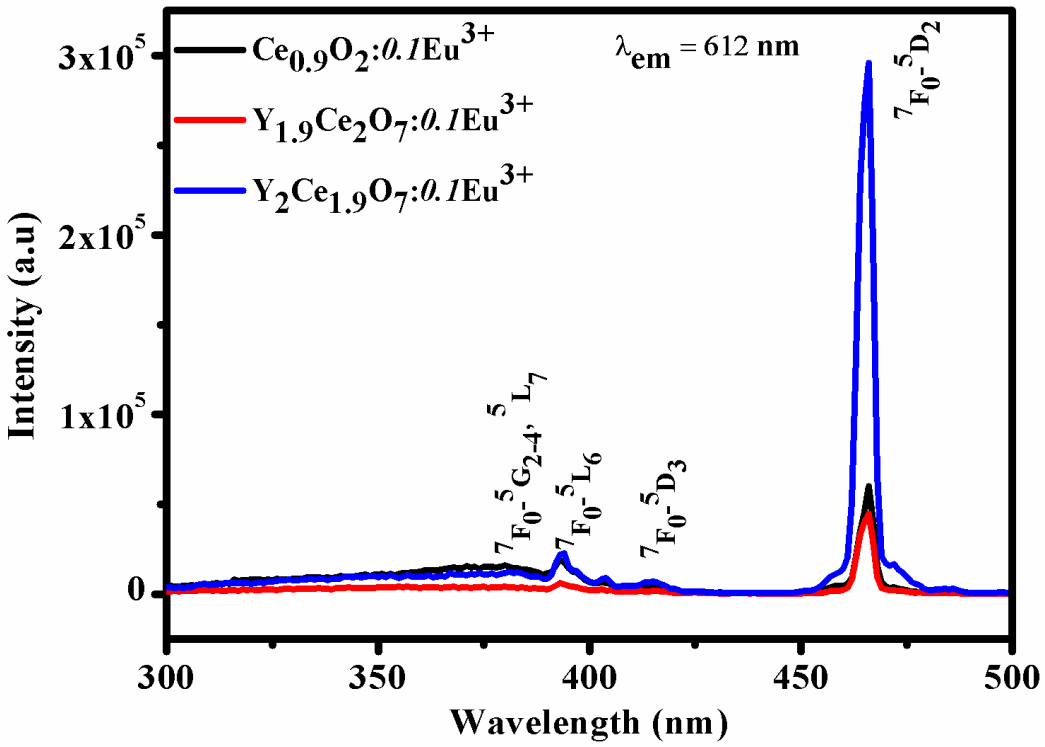

Fig. 4.6 Excitation spectra with emission at 612nm for $Y_2Ce_2O_7$, $Y_{1.9}Ce_2O_7$:*0.1*Eu^{3+} and $Y_2Ce_{1.9}O_7$:*0.1*Eu^{3+} red phosphors. The excitation spectra show intense $^7F_0$-$^5D_2$ (blue) absorption.

Fig. 4.7 shows the PL emission spectra for the as-prepared samples excited at 466 nm. The spectra consist of a series of well-resolved peaks at 580, 593, 612, 630, 654, 682, 696 and 711 nm, which can be assigned to the $^5D_0$–^7F_J (J = 0, 1, 2, 3 and 4) transitions of the Eu^{3+} ions, namely, the $^5D_0$–$^7F_0$ (580 nm), $^5D_0$–$^7F_1$ (593 nm), $^5D_0$–$^7F_2$ (612 and 630 nm), $^5D_0$–$^7F_3$ (654 nm) and $^5D_0$–$^7F_4$ (682, 696 and 711 nm) transitions, respectively (Mariyam et al. 2012). Based on the J–O theory (Juddet al. 1962; Ofelt et

al. 1962), the emission lines are a cumulative effect of the magnetic dipole (MD) transition and the electric dipole (ED) transition depending on the specific environment of Eu^{3+} in any matrix. The ED transition ($^5D_0$–$^7F_2$) centered at about 612 and 630 nm is only allowed in the absence of inversion symmetry and is hypersensitive to the local electric field, whereas the MD transition ($^5D_0$–$^7F_1$) with emission at 591 nm is an allowed transition, which is insensitive to the crystal environment. In this study the intensity of the ED transition at 612 nm was higher, which indicates that Eu^{3+} mainly occupies the lattice sites that reduce the O_h symmetry of the C-type structure. The emission intensity of the $Y_2Ce_{1.9}O_7$:0.1Eu^{3+} sample was 3.8 times greater than that of $Ce_{0.9}O_2$:0.1Eu^{3+} and $Y_{1.9}Ce_2O_7$:0.1Eu^{3+}. From the decay curves shown in Fig. 4.8, the lifetime values of the $^5D_0$–$^7F_2$ transitions for $Y_2Ce_{1.9}O_7$:0.1Eu^{3+} and $Y_{1.9}Ce_2O_7$:0.1Eu^{3+} are 0.640 and 0.598 ms, respectively.

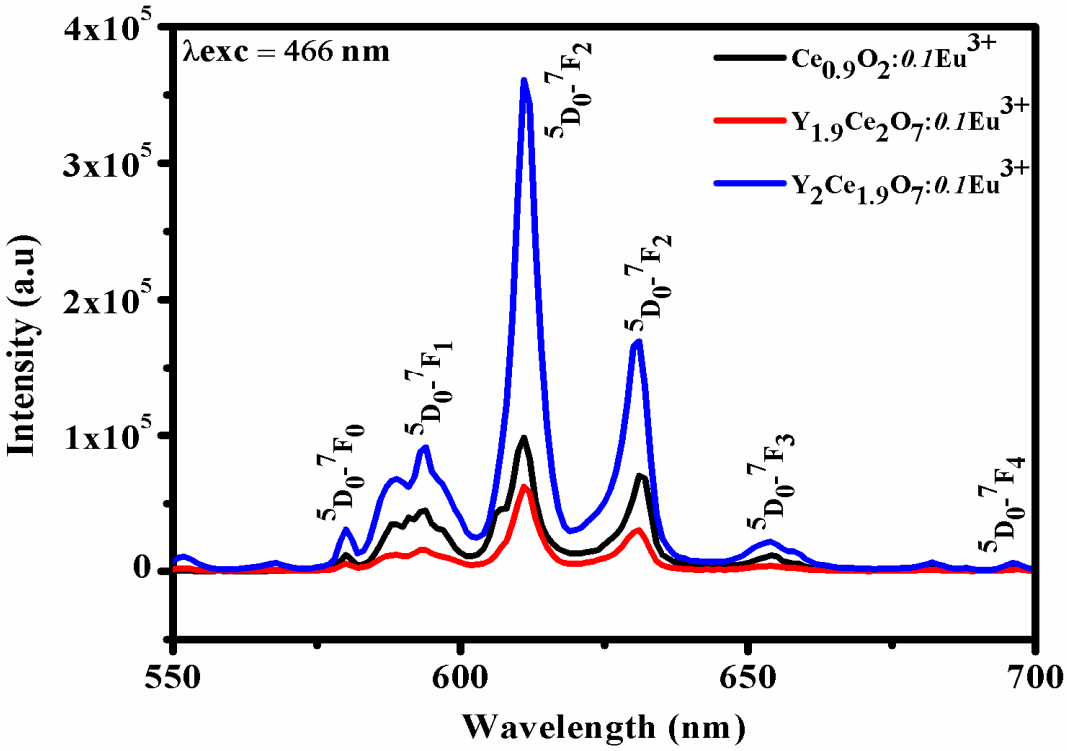

Fig. 4.7 Luminescence emission spectra (excited at 466 nm)for the as prepared samples shows that the PL intensity was found maximum in Cerium substituted Eu^{3+} phosphor and is 3.8 times greater than that of the $Ce_{0.9}O_2$:*0.1*$Eu^{3+}$and $Y_{1.9}Ce_2O_7$:*0.1*Eu^{3+}phosphors.

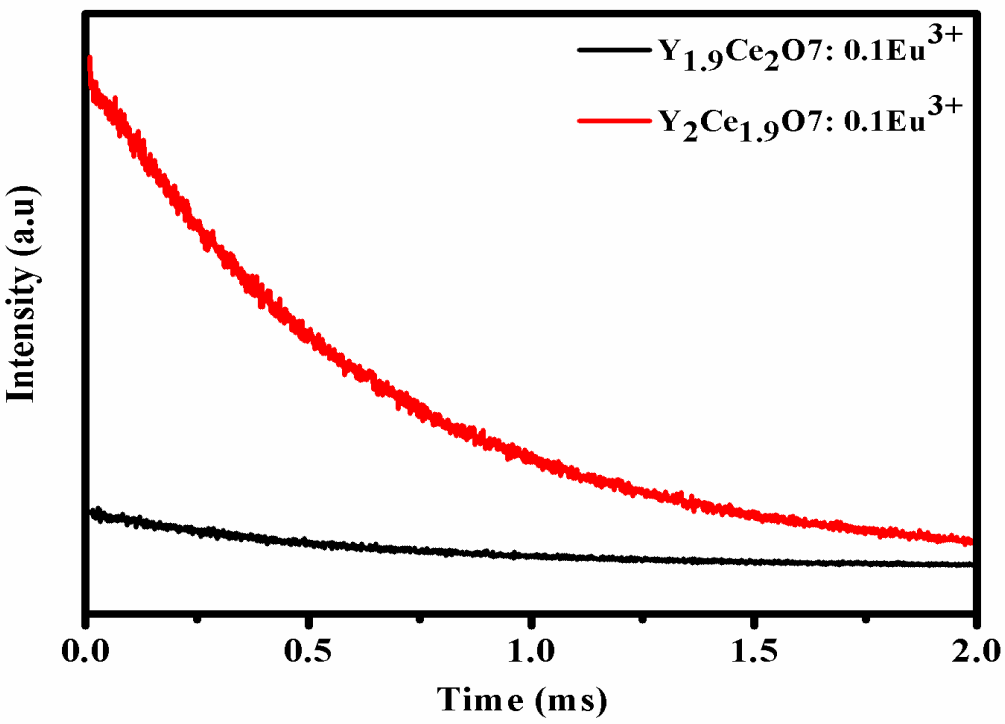

Fig. 4.8 Life time decay curves of $^5D_0{}^7F_2$ transition (wavelength 612 nm) in $Y_{1.9}Ce_2O_7$:*0.1*Eu^{3+} and $Y_2Ce_{1.9}O_7$:*0.1*Eu^{3+} under 466 nm excitation. Decay curves are well fitted with a single exponential decay function $y = Ae^{(-x/t)}$, where "A" is a constant and "t" is the decay time.

The enhancement of the PL properties of the phosphors studied in this work can be explained as follows. Luminescence properties are mainly influenced by the crystallographic structure, including the symmetry of the activator and its surroundings and the ordering of the activator in the lattice. The substitution of a trivalent ion such as Eu^{3+} in a simple fluorite lattice of CeO_2 leads to the formation of oxygen vacancies for charge compensation. These oxygen vacancies act as PL-quenching centers and reduce radiative transitions, which limits the enhancement of luminescence in the simple fluorite lattice. In the structures studied here, the substitution of Eu^{3+} at A and B sites illustrates the influence of the structure and the symmetry of Eu^{3+} on the luminescence properties of the phosphor materials. The substitution of Eu^{3+} at an A-site does not create any oxygen vacancies, but retains the biphasic nature of the defect fluorite and C-type structure that inherits the disordered oxygen vacancies and adversely affects the luminescence. The oxygen vacancies favour the reduction of Ce^{4+} to Ce^{3+}, so more Ce^{3+} states are observed in the A-site substitution. In such a situation, Eu^{3+} is more likely to exist as Ce^{3+}–O^{2-}–

Eu^{3+}. The ionic size of Eu^{3+} is closer to that of Ce^{3+} than Ce^{4+}. It is expected the configuration Ce^{3+}–O^{2-}–Eu^{3+} has more symmetry than the Ce^{4+}–O^{2-}–Eu^{3+} configuration. Under similar conditions, the increased symmetry of Eu^{3+} favors MD-induced emission. This is further evidenced by the asymmetric ratio $I(^5D_0–^7F_2)/I(^5D_0–^7F_1)$, which provides information on the site symmetry of Eu^{3+}. This value (3.5) is also observed to be lower than the phosphor substituted at the B-site (3.9). In summary, disorder in the lattice, the presence of oxygen vacancies and the increase in the number of Ce^{3+} oxidation states adversely affect the luminescence in A-site substitution.

In contrast, Eu^{3+} substituted at the B-site causes a structural variation from a defect fluorite to C-type structure. It has been reported previously (Coduri et al. 2013) that heavily doped higher ionic radii REEs strongly influence the transformation from a fluorite to a C-type structure and also the oxygen vacancy ordering in the lattice. The higher degree of ordering with substitution blocks the oxygen vacancies and the mobility in the lattice. In turn, this inhibits the reduction of Ce^{4+} to Ce^{3+}. The XPS results support the decreased number of Ce^{3+} states with the B-site substitution. In this situation, the probability of the existence of Eu^{3+} increases in the Ce^{4+}–O^{2-}–Eu^{3+} configuration, thus reducing the Eu^{3+} symmetry.

A C-type structure is formed from eight unit cells of the fluorite structure by removing 25% of the oxygen ions by introducing small ionic shifts. It has also been reported (Ikuma et al. 2005) that the C-type structures derived from the fluorite structure of Y^{3+}-doped CeO_2 tolerate excess oxygen as a result of the larger oxygen coordination of Ce^{4+}. The presence of oxygen vacancy induces distortion in the Ce polyhedra via oxygen relaxation towards the vacancies. These observations suggest that the Eu^{3+} in the transformed C-type lattice experiences more distortion and ordering in the lattice. The relatively higher asymmetric ratio obtained further confirms this assessment compared with A-site substitution. The $^5D_0$ lifetime of Eu^{3+} for the Ce^{4+} substitution is higher than the Y^{3+} substituted lifetime, indicating a more uniform distribution of Eu^{3+} as a result of structural ordering in the lattice. All these factors significantly enhanced the PL properties for the B-site substituted compound and hence further investigations were confined to $Y_2Ce_{2-x}O_7$:$x$$Eu^{3+}$ with respect to the variation of Eu^{3+} concentration.

4.3.2 Photoluminescent studies of $Y_2Ce_{2-x}O_7$:xEu^{3+} (x = 0.05, 0.10, 0.15, 0.20, 0.25, 0.50) red phosphors

4.3.2.1 Powder X-ray diffraction studies

Fig. 4.9 shows the powder XRD patterns of $Y_2Ce_{2-x}O_7$:xEu^{3+} (x = 0.05, 0.10, 0.15, 0.20, 0.25, 0.50) phosphors. The XRD patterns of the Eu^{3+}-doped samples can be indexed completely to the C-type structure. No impurity peak was observed in the XRD patterns with different amounts of doping of Eu^{3+}, which suggests that doping of a small percentage of Eu^{3+} ions does not change the crystal structure. Table 4.1 gives the cell parameters, which conform to the C-type phase.

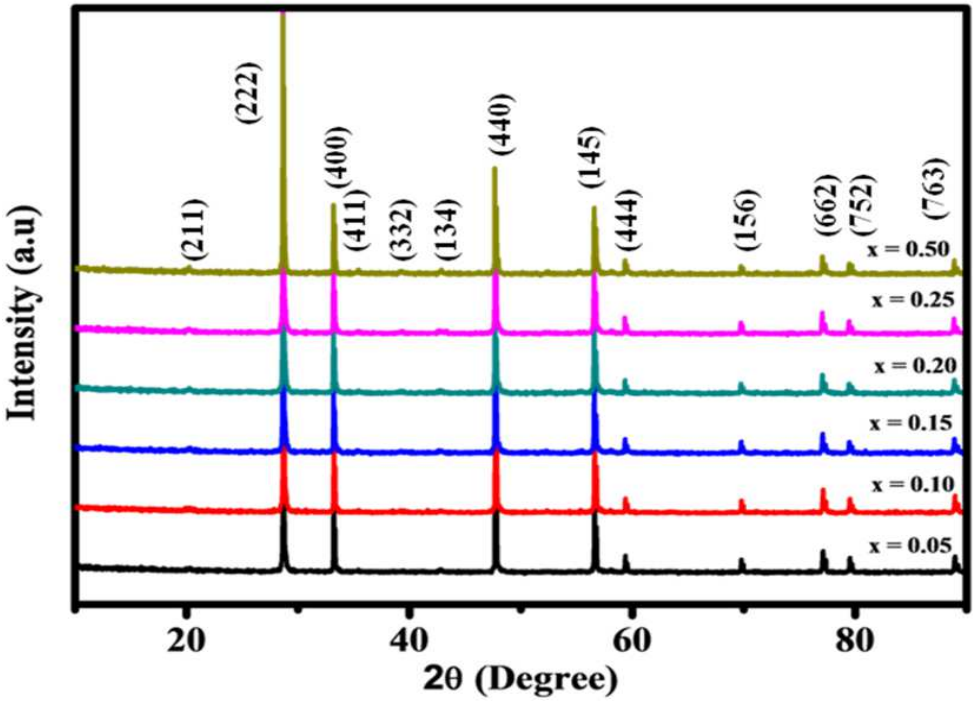

Fig. 4.9 Powder XRD patterns of $Y_2Ce_{1-x}O_7$:xEu^{3+} (x = 0.05, 0.10, 0.15, 0.20, 0.25, 0.50) red phosphors.

It can be seen from the cell parameters that the lattice parameter increases with increasing Eu^{3+} concentration as expected because the ionic radius of Eu^{3+} (r = 0.1066 nm when the coordination number = 8) is larger than that of the Ce^{4+} (r = 0.097 nm when the coordination number = 8). This further confirms that the substitution of Eu^{3+} takes place in the lattice site of Ce^{4+}. The average crystallite size of the as-prepared samples is nearly constant at about 135 nm, which also implies that there is no structural variation with Eu^{3+} substitution.

Table 4.1 Variation of Lattice parameter and full width half maximum (FWHM) of 385 cm^{-1} Raman mode of the $Y_2Ce_{2-x}O_7$:xEu^{3+} (x = 0.05, 0.10, 0.15, 0.20, 0.25, 0.50) red phosphors.

x	Lattice parameter (Å)	FWHM of 385 cm^{-1} Raman mode (nm)
0.05	10.7750 (8)	52.43
0.10	10.7764 (7)	70.18
0.15	10.7766 (7)	71.12
0.20	10.7784 (5)	71.43
0.25	10.7804 (4)	75.29
0.50	10.7772 (8)	99.21

4.3.2.2 Raman spectroscopic studies

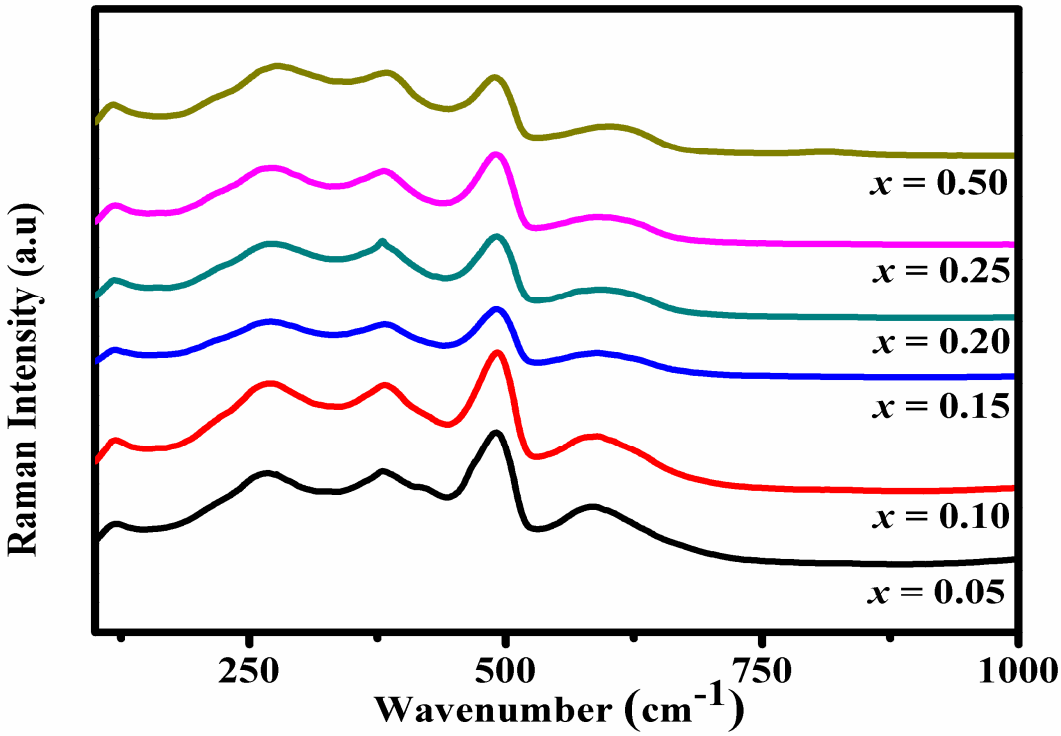

Fig. 4.10 Raman spectra for room-temperature $Y_2Ce_{2-x}O_7$:xEu^{3+} (0.05, 0.10, 0.15, 0.20, 0.25 and 0.50) red phosphors. With progressive Eu^{3+} doping the line shape of the allowed modes appears to be broadened.

Fig. 4.10 shows the Raman spectra for the $Y_2Ce_{2-x}O_7$:xEu^{3+} (x = 0.05, 0.10, 0.15, 0.20, 0.25, 0.50) phosphors. It is clear that the Raman spectrum for the samples substituted at the B (Ce^{4+}) site exhibits the characteristic modes of a C-type structure. The modes gradually become broader with decreased intensity with Eu^{3+} substitution. As a consequence, the FWHM of the modes increases, indicating the increasing oxygen vacancy formation. Table 4.1 gives the typical FWHM values for the 385 cm^{-1} mode.

4.3.2.3 X-ray photoelectron spectroscopy studies

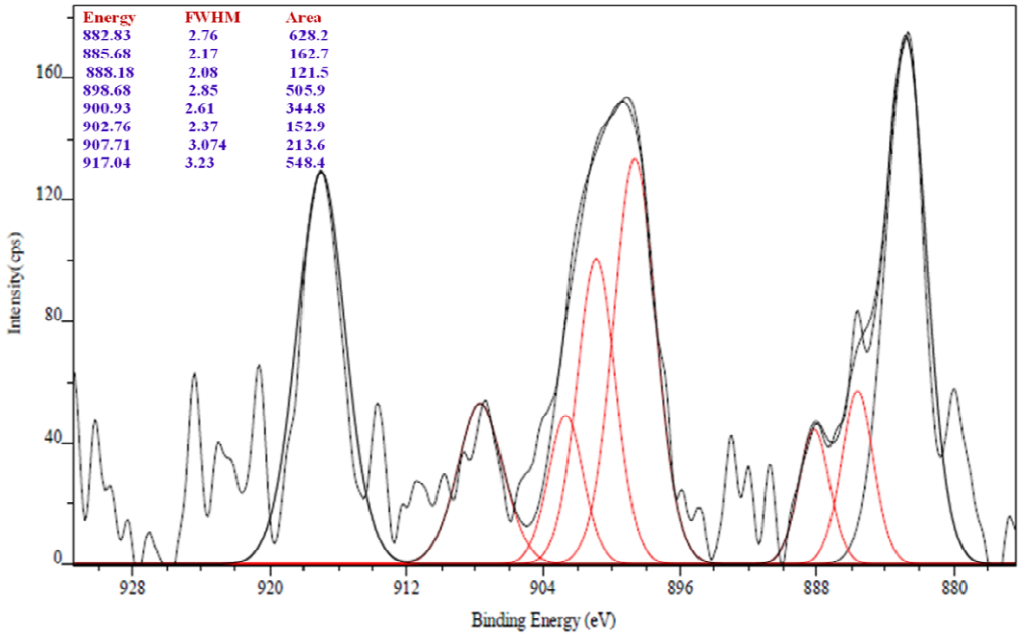

Fig. 4.11 XPS spectra of Ce 3d for $Y_2Ce_{1.5}O_7$:*0.5*Eu^{3+} red phosphor and the concentration of Ce^{3+} state is decreased compared to the lower substituted one (*x* = 0.10) and is found to be 11.5%.

Fig. 4.11 presents the XPS spectra of Ce 3d core levels for $Y_2Ce_{1.5}O_7$:0.5Eu^{3+} phosphors. The six peaks of the spectrum refer to the three pairs of spin–orbit doublets, which are characteristic of the Ce^{4+} 3d final states. In addition, the characteristic peaks of the Ce^{3+} species were also observed. By fitting the curves and then calculating the area of the fitted peaks, we conclude that the concentration of Ce^{3+} in the $Y_2Ce_{1.5}O_7$:0.5Eu^{3+} phosphor decreased compared with the lower substituted phosphor (x = 0.10) and was 11.5%. This decrease in the

number of Ce^{3+} states can be attributed to the increased ordering of the oxygen vacancies in the lattice inhibiting the reduction of Ce^{3+}.

4.3.2.4 Morphological studies

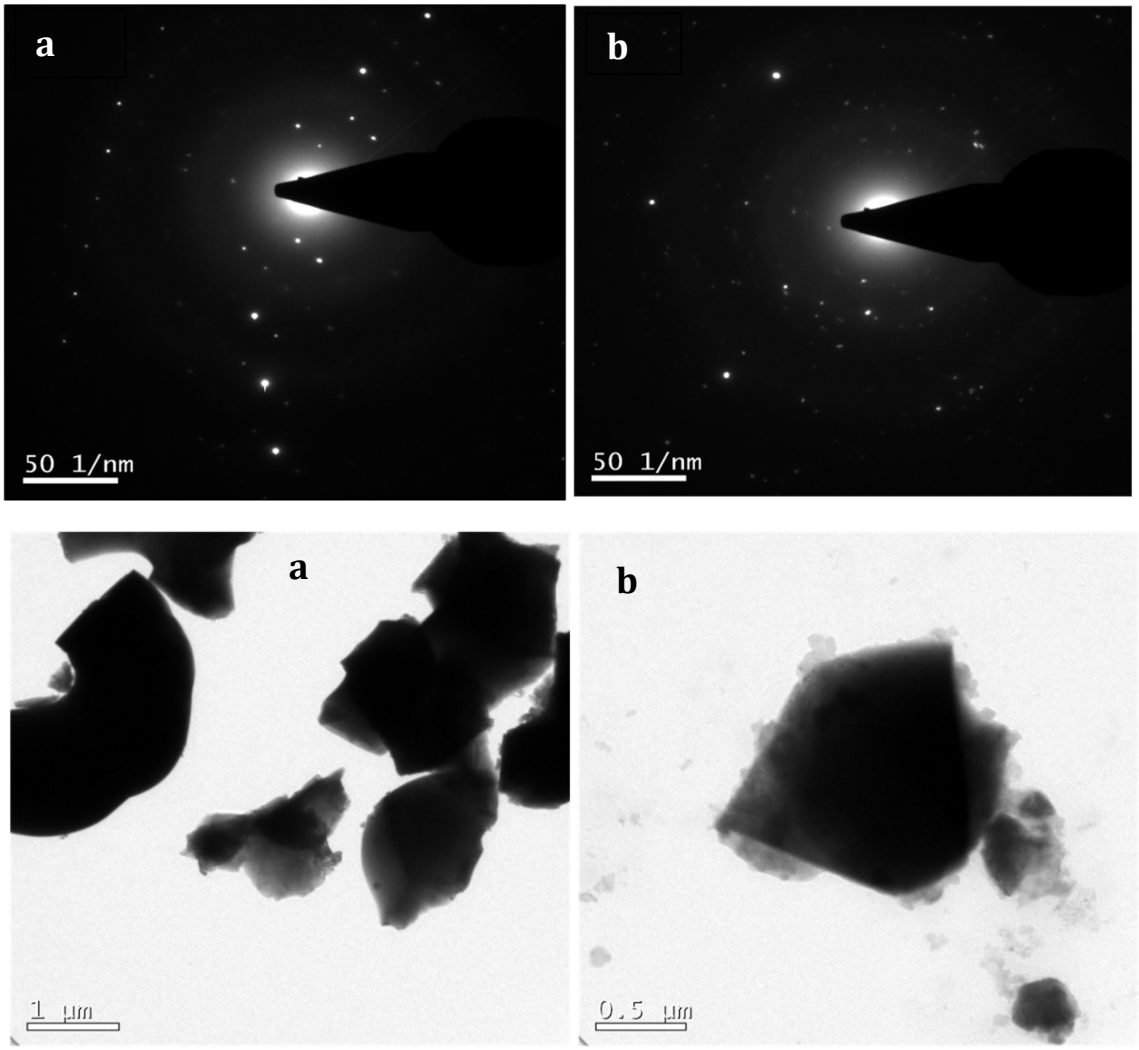

Fig. 4.12 Selected area electron diffraction patterns (SEAD) and TEM micrographs a) $Y_2Ce_{1.8}O_7$:*0.2*Eu^{3+} and b) $Y_2Ce_{1.5}O_7$:*0.5*Eu^{3+} red phosphors.

Fig. 4.12 shows the electron diffraction patterns from a single particle of $Y_2Ce_{1.8}O_7$:0.2Eu^{3+} and $Y_2Ce_{1.5}O_7$:0.5Eu^{3+} red phosphors. The SAED pattern shows a polycrystalline structure and is consistent with a C-type unit cell indicating diffraction maxima with many weak diffraction spots of the super-lattice planes. The chemical composition of the phosphors was checked using energy-dispersive

spectrometry analysis with TEM and identified the presence of all the expected elements (Fig 4.13). This further confirms the homogeneity of the phase formed. The compositions derived from the microchemical analysis of the phosphors are in close agreement with the stoichiometry of the formulae.

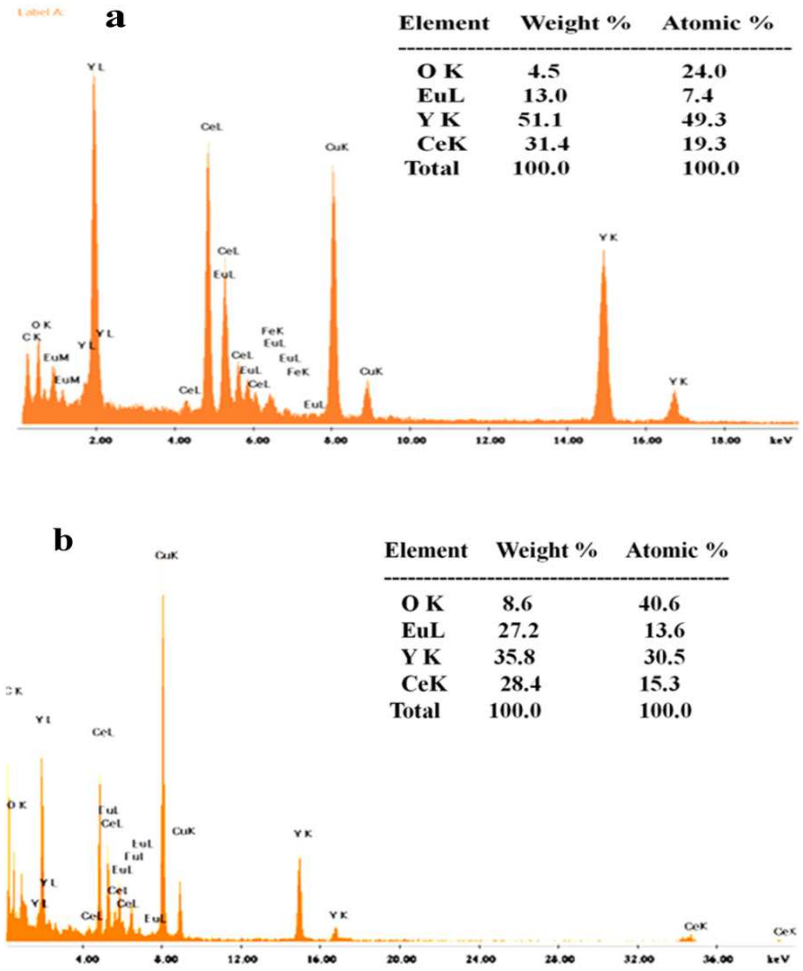

Fig. 4.13 Energy dispersive spectrophotometer (EDS) spectra of a) $Y_2Ce_{1.8}O_7$:*0.2*Eu^{3+} and b) $Y_2Ce_{1.5}O_7$:*0.5*Eu^{3+} red phosphors

Fig. 4.14 shows the typical SEM microstructure of $Y_2Ce_{2-x}O_7$:*x*Eu^{3+} (x = 0.05, 0.10, 0.15, 0.20, 0.25, 0.50) red phosphors. The micrographs show slightly agglomerated particles in the range 1–3 µm. Fig. 4.15 shows the elemental mapping analysis of typical $Y_2Ce_{1.5}O_7$:0.50Eu^{3+} red phosphor calcined at 1500°C for 12 h. This confirms that all the elements are uniformly distributed in the sample.

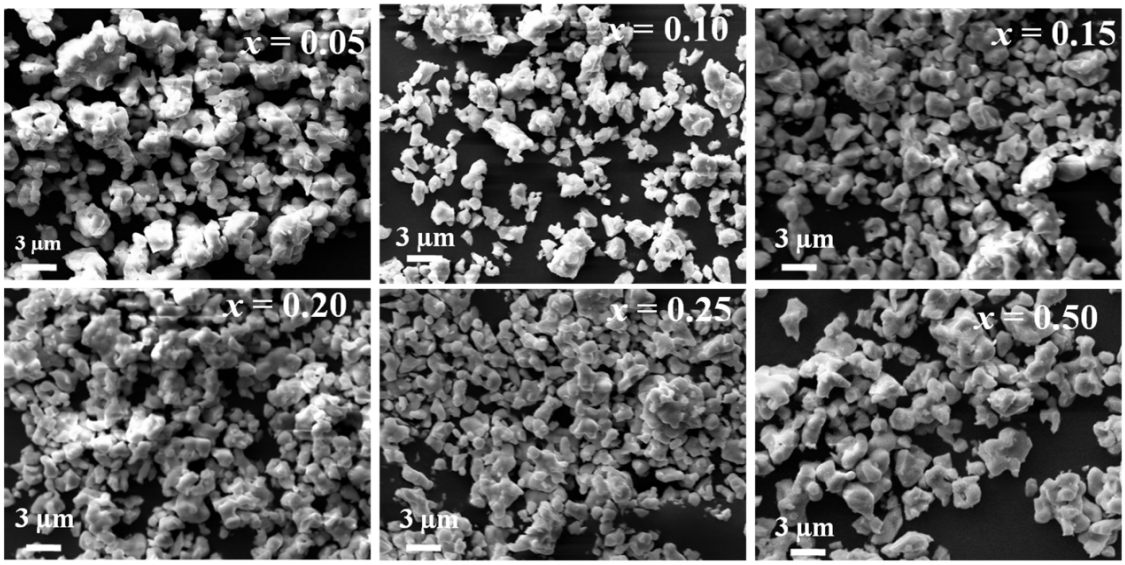

Fig. 4.14 Typical SEM images of $Y_2Ce_{2-x}O_7$:xEu^{3+}(x = 0.05, 0.10, 0.15, 0.20, 0.25 and 0.50) red phosphors.

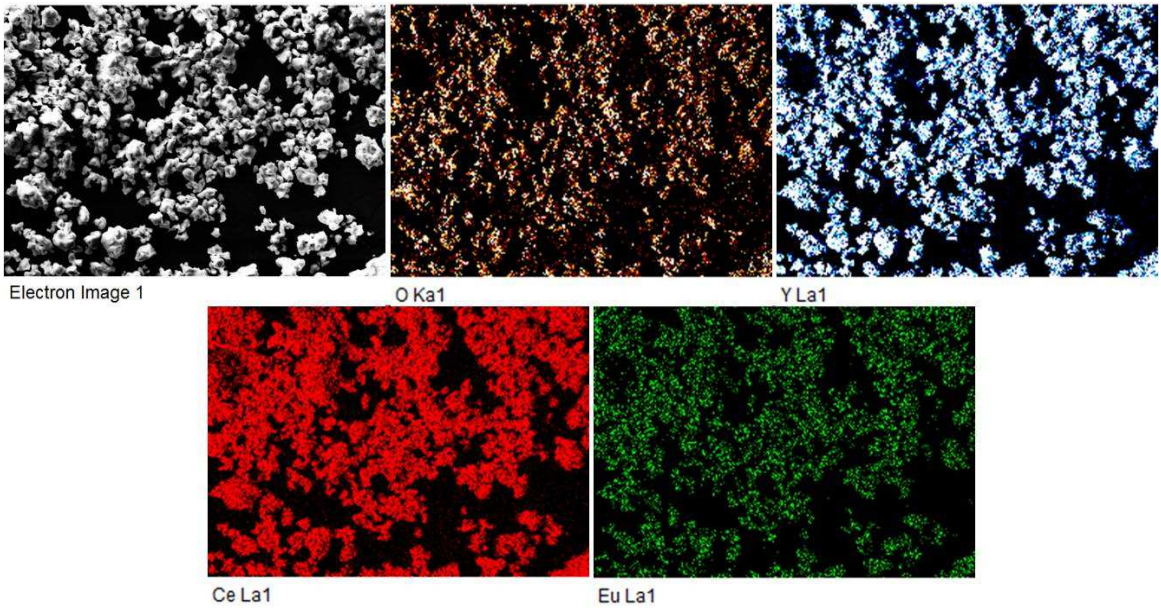

Fig. 4.15 Elemental mapping of typical $Y_2Ce_{1.5}O_7$:*0.5*Eu^{3+} red phosphor and it conforms that all the elements are uniformly distributed in the lattice.

4.3.2.5 Absorption studies

Fig. 4.16 shows the UV-visible absorption spectra of the $Y_2Ce_{2-x}O_7$:xEu^{3+} (x = 0.05, 0.10, 0.15, 0.20, 0.25, 0.50). The absorption spectra of all the samples show a strong absorption band below 400 nm in the UV region that is mainly attributed to the CT transition from the O^{2-}(2p) to the Ce^{4+} (4f) orbital in $Y_2Ce_{2-x}O_7$:xEu^{3+}. The

absorption spectrum showed a blue shift compared with that of the lower concentration of Eu^{3+}. A blue shift is seen with increasing concentration of Eu^{3+} and the band gap was calculated from the absorption spectra using Shapiro's method by extrapolating the onset of absorption to the wavelength axis (Table 4.2). Previously published work suggested that the blue shift in the band gap may occur as a result of several factors, e.g. the grain size effect (Kuo et al. 1999), stress in the matrix (Thomas et al. 1999), the amorphous nature of the material (Thomas et al. 2000) and oxygen vacancies on the outermost surface (Shyu et al. 1988). In this instance, however, a significant blue shift was observed and there was no detectable reduction in grain size. Hence the grain size effect did not play an important part in the observed blue shift. The diffraction pattern for the samples suggests a highly crystalline structure, therefore the blue shift is not due to an amorphous nature. The blue shift in the UV-visible absorption spectra may therefore be attributed to the decrease in valence change from Ce^{4+} to Ce^{3+} indicated by the XPS results and the increasing number of oxygen vacancies in the lattice.

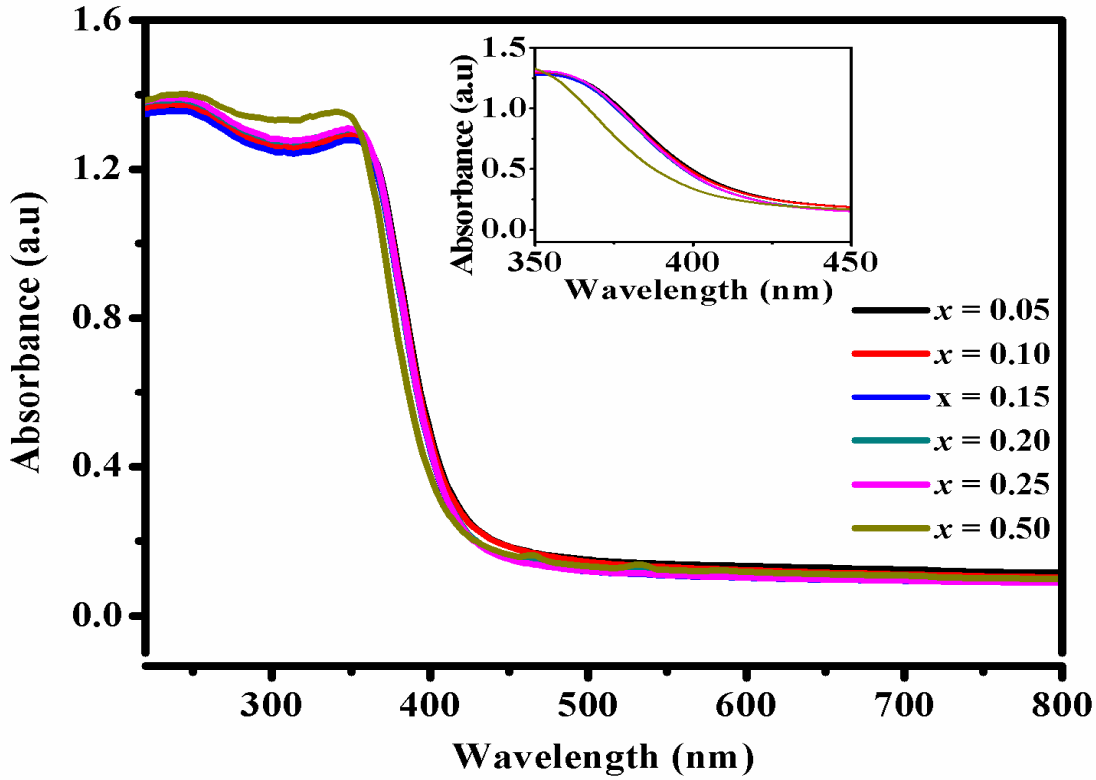

Fig. 4.16 UV-vis absorption spectra of $Y_2Ce_{2-x}O_7$:xEu^{3+}(0.05, 0.10, 0.15, 0.20, 0.25 and 0.50) red phosphors.

4.3.2.6 Photoluminescence studies

Fig. 4.17 and 4.18 show the excitation and emission spectra of $Y_2Ce_{2-x}O_7$:xEu^{3+} (x = 0.05, 0.15, 0.20, 0.25, 0.50) phosphors. One of the remarkable changes in the excitation spectra is the prominent enhanced f–f transition intensity at 466 nm. The emission spectra show a gradual increase in the intensity of the red emission (612 nm), which increases as the Eu^{3+} doping increases. The intensity of a 50 mol% concentration of Eu^{3+} is 8.5 times greater than the lower concentration, i.e. no concentration quenching is observed.

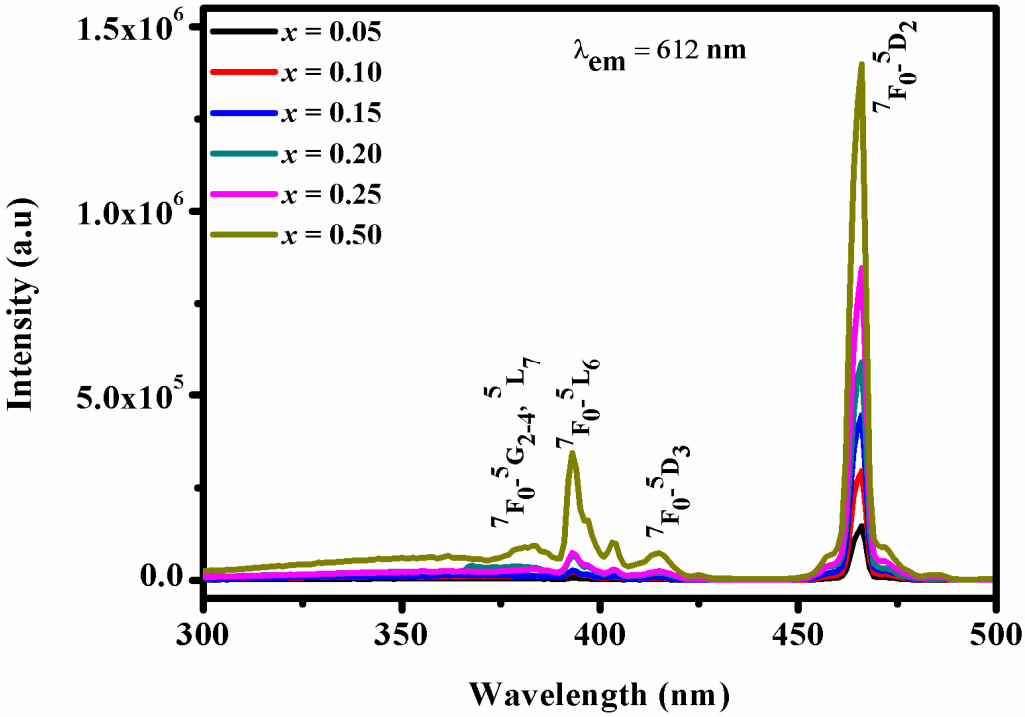

Fig. 4.17 Excitation spectra of $Y_2Ce_{2-x}O_7$:xEu^{3+}(0.05, 0.10, 0.15, 0.20, 0.25 and 0.50) red phosphors for 612 nm emission. With Eu^{3+} substitution the charge transfer band as well as the intra-4f transitions is also enhanced.

The intensity (R/O) ratio (also known as the asymmetry ratio) is a measure of the degree of distortion from the inversion symmetry of the local environment of the Eu^{3+} ion in the lattice. The R/O value can be calculated using the following equation and Table 4.2 gives the values for the as-prepared samples:

$$Asymmetric\ ratio = \frac{I(5D0 \rightarrow 7F2)}{I(5D0 \rightarrow 7F1)} \qquad (4.3)$$

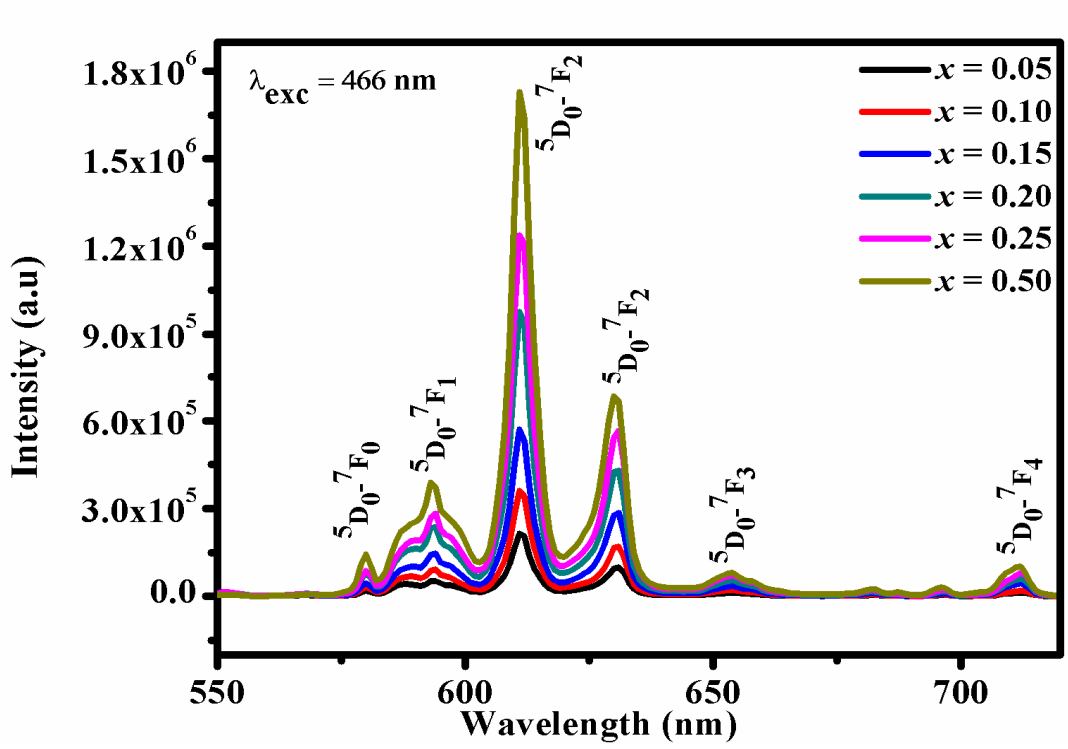

Fig. 4.18 Emission spectra of $Y_2Ce_{2-x}O_7$:xEu^{3+} (0.05, 0.10, 0.15, 0.20, 0.25 and 0.50) red phosphors under 466 nm excitation. As $^5D_0$-$^7F_2$ electric dipole transition intensity dominates over magnetic dipole transition, Eu^{3+} sites have no inversion symmetry. As the Eu^{3+} concentration increases, the asymmetric ratio increases.

Table 4.2 The peak intensity and FWHM of $^5D_0$-$^7F_2$ transition at 612 nm red emission, asymmetric ratio and band gap energy of the as prepared $Y_2Ce_{2-x}O_7$:xEu^{3+} (0.05, 0.10, 0.15, 0.20, 0.25, 0.50) phosphors under 466nm excitation.

x	Peak Intensity of 612 nm red emission (λ_{exc}= 466 nm) (a.u)	Asymmetric Ratio	FWHM (nm)	Band Gap Energy (E_g) (eV)
0.05	2.2 x 10^5	3.93	4.75	2.93
0.10	3.6 x 10^5	3.96	4.82	2.97
0.15	5.7 x 10^5	4.02	4.89	2.99
0.20	9.9 x 10^5	4.12	4.88	3.01
0.25	1.2 x 10^6	4.39	4.94	3.02
0.50	1.7 x 10^6	4.42	4.93	3.07

It can be clearly seen that the intensity ratio increases from 3.93 to 4.42 with the increase in Eu^{3+} concentration with excitation at 466 nm. These results imply that the entry of Eu^{3+} into $Y_2Ce_{2-x}O_7$ perturbs the host structure, i.e. most of the Eu^{3+} ions occupy sites without inversion symmetry. This may be also due to oxygen deficiencies in the Eu^{3+}-doped yttrium cerate particles. This is because Ce can exist in both the 3+ and 4+ oxidation states and therefore, with the presence of Y^{3+} ions, the coexistence of (Ce^{3+}–O–Eu^{3+}), (Ce^{4+}–O–Eu^{3+}) and (Y^{3+}–O–Eu^{3+}) arrangements in the crystalline environment is possible. The size of the Eu^{3+} ion (0.095 nm) is closer to that of Ce^{3+} (0.102 nm) than to that of Ce^{4+} (0.087 nm), which implies that the (Ce^{3+}–O–Eu^{3+}) configuration has more symmetry than the (Ce^{4+}–O–Eu^{3+}) configuration. The R/O intensity ratio suggests that the higher mol% of Eu^{3+} ions are found at the Ce^{4+} sites and that lattice distortion of the local environment is generated around the Eu^{3+} ions, favouring ED-induced emission ($^5D_0$–$^7F_2$). On increasing the Eu^{3+} concentration, the Ce^{3+} concentration decreases and, at the same time, the Ce^{4+} concentration becomes predominant, as supported by the XPS results, and thus the probability of the asymmetrical (Ce^{4+}–O–Eu^{3+}) configuration in the lattice increases, suggesting that the ED transition is more favorable than the MD transition.

The C-type structures derived from the defect fluorite structure lead to the formation of two different sets of shorter and longer cation–cation distances, whereas the only one cation–cation distance is observed in the fluorite structures. The different distances in the C-type lattice are caused by the occupation of the oxygen site in between the two cations. The lattice transformation drives the oxygen vacancy ordering in which the smaller cations are in octahedral coordination and the second ion is either in eight-fold coordination, as in the fluorite structure, or seven-fold, or both. In this study, the results of the XRD and Raman studies indicate the formation of a C-type structure with excess oxygen. In such a situation the Y^{3+} ion is in octahedral coordination while the Ce^{4+} ion is in eight-fold or less coordination. Our results confirm the substitution of Eu^{3+} at the Ce^{4+} site. The Eu^{3+} exists mainly in the repeated configuration Y^{3+}–O^{2-}–Eu^{3+}–O^{2-}–Y^{3+}–O^{2-}–Ce^{4+} as a result of cation ordering linked to the oxygen vacancy ordering. This facilitates the more uniform distribution of Eu^{3+} in the lattice. The emission intensities increase with

increasing Eu^{3+} concentration up to 50 mol% without quenching. Concentration quenching mainly takes place through a cross-relaxation mechanism among the Eu^{3+} ions when the distance between them is reduced to a critical level. When the Eu^{3+}–Eu^{3+} distance is less than this critical level, the excited energy of the activator is lost by non-radiative energy transfer by the creation of some oxygen vacancy defects in the host or by Eu^{3+}–Eu^{3+} interaction. In addition, multiphonon-assisted nonradiative energy transfer also contributes to the quenching (Som et al. 2014). In general, concentration quenching is mainly observed as a result of the reduction in the distance between ions to less than the critical distance in most of the host lattices. However, in this system, there is a preferential cation ordering linked to the oxygen vacancy ordering that facilitates the uniform distribution of Eu^{3+} ions in the lattice, preventing the formation of clustering of the ions. Thus the cross-relaxation between Eu^{3+}–Eu^{3+} ions is reduced, allowing the substitution of a higher concentration of Eu^{3+} in this type of lattice. Therefore no concentration quenching is observed up to 50 mol% of Eu^{3+}, although concentration quenching is observed in the fluorite lattice CeO_2 above 15mol% of Eu^{3+} doping (Kumar et al 2009). Such preferential Eu^{3+} occupancy is absent in the disordered lattice of CeO_2 in which the Eu^{3+}–Eu^{3+} distance decreases at higher substitution rates, leading to effective energy transfer between the neighboring ions. Hence the excited state moves to the quenching sites, dissipating the energy nonradiatively. As a result, concentration quenching takes place in the CeO_2 lattice at >15 mol% of Eu^{3+} doping.

To assess the site symmetry and luminescence behavior of Eu^{3+} ions in $Y_2Ce_{2-x}O_7$ (x = 0.05, 0.20, 0.25 and 0.50) the Judd– Ofelt intensity parameters Ω_t (2, 4 and 6) were calculated for typical compositions. These intensity parameters provide the radiative probabilities of the activator ions in different hosts. Ω_2 signifies the polarization and asymmetric behavior of the activator and the ligand, whereas the other two parameters depend on long-range effects. These parameters Ω_{2-4}, the branching ratio (β) and the stimulated emission cross-section (σ) were determined as described previously (Som et al. 2014; Vinod et al. 2014) and the parameters are calculated from the luminescence emission. The integrated emission intensities (areas below the luminescence bands) are associated with the radiative emission rates and can be written as:

$$\frac{A_{0-2,4}}{A_{0-2,4}} = \frac{I_{0-2,4}}{I_{0-2,4}} \frac{h\nu_{0-2,4}}{h\nu_{0-2,4}} \quad (4.4)$$

where I_{0-J} is the integrated emission intensity and $h\nu_{0-J}$ is the energy corresponding to transition $^5D_0 \rightarrow {}^7F_J$ (J= 1, 2, 4). The transition $^5D_0 \rightarrow {}^7F_J$ is left out due to their small emission intensities. The magnetic dipole radiative emission rate A_{0-1} has a value of ≈50 s^{-1}. The radiative emission rates $A_{0-2,\ 4}$ are related to forced electric dipole transitions and they may be written as a function of the J–O intensity parameters:

$$A_{0-J} = \frac{64\pi^4(\nu_{0-2,4})^3 e^2}{3hc^3} \frac{1}{4\pi\epsilon_0} \chi \sum_{j=2,4,6} \Omega_j < 5D_0 \left| U^{(J)} \right| 7F_{2,4} >^2 \quad (4.5)$$

where, χ is the Lorentz local field correction factor given as function of the index of refraction n of the host $\chi = n(n2+ 2)^{2/9}$. The non-zero square reduced matrix elements are solely $< \langle 5D_0 \left| U^{(2)} \right| 7F_2 > \rangle^2 = 0.0032$ and $< \langle 5D_0 \left| U^{(4)} \right| 7F_4 > \rangle^2 = 0.0023$. Thus, using Eqs. (4) and (5) the values of $\Omega_{2,4}$ were obtained. The value of Ω_6 could also be estimated by analysing the $^5D_0 \rightarrow {}^7F_6$ transition but in the present case, this emission could not be observed. The calculated Judd–Ofelt parameters have been used to predict some important radiative properties such as transition probabilities, radiative lifetime and branching ratios and lifetimes for the excited states of Eu^{3+} ions. The radiative transition probability for a transition $\Psi J \rightarrow \Psi' J'$ can be calculated from Eq. (3) as $A_{rad}(\Psi J, \Psi' J') = A_{J-J'}$.

The total radiative transition probability (A_T) can be calculated using the equation below:

$$A_T(\Psi J) = \Sigma_{J'} A_{J-J'} \quad (4.6)$$

The radiative lifetime $\tau_{rad}(\Psi J)$ of an excited state in terms of A_T, is given by:

$$\tau_{rad}(\Psi J) = \frac{1}{AT(\Psi J)} \quad (4.7)$$

The branching ratio $\beta(\Psi J)$ corresponding to the emission from an excited level to its lower levels is given by:

$$\beta(\Psi J) = \frac{1}{AT(\Psi J)} \quad (4.8)$$

The stimulated emission cross-section ($\sigma(\lambda_p)$) can be expressed as:

$$(\sigma(\lambda_p))(J \rightarrow J') = \frac{\lambda_p^4}{8\pi c n^2 \Delta\lambda_{eff}} A_{rad}(J \rightarrow J') \quad (4.9)$$

where λ_p is the peak wavelength and $\Delta\lambda_{eff}$is its effective line width found by dividing the area of the emission band by its maximum height.

Table 4.3 Spectral Parameters of $Y_2Ce_{2-x}O_7$:xEu^{3+} (x = 0.05, 0.20, 0.25 and 0.50).

x	J-O intensity Parameters		Transition	$A_{0\text{-}2,4}$ (s^{-1})	A_τ (s^{-1})	τ_{rad} (ms)	β (%)	$\sigma(\lambda_p)$ (pm^2)	τ (ms)	η (%)
	Ω_2 (pm^2)	Ω_4 (pm^2)								
0.05	1.88	0.31	$^5D_0$-$^7F_1$	-	175	5.73	28.6	108.9		
			$^5D_0$-$^7F_2$	105.8			60.6	249.0	0.618	10.8
			$^5D_0$-$^7F_4$	7.98			4.6	722.8		
0.20	2.06	0.34	$^5D_0$-$^7F_1$	-	186	5.38	26.9	141.4		
			$^5D_0$-$^7F_2$	115.9			62.4	257.2	0.710	13.2
			$^5D_0$-$^7F_4$	8.7			4.7	795.9		
0.25	2.25	0.36	$^5D_0$-$^7F_1$	-	199	5.02	25.1	158.0		
			$^5D_0$-$^7F_2$	127.5			64.0	274.0	0.712	14.1
			$^5D_0$-$^7F_4$	9.22			4.6	1253		
0.50	2.26	0.36	$^5D_0$-$^7F_1$	-	196	5.10	25.5	157.5		
			$^5D_0$-$^7F_2$	126.8			64.6	276.6	0.718	14.2
			$^5D_0$-$^7F_4$	9.16			4.7	854.7		

Table 4.3 lists the intensity parameters obtained. The Ω_2 value was the most sensitive to the asymmetric environment of the Eu^{3+} site. The value of Ω_2 increases with Eu^{3+} concentration, indicating the increasing asymmetric nature of Eu^{3+} in this host; this is also evidenced by the higher asymmetric ratio (Table 4.2). The order of the Ω_t parameters in general is $\Omega_2 < \Omega_4$, but in this system the trend for the Ω_t parameters is $\Omega_2 > \Omega_4$. This change in trend of the intensity parameters in this system is in agreement with those reported previously (Kumar et al. 2009). This implies that the efficiency of the $^5D_0$–$^7F_2$ transition becomes weak at the cost of the $^5D_0$–$^7F_1$ transition. The emission intensity could also be characterized by the Ω_4 parameters. The continuous increase in the Ω_4 parameter with Eu^{3+} concentration suggests increased efficiency of the $^5D_0$–$^7F_2$ transitions. This is further supported by the dominant value of the branching ratio (β) for the $^5D_0$–$^7F_2$ transition rather than the other transitions. The emission cross-section values (σ) change differently for the $^5D_0$–$^7F_1$ and $^5D_0$–$^7F_2$ transitions. The assessment of the J–O intensity parameters indicates the ionic nature of the Eu^{3+} ion at more asymmetric sites in the lattice.

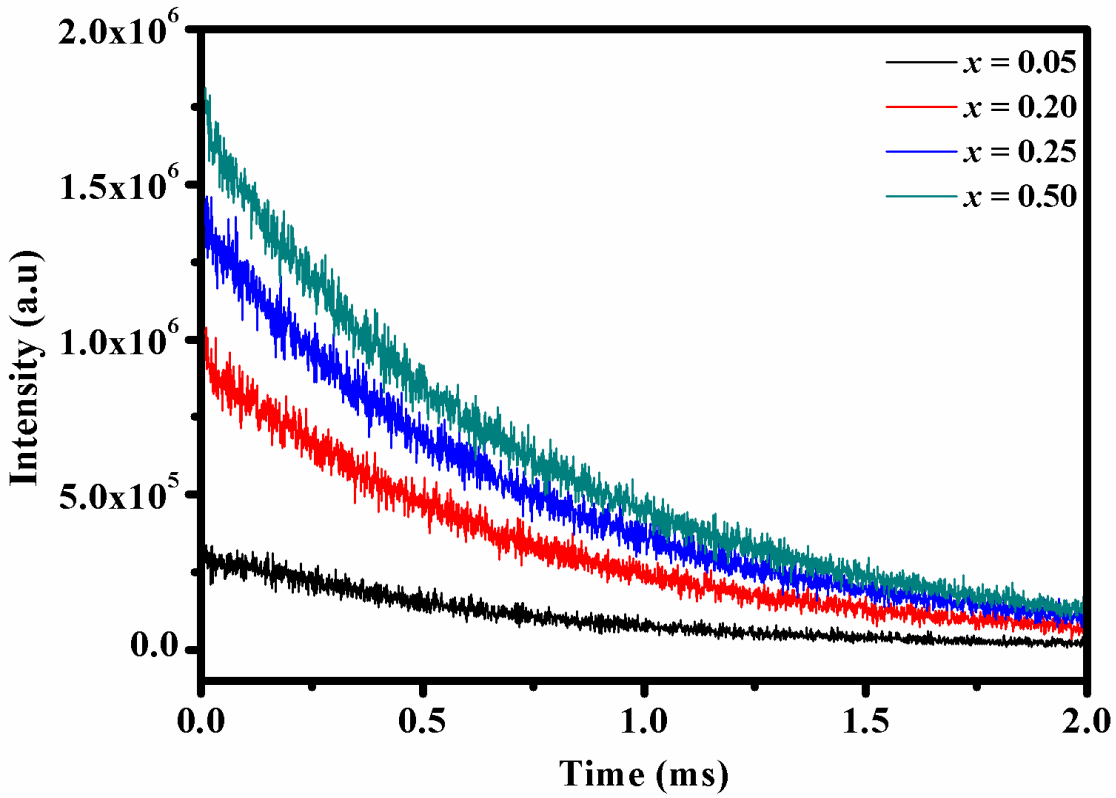

Fig. 4.19 Life time decay curves of $Y_2Ce_{2-x}O_7$:xEu^{3+} (x = 0.05, 0.20, 0.25 and 0.50) under 466 nm excitation.

Fig. 4.19 shows the decay curves for the $^5D_0$–$^7F_2$ (λ_{em} = 612 nm) transition of $Y_2Ce_{2-x}O_7$:xEu^{3+} (x = 0.05, 0.20, 0.25, 0.50) phosphors with excitation at 466 nm. All the decay curves can be well fitted with the single exponential function I = A exp(-x/τ) where I, τ and A are the intensity, decay time and fitting parameter, respectively. Table 4.3 lists the luminescence decay time of the red emission (612 nm) of $Y_2Ce_{2-x}O_7$:xEu^{3+} (x = 0.05, 0.20, 0.25, 0.50) phosphors. The lifetime of the $^5D_0$ excited state is mainly a result of the radiative and non-radiative decay rates. As the Eu^{3+} content increases, the mean lifetime increases steadily with excitation as a result of the partition of more Eu^{3+} ions into the yttrium cerate lattice due to cation ordering. The quantum efficiency was calculated from the lifetime values (Procedure is given in the Chapter 2) and was in the range 10–14% with increasing Eu^{3+} concentrations (Table 4.3). These values are slightly better than those for the well known Eu^{3+}-doped $CaMoO_4$ (Linda et. al 2014).

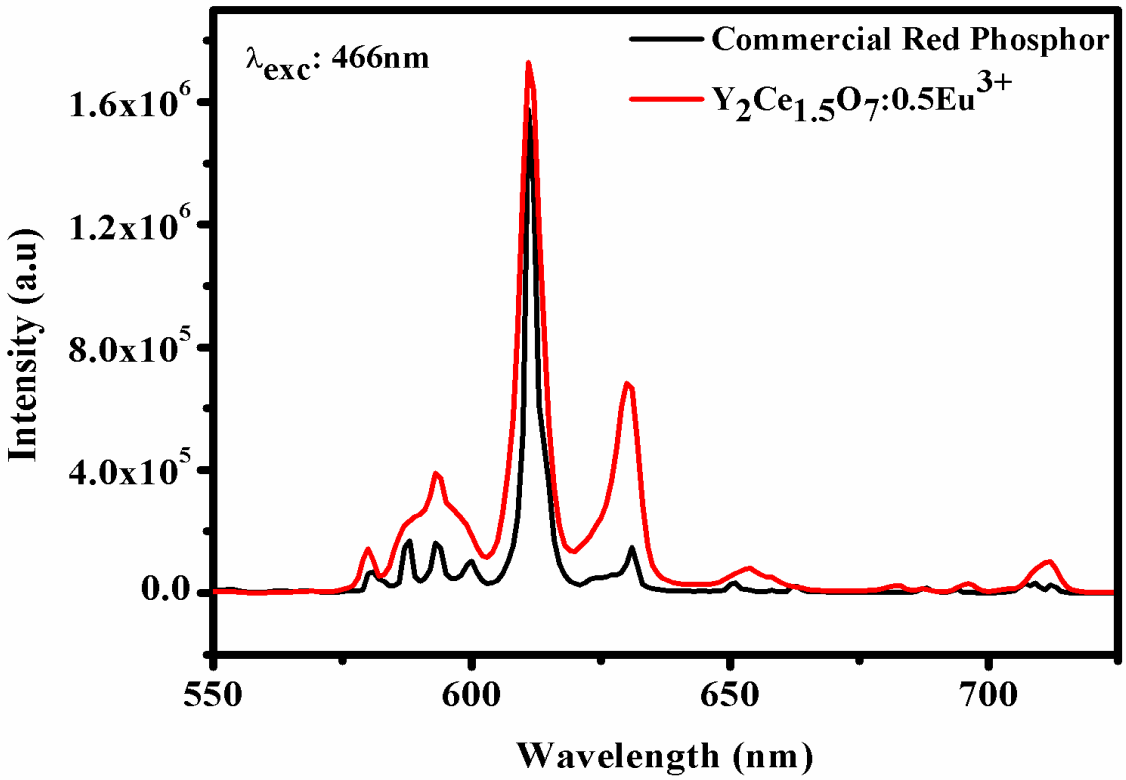

Fig. 4.20 Comparison of emission spectra of the Commercial red phosphor and $Y_2Ce_{1.5}O_7$:*0.5*Eu^{3+} under 466 nm excitation.

For the application of red phosphors in white LEDs with blue GaN-based chips as the excitation source, the emission spectra of $Y_2Ce_{1.5}O_7$:0.50Eu^{3+} and the commercial red phosphor (Y_2O_3:Eu^{3+}) from Philips were compared using the same excitation wavelength of 466 nm (blue region) (Fig. 4.20). It is observed that the red emission intensity of $Y_2Ce_{1.5}O_7$:0.50Eu^{3+} is slightly larger than that of the commercial red phosphor. This clearly demonstrates that $Y_2Ce_{1.5}O_7$:0.50Eu^{3+} is a promising red phosphor under blue light excitation for the phosphor-converted white LEDs.

4.4 Conclusions

A new series of red phosphor materials: $Y_{1.9}Ce_2O_7$:0.1Eu^{3+}, $Y_2Ce_{1.9}O_7$:0.1Eu^{3+} and $Y_2Ce_{2-x}O_7$:*x*Eu^{3+} (*x* = 0.05, 0.10, 0.15, 0.20, 0.25, 0.50) were prepared by a conventional solid-state route. The substitution of Eu^{3+} at the Ce^{4+} site induced a structural transition from a defect fluorite structure to a C-type structure, whereas substitution at the Y^{3+} site showed a biphasic nature of defect fluorite and C-type structures. The structural transition enhanced the Eu^{3+} luminescence as a result of increased oxygen vacancy ordering, a reduction in the Ce^{3+} oxidation states and distortion of the environment. The structural transition also allowed an increased Eu^{3+} doping concentration without quenching (up to 50 mol%) and increased lifetime; these are mainly attributed to the uniform distribution of Eu^{3+} ions in the lattice due to cation ordering linked with oxygen vacancy. This study suggests that sizeable Eu^{3+} luminescence in a Ce-based lattice can be achieved under blue light excitation, which matches well with the emission of commercial GaN LED (440–470 nm) chips. These phosphors are therefore suitable as promising red phosphors under blue light excitation for application in white LEDs.

Chapter 5

Pigments based on terbium doped lanthanide cerate with high NIR reflectance for cool roof and surface coating applications

A new class of intense red pigments with enhanced near infrared (NIR) reflectance of lanthanide cerate are obtained by the substitution of terbium ions into the cerium site of $A_2Ce_2O_7$ (A = La, Sm, Gd & Y) without any toxic metal ions like cadmium, lead, cobalt etc. The Tb substitution extends the absorption edge to longer wavelengths by introducing an additional electronic level between the valence band and conduction band leading to various red colors by fine tuning the band gap from ~ 3.11 eV (ivory white) to 1.87 eV (red). The terbium doped $Y_2Ce_2O_7$ displayed intense red color (a = 26) with high near infrared reflectance (80%). The applicability studies of these pigments in polymer matrix (poly methyl methacrylate), cement slab, asbestos sheet and ceramic glazes exhibited good coloring performance with high near infrared reflectance. These results demonstrate the synthesized pigments as potential near infrared reflective candidates for cool roof and surface coating applications.*

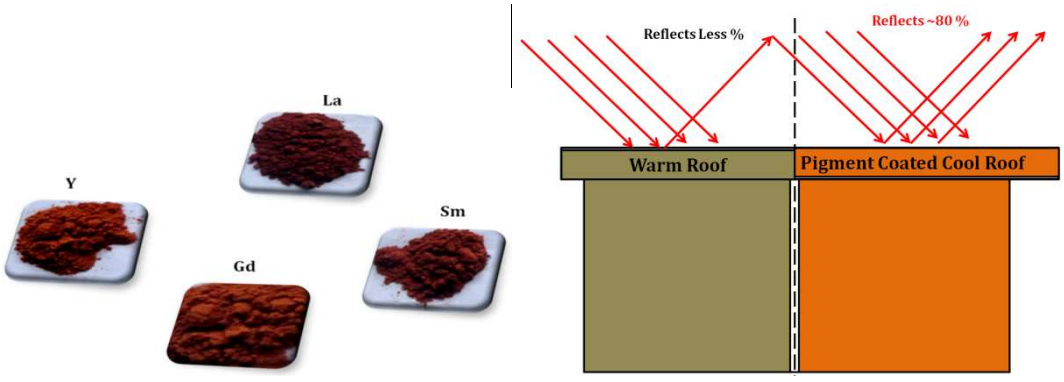

Athira et al. ***Dyes Pigm.,*** *122,* ***2015,*** *116-125.*

5.1. Introduction

Inorganic pigments with high NIR reflectance are in great demand for exterior coloring applications on roofs and walls as energy saving products. The development of such pigments is an effective means to conserve energy from the electrical power consumed in cooling buildings and automotives. Air-conditioning energy saving can be achieved by reducing the temperature of the building envelop which in turn reduces the heat penetrating into the building or any surface. Building roof and exterior surface temperatures can be reduced by covering materials which prevents the heat penetration into the building or surfaces. Recent times, colored pigments with high NIR reflectance gained a lot of importance to serve the purpose of reducing the heat build up of mainly urban areas in addition to their aesthetic look. Consequently they have been widely used for coatings on roofs and walls. Conventional inorganic pigments for the above applications contain heavy metals such as cadmium, cobalt, chromium, lead, antimony or selenium (Jansen et al. 2000), that can unfavourably affects the environment and human health when decisive levels are exceeded (Kumari et al. 2008). Further, currently developed red pigments are not well explored for their NIR reflecting properties. Hence, the development of red ceramic pigments with high NIR reflectance along with high temperature stability is of great importance to ceramic industry for the conservation of energy.

The industrially available red pigments are almost fatigued by the following systems: $Al_2O_3:Cr^{3+}$ (corundum), $ZnAl_2O_4:Cr$, $CaSnSiO_5:Cr^{3+}$ (sphene), $MnAl_2O_4:Cr^{3+}$ (spinel), $ZrSiO_4:Fe^{3+}$ (zircon) and CdS: CdSe (greenockite) and $Y_2Sn_{2-x}Cr_xO_{7-\delta}$ (Eppler et al. 1994). The cadmium based pigments give superior red shades in which toxic cadmium can enter the environment in a bioavailable form through waste-disposal sites and incineration plants (Buxbaum et al. 1997). This toxicity issue has led to restrictions, based on the precautionary measures that strongly limit the use of cadmium, lead and chromium based pigments whereas the Fe_2O_3 included in a zircon matrix is also limited due to the lack of sufficient color purity and reproducibility (Llusar et al. 2001). Since there is no alternative to inorganic pigments for mass coloration of materials such as glasses, glazes and ceramic bodies, inorganic pigments which are free from toxic elements are in high demand for decorative and protective coating applications (Pavlov et al. 2002). The rare earth element offers an enormous opportunity for developing environmentally

secure alternatives. The unique electronic configuration of partially filled f orbitals of the rare earths shows unusual magnetic and optical properties (Sreeram et al. 2008). The pigments derived from the rare earths show their characteristic intense color due to charge transfer interaction between a donor and an acceptor with the metal ion playing generally the role of an acceptor. Dopants based on rare earth elements in mixed oxide systems offer an opportunity to tune the color response through manipulation of energy gaps and delocalization phenomenon in conduction and valence bands (Silversmith et al. 2006).

Cerium dioxide, commonly known as "ceria", has established its role as one of the most promising material for environment and energy applications (Melchionna et al. 2014). Pigments based on cerium dioxide are less known and recently a few studies were reported as potential red pigments. In response to growing concerns challenging environmentally benign and commercially viable ceramic pigments, CeO_2 and ceria-based solid solutions have become interesting because of its low-toxicity, opacity and high temperature stability alternatives to other traditionally used orange-red ceramic pigments. Pr-doped ceria is employed in the ceramic industry since 1960 as red ceramic pigment and was first reported in French patent (Rhone et al. 1960) and it gives various pink-orange to red-brown hues, depending on the quantity of praseodymium incorporation into the CeO_2 host lattice and synthesis temperature. During the course Pr-doped CeO_2 system has been extensively studied as ceramic pigments by various synthesis routes by different authors (Kumari et al. 2012; Sulcova et al. 2003; Bonbioli et al. 2005; Nahum et al. 2003; Aruna et al. 2001). Similarly Tb doped CeO_2 based ceramic pigments have also been studied which yielded good red hues (Llusar et al. 2010; Sulcova et al. 2008; Sulcova et al. 2010). However, the studies about synthesis optimization and pigmenting properties of Tb-doped ceria are still inadequate, since most of the research concerning this system is focused on catalytic or redox properties. However, in all the above compounds the coloristic performance is not adequate and their NIR reflectance has not been investigated. Hence developing novel red colored with high NIR reflective inorganic pigments become an important issue. Thus further studies are still needed to optimize the NIR reflectance and color properties of CeO_2 based red pigments, which could be an interesting alternative to the existing Pr/Tb doped CeO_2 system.

Recently $Y_2Ce_2O_7$ which is considered as a promising optical material with a band gap of 3.11 eV close to cerium oxide and its molybdenum, iron, erbium and europium doped compositions have been investigated for pigment and phosphor materials (Vishnu et al. 2011; Zhao et al. 2013; Jiang et al. 2013). In this context, we synthesized a cerium oxide based host lattice with the general formula $A_2Ce_2O_7$ (A = La, Sm, Gd & Y) and terbium was substituted in Ce^{4+} site via a conventional solid state method to obtain a new class of red, less-toxic pigments possessing NIR reflectance. Further, to understand the effect of the terbium concentration, the pigmentary properties of the as-prepared $Y_2Ce_{2-x}O_7$:xTb (x = 0, 0.20, 0.40, 0.60, 0.80 and 1.0) were also studied in detail. The properties of these pigments to confer high red hue as well as high NIR reflectance have also been evaluated in this chapter. The structure, morphology, optical and coloristic properties of the prepared powders were characterized by powder X-ray diffractometer (XRD), FT-Raman spectroscopy, scanning electron microscope (SEM) with energy dispersive spectrometry (EDS), UV-vis NIR Spectroscopy and CIE 1976 L*a*b* color scales.

5.2 Experimental

5.2.1 Materials and Methods

The lanthanide cerate-based pigments with a general formula: $A_2Ce_{1.6}O_7$:0.4Tb (A = La, Sm, Gd & Y) and $Y_2Ce_{2-x}Tb_xO_7$ (x = 0, 0.2, 0.4, 0.6, 0.8, and 1.0) were synthesized by the conventional solid-state route. The raw materials, La_2O_3, Sm_2O_3, Gd_2O_3, Y_2O_3, CeO_2, and Tb_4O_7 (Sigma Aldrich, 99.99% purity) were weighed in stoichiometric ratio and homogenized by wet mixing with acetone in an agate mortar until fine slurry was obtained. The slurry was dried by placing it in an air oven at a temperature of 100°C. The mixing and drying was repeated thrice to obtain a homogenous mixture. The homogeneous mixture was then calcined in platinum crucibles in an electric furnace at 1500°C for 12 h. The temperature of the furnace is programmed with an initial heating rate of 10 °C /min up to 900°C followed by a heating rate of 5 °C /min to attain 1500 °C.

5.2.2 Characterization

The crystalline structure of the calcined powders were characterized by means of X-ray powder diffraction (XRD) using a Nifiltered Cu-K_α radiation with a PANalytical X'pert Pro diffractometer operated at 45 kV and 30 mA. Data were

collected from 10 to 90° 2θ range with a step size of 0.016°. The Raman spectra of the powder samples were acquired using an integrated micro-Raman system of a Labram HR 800 spectrometer (Horiba Scientific) using a 784 nm helium neon laser with a spatial resolution of 2 mm to record the spectra of the powdered samples. Particle morphological analysis of the powder was performed by means of a scanning electron microscope with a JEOL JSM-5600 LV SEM with an acceleration voltage of 15 kV. The X-ray microchemical analysis and elemental mapping of the samples were carried out using a silicon drift detector -X-Max^N attached with a Carl Zeiss EVO18 SEM. The particle size analysis of the samples was analysed in water medium with calgon as the dispersing agent using the PSA MALVERN Zetasizer Nano Series particle size analyser. The UV-vis NIR spectra of the pigments were recorded by a Shimadzu, UV-3600 spectrometer through diffuse reflectance technique using polytetrafluoroethylene (PTFE) as a reference. The tauc plot was employed to estimate band gap energies (E_g) of the synthesized samples from diffuse reflectance data which was used to calculate the absorption coefficient from the Kubelka-Munk (KM) function (Kubelka et al. 1931; Kortum et al. 1969) defined as:

$$F(R_\infty) = \alpha/S = 1 - (R_\infty)^2/2\,R_\infty \quad (5.1)$$

where $R_\infty = R_{sample}/R_{PTFE}$. Here α is the absorption coefficient, S is the scattering coefficient, and $F(R_\infty)$ is the KM function. The energy dependence of semiconductors near the absorption edge is expressed as:

$$\alpha h\nu = K(E - E_g)^\eta \quad (5.2)$$

Here E is the incident photon energy (hν), E_g is the optical absorption edge energy, K is a constant, and the exponent η is dependent on the type of optical transition as a result of photon absorption (Barton et al. 1999). The band gap can be evaluated using tauc plot by extrapolating the linear portion of $(F(R_\infty)h\nu)^2$ versus (hν) and the intercept of the line on the abscissa $(F(R_\infty)h\nu) = 0$ gives the value of optical absorption edge energy. The NIR solar reflectance is expressed as the integral of the present reflectance times the solar irradiance divided by the integral of the solar irradiance when integrated over 700-2500 nm range in the formula,

$$R = \frac{\int_{700}^{2500} r(\lambda)\, i(\lambda) d\lambda}{\int_{700}^{2500} i(\lambda) d\lambda} \quad (5.3)$$

where r(λ) is the spectral reflectance obtained from the experiment and i(λ) is the standard solar spectrum (Wm^{-2} mm^{-1}). The NIR solar reflectance was determined from ASTM Standard G173-03. The color parameters of the pigments were determined by UVPC color analysis software coupled to the UV-3600 spectrophotometer at the measurement conditions kept as an illuminant D65, 10° complementary observer and measuring geometry d/8°. The CIE1976 $L^*a^*b^*$ colorimetric method was used as recommended by the Commission Internationale del' Eclairage (CIE). In this system, L^* is the color lightness (0 for black, 100 for white), a^* is the green (-)/red (+) axis, and b^* is the blue (-)/yellow (+) (Johnston et al. 1973). The chroma is defined as $C^* = [(a^*)^2 + (b^*)^2]^{1/2}$. The hue angle, h° is expressed in degrees and ranges from 0° to 360° and is calculated using the formula $h° = \tan^{-1}(b^*/a^*)$.

5.2.3 Application Studies

To evaluate the red hue consistency and the NIR reflectance of the synthesized pigment for various applications, we estimated the color characteristics on various substrates such as in the coloration of plastics, cement slabs, asbestos cement sheet and in ceramic glaze. The typical $Y_2Ce_{1.8}Tb_{0.2}O_7$ red pigment that exhibited better chromatic properties as well as reflectance was selected for the studies. For the coloration of plastics, Poly(methyl methacrylate) (PMMA) was used as the polymer matix for making the pigmented compact. PMMA is a well known water soluble polymeric material extensively used for cold extrusion of many inorganic oxides such as alumina and zirconia. A viscous solution of PMMA (90 wt %) was made using a conventional electric coil heater and 10 wt% of the pigment was slowly added with stirring and converted to a thick paste. The paste was then transferred in a mould and compressed into a cylindrical disc. The particular pigment was selected to prepare NIR reflecting coatings on a building roofing material like asbestos cement sheet (made up of small amounts of asbestos fibres locked in cement slurry) as well as the cement slab with and without TiO_2 base coat. The coating was undertaken in a two-step process. In the first step, the substrate surfaces are pre-coated with TiO_2, an inexpensive white pigment possessing high NIR reflectance. In the second step, the designed typical pigment is applied to the pre-coated substrate materials. The pigment samples were ground and was

ultrasonicated (Vibronics, 250W, India) for 10 min to ensure the complete dispersion of the pigment particles in acrylic acid using polyurethane as a binder. The resulted viscous solution was coated on the substrate surfaces and was allowed to dry in an oven at 150 °C.

The scope of the application of the typical pigment synthesized in the present research is further studied on reflective coating such as ceramic glaze. In the preparation of reflective coating, the typical $Y_2Ce_{1.8}Tb_{0.2}O_7$ red pigment powder was divided into three different groups. Each group was then mixed with ceramic glaze (Pb free) in the ratio 1:5, 2:5 and 3:5 respectively. The mixtures were ground in water by a ball mill for 20 min at a speed of 100 rpm to obtain very homogenous slurry. The prepared samples were coated on the clay tile. The coated clay tile substrate was heated at an initial heating rate of 10 °C/min up to 500 °C followed by a heating rate of 5 °C/min to attain the desired temperatures i.e 900 °C, 1000 °C and 1100 °C and then soaked for 3 h. The pigmented glazes were evaluated for the color and NIR reflectance.

5.3. Results and discussion

5.3.1 Pigmentary properties of terbium doped $A_2Ce_{1.6}O_7$:0.4Tb (A = La, Sm, Gd & Y) red pigments

5.3.1.1 Powder X-Ray diffraction studies

Powder X-ray diffraction patterns of $A_2Ce_{1.6}O_7$:0.4Tb (A = La, Sm, Gd & Y) are shown in Fig. 5.1. The intense and sharp peaks found in the diffraction patterns reveal the crystalline nature of the powders. It was found that both $La_2Ce_{1.6}O_7$:0.4Tb and $Sm_2Ce_{1.6}O_7$:0.4Tb are attributed to the cubic defect fluorite structure and all the diffraction peaks are well matching with the JCPDS File no: 01-071-4807. Similarly, it was noticed that both the $Gd_2Ce_{1.6}O_7$:0.4Tb and $Y_2Ce_{1.6}O_7$:0.4Tb crystallizes in cubic C-type structure all the diffraction peaks are well matching with the JCPDS File no: 01-074-7393 (Table 5.1). Earlier reports on lanthanide doped ceria reveals that the bigger ions like La and Sm repels the oxygen vacancy and allows the formation of cubic O_h symmetry while the smaller ions like Gd and Y trap the oxygen vacancy and losing its O_h symmetry (Sorbella et al. 2014).

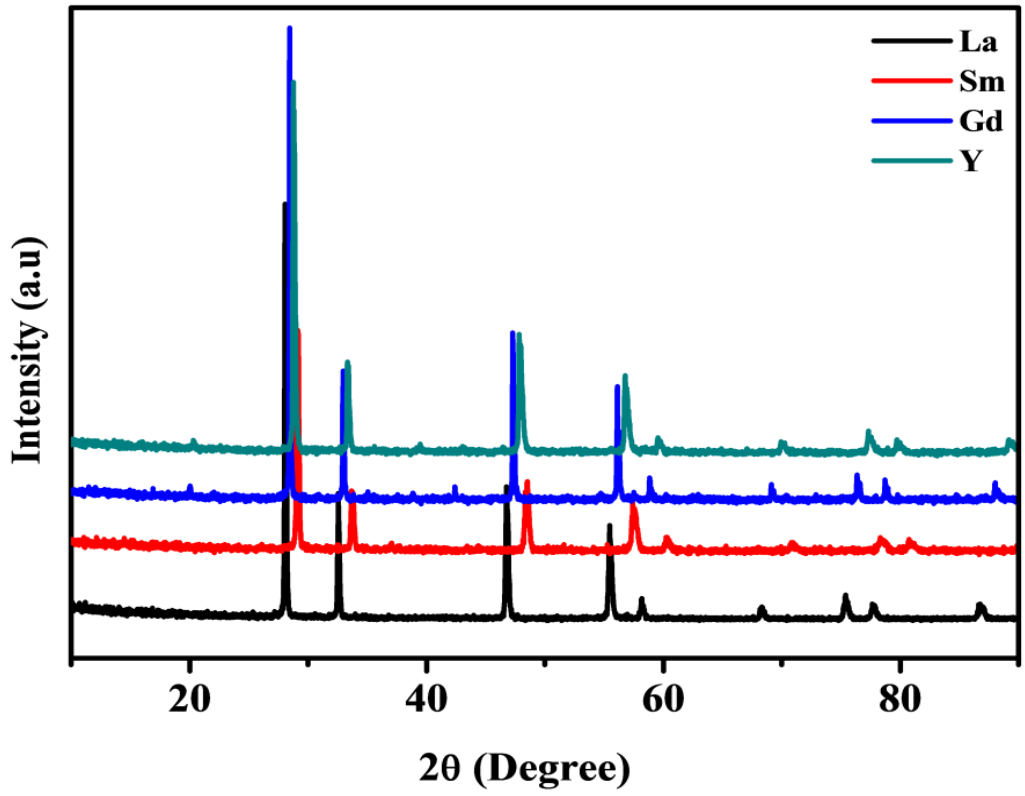

Fig. 5.1 Powder X-ray diffraction patterns of $A_2Ce_{1.6}O_7$:0.4Tb (A = La, Sm, Gd & Y).

Table 5.1 Crystal structure and space group of $A_2Ce_{1.6}O_7$:0.4Tb (A = La, Sm, Gd & Y).

Composition	Crystal Structure	Space group
$La_2Ce_{1.6}O_7$:0.4Tb	Cubic	Fm-3m
$Sm_2Ce_{1.6}O_7$:0.4Tb	Cubic	Fm-3m
$Gd_2Ce_{1.6}O_7$:0.4Tb	Cubic	I-a3
$Y_2Ce_{1.6}O_7$:0.4Tb	Cubic	I-a3

5.3.1.2 Morphological studies

Typical scanning electron micrographs of the four samples $A_2Ce_{1.6}O_7$:0.4Tb (A = La, Sm, Gd & Y) are given in Fig. 5.2. All the four samples are slightly agglomerated and the particle size are in between 1 – 2 μm. The chemical composition formation was checked by energy dispersive spectrometer (EDS) analysis attached with SEM. Fig. 5.3 shows the EDS micro-chemical analysis of $A_2Ce_{1.6}O_7$:0.4Tb (A = La, Sm, Gd &

Y) samples and identifies the presence of all the expected elements. This also further confirms the homogeneity of the phase formed. Elemental X-ray dot mapping analysis of typical red pigments are shown in Fig. 5.4. This mapping shows that all the elements are uniformly distributed in the sample.

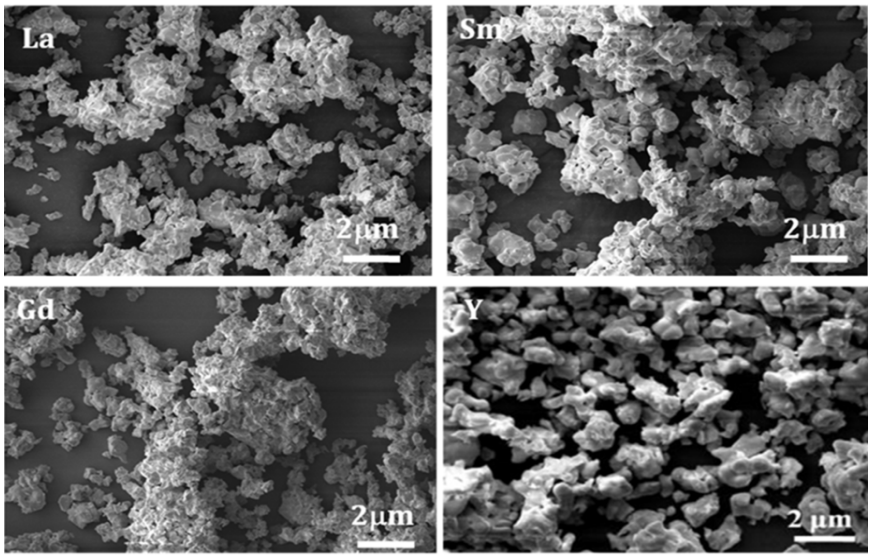

Fig. 5.2 Scanning electron micrographs of $A_2Ce_{1.6}O_7$:0.4Tb (A = La, Sm, Gd & Y) samples.

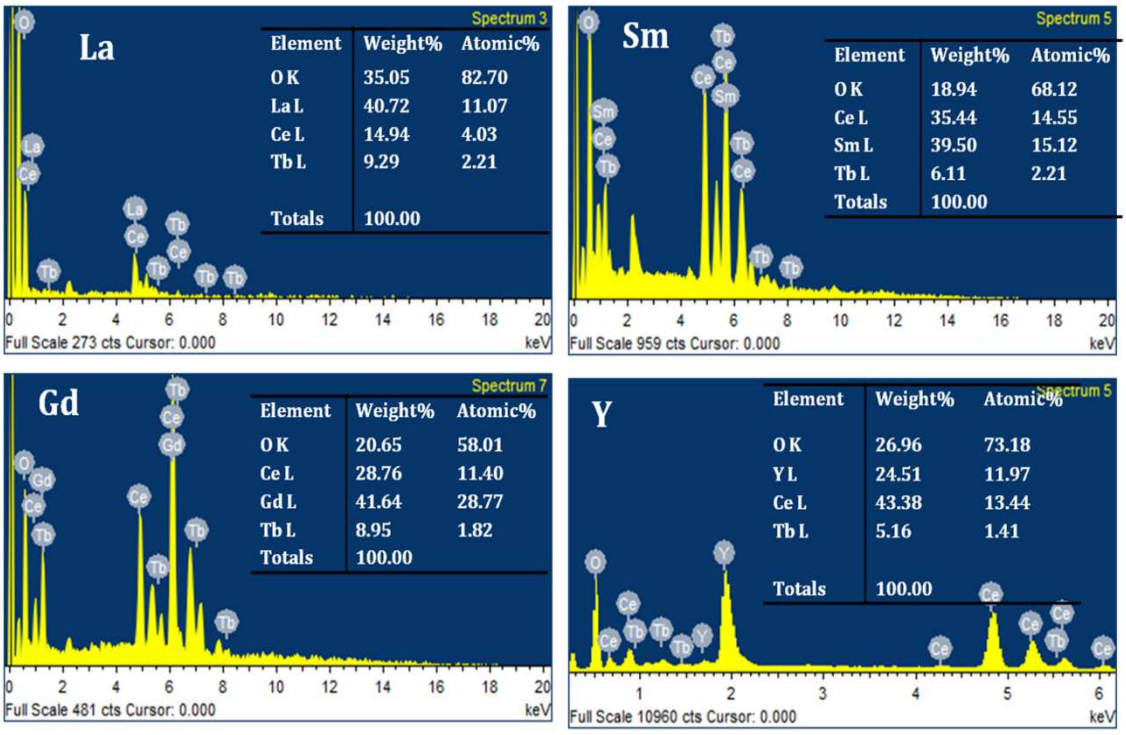

Fig. 5.3 EDS spectra of $A_2Ce_{1.6}O_7$:0.4Tb (A = La, Sm, Gd & Y) samples.

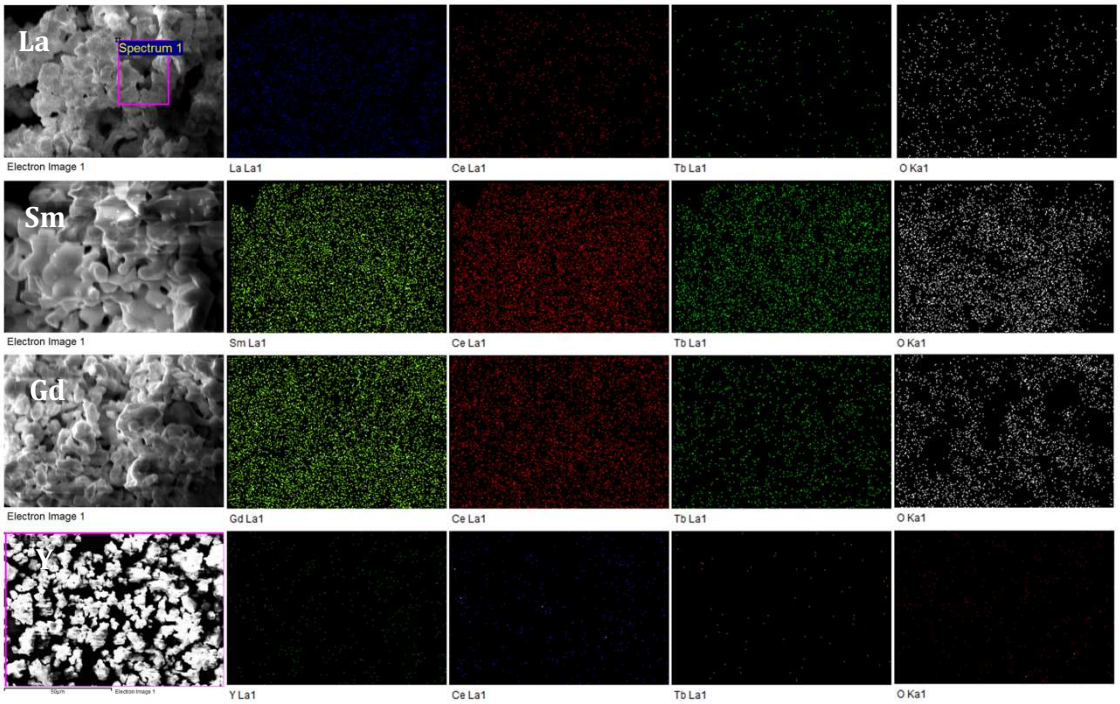

Fig. 5.4 Elemental dot mapping of $A_2Ce_{1.6}O_7$:0.4Tb (A = La, Sm, Gd & Y) samples.

5.3.1.3 UV-vis NIR spectroscopic studies

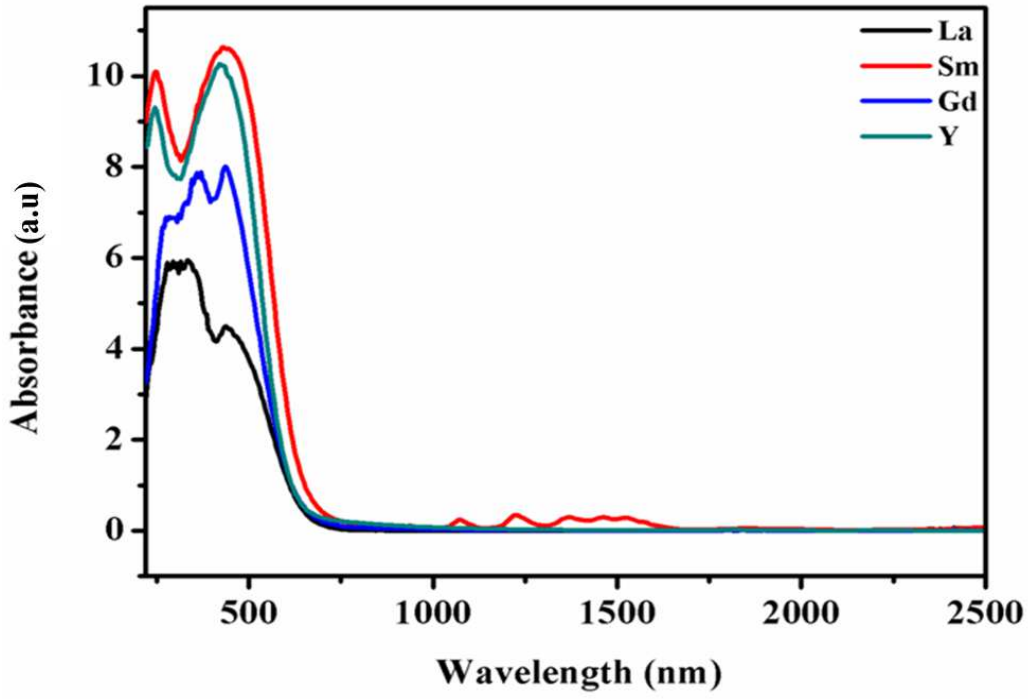

Fig. 5.5 Absorption spectra of $A_2Ce_{1.6}O_7$:0.4Tb (A = La, Sm, Gd & Y) samples.

The absorption spectra of the $A_2Ce_{1.6}O_7$:0.4Tb (A = La, Sm, Gd & Y) samples in the UV-vis-NIR region are displayed in Fig. 5.5. In lanthanide cerate doped red

pigments, the coloring mechanism is based on the shift of the charge transfer band of O (2p) to Ce (4f) by introducing an additional electronic level by doping terbium. By Tb doping in $A_2Ce_2O_7$, the 4f electrons of terbium valence shell introduce an additional electronic level of energy between the O^{2-} valence band and Ce^{4+} conduction band and the band gap was calculated and listed in Table 5.2. All the samples show a strong absorption band below the wavelengths of 600 nm and producing a red color.

NIR reflectance spectra of the newly developed pigments recorded in the range 200 to 2500 nm are shown in Fig. 5.6. All the synthesized pigments show high NIR reflectance value over the whole range except some weak absorption rare earth absorption bands at lower energies. In the reflectance spectra all the compounds display a remarkable reflectance in the range 57 – 92% which is high to reflect almost all the sun radiation energy NIR region and the $La_2Ce_{1.6}O_7$:0.4Tb sample posses high NIR reflectance value of 92.41%.

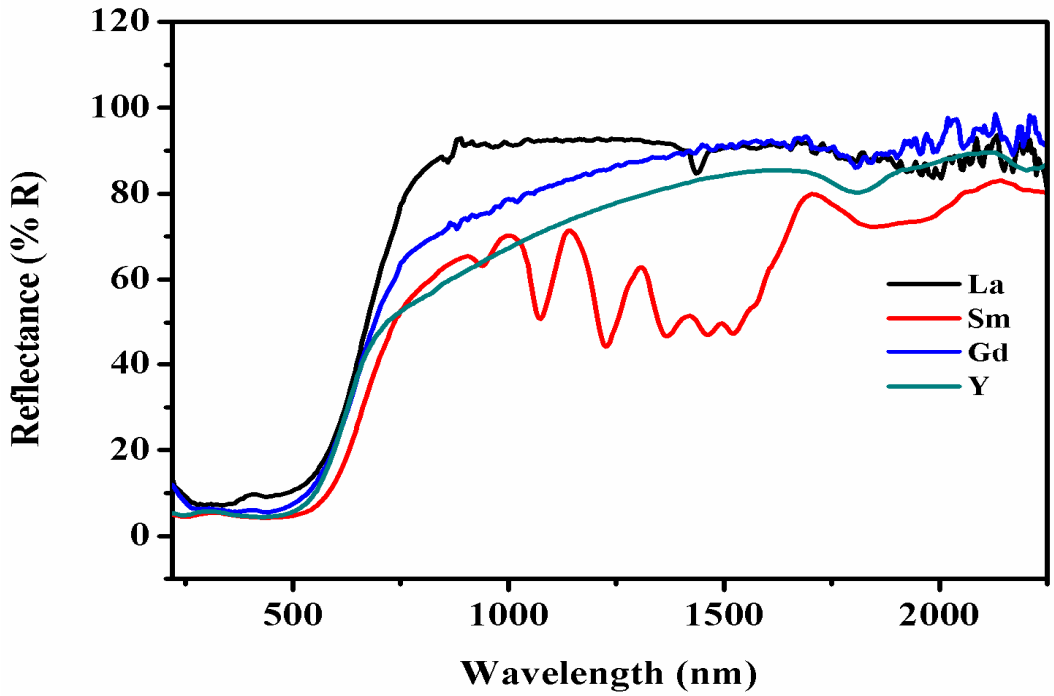

Fig. 5.6 Reflectance spectra of $A_2Ce_{1.6}O_7$:0.4Tb (A = La, Sm, Gd & Y) samples.

5.3.1.4 Color performance

The chromatic properties of the $A_2Ce_{1.6}O_7$:0.4Tb (A = La, Sm, Gd & Y) pigments can be numerically expressed in terms of color co-ordinates from their CIE 1976 color coordinate values and are listed in Table 5.2. All the sample posses good

red hue with Tb doping and the typical terbium doped yttrium cerate posses high red (a^* = 25.58). Further, the red hues of the synthesized pigments are significantly higher than the commercially available brown pigment (BR 300), (L^* = 34.91, a^* = 11.38, b^* =9. 86) of Kawamura Chemicals Co. Ltd. Japan. The hue angle values reveal that the terbium doped lanthanide cerate pigments lie in the reddish brown region of the cylindrical color space. The photographs of the synthesized pigments are shown in Fig. 5.7. Since the $Y_2Ce_{1.6}O_7$:0.4Tb sample shows enhanced pigmentary properties and hence further investigations were confined to $Y_2Ce_{2-x}O_7$:xTb with respect to the variation of Tb concentration.

Table 5.2 Color coordinates, band gap and reflectance values of the $A_2Ce_{1.6}O_7$:0.4Tb (A = La, Sm, Gd & Y) pigments.

x	***L***	***a****	***b****	***C****	***h*^{0}**	***Eg*** **(eV)**	**R %**
La	52.95	20.15	26.24	33.08	52.47	1.90	92.41
Sm	41.4	19.86	23.38	30.68	41.4	1.87	57.79
Gd	50.13	19.94	33.26	38.78	59.05	1.90	82.47
Y	**43.08**	**25.58**	**27.04**	**37.23**	**46.58**	**1.91**	72.32

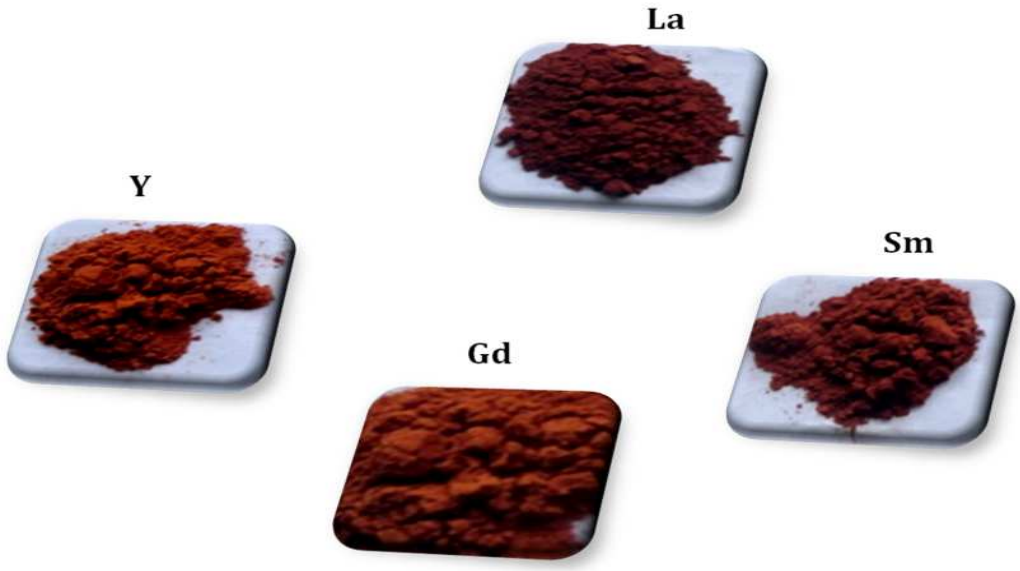

Fig. 5.7 Photographs of the $A_2Ce_{1.6}O_7$:0.4Tb (A = La, Sm, Gd & Y) pigments.

5.3.2 Pigmentary properties of $Y_2Ce_{2-x}Tb_xO_7$ (x = 0, 0.2, 0.4, 0.6, 0.8, and 1.0) red pigments

5.3.2.1 Powder X-Ray diffraction studies

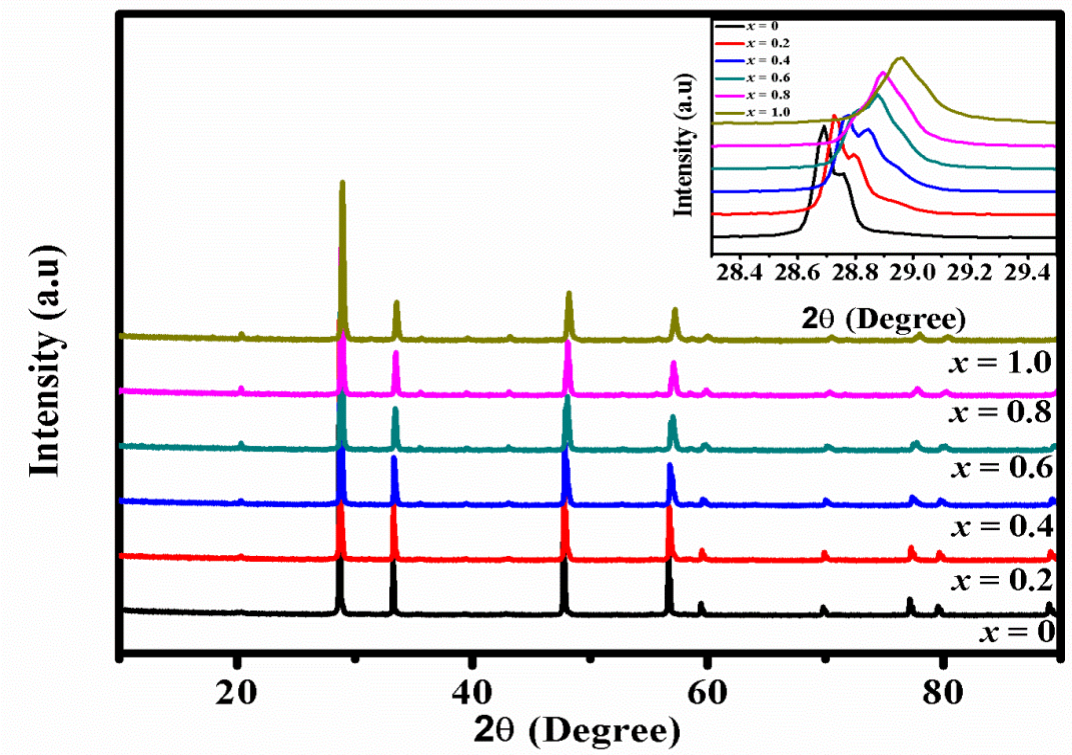

Fig. 5.8 Powder X-ray diffraction patterns of $Y_2Ce_{2-x}Tb_xO_7$ (x = 0, 0.2, 0.4, 0.6, 0.8, and 1.0) red pigments. The inset figure shows the expanded XRD of the peak around 2θ 28.2 - 29.2°.

The crystallinity, phase purity and crystallite size of the $Y_2Ce_{2-x}Tb_xO_7$ (x = 0, 0.2, 0.4, 0.6, 0.8, and 1.0) red pigments can be analyzed from the powder diffraction patterns and it is shown in Fig. 5.8. The intense and sharp peaks found in the diffraction patterns reveal the crystalline nature of the powder. The XRD analysis confirms these oxides crystallizing into rare earth C-type structure. In reference to the powder diffraction file no. 01-074-7393, all the diffraction lines were successfully indexed to the rare earth C-type phase with a space group *Ia3* (Z = 16). The C-type structure can be recognized as an F-type structure with ordered oxygen vacancies in the anionic sub-lattice (Nishino et al. 2004). As the terbium concentration increases, the intensity of C-type reflections are more prominent. This result is in agreement with the reported literature as heavily doped higher ionic radii for cerium strongly influence the structural transformation from a fluorite to a

C-type structure (Coduri et al. 2013). The introduction of terbium into $Y_2Ce_2O_7$ slightly shrinks the lattice, which is evident from the shift in diffraction peaks to higher 2θ angle in comparison with the host (Inset of Fig. 5.8). Ce ion can exist in two different oxidation states of 3+ and 4+ having ionic radii of 0.1143 and 0.097 nm in 8 CN respectively, whereas Tb can also exist in 3+ and 4+ having ionic radii of 0.104 and 0.88 nm. The lattice parameters were refined using X-pert Highscore plus software and are given in Table 5.3. As observed the decreasing trend of lattice parameter on Tb substitution points out the presence of Tb in predominantly 4+ oxidation states based on the ionic size consideration. The crystallite size was calculated from Debye Scherrer equation and was found to decrease with increase in concentration of Tb (Table 5.3).

Table 5.3 The variation of lattice parameter and the crystallite size of the $Y_2Ce_{2-x}Tb_xO_7$ (x = 0, 0.2, 0.4, 0.6, 0.8, and 1.0) red pigments.

x	**Lattice Parameter (Å)**	**Crystallite Size (nm)**
0	10.7733	135.5
0.20	10.7576	135.6
0.40	10.7445	101.7
0.60	10.7335	101.6
0.80	10.7038	99.0
1.0	10.6830	55.0

5.3.2.2 Raman spectroscopic studies

The structure of the prepared samples was further investigated by Raman spectroscopy. Fig. 5.9 shows Raman spectra for the $Y_2Ce_{2-x}Tb_xO_7$ (x = 0, 0.2, 0.4, 0.6, 0.8, and 1.0) red pigments. The characteristic Raman modes of C-type structure are observed more prominently at 264, 323, 419, 496 and 585 cm^{-1} wavenumbers. These modes are in agreement with the reported literature for rare earth C-type phase (Ikuma et al. 2005; Mandal et al. 2007; Dilawar et al. 2008. It is further observed that the intensity of the modes decreases substantially on Tb substitution due to strong absorption of the excitation radiation because of the intense red color

development. The Raman modes around 323 and 585 cm^{-1} shifts to higher wavenumbers regularly indicating change in the Ce-O bond environment. When Ce^{4+} (0.097 nm) is substituted with Tb^{4+} (0.88 nm), the oxygen atom moves close to the metal resulting contraction in the lattice consequently increases the bond frequencies. These results are consistent with the XRD analysis.

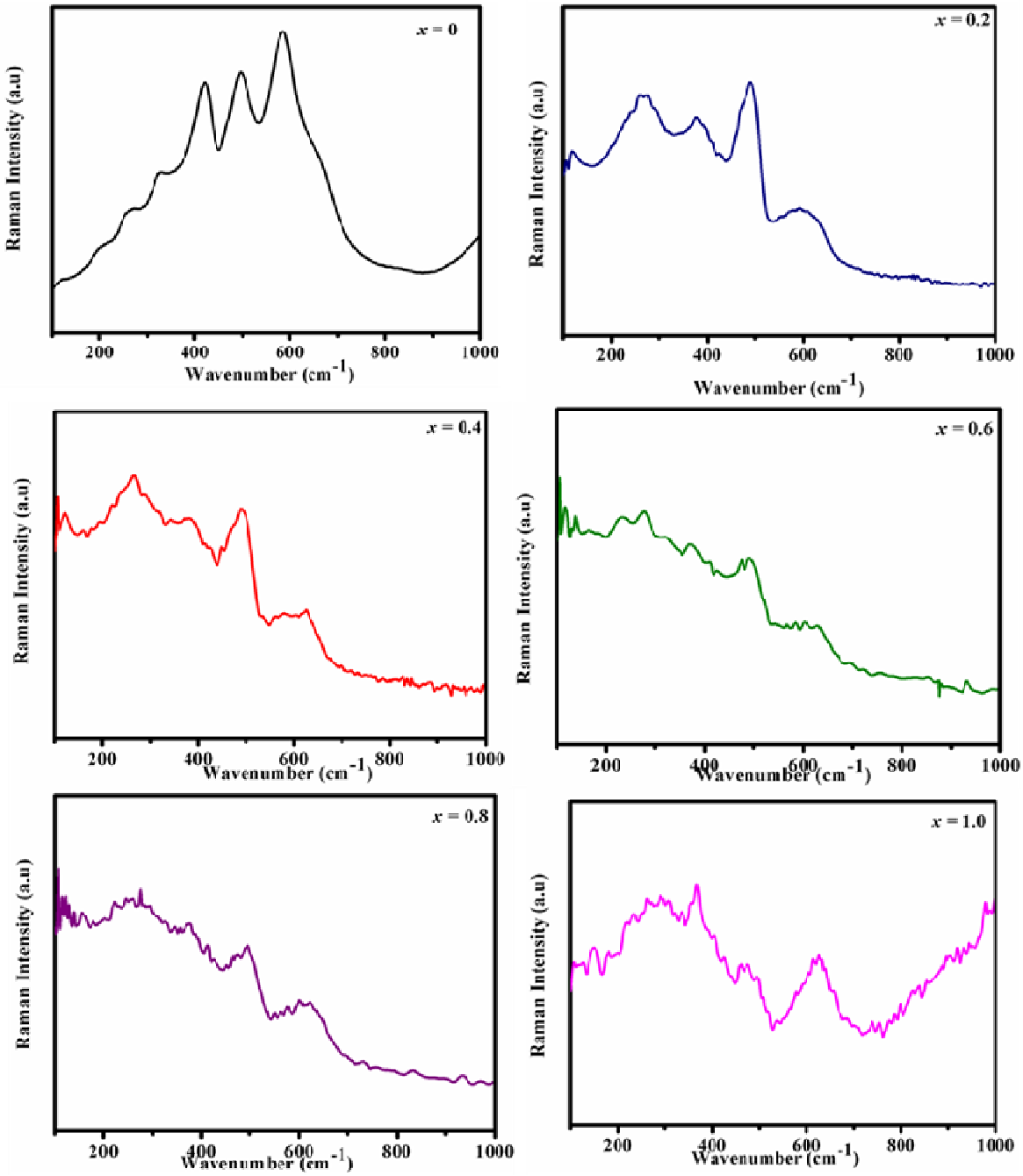

Fig. 5.9 Raman Spectra of $Y_2Ce_{2-x}Tb_xO_7$ (x = 0, 0.2, 0.4, 0.6, 0.8, and 1.0) red pigments.

5.3.2.3 Morphological and particle size studies

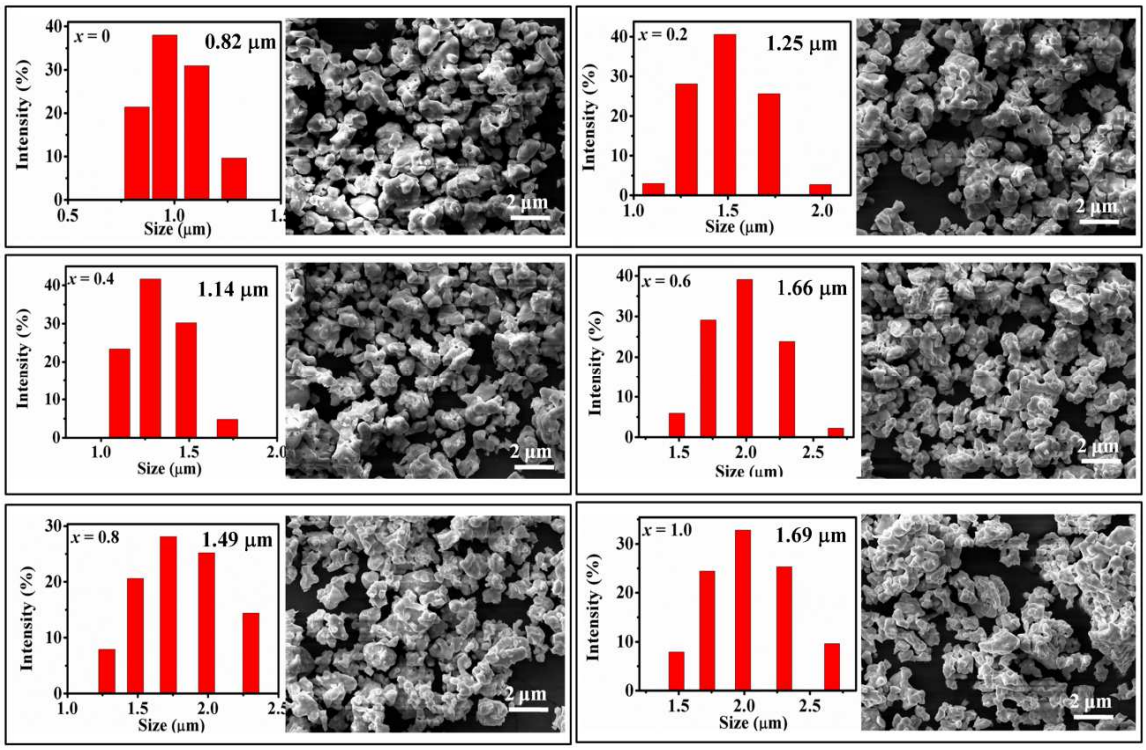

Fig. 5.10 Typical SEM images and particle size distribution of $Y_2Ce_{2-x}Tb_xO_7$ (x = 0, 0.2, 0.4, 0.6, 0.8, and 1.0) red pigments. The particles are slightly agglomerated and there is a broad distribution of particle size with an average size of 1-2 µm.

Fig. 5.10 shows the SEM micrographs and the particle size distribution of $Y_2Ce_{2-x}Tb_xO_7$ (x = 0, 0.2, 0.4, 0.6, 0.8, and 1.0) samples. The particles are slightly agglomerated with an average size of 1-2 µm. The mean particle size of the pigment powders is in the range 0.818 -1.689 µm for x = 0 to 1.0. As can be seen the particle size increases on terbium substitution with slight increasing trend in the composition range. The narrow size distribution of particles makes them suitable for pigment applications. The chemical composition formation was checked by energy dispersive spectrometer (EDS) analysis attached with SEM. Elemental X-ray dot mapping analysis of typical $Y_2Ce_{1.8}Tb_{0.2}O_7$ red pigment calcined at 1500 °C for 12 h is shown in Fig. 5.11. This mapping shows that all the elements are uniformly distributed in the lattice. Fig. 5.12 shows the EDS micro-chemical analysis of selected samples (x = 0, 0.8 and 1.0) and identifies the presence of all the expected elements. This also further confirms the homogeneity of the phase formed. The

compositions derived from the micro-chemical analysis of the pigments are in close agreement with the stoichiometry of the formulae.

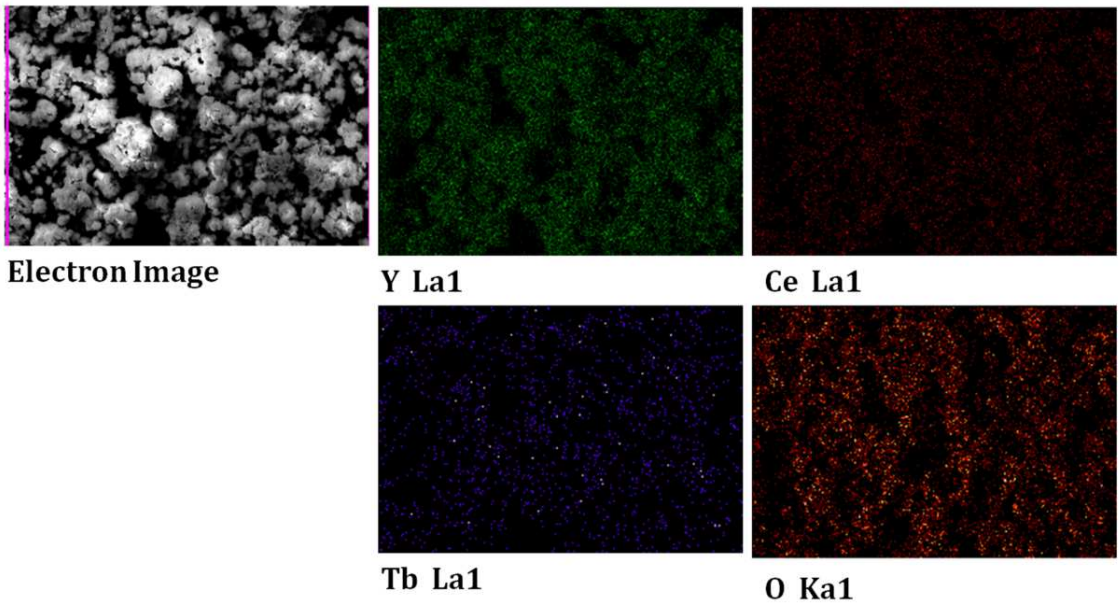

Fig. 5.11 Elemental mapping of typical $Y_2Ce_{1.8}Tb_{0.2}O_7$ red pigment and it conforms that all the elements are uniformly distributed in the lattice.

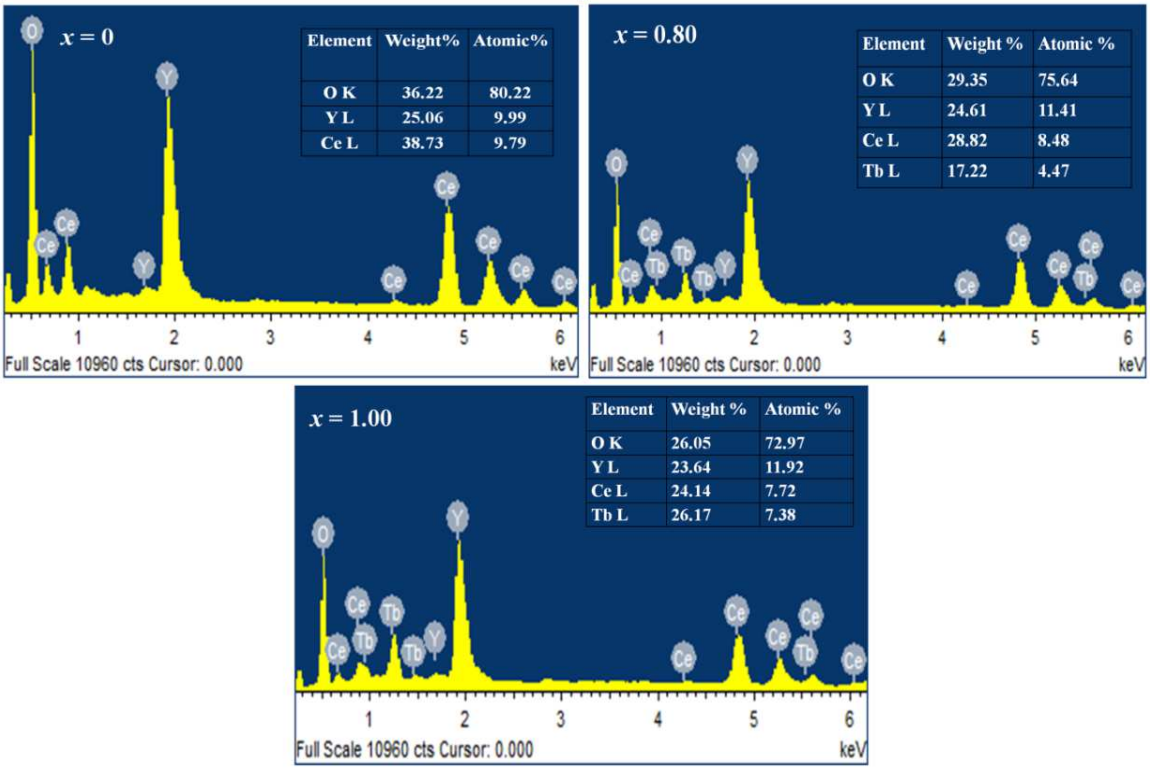

Fig. 5.12 EDS spectra of $Y_2Ce_{2-x}Tb_xO_7$ (x = 0, 0.80 and 1.0) red pigments which identifies the presence of all expected elements.

5.3.2.4. UV-vis NIR spectroscopic studies

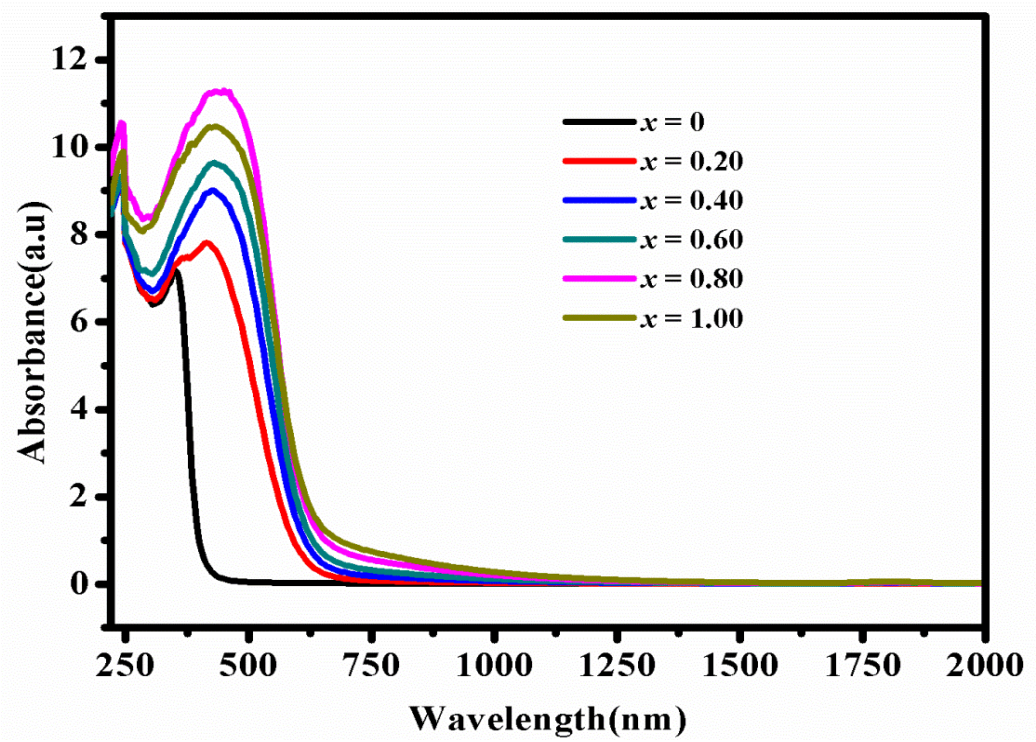

Fig. 5.13 Absorption spectra of $Y_2Ce_{2-x}Tb_xO_7$ (x = 0, 0.2, 0.4, 0.6, 0.8, and 1.0) red pigments.

The absorption spectra of the $Y_2Ce_{2-x}Tb_xO_7$ (x = 0, 0.2, 0.4, 0.6, 0.8, and 1.0) red pigments in the UV-vis-NIR region are shown in Fig. 5.13. In yttrium cerate doped red pigments; the coloring mechanism is based on the shift of the charge transfer band of O(2p)- Ce(4f) to higher wavelengths i.e. red shifting, introducing an additional electronic level by doping terbium. The UV-vis NIR reflectance spectra of $Y_2Ce_{2-x}Tb_xO_7$ (x = 0, 0.2, 0.4, 0.6, 0.8, and 1.0) red pigments are shown in Fig. 5.14 and the inset shows the corresponding Tauc plots. As it is clear from the reflectance spectra of the red pigments that the charge transfer band of $Y_2Ce_2O_7$ at 410 nm is dramatically shifted to longer wavelengths (600 nm) with the substitution of 50 mol% of terbium ions. In $Y_2Ce_2O_7$, the band gap energy is related to the valence band consisting of filled O 2p orbitals and the conduction band derived from the empty 4f orbitals of Ce^{4+} ions. The band gap between the anionic band and cationic band of $Y_2Ce_2O_7$ is 3.11 eV. By doping $Y_2Ce_2O_7$ with Tb ions, the 4f electrons of terbium valence shell introduce an additional electronic level of energy between the O^{2-} valence band and Ce^{4+} conduction band and a reduction in band gap is observed

from 3.11 eV to 1.86 eV and the variation of band gap with increasing terbium doping is tabulated in Table 5.5. The $Y_2Ce_2O_7$ band gap falls in violet region of visible wavelengths, and a complementary light yellow color is observed. On the other hand, the terbium doped $Y_2Ce_2O_7$, the band gap falls in the wavelength region below 600 nm producing a red color.

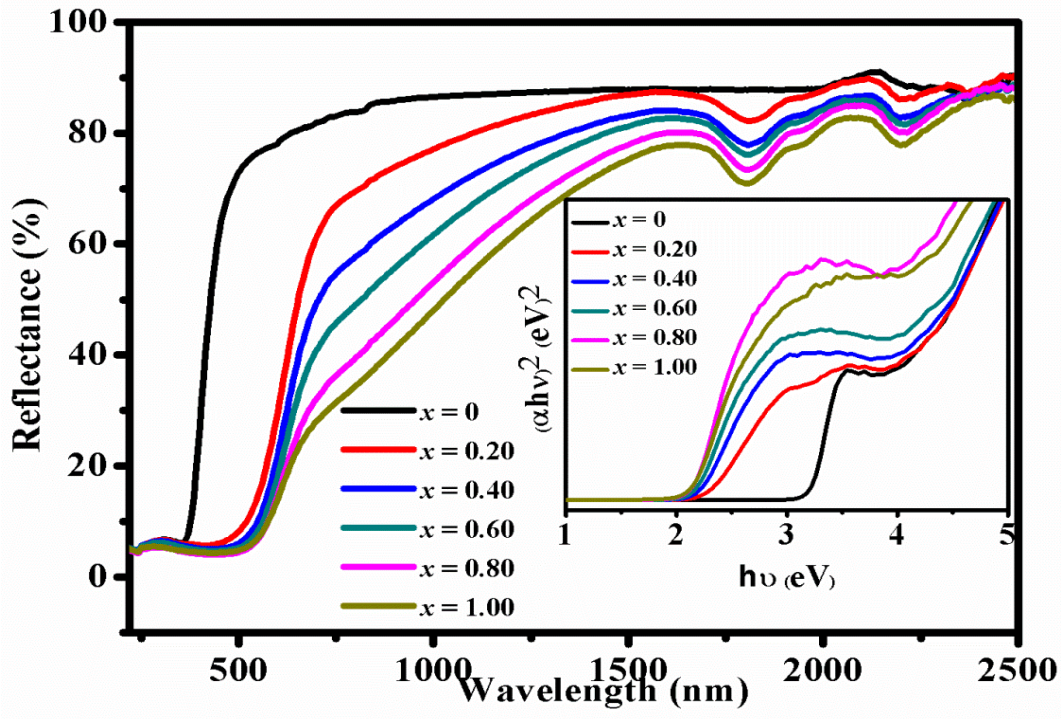

Fig. 5.14 Reflectance spectra of $Y_2Ce_{2-x}Tb_xO_7$ (x = 0, 0.2, 0.4, 0.6, 0.8, and 1.0) red pigments (Tauc plots in the inset).

The $Y_2Ce_2O_7$ exhibits highest NIR reflectance of about 86.9%. At the same time, with doping of Tb ions to substitute Ce^{4+} ions, the NIR reflectance of the pigments slightly decreases and falls in the range 80.0 % (x = 0.20) to 55.0 %(x = 1.0). Table 5.4 presents the NIR reflectance and solar reflectance of the pigment powdered samples. A cool non white coating that absorbs in the visible region should be highly reflective in the NIR part of the electromagnetic spectrum in order to maintain a high solar reflectance (Sameera et al. 2014. The NIR solar reflectance spectra determined in accordance with ASTM standard G173-03 of powdered $Y_2Ce_{2-x}Tb_xO_7$ (x = 0, 0.2, 0.4, 0.6, 0.8, and 1.0) red pigments are presented in Fig. 5.15. The higher NIR reflectance displayed by all the newly designed red colored pigments encourage them as interesting cool colorants for roofing applications to mitigate the urban island effect.

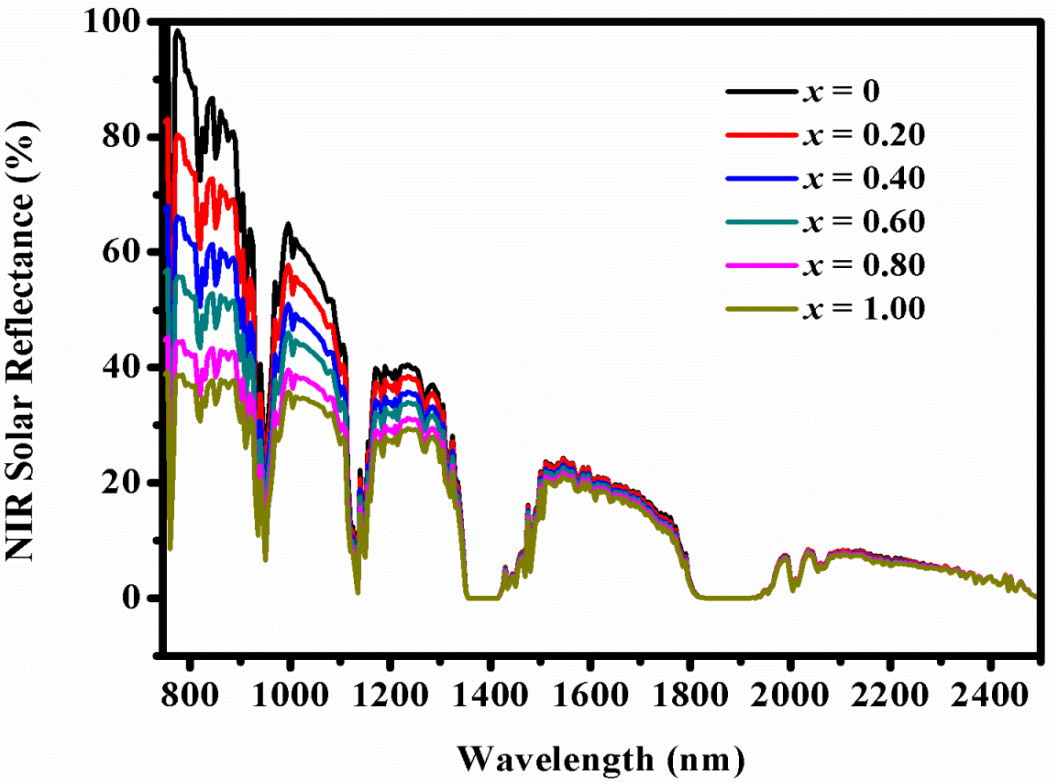

Fig. 5.15 NIR Solar Reflectance of $Y_2Ce_{2-x}Tb_xO_7$ (x = 0, 0.2, 0.4, 0.6, 0.8, and 1.0) red pigments.

Table 5.4 The values of NIR reflectance and the solar reflectance of $Y_2Ce_{2-x}Tb_xO_7$ (x = 0, 0.2, 0.4, 0.6, 0.8, and 1.0) red pigments.

Pigment composition (x)	**0**	**0.20**	**0.40**	**0.60**	**0.80**	**1.0**
NIR reflectance of the pigments	86.9%	80.0%	72.3%	67.1%	60.0%	55.1%
Solar reflectance of the pigments	42.2%	38.8%	35.1%	32.6%	30.0%	26.7%

5.3.2.5. Color performance

The chromatic properties of the synthesized powdered pigments can be numerically expressed in terms of color co-ordinates from their CIE 1976 color coordinate values and are listed in Table 5.5. The Lightness (L^*) of the samples

decreases with increase in terbium concentration. The doping of terbium (x = 0.20) results in an increase in the red component (a^*) to 26.01 and yellow component (b^*) to 33.4. A further increase in dopant concentration (up to x = 1.0) brings about a slight decrease in the red and yellow hues, as denoted by the chromatic coordinates a^* and b^*, consequently the color changes to dark-brown. The photographs of the synthesized pigments are shown in Fig. 5.16. The color coordinates of the typical pigment powder ($Y_2Ce_{1.8}Tb_{0.2}O_7$) are significantly higher than that of the recently reported ones i.e in CeO_2.(0.05)Pr_6O_{11}.($_x$)α-Fe_2O_3 (L^* = 35.80, a^* = 24.17, b^* = 20.67) (Olegario et al. 2013), (L^* = 76.3, a^* = 8.5, b^* = 17.2)(Grcia et al. 2001), $LaFe_{1-x}Al_xO_3$ (L^* = 62.58, a^* = 17.08, b^* = 30.39) (Liu et al. 2015) and commercially available brown pigment (BR 300), (L^* = 34.91, a^* = 11.38, b^* = 9.86) of Kawamura Chemicals Co. Ltd. Japan. The hue angle values reveal that the terbium doped $Y_2Ce_2O_7$ pigments lie in the reddish brown region of the cylindrical color space (h° = 0-35 for red and 35-70 for orange). The merit of the present results is that, chemical manipulations based on the rare earth oxides bid a scope for color performance studies replacing them in the class of non toxic (lead free) inorganic red pigments for coloring applications.

Table 5.5 Color coordinates and band gap values of the $Y_2Ce_{2-x}Tb_xO_7$ (x = 0, 0.2, 0.4, 0.6, 0.8, and 1.0) red pigments.

x	L^*	a^*	b^*	C_{ab}	h°	E_g eV
0	89.69	-2.60	12.96	13.22	101.34	3.11
0.2	49.57	26.01	33.4	42.33	52.08	2.02
0.4	43.08	25.58	27.04	37.23	46.58	1.91
0.6	39.49	24.10	22.84	33.21	43.46	1.89
0.8	35.87	22.27	20.26	30.11	42.30	1.86
1.0	35.70	19.60	18.24	26.77	42.93	1.87

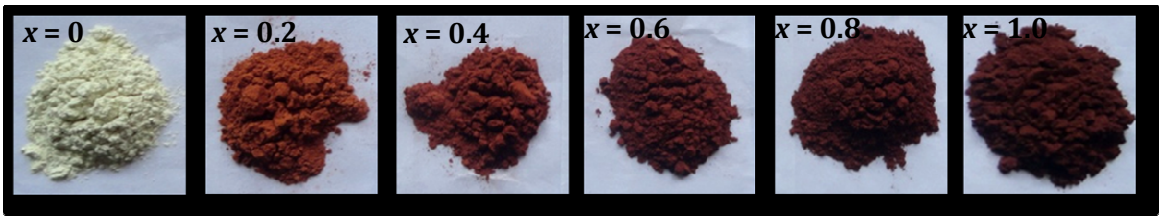

Fig. 5.16 Photographs of $Y_2Ce_{2-x}Tb_xO_7$ (x = 0, 0.2, 0.4, 0.6, 0.8, and 1.0) red pigments.

5.3.2.6 Application Studies

The coloring performance of the typically synthesized pigments was tested for its coloring application in a substrate like PMMA. Typically, 10 wt% $Y_2Ce_{1.8}Tb_{0.2}O_7$ pigment powder was dispersed in PMMA and compressed to a cylindrical disc and is shown in Fig. 5.17. The intensity of the color of plastics will depend on the concentration of the pigment. The color coordinates of the polymer plastic were measured at different locations on the surface and the $L^*a^*b^*$ values obtained were more or less the same revealing the uniform distribution of the pigment particles in the polymer matrix. Thus the developed pigments may find potential application in the coloring of various plastic materials.

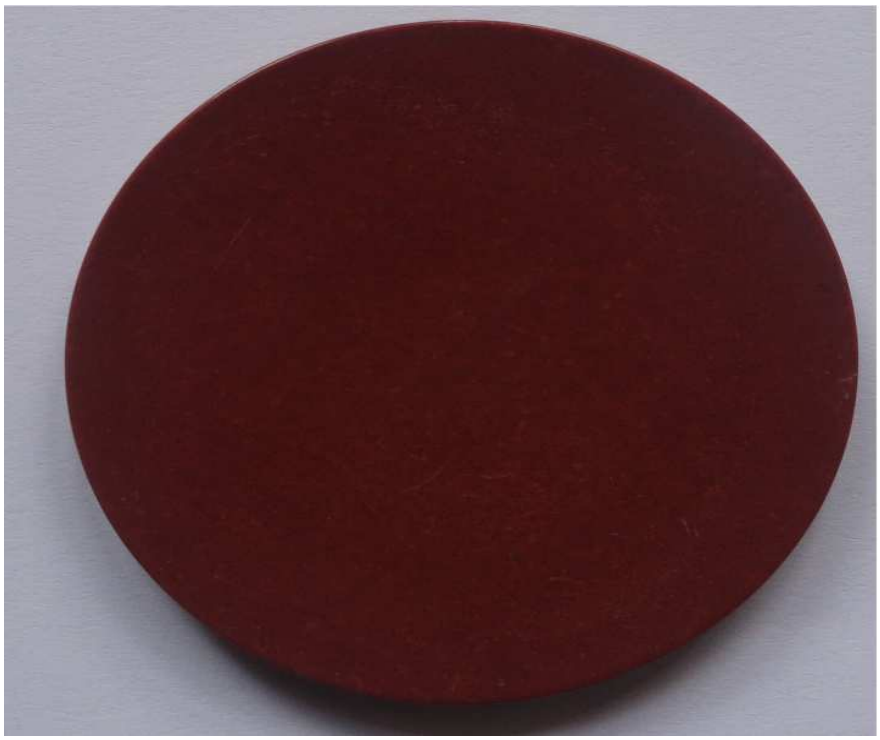

Fig. 5.17 Photograph of 10 wt% $Y_2Ce_{1.8}Tb_{0.2}O_7$ + PMMA. The polymer matrix exhibit uniform distribution of pigment particles in the substrate.

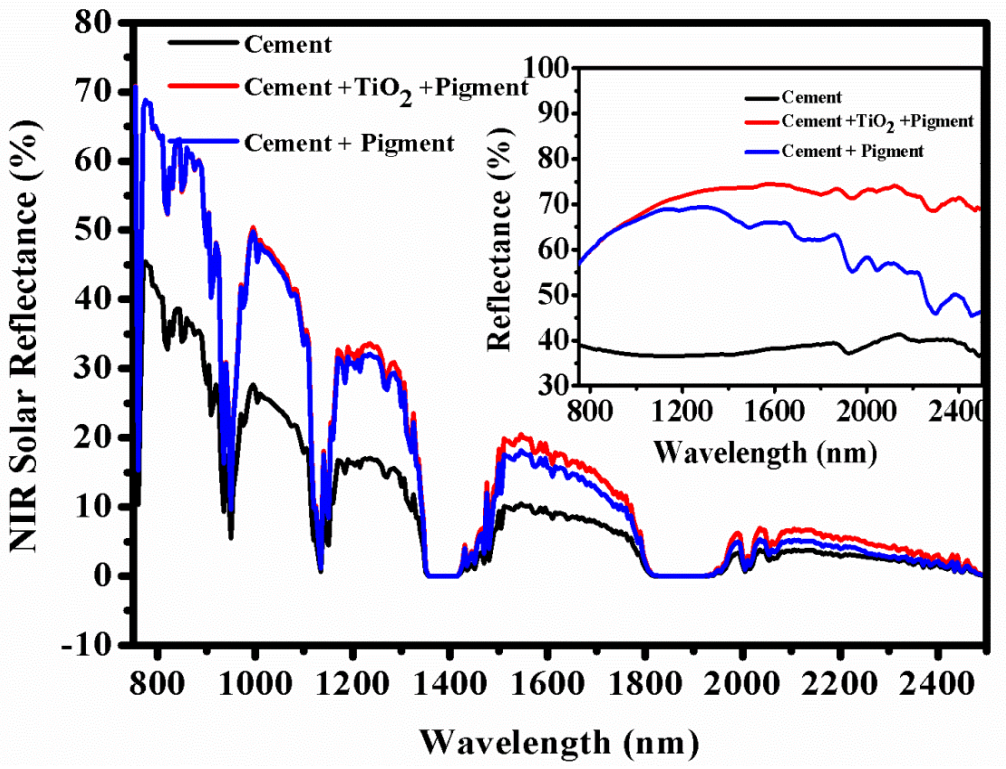

Fig. 5.18 NIR solar reflectance spectra of pigment coated cement slabs with and without TiO_2 base coat (NIR reflectance in the inset).

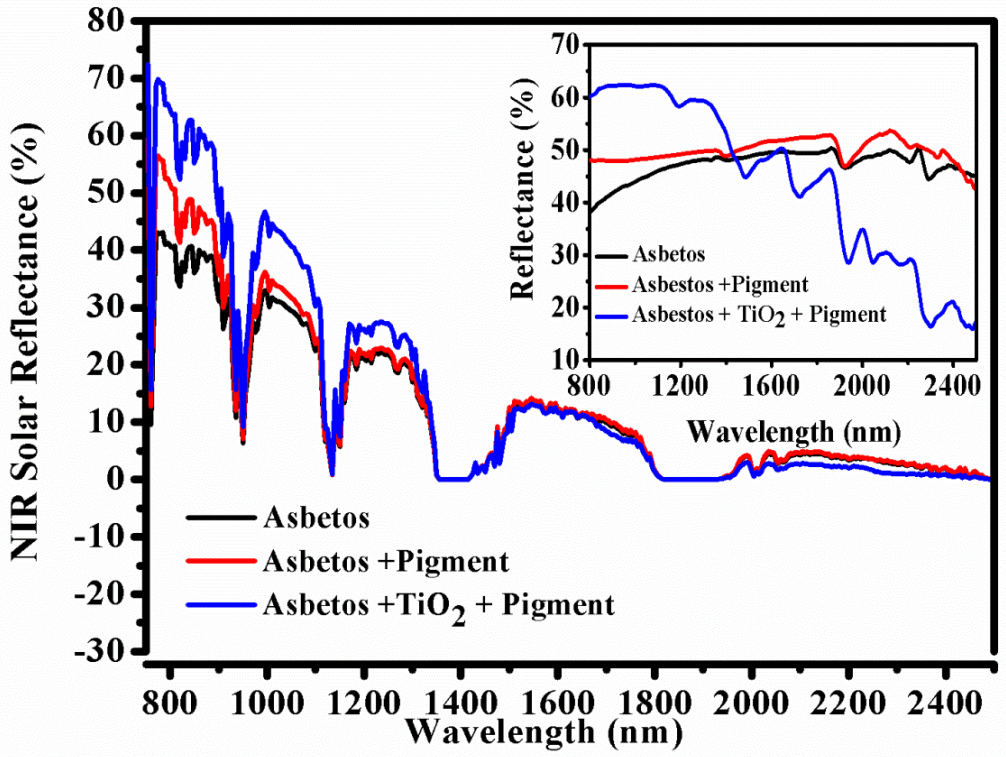

Fig. 5.19 NIR solar reflectance spectra of pigment coated asbestos sheet with and without TiO_2 base coat (NIR reflectance in the inset).

Colored cool coatings that absorb less NIR radiation can provide coatings similar in color to that of conventional roofing materials, but with high solar reflectance. In order to assess the performance of the pigments as cool colorants for reducing the heat build-up, we have evaluated the NIR reflectance of the designed pigments by coating on to the roofing materials like cement slabs and asbestos cement sheet. The NIR solar reflectance spectra of the typical white (x = 0) and red (x = 0.2) pigment coated on the cement slab and the red pigment on the asbestos cement sheet with and without base coat are shown in Fig. 5.18 and Fig. 5.19 respectively. The photographs of the coating materials are displayed in Fig. 5.20 and Fig. 5.21. The NIR reflectance of the red pigment coatings are depicted in Table 5.6. It is very interesting to note that the NIR reflectance and the corresponding solar reflectance of both pigment coated substrates are found to be higher than that of the bare substrates. Thus these coatings can reduce the surface temperature of the building roofs and lead to energy savings.

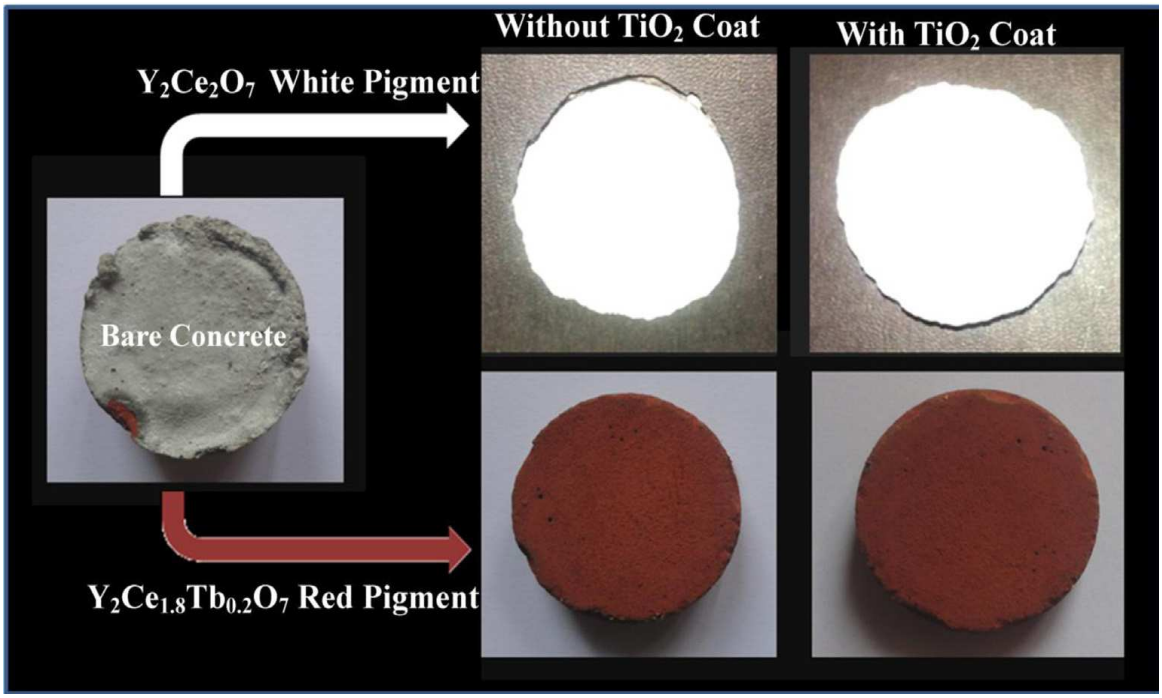

Fig. 5.20 Photographs of bare cement slab and white (x = 0) and red (x = 0.2) pigment coated cement slab without and with TiO_2 base coat in sequence.

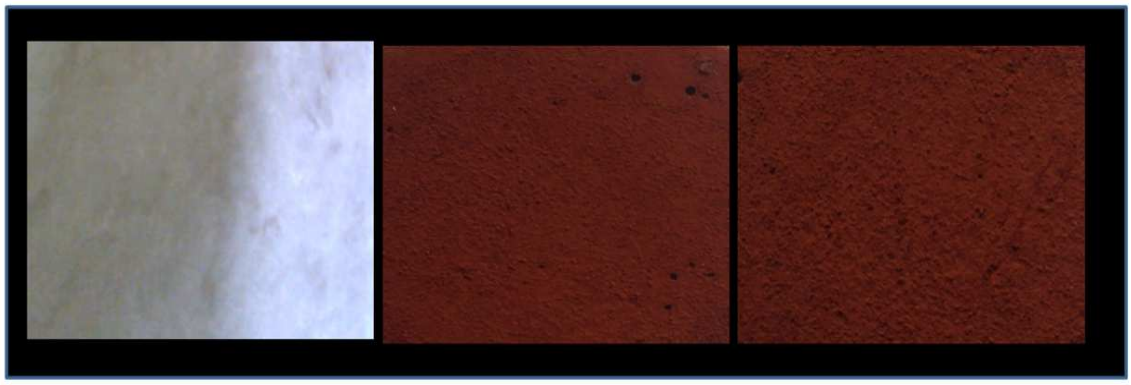

Fig. 5.21 Photographs of bare asbestos and pigment coated asbestos without and with TiO_2 base coat in sequence.

Table 5.6 NIR reflectance and the solar reflectance data of $Y_2Ce_{1.8}Tb_{0.2}O_7$ red pigment coated on concrete cement block and asbestos sheet.

Parameter	Concrete coating			Asbestos coating		
	Bare	Without TiO_2 base coat	With TiO_2 base coat	Bare	Without TiO_2 base coat	With TiO_2 base coat
NIR reflectance of the pigments	36.6%	68.7%	70.1%	46.1%	48.6%	62.3%
Solar reflectance of the pigments	17.8%	33.5%	34.1%	22.4%	23.6%	30.2%

The $Y_2Ce_{1.8}Tb_{0.2}O_7$ pigment powder of different amounts was mixed with ceramic glaze in the respective ratio (Section 5.2.3) and sprayed on clay tile substrates and the spectral reflectance as well as the color coordinates was measured for different firing temperatures and the photographs are shown in Fig. 5.22. The NIR solar reflectance values of the coated clay tile substrates are shown in Table 5.7. It is seen that maximum NIR and solar reflectance value was obtained from 1:5 ratio for glazing at 1000 °C and the good coloring performance was obtained for the glazing at 1100 °C. These glazed tiles are highly effective to prevent

the heat build up and thus they are potential for roofing and exterior tiles as energy saving products.

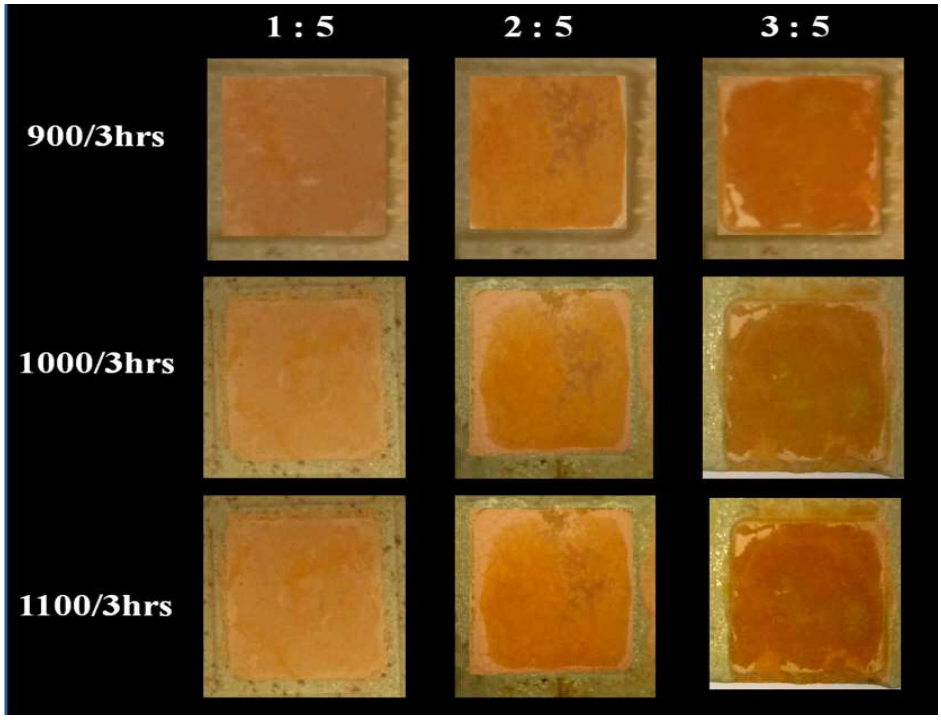

Fig. 5.22 Photographs of glazed tile substrates for different amounts of $Y_2Ce_{1.8}Tb_{0.2}O_7$ pigment powder calcined at different temperatures.

Table 5.7 Color coordinates, NIR reflectance and solar reflectance values of coated clay tile substrates for different amounts of $Y_2Ce_{1.8}Tb_{0.2}O_7$ pigment powder.

	Ratio	L^*	a^*	b^*	NIR reflectance (R%)	NIR Solar reflectance (R%)
900°C	1:5	69.47	14.77	18.68	88.29	42.89
	2:5	69.56	18.91	30.06	90.04	43.74
	3:5	66.95	16.21	24.30	80.80	39.25
1000°C	1:5	71.24	16.48	20.10	93.33	45.34
	2:5	72.43	19.26	30.90	93.04	45.20
	3:5	66.41	16.73	27.23	65.34	31.74
1100°C	1:5	71.09	13.35	17.17	90.78	44.10
	2:5	68.28	20.52	32.01	91.90	44.64
	3:5	63.15	26.42	31.05	64.12	3.12

5.4. Conclusions

A new series of $A_2Ce_{1.6}O_7$:0.4Tb (A = La, Sm, Gd & Y) and $Y_2Ce_{2-x}Tb_xO_7$ (x = 0, 0.2, 0.4, 0.6, 0.8, and 1.0) red pigments with high NIR reflectance have been successfully prepared via a conventional solid-state route. The doping of Tb ions changes the color of pigments from ivory white to reddish brown which find use in formulating less toxic red pigments for paints and plastics. Moreover, all the powder samples possess very high NIR reflectance (92% at 1100 nm), and when used as various building roofing substrates as well as clay tile glazing, the pigmented coatings show high solar reflectance thus makes the developed pigments in cool roof as well as glazing applications as energy saving products.

Chapter 6

Tuning the colour from yellow to red in Sr_2CeO_4 system by Ba-Tb substitutions having NIR reflectance for energy saving applications

Novel yellow/red inorganic pigments $A_2Ce_{1-x}Tb_xO_4$ (A = Sr and Ba) were synthesized by the conventional solid-state route. The Tb substitution extends the absorption edge to longer wavelengths by introducing an additional electronic level between the valence and conduction bands. Consequently, the prepared pigments exhibit various colors by fine tuning of the band gap from 3.03 (white) to 2.37 (yellow) to 1.86 eV (red). Doping of Tb into Sr_2/Ba_2CeO_4 enhances the NIR reflectance at 1100nm from 87% to 91%. The coloring performance of the synthesized pigments was investigated in the polymer matrix and concrete cement for plastic coloring and cool roof applications. The exhibition of high NIR reflectance with comparable color properties of these pigments makes them potential candidates as cool colorants to reduce the heat build-up.

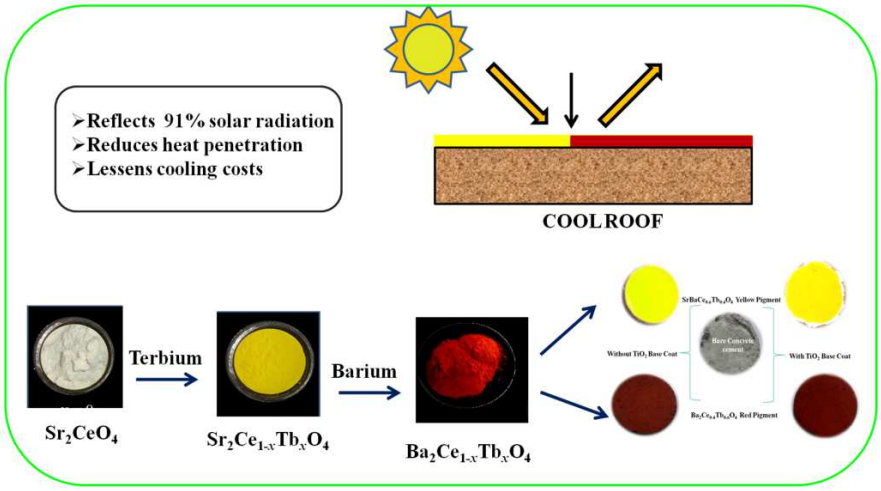

Athira et al. ***Chem. Lett.,*** *43,* ***2014,*** *985-987.*

Athira et al. ACS. Sustainable Chem. Eng. 7, ***2019****, 8804-8815.*

6.1 Introduction

Designing of sustainable products and processes that minimise the use and generation of hazardous substances is a great demand in the emerging world. The ability to "smarter" has to be of way to reduce the energy consumption in the global warming. Inorganic pigments plays as sustainable products in a smarter way that the colored pigments with high NIR reflectance reduces the heat build up of mainly urban areas in addition to their aesthetic look. Cool pigments absorb less solar energy that keeps the surface cool and decreases energy transfer by radiation. Recently, the pigment industry is focused on the synthesis of "smarter pigments" (nontoxic cool pigments) that aid in energy savings (Levinson et al. 2005). In view of this, eco-friendly inorganic pigments with high NIR reflectance has been studied well (Cerro et al. 2018; Bhim et al. 2018; Li et al. 2018). In particular, inorganic yellow and red pigments are in great demand in the pigment industry due to its wide applicability. Bright yellow pigments are mostly demanding as a replacement of cadmium and lead chromates pigments within the surface coating markets. The Color Pigment manufacturers Association, Inc. recorded that the hematite, rutile and spinel structures of complex inorganic compounds gives good red or reddish-brown hues (Marinova et al. 2003). Hence there is an interest for developing more thermally stable red/brown pigments which are in agreement with the technological and environmental requirements.

Several yellow colors are already commercially available for various ceramic decoration applications. They include zirconia vanadium, tin vanadium, and praseodymium yellow. In ceramic coatings, zirconia vanadium yellows are often weaker in color than the tin vanadium yellows and rather muddier than praseodymium zircon yellows (Kar et al. 2004). However, the praseodymium yellow ($ZrSiO_4$:Pr) pigment requires high calcination temperatures during preparation, which tends to induce the particle growth of the pigment (Vishnu et al. 2009). Hence, it is difficult to apply the praseodymium yellow to paints and inks in which the fine dispersion of the pigment is essential. Similarly several inorganic red pigments mostly based on ceria have developed. But their NIR reflectance is not well explored. Several studies were reported on new environmentally friendly inorganic yellow and red pigments with high NIR reflectance, but it is very difficult to obtain

these two colors within the same system by tuning the band gap energy. In the present study, we focused on the tuning of color from yellow to red by adjusting the cations which is alternative to the commercial toxic colorants.

During the course, terbium-based yellow pigments $BaSnO_3$ (Lunakova et al. 2013) and $ATbO_3$ [U.S. Patent No. 5688316] have been reported; however, higher concentrations of terbium is required to obtain good color characteristics, which make them not very cost-effective for commercial use. Among the several candidates for the alternative nontoxic yellow pigments, CeO_2 and its related materials are attractive because of the opacity, low toxicity, and high temperature stability. Cerium, which is one of the rare earth elements, has the Ce^{3+} or Ce^{4+} ionic state. However, it is reported that the charge-transfer energy of a tetravalent ion of the rare-earth element is low because of its tendency to convert to the trivalent ion. On the other hand, the Ce^{3+} ion has one unpaired electron within the 4f orbit. The 5d level of the Ce^{3+} ion is the lowest among the trivalent rare-earth ions. From these facts, the cerium element has a potential to be the basis of new inorganic pigments using the charge-transfer energy or transition of 4f to 5d. In this regard, some yellow pigments based on cerium oxide have also been reported; however, their chromatic properties are not satisfactory for industrial use (Masui et al. 2004; Sulcova et al. 1999).

In 1998, Danielson et al reported a new efficient rare earth based optical material: Sr_2CeO_4 which crystallises in an orthorhombic crystal system with the space group *Pbam* (No. 55) (cell parameters a = 6.1347 Å, b =10.3450 Å, and c = 3.5962 Å) and was widely utilized in various optoelectronic and displaying devices due to their high thermal stability, chemical stability and optical properties (Danielson et al. 1998). Its structure exhibits strong anisotropy, which is governed by a set of one-dimensional chains of trans-edge-sharing CeO_6 octahedrons linked by interchain Sr^{2+} ions (Grzyb et al. 2012). Europium-doped Sr_2CeO_4 compositions, has been extensively investigated for red phosphor materials (Monika et al. 2014). And also the environmentally friendly composition of strontium cerate offers a possible candidate as an inorganic pigment. In the present study, novel yellow pigments based on strontium cerate, $Sr_2Ce_{1-x}Tb_xO_4$ ($0 \leq x \leq 1.0$), were synthesized, and their color properties were characterized from the view point of a possible ecological

inorganic pigment. The pigment color depends on the terbium content, and bright yellow colors are obtained for even lower concentrations of terbium (b^* = 70.30). This invention opened up a new system in the field of novel inorganic yellow pigments. Further, through cation substitution the tuning of color can be produced. Starting from the orthorhombic Sr_2CeO_4 parent compound, a small amount of terbium substitution in cerium site produces intense yellow colors having same structure with different space group and replacing some or all strontium with barium gives red colors having tetragonal structure by changing the terbium oxidation state from 4+ to 3+.

In this context we synthesized the compounds having the general formulae: $Sr_2Ce_{1-x}Tb_xO_4$ (x = 0, 0.2, 0.4, 0.6, 0.8, and 1.0); $Sr_{2-x}Ba_xCe_{0.6}Tb_{0.4}O_4$ (x = 0.25, 0.50, 0.75, 1.0, 1.25, 1.50 and 2.0) and $Ba_2Ce_{1-x}Tb_xO_4$ (x = 0, 0.20, 0.40, 0.60, 0.80 and 1.0) were synthesized by the conventional solid-state route in order to tune the color from yellow to red. The pigment color depends on the barium/terbium content which produces very high yellow as well as red hue higher than that of the commercially available pigments. The structure, morphology, optical and coloristic properties of the prepared powders were characterized by powder X-ray diffractometer (XRD), scanning electron microscope (SEM) with energy dispersive spectrometry (EDS), X-ray photoelectron spectroscopy, UV-vis NIR Spectroscopy and CIE 1976 $L^*a^*b^*$ color scales.

6.2 Experimental

6.2.1 Materials and Methods

The terbium doped strontium/barium cerium-based pigments with the general formula $Sr_2Ce_{1-x}Tb_xO_4$ (x = 0, 0.2, 0.4, 0.6, 0.8, and 1.0); $Sr_{2-x}Ba_xCe_{0.6}Tb_{0.4}O_4$ (x = 0.25, 0.50, 0,75, 1.0, 1.25, 1.50 and 2.0) and $Ba_2Ce_{1-x}Tb_xO_4$ (x = 0, 0.20, 0,40, 0.60, 0.80 and 1.0) were synthesized by the conventional solid-state route. The raw materials: $SrCO_3$, $BaCO_3$, CeO_2 and Tb_4O_7 (Sigma-Aldrich, 99.99% purity) were weighed in the stoichiometric ratio and homogenized by wet mixing with acetone in an agate mortar until the fine slurry was obtained. The slurry was dried by placing it in an air oven at a temperature of 100°C. The mixing and drying were repeated thrice to obtain a homogenous mixture. The mixed product was then calcined in platinum crucibles in an electric furnace at 1300°C ($Sr_2Ce_{1-x}Tb_xO_4$); 1250°C (Sr_{2-}

$_xBa_xCe_{0.6}Tb_{0.4}O_4$) and 1300°C ($Ba_2Ce_{1-x}Tb_xO_4$) for 6 h. The temperature of the furnace is programmed with an initial heating rate of 10°C/min up to 1000°C followed by a heating rate of 5°C/min to attain the respective temperatures.

6.2.2 Characterization

The crystalline structure of the calcined powders was characterized using X-ray powder diffraction (XRD) using a Ni-filtered Cu-K_α radiation with a PANalytical X'pert Pro diffractometer operated at 45 kV and 30 mA. Data were collected from 10 to 90° 2θ range with a step size of 0.016°. X-ray photoelectron Spectroscopy (XPS) of the synthesized samples were recorded on a PHI 5000 Versa probe II having Al Kα monochromatic source. Particle morphological analysis of the powder was performed by means of a JEOL scanning electron microscope (model JSM-5600 LV) with an acceleration voltage of 15 kV. The X-ray microchemical analysis and elemental mapping of the samples were carried out using a Silicon Drift Detector–X-Max^N attached with a Carl Zeiss EVO SEM. The UV-vis NIR spectra of the pigments were recorded by a Shimadzu, UV-3600 spectrometer through diffuse reflectance technique using polytetrafluoroethylene (PTFE) as a reference. The Kubelka–Munk (KM) function which was used to calculate the absorption coefficient from the diffuse reflectance data. The optical band gap (Eg) of the synthesized samples was calculated using tauc plot. The NIR solar reflectance is expressed as the integral of the present reflectance times the solar irradiance divided by the integral of the solar irradiance when integrated over 700-2500 nm range. The NIR solar reflectance was determined from ASTM Standard G173-03. The color parameters of the pigments were determined by UVPC color analysis software coupled to the UV-3600 spectrophotometer at the measurement conditions kept as an illuminant D65, 10° complementary observer and measuring geometry d/8°. The CIE1976 $L^*a^*b^*$ colorimetric method was used as recommended by the Commission Internationale de l'Eclairage (CIE). In this system, L^* is the color lightness (0 for black, 100 for white), a^* is the green (-) / red (+) axis, and b^* is the blue (-) / yellow (+). The chroma is defined as $C^*= [(a^*)^2+(b^*)^2]^{1/2.}$ The hue angle, h° is expressed in degrees and ranges from 0° to 360° and is calculated using the formula $h^\circ= \tan^{-1}(b^*/a^*)$. The thermal stability of the typical pigments: $SrBaCe_{0.6}Tb_{0.4}O_4$, $Ba_2Ce_{0.2}Tb_{0.8}O_4$ was checked in the temperature range of 50 - 1000°C by SII Nanotechnology Inc., thermo

gravimetric/differential thermal analysis (TG/DTA) 6200 in air atmosphere at a heating rate of rate of 10°C/min. Chemical resistance tests using acid/base solutions and water were performed. A pre-weighed amount of the typical pigments: $SrBaCe_{0.6}Tb_{0.4}O_4$, $Ba_2Ce_{0.2}Tb_{0.8}O_4$ with best coloristic property was treated with 5% HCl, HNO_3, NaOH, and H_2O and soaked for 1 h with continuous stirring using a magnetic stirrer. The pigment powder was then filtered, washed with deionized water, dried, and weighed. The CIE color coordinates were measured, and the color difference (ΔE^*_{ab}) was calculated from the following equation.

$$\Delta E^*_{ab} = \sqrt{(\Delta L^*)^2 + (\Delta a^*)^2 + (\Delta b^*)^2} \quad (6.1)$$

6.2.3 Application Studies

In order to test the capacity of the pigment samples to impart the yellow and red hues, the selected pigments were incorporated into a polymer substrate like Poly(methyl methacrylate) (PMMA) which is a well known water soluble polymeric material extensively used for cold extrusion of many inorganic oxides such as alumina and zirconia. A viscous solution of PMMA (90 wt%) was made using a conventional electric coil heater and 10 wt% of the pigment was slowly added with stirring and converted to a thick paste. The paste was then transferred in a mould and compressed into a cylindrical disc. These pigments was selected to prepare NIR reflecting coatings on a building roofing material like cement slab with and without TiO_2 base coat. The pigment samples were ground and was ultrasonicated (Vibronics, 250W, India) for 10 min to ensure the complete dispersion of the pigment particles in acrylic acid using polyurethane as a binder. The resulted viscous solution was coated on the substrate surfaces and was allowed to dry in an oven at 150 °C.

6.3. Results and discussion

6.3.1 Synthesis of Novel Nontoxic Yellow Pigments: $Sr_2Ce_{1-x}Tb_xO_4$

6.3.1.1 Powder X-Ray diffraction studies

The powder XRD patterns of the pigments are given in Fig. 6.1. The intense and sharp peaks found in the diffraction patterns reveal the crystalline nature of the powders. All the compounds crystallize with the orthorhombic structure, and the

XRD patterns are in good agreement with the powder X-ray diffraction file JCPDS card No. 01-089-5546. The XRD results indicate that the phase stability was achieved up to 40 mol% terbium doping and that a trace impurity phase is detected with further doping. It has been observed that phase-pure Sr_2CeO_4 is difficult to obtain even when different methods are used (Grzyb et al. 2012). The crystallite size was calculated from the Debye-Scherrer formula $D = 0.9\lambda/\beta \cos\theta$, where D is the crystallite size, λ is the wavelength of X-ray used, and β and θ are the half width of X-ray diffraction lines and half diffraction angle of 2θ, respectively. The crystallite size of Sr_2CeO_4 is found to be 204nm and decreases with terbium substitution, ranging from 80 to 140 nm.

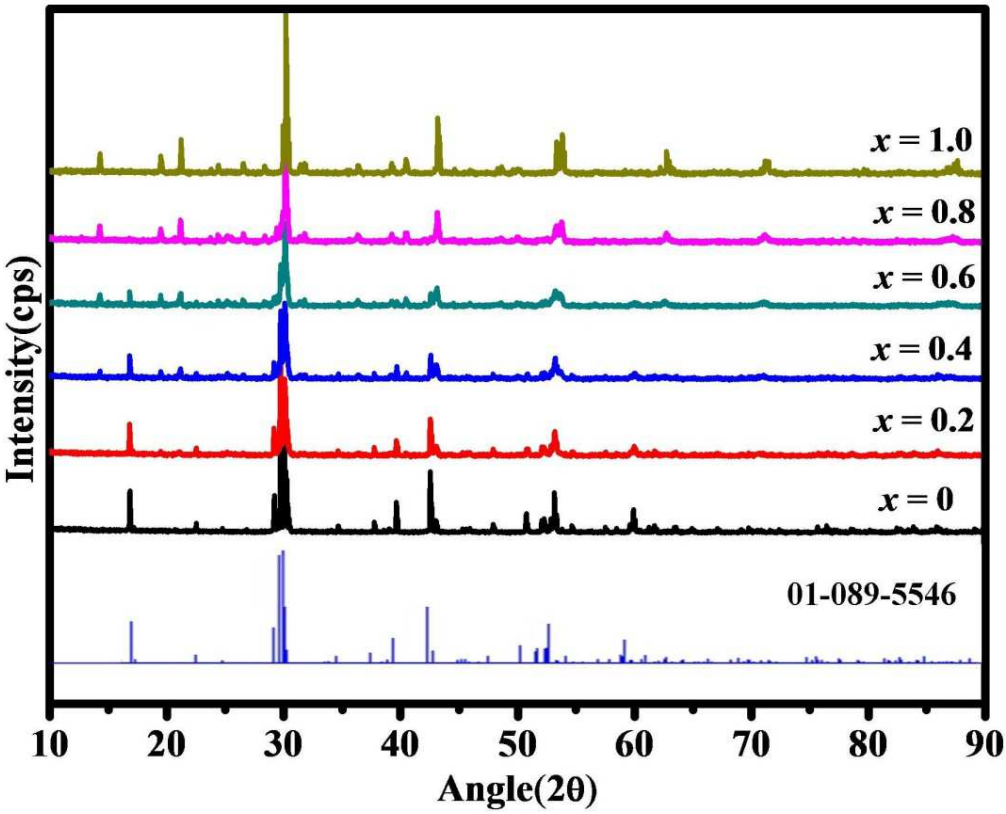

Fig. 6.1 Powder XRD patterns of $Sr_2Ce_{1-x}Tb_xO_4$ (x = 0, 0.2, 0.4, 0.6, 0.8, and 1.0) (* indicates $SrTb_2O_4$ phase).

6.3.1.2 Morphological studies

Fig. 6.2 shows the typical SEM microstructure of terbium doped Sr_2CeO_4 samples for different doping concentrations. The micrographs show slightly agglomerated particles in the size range 1-5 μm.

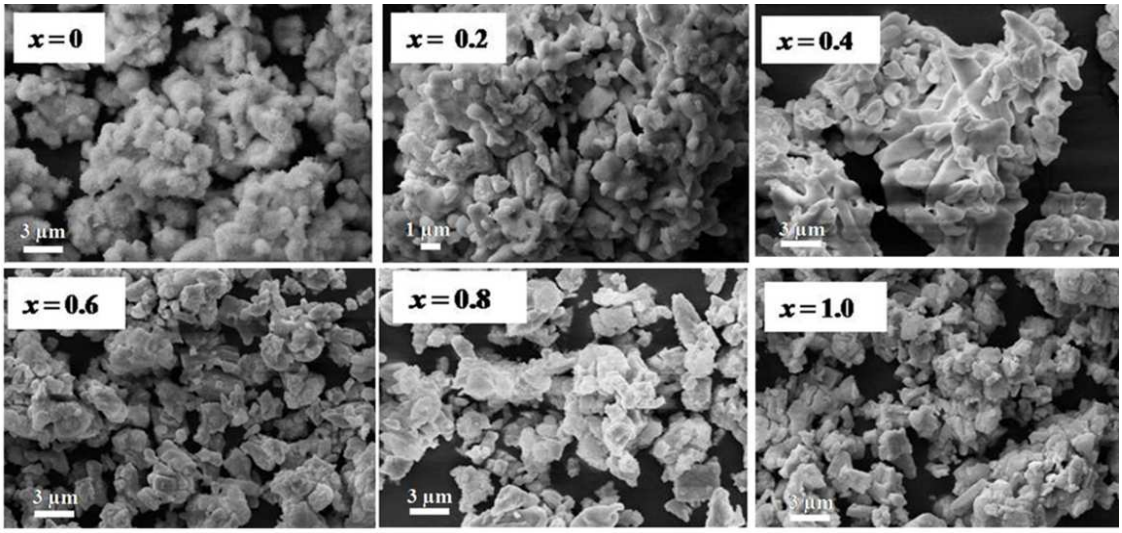

Fig. 6.2 Typical SEM photographs of $Sr_2Ce_{1-x}Tb_xO_4$ (x = 0, 0.2, 0.4, 0.6, 0.8, and 1.0).

6.3.1.3 UV-vis NIR spectroscopic studies

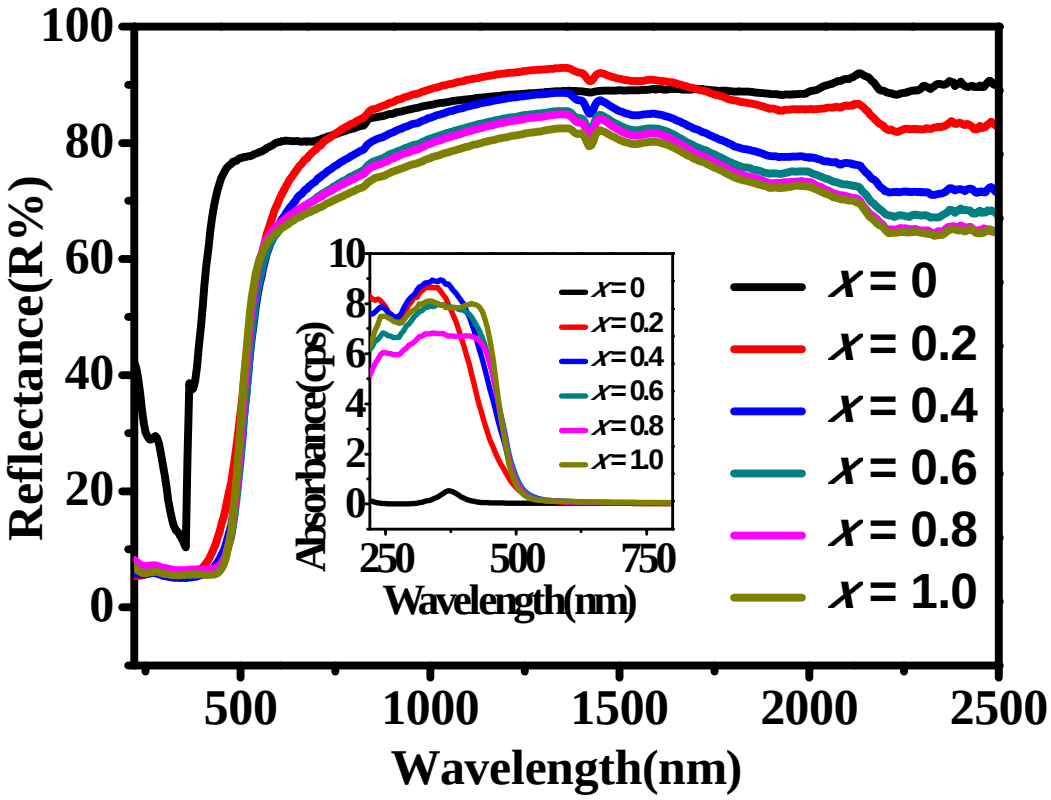

Fig. 6.3 Diffuse reflectance spectra of $Sr_2Ce_{1-x}Tb_xO_4$ pigment powders (x = 0, 0.2, 0.4, 0.6, 0.8, and 1.0) (absorption spectra shown in inset).

The diffuse reflectance spectra of the $Sr_2Ce_{1-x}Tb_xO_4$ (x = 0, 0.2, 0.4, 0.6, 0.8, and 1.0) pigments in the UV-NIR region are displayed in Fig. 6.3, and absorption spectra in the UV-vis are shown in the inset. Strong visible absorption in the blue

region (complimentary of yellow) is observed, and the absorption edge is shifted to the long wavelength by substituting terbium ions into Sr_2CeO_4, leading to a change in the pigment color from white to reddish-greenish yellow.

This observation can be explained on the basis of the shift of the charge-transfer band to higher wavelengths introducing an additional electronic level by Tb doping. In Sr_2CeO_4, the band gap energy is related to the valence band consisting of filled O2p orbitals and the conduction band derived from the empty 4f orbitals of Ce^{4+} ions; the band gap of Sr_2CeO_4 is 3.03 eV. By doping Sr_2CeO_4 with Tb ions, the 4f electrons of the terbium valence shell introduces an additional electronic level of energy between the O^{2-} valence band and Ce^{4+} conduction band; a reduction in band gap is observed from 3.03 to 2.52 eV (Table 6.1). Further, it can be observed that there is a decreasing trend of band gap upto x = 0.6 and beyond this slight increasing trend without following the crystal field splitting of Tb5d energy levels on contraction of lattice on substitution. This can be attributed to the small amount of secondary phase formation on higher substitution, which precludes the complete substitution of Tb into lattice. Prokofiev et al. studied periodicity in the optical band gap variation of Ln sesquioxides (Prokofiev et al. 1996). According to their report, the occupied 4f band in Tb_2O_3 lies above the O2p band, and thus, 4f5d transition may determine the band gap energy.

6.3.2.4. Color performance

Table 6.1 Color coordinates of $Sr_2Ce_{1-x}Tb_xO_4$ (x = 0, 0.2, 0.4, 0.6, 0.8, 1.0) pigments.

x	***L****	***a****	***b****	C_{ab}	***h°***	***NIR R(%)***	***Eg (eV)***
0	90.98	-0.59	4.52	4.56	97.48	87.51	3.03
0.2	78.86	5.49	54.92	55.19	84.28	90.84	2.66
0.4	76.20	6.46	63.65	63.97	84.20	86.26	2.52
0.6	76.08	5.22	67.33	67.53	85.56	82.72	2.48
0.8	77.58	2.38	68.53	68.57	88.0	81.94	2.50
1.0	77.80	-0.35	70.3	70.3	90.29	79.36	2.52

Color coordinates of the synthesized pigments are listed in Table 6.1. The pigments show lightness value L^* ranging from 76 to 79, with low a^* and high b^* (+ve) values. An ideal yellow color is characterized by high lightness L^* > 60, yellowness b^* > 50, high purity C_{ab} = 0-100, and h° = 90°. From Table 6.1, it is seen that the b^* value increases with the increasing addition of terbium; the complete replacement of cerium with terbium enhances the yellow component up to 70.30. The red hue of the pigment as denoted by the color coordinate, a^*, shows a slight increase up to 40 mol% of Tb and decreases thereafter. The yellow hue becomes purer, as evident from the increase in the chroma (C^*) values from 4.56 to 70.30; the photographs of the synthesized pigments are shown in Fig. 6.4. The hue angle values of the pigments lie in the cylindrical color space (h° = 70-105° for yellow) (Sulcova et al. 2007). The chromatic properties, especially the hue angle (90.29°) of this pigment, is comparable with a number of industrial pigments such as $PbCrO_4$ (87.8°), $BiVO_4$ (95.8°), CdS (93.6°), and praseodymium yellow (92.7°) (Vishnu et al. 2012).

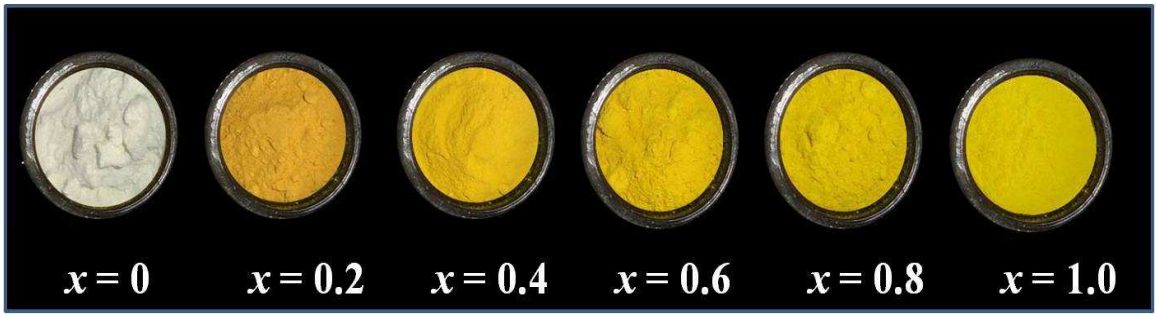

Fig. 6.4 Photographs of the $Sr_2Ce_{1-x}Tb_xO_4$ (x = 0, 0.2, 0.4, 0.6, 0.8, 1.0) samples.

Doping of 20mol% Tb into Sr_2CeO_4 enhances the NIR reflectance at 1100 nm from 87.5% to 90.84%. A slight decrease in the reflectance is observed with further doping. The exhibition of high NIR reflectance of these pigments makes them potential candidate as cool colorants to reduce the heat build-up.

6.3.2.5 Application Studies

The pigment having the best chromatic properties, $Sr_2Ce_{1.4}Tb_{0.6}O_4$, was evaluated for its coloring performance by incorporating it into a polymer substrate such as poly(methylmethacrylate) (PMMA). Typically, 10 wt% of the pigment sample was dispersed in PMMA and compressed to a cylindrical disk (Figure 6.5).

The intensity of the color of plastics will depend on the concentration of the pigment. The color coordinates of the test pieces were measured at different locations. The L^*, a^*, and b^* values obtained were more or less the same, indicating the uniform distribution of the pigment particles in the polymer matrix. Thus, the developed pigments may find potential application in the coloring of various plastic materials.

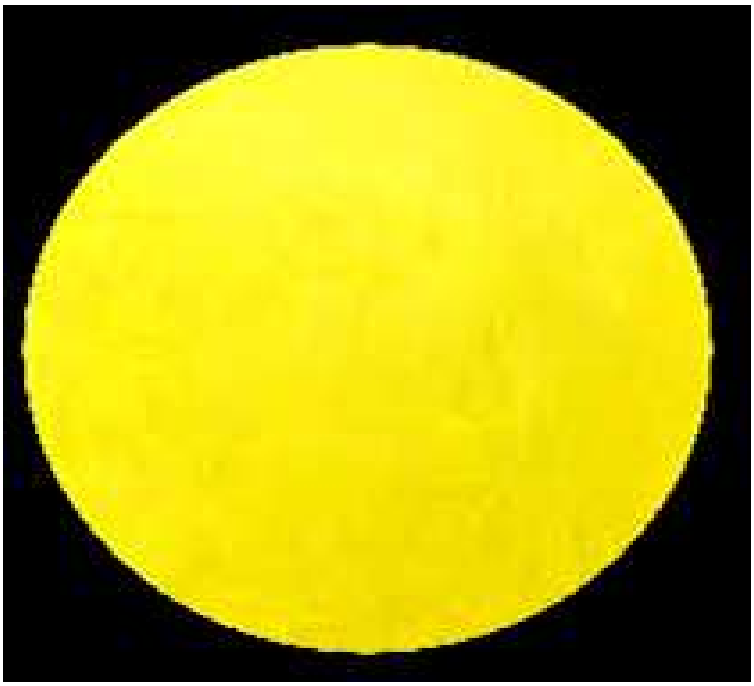

Fig. 6.5 Photographs of $Sr_2Ce_{1.4}Tb_{0.6}O_4$ + PMMA (10 wt%). The test pieces exhibit uniform distribution of pigment particles in the polymer matrix.

Novel inorganic yellow pigments, $Sr_2Ce_{1-x}Tb_xO_4$ (x = 0, 0.2, 0.4, 0.6, 0.8, and 1.0), have been synthesized by solid-state reaction method. The investigations on the optical and color characteristics of these pigments suggest that these pigments have the potential to be used as environmentally benign yellow pigments for plastic coloring and cool roof applications.

6.3.2 Effect of Ba Substitution on the Color Tunable Properties of $Sr_2Ce_{0.6}Tb_{0.4}O_4$ Yellow Pigments

6.3.2.1 Powder X-Ray diffraction studies

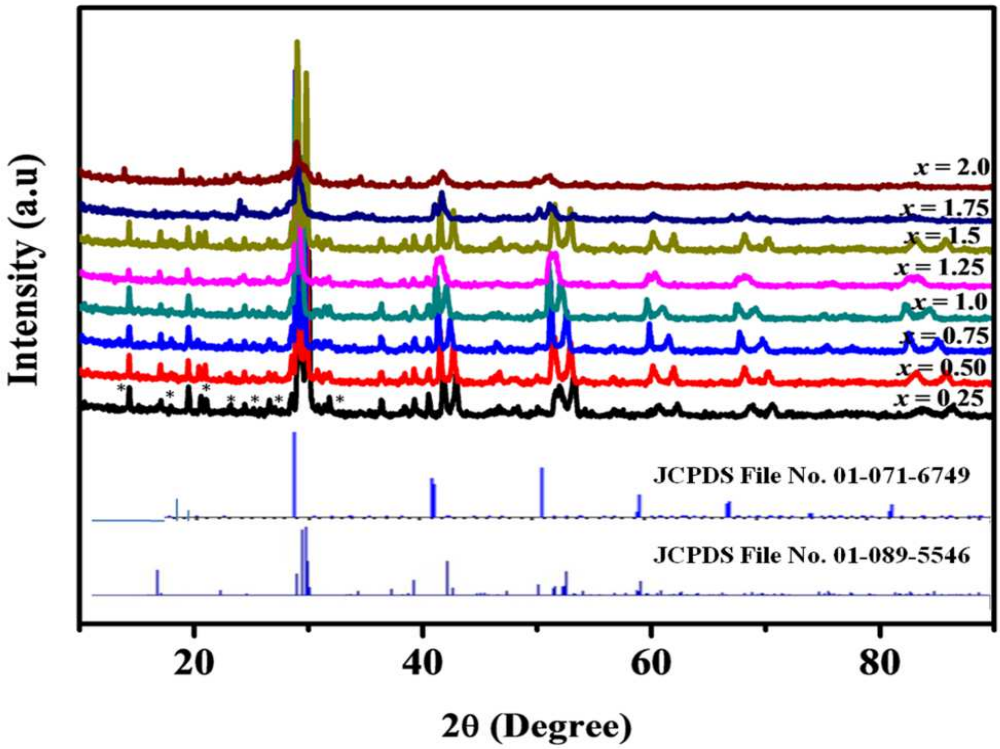

Fig. 6.6 X-ray powder diffraction patterns of $Sr_{2-x}Ba_xCe_{0.6}Tb_{0.4}O_4$ (x = 0.25, 0.50, 0.75, 1.0, 1.25, 1.50 and 2.0) pigments (* indicates $SrTb_2O_4$ phase)

The X-ray diffraction patterns of $Sr_{2-x}Ba_xCe_{0.6}Tb_{0.4}O_4$ (x = 0.25, 0.50, 0,75, 1.0, 1.25, 1.50 and 2.0) samples are shown in Fig 6.6. The intense and sharp peaks in the diffraction patterns confirm the crystalline nature of the powders. All the compositions are isostructural with the cubic orthorhombic crystal system. As can be seen from the XRD patterns, the diffraction peaks of the compounds (x = 0.25 to 1.25) well matches with the JCPDS file number 01-089-5546, forming an orthorhombic phase having the space group *Pbam*. Further, the compositions with x = 1.50, 1.75 and 2.0 crystallises into the orthorhombic phase having the space group *Pmcn*, which can be indexed as per the JCPDS card number 01-071-6749. This shows that progressive doping of Ba^{2+} brings a structural transition. Minor peaks of $SrTb_2O_4$ can be seen from x = 0.25 doping. From the previously reported literatures, it has been observed that phase pure Sr_2CeO_4 is difficult to obtain even when different methods are used (Gryb et al. 2012). The doping of Ba^{2+} (0.142 nm) into

Sr^{2+} (0.126 nm) results in small distortions in the lattice and the lattice volume increases with increasing dopant concentration which signifies the formation of solid solution by the substitution of Ba^{2+}. The lattice parameters and the volume of the cell obtained at various dopant concentrations are shown in Table 6.2.

Table 6.2 Variation of lattice parameters and volume of the cell of $Sr_{2-x}Ba_xCe_{0.6}Tb_{0.4}O_4$ (x = 0.25, 0.50, 0.75, 1.0, 1.25, 1.50 and 2.0) pigments.

	Lattice Parameter			**Volume**	**Structure**
	***a*(Å)**	***b*(Å)**	***c*(Å)**	**(Å)^3**	
x = 0.25	6.1020	10.3454	3.6155	228.23	
x = 0.50	6.1037	10.4137	3.6436	231.59	
x = 0.75	6.1088	10.3774	3.6334	2330.33	*Pbam* Orthorombic
x = 1.0	6.1465	10.3939	3.6485	233.08	
x = 1.25	6.1768	10.3788	3.6453	233.70	
x = 1.50	8.7944	6.1183	6.2489	336.23	
x = 1.75	8.8181	6.4526	6.1915	352.26	*Pmcn* Orthorombic
x = 2.0	8.7736	6.3012	6.4281	355.37	

6.3.2.2 X-ray Photoelectron Spectroscopic studies

X-ray photoelectron spectra of the $Sr_{2-x}Ba_xCe_{0.6}Tb_{0.4}O_4$ (x = 0.25, 0.50, 0.75, 1.0, 1.25, 1.50 and 2.0) pigments were carried out and the wide survey scan in the range 0–1300 eV are shown in Fig. 6.7. The recorded XPS spectra were charge-corrected with respect to an adventitious C 1s signal at 284.6 eV. A series of peaks from Sr 2d, Ba 2d, Ce 3d, Tb 3d, C 1s and O 1s are clearly observed. The XPS of Ce 3d and Tb 3d core levels spectra for the synthesised samples are shown in Fig. 6.8 and 6.9 respectively. It was found that the mixed valence states of the cerium and terbium species (+3 and + 4) present in the system. The broad Ce 3d and Tb 3d photoelectron peaks are deconvoluted for accurate assignment and allow an inference of the composition of different chemical states present in the samples (Fig. 6.10).

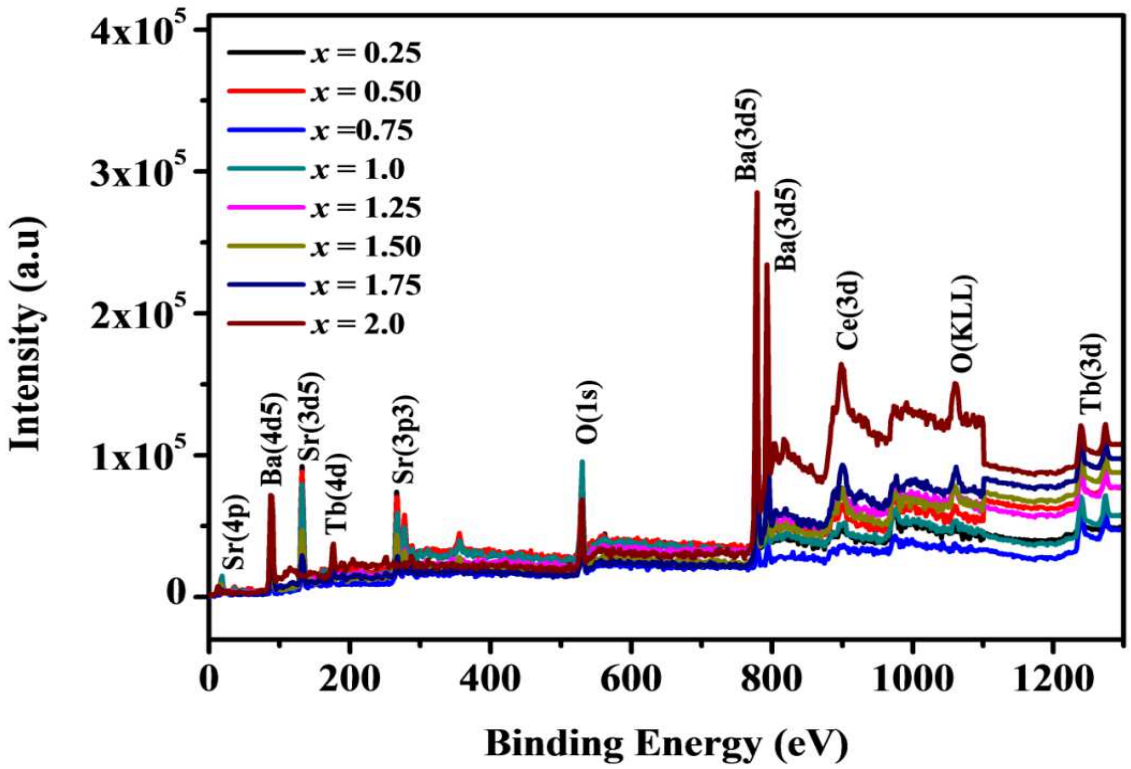

Fig. 6.7 XPS survey spectra of $Sr_{2-x}Ba_xCe_{0.6}Tb_{0.4}O_4$ (x = 0.25, 0.50, 0.75, 1.0, 1.25, 1.50 and 2.0) pigments.

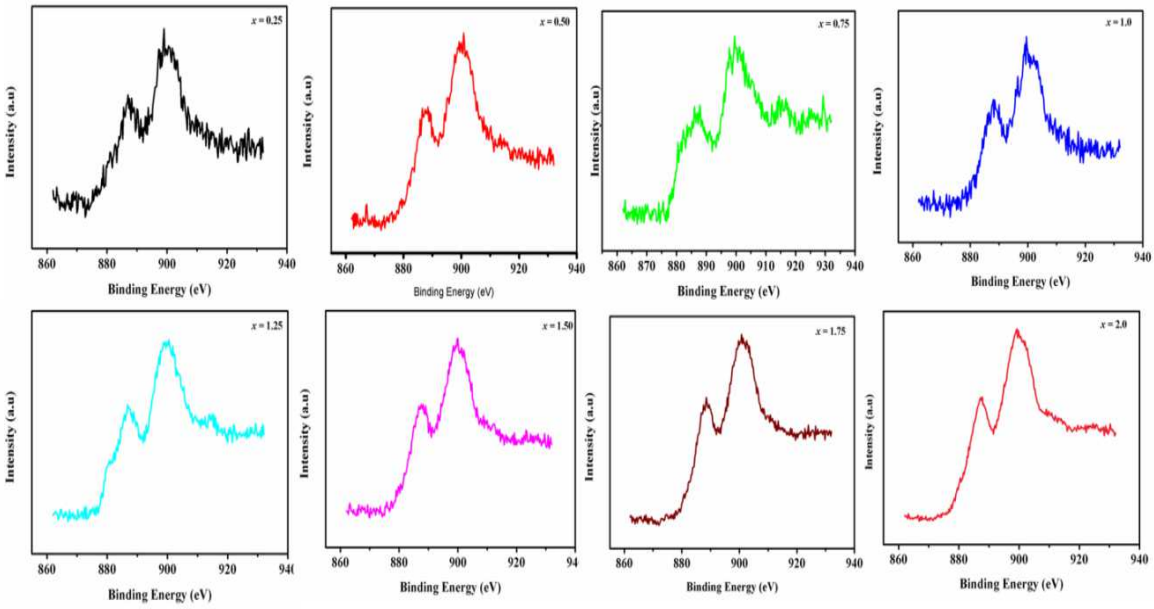

Fig. 6.8 XPS spectra of Ce (3d) core levels of $Sr_{2-x}Ba_xCe_{0.6}Tb_{0.4}O_4$ (x = 0.25, 0.50, 0.75, 1.0, 1.25, 1.50 and 2.0) pigments.

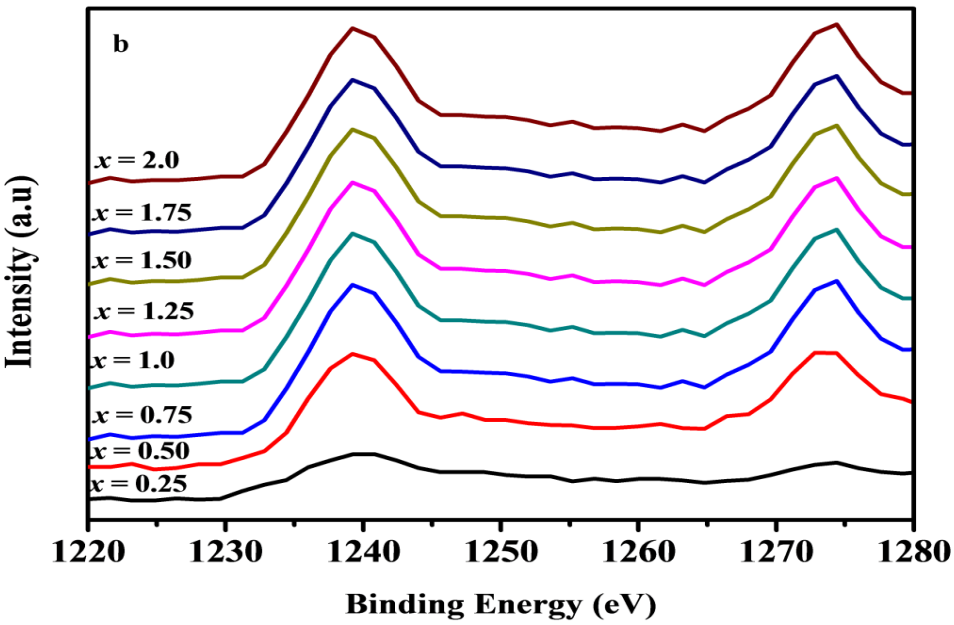

Fig. 6.9 XPS spectra of Tb (3d) core levels of $Sr_{2-x}Ba_xCe_{0.6}Tb_{0.4}O_4$ (x = 0.25, 0.50, 0.75, 1.0, 1.25, 1.50 and 2.0) pigments.

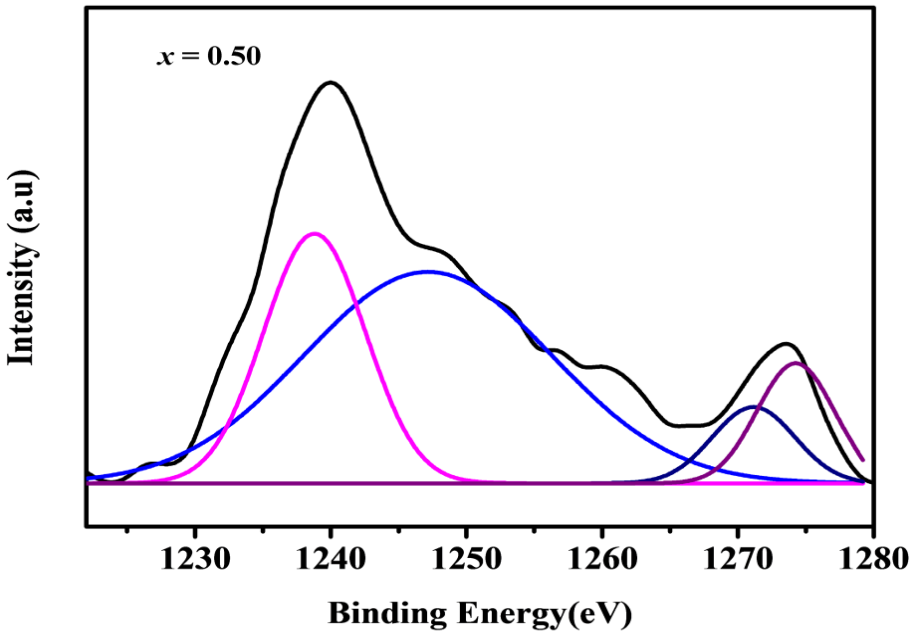

Fig. 6.10 Deconvoluted XPS spectra of Tb (3d) of $Sr_{1.5}Ba_{0.5}Ce_{0.6}Tb_{0.4}O_4$ pigments

The XPS results indicate that Ce and Tb is in a mixed valence state; Ce: 3+ (880.4, 885.5, 898.81 and 904.07 ± 0.7 eV), and 4+ (882.7, 888.96, 898.2, 901.30, 907 and 916.7 ± 0.7 eV) (Amit et al. 2009), Tb: 3+ (1239.09 and 1274.94 ± 0.7 eV)

and Tb: 4+ (1242.59 and 1276.28 ± 0.7 eV) (Li et al. 2016) corresponding to the $3d_{5/2}$ and $3d_{3/2}$ spin-orbit doublets. The peak areas of Ce^{3+} / Tb^{3+} were used to calculate the relative amount of Ce^{3+} / Tb^{3+} concentration in the lattice (Sharma et al. 2015). The Ce^{3+} / Tb^{3+} concentration was calculated from the relative molar ratio of Ce^{3+} / Tb^{3+} to the (Ce^{3+} + Ce^{4+} / Tb^{3+} + Tb^{4+}) and the values are listed in Table 6.3. These results demonstrated that the mixed valence states of the cerium and terbium species (+3 and +4) in the system and Ce^{4+} / Tb^{4+} is more dominant in the synthesized system. When Ba^{2+} was substituted into $Sr_2Ce_{0.6}Tb_{0.4}O_4$, the Ce 3d XPS shows that the peaks of Ce^{4+} $3d_{3/2}$, and Ce^{4+} $3d_{5/2}$ become stronger indicating the decrease of Ce^{3+} concentration in the sample with respect to the increase in dopant concentration. While the Tb^{4+} $3d_{3/2}$ and Tb^{4+} $3d_{5/2}$ the peaks of Tb 3d XPS become decreasing and Tb^{3+} $3d_{3/2}$ and Tb^{3+} $3d_{5/2}$ peaks increasing indicating the increase of Tb^{3+} concentration in the sample with respect to the Ba^{2+} concentration. This change in terbium oxidation states leads to the tuning of bang gap in turn changes the color from yellow to red by Ba^{2+} substitution.

Table 6.3 Ce^{3+} and Tb^{3+} concentration values of $Sr_{2-x}Ba_xCe_{0.6}Tb_{0.4}O_4$ (x = 0.25, 0.50, 0.75, 1.0, 1.25, 1.50 and 2.0) pigments.

	[Ce^{3+}] %	[Tb^{3+}]
x = 0	33.92	39.76
x = 0.25	32.68	38.32
x = 0.50	32.59	35.71
x = 0.75	32.51	36.90
x = 1.0	33.34	38.33
x = 1.25	31.76	39.19
x = 1.50	30.30	43.76
x = 1.75	29.95	52.59
x = 2.0	29.38	54.32

6.3.2.3 Morphological Studies

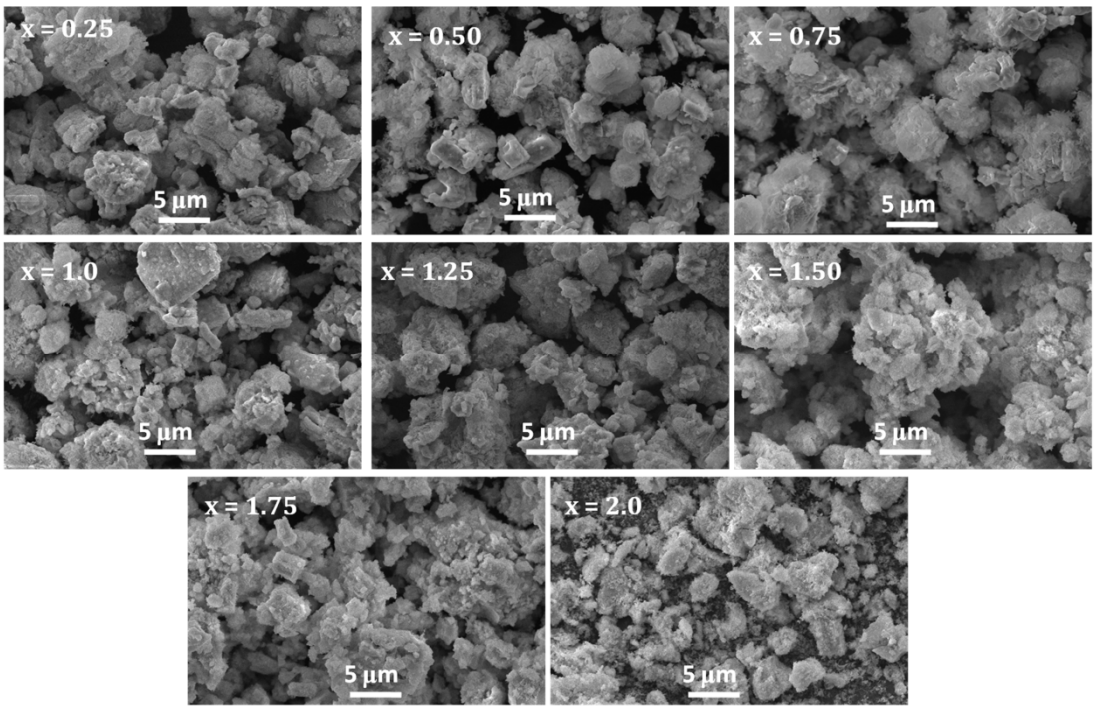

Fig. 6.11 Typical SEM photographs of $Sr_{2-x}Ba_xCe_{0.6}Tb_{0.4}O_4$ (*x* = 0.25, 0.50, 0.75, 1.0, 1.25, 1.50 and 2.0) pigments.

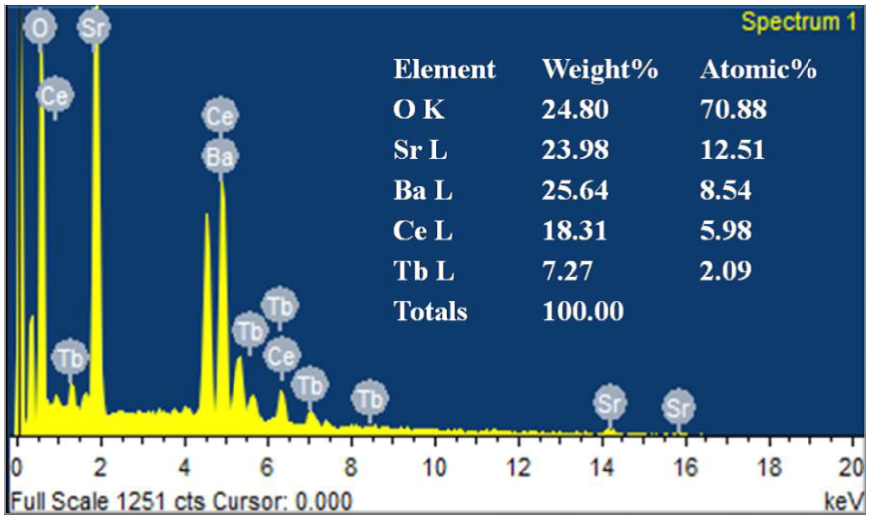

Fig 6.12 EDS spectra of $BaSrCe_{0.6}Tb_{0.4}O_4$ yellow pigment.

The synthesis condition and treatment process affect the morphological features and size of the material which can be analysed using Scanning electron microscopy (SEM) (Huang et al. 2018; Thara et al. 2017). Fig. 6.11, shows the typical SEM micrographs of $Sr_{2-x}Ba_xCe_{0.6}Tb_{0.4}O_4$ (x = 0.25, 0.50, 0.75, 1.0, 1.25, 1.50 and 2.0)

pigments. The particles are slightly agglomerated with size range of 1–4 μm. The chemical composition was checked by energy dispersive spectrometer (EDS) analysis attached with SEM. Fig. 6.12 shows the EDS micro-chemical analysis of the $SrBaCe_{0.6}Tb_{0.4}O_4$ sample and identifies the presence of all the expected elements in the desired atomic and weight percentages. Elemental X-ray dot mapping analysis of the synthesized $SrBaCe_{0.6}Tb_{0.4}O_4$ pigments is shown in Fig. 6.13. This mapping shows that all the elements are uniformly distributed in the sample.

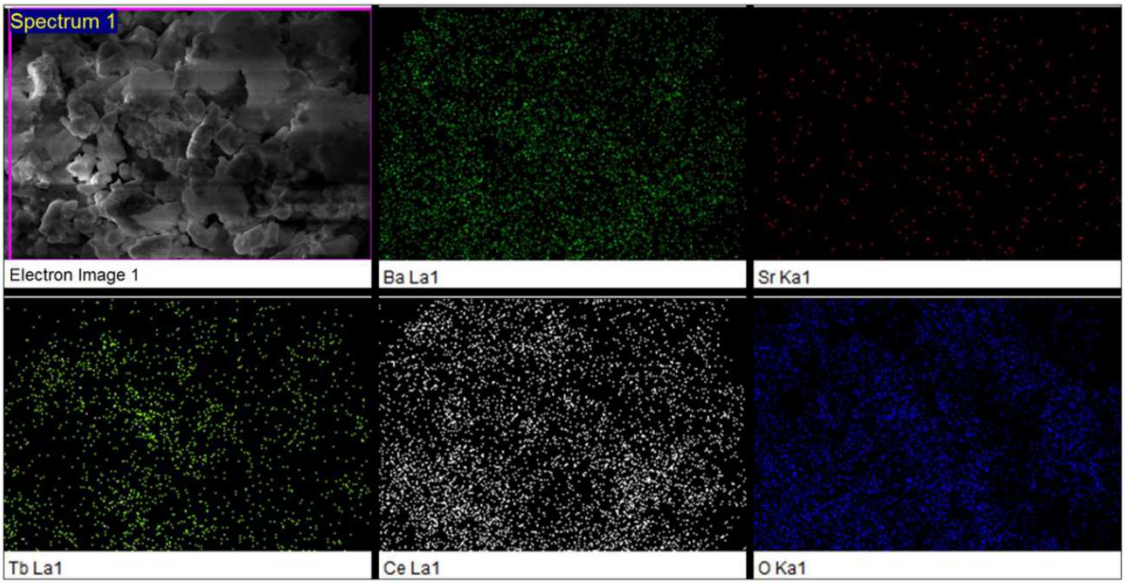

Fig. 6.13 Elemental dot mapping of $SrBaCe_{0.6}Tb_{0.4}O_4$ yellow pigment.

6.3.2.4 UV-visible Studies

The absorption spectra of the $Sr_{2-x}Ba_xCe_{0.6}Tb_{0.4}O_4$ (x = 0.25, 0.50, 0.75, 1.0, 1.25, 1.50 and 2.0) pigments in the UV–vis–NIR region are shown in Fig. 6.14. The absorption spectra of the pigments is characterized by a broad absorption band due to charge transfer transition from the valence band consisting of the O(2p) orbitals to the conduction band derived from the Tb(4f) orbitals and the secondary Ba(2p) orbitals. Strong visible absorption in the blue region (below 490 nm) is observed and by the Ba^{2+} substitution the absorption edge is gently red shifted to the longer wavelength side. The band gap energies (Eg) of the synthesized samples are calculated by tauc plot method from the absorption spectra and the variation of the band gap is listed in Table 6.4. Consequently, the prepared pigments exhibit the fine tuning of colors from yellow to red by tuning the band gap from 2.45 eV to 2.08 eV.

From the XPS analysis, the increase in the Ce^{4+} concentrations with respect to the increase in the Ba^{2+} enabling the charge transfer energy to a lower level (Athira et al. 2019). Thus the decrease in band gap can be explained on the basis of the shift of charge transfer band to higher wavelengths due to a reduction in the CTB energy by Ba^{2+} doping. Hence, the Ba^{2+} substitution allows fine tuning the color from yellow to red hues by tuning the band gap energy.

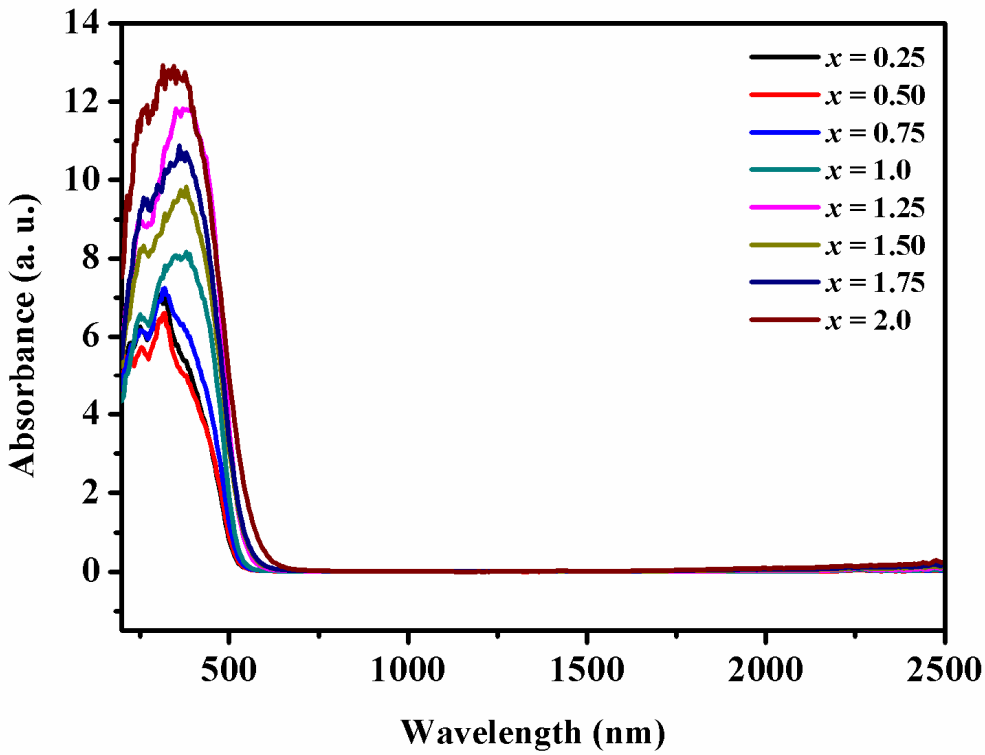

Fig. 6.14 Absorption spectra of $Sr_{2-x}Ba_xCe_{0.6}Tb_{0.4}O_4$ (x = 0.25, 0.50, 0.75, 1.0, 1.25, 1.50 and 2.0) pigments.

6.3.2.5 Color performance

The chromatic properties of the pigments can be numerically expressed in terms of color co-ordinates by using CIE 1976 color coordinate system. The CIE 1976 color coordinates of the Ba^{2+} doped $Sr_2Ce_{0.6}Tb_{0.4}O_4$ powdered pigment samples are listed in Table 6.4. This shows that the Ba^{2+} substitution increases the b^* value from 64.81 (x = 0.25) to 75.36 (x = 1.0) i.e the yellowness of the pigment samples is enhanced and further increase in Ba^{2+} substitution reduces the b^* to 48.60. Simultaneously, the increase in doping concentration leads to an increase in red hue of the pigment that is evident from the increasing values of the color coordinate a^* i.e

from 8.26 (x = 0.25) to 28.92 (x = 2.0). The hue angle (h°) of the synthesized pigments decreases gradually from 82.73 to 61.96. The hue angles (h°) of the powdered $Sr_{2-x}Ba_xCe_{0.6}Tb_{0.4}O_4$ (x = 0.25, 0.50, 0.75 and 1.0) pigment samples were found to be in the yellow region of the cylindrical color space (h° = 70°–105° for yellow) and $Sr_{2-x}Ba_xCe_{0.6}Tb_{0.4}O_4$ (x = 1.25, 1.50 and 2.0) in the orange-red region of the cylindrical color space (h° = 35-70 for orange-red). Among these pigments $SrBaCe_{0.6}Tb_{0.4}O_4$ showed the most brilliant yellow hue with a yellowness b^* = 75.36 which is higher than that of the terbium doped Sr_2CeO_4 yellow pigments (Athira et al. 2014) and comparable with the commercially available pigment sicopal yellow (b^* = 76.9, C^* = 78.7) (Wendusu et al. 2013). However in this study, only lower concentrations of terbium is required to obtain good color characteristics, which make them very cost-effective for the commercial use. Photographs of the developed pigments are shown in Fig. 6.15. From these values/photographs it was clear that the substitution of Ba^{2+} in the Sr^{2+} site of $Sr_2Ce_{0.6}Tb_{0.4}O_4$ yellow pigment leads to the fine tuning the color from yellow to red hues by tuning the band gap energy.

Table 6.4 Color coordinates, band gap NIR reflectance and solar reflectance values of the $Sr_{2-x}Ba_xCe_{0.6}Tb_{0.4}O_4$ (x = 0.25, 0.50, 0.75, 1.0, 1.25, 1.50 and 2.0) pigments.

	L^*	a^*	b^*	C_{ab}	h°	E_g (eV)	R (%)	R' (%)
x = 0.25	82.03	8.26	64.81	65.34	82.73	2.45	89	84
x = 0.50	81.57	9.69	64.66	65.39	81.47	2.42	89	85
x = 0.75	79.78	12.25	67.96	69.05	79.78	2.38	90	87
x = 1.00	77.34	18.09	75.36	77.56	78.14	2.37	91	89
x = 1.25	67.58	28.20	68.14	73.75	67.51	2.35	91	89
x = 1.50	64.56	27.70	58.86	65.05	65.12	2.32	90	89
x = 1.75	65.55	27.18	58.63	64.63	64.79	2.29	88	83
x = 2.0	58.82	28.92	48.60	55.06	61.96	2.08	86	81

Fig. 6.15 Photographs of the $Sr_{2-x}Ba_xCe_{0.6}Tb_{0.4}O_4$ (x = 0.25, 0.50, 0.75, 1.0, 1.25, 1.50 and 2.0) pigments.

6.3.2.6 NIR Reflectance Studies

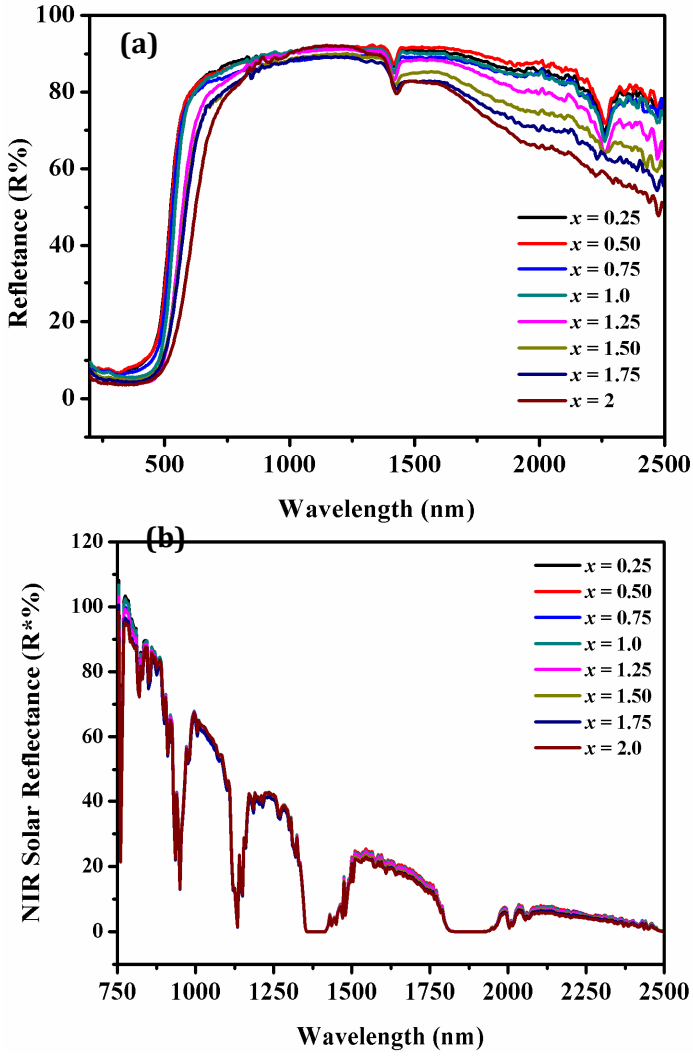

Fig. 6.16 (a) NIR reflectance and (b) NIR solar reflectance spectra of the $Sr_{2-x}Ba_xCe_{0.6}Tb_{0.4}O_4$ (x = 0.25, 0.50, 0.75, 1.0, 1.25, 1.50 and 2.0) pigments

Non white coating that absorbs more solar energy in the visible region should be less reflective whereas a cool non white coating that absorbs less should be highly reflective in the near-infrared (NIR) part of the electromagnetic spectrum which is main responsible for heat buildup (Sameera et al. 2014). In order to study reflectance properties of the pigments, the NIR reflectance and NIR solar reflectance spectra of the $Sr_{2-x}Ba_xCe_{0.6}Tb_{0.4}O_4$ (x = 0.25, 0.50, 0.75, 1.0, 1.25, 1.50 and 2.0) pigments in the range 200 to 2500 nm by using PTFE as reference are shown in Fig. 6.16 a–b and the values are listed in Table 6.4. Successive doping of Ba^{2+} into $Sr_2Ce_{0.6}Tb_{0.4}O_4$ enhances the NIR and NIR solar reflectance up to 92% for x = 1.0 and further increases in the Ba^{2+} concentration reduces the reflectance value to a small degree. Moreover, all the synthesized pigments possess a very high reflectance values which makes them as interesting cool colorants to reduce heat buildup.

6.3.3 The Influence of Tb doping on the Color Performance of Ba_2CeO_4 as High NIR Reflecting Red Pigments

6.3.3.1 Powder X-ray diffraction studies

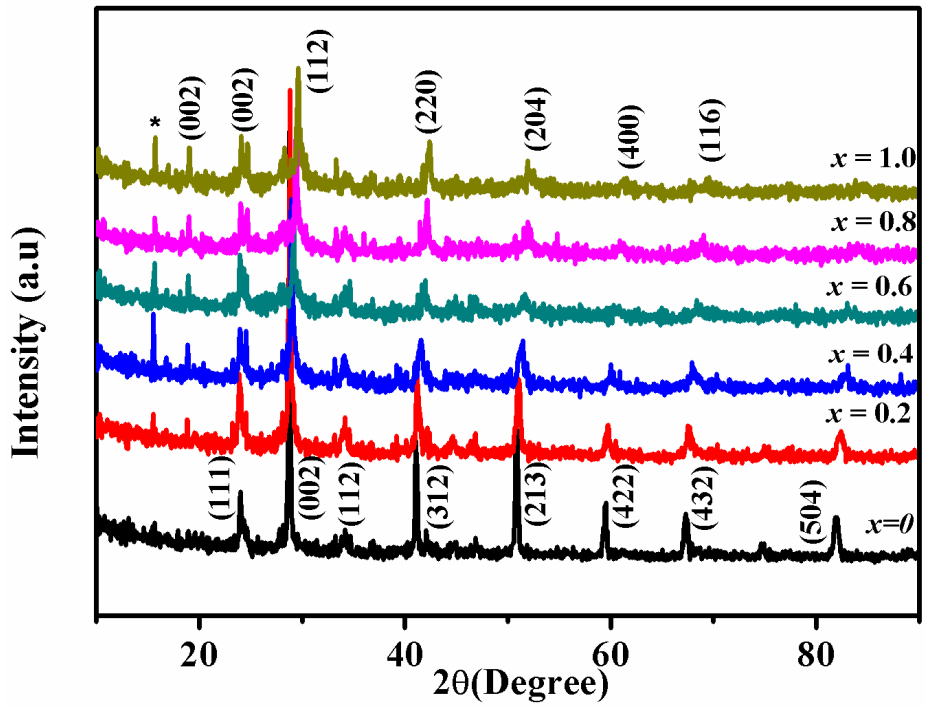

Fig. 6.17 X-ray powder diffraction patterns of $Ba_2Ce_{1-x}Tb_xO_4$ (x = 0, 0.20, 0.40, 0.60, 0.80 and 1.0) pigments (* indicates $BaTbO_3$ phase)

The powder XRD patterns of the $Ba_2Ce_{1-x}Tb_xO_4$ (x = 0, 0.20, 0.40, 0.60, 0.80 and 1.0) pigments synthesized via conventional solid state reaction method are shown in Fig. 6.17. The sharp and intense peaks in the diffraction patterns confirm the crystalline nature of the powders. It was found that the progressive doping of Tb^{4+} brings a structural transition from the perovskite orthorhombic to the tetragonal form i.e the compositions x = 0 to x = 0.4 crystallizes the pure orthorhombic phase with space group Pmcn, and all the peaks are indexed according to the JCPDS database with File No. 01-071-6749. Partial phase transformation occurred for x = 0.4 substitution from orthorhombic to tetragonal. Further, the compositions with x = 0.6 to x =1.0 form the tetragonal phase, which can be indexed as per the JCPDS File No. 01-073-9083 with the space group I4/mcm. In orthorhombic perovskite Ba_2CeO_4, the Ce site bounded with six oxygen atoms forms a CeO_6 octahedron and Ba site bounded with twelve oxygen atoms forms a BaO_{12}

polyhedron. The amount of rare earth element determines the structure of the synthesized compounds. The doping of Tb^{4+} (0.076 nm; CN = 6) in the Ce^{4+} site (0.087 nm; CN = 6) results a small distortion in CeO_6 octahedron of the lattice due to the difference in ionic radius. The lattice volume increases with increase in dopant concentration from x = 0 - 0.4 and then decreases for further doping of x = 0.6-1.0. This ambiguity in the lattice volume is because of due to the structural transformation by Tb^{4+} substitution which leads to the variation in unit cell volume and band gap narrowing (Jo et al. 2015). The variation of lattice parameters and the volume of the cell obtained at different dopant concentrations are shown in Table 6.5.

Table 6.5 Variation of lattice parameters and volume of the cell of $Ba_2Ce_{1-x}Tb_xO_4$ (x = 0, 0.20, 0.40, 0.60, 0.80 and 1.0) pigments.

	Lattice Parameter			Volume	Structure
	a(Å)	b(Å)	c(Å)	(Å)^3	
x = 0	8.8066	6.2414	6.2026	340.93	*Pmcn* Orthorombic
x = 0.20	8.7679	6.5984	6.1919	358.22	
x = 0.40	8.7187	6.5728	6.1532	352.61	
x = 0.60	6.0483	6.0483	8.5860	340.92	*I4/mcm* Orthorombic
x = 0.80	6.0870	6.0870	8.5740	314.09	
x = 1.0	6.0285	6.0285	8.5276	3.09.91	

6.3.3.2 X-ray Photoelectron Spectroscopic studies

X-ray photoelectron spectra of the $Ba_2Ce_{1-x}Tb_xO_4$ (x = 0, 0.20, 0.40, 0.60, 0.80 and 1.0) pigments were carried out and the wide survey scan in the range 0–1300 eV are shown in Fig. 6.18. The XPS of Ce 3d and Tb 3d core levels spectra for the synthesised samples are shown in Fig. 6.19. The Ce XPS spectrum clearly shows three pairs of spin–orbit doublets, which suggests that Ce(IV) dominates in our system. The deconvolution of the Ce 3d and Tb 3d photoelectron peaks were done

for the quantitative measurement of Ce^{3+} / Tb^{3+} concentrations in the systems and the values are listed in Table 6.6. It was found that the concentration of Ce^{3+} reduces with the increase in dopant concentration and comparatively less with that of the Sr_2CeO_4 systems. As the terbium concentration increases, Tb^{3+} is more dominant in the synthesized system.

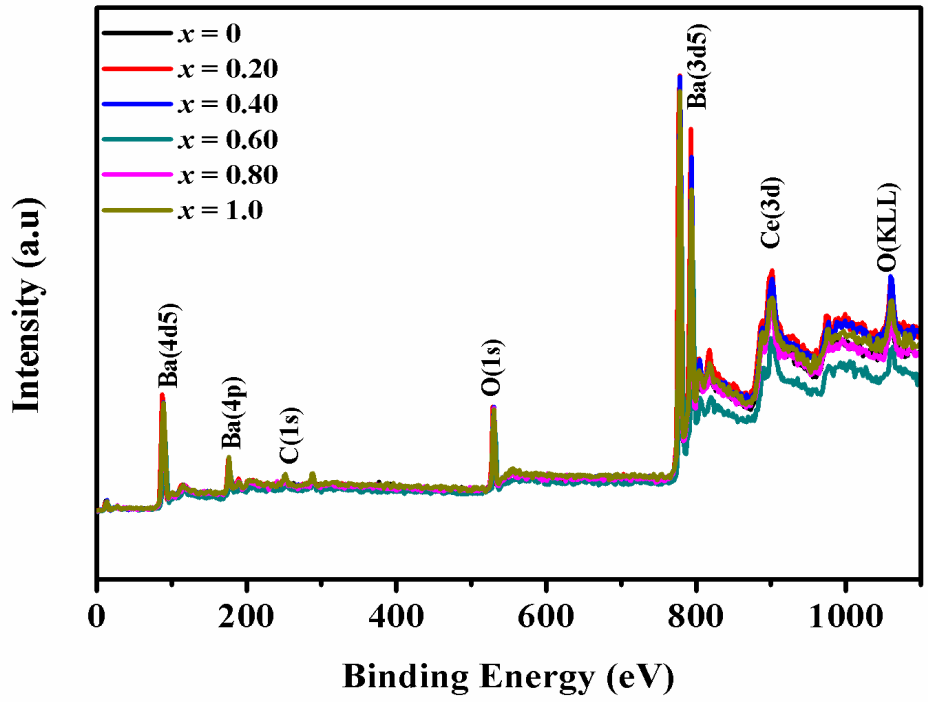

Fig. 6.18 XPS survey spectra of $Ba_2Ce_{1-x}Tb_xO_4$ (x = 0, 0.20, 0.40, 0.60, 0.80 and 1.0) pigments.

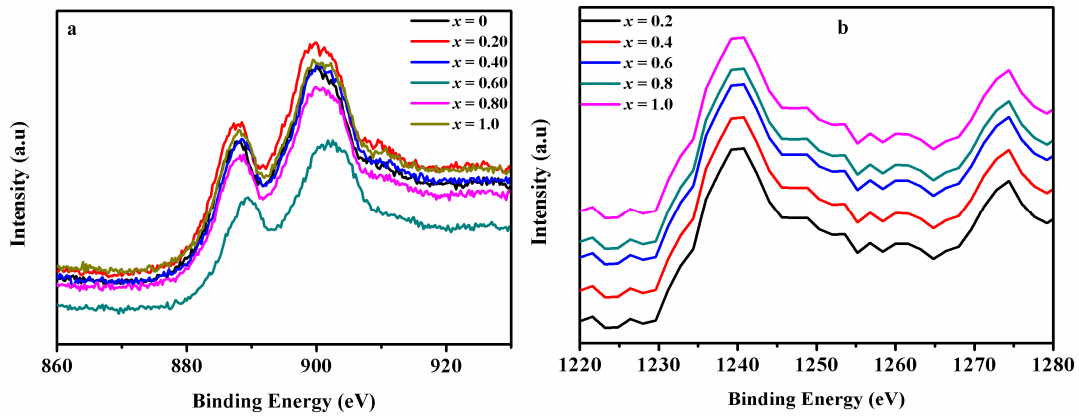

Fig. 6.19 XPS spectra of a) Ce (3d) and b) Tb (3d) core levels of $Ba_2Ce_{1-x}Tb_xO_4$ (x = 0, 0.20, 0.40, 0.60, 0.80 and 1.0) pigments.

Table 6.6 Ce^{3+} and Tb^{3+} concentration values of $Ba_2Ce_{1-x}Tb_xO_4$ (x = 0, 0.20, 0.40, 0.60, 0.80 and 1.0) pigments.

	$[Ce^{3+}]$ %	$[Tb^{3+}]$
x = 0	32.74	--
x = 0.2	29.40	54.32
x = 0.4	29.38	55.79
x = 0.6	28.38	58.13
x = 0.8	17.99	56.20
x = 1.0	--	55.92

6.3.3.3 Morphological Studies

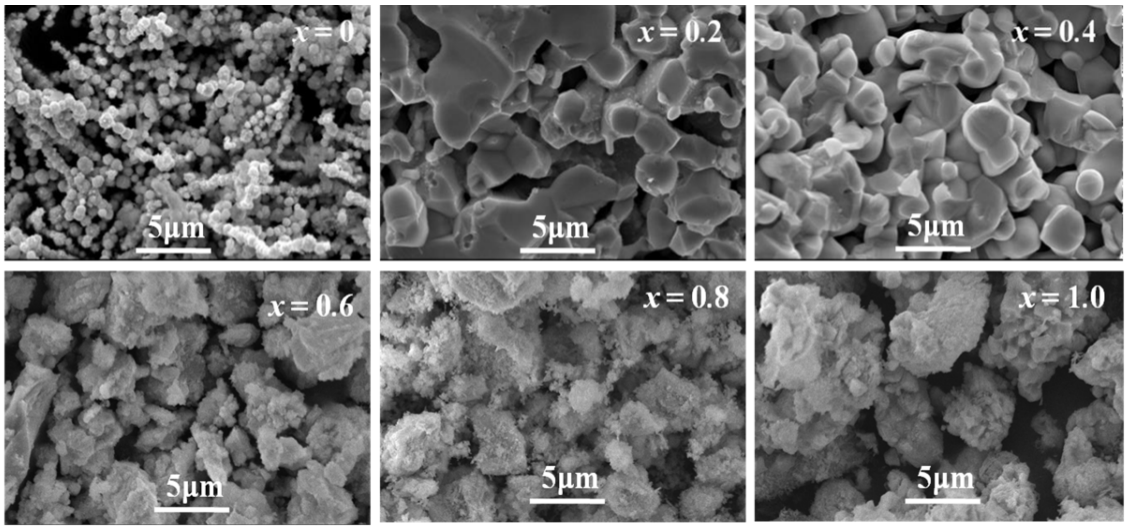

Fig. 6.20 Typical SEM photographs of $Ba_2Ce_{1-x}Tb_xO_4$ (x = 0, 0.20, 0.40, 0.60, 0.80 and 1.0) pigments.

Fig. 6.20 shows the typical SEM micrographs of $Ba_2Ce_{1-x}Tb_xO_4$ (x = 0, 0.20, 0.40, 0.60, 0.80 and 1.0) pigments. The particle size increases with the dopant concentration and are slightly agglomerated with size of 1-5 µm. EDS spectra of typical $Ba_2Ce_{0.6}Tb_{0.4}O_4$ sample shows in Fig. 6.21 which identifies the presence of all the expected elements (Ba, Ce, Tb and O) in the sample. Elemental X-ray dot

mapping analysis of this pigment is shown in Fig. 6.22 which confirms the uniform distribution of elements in the sample.

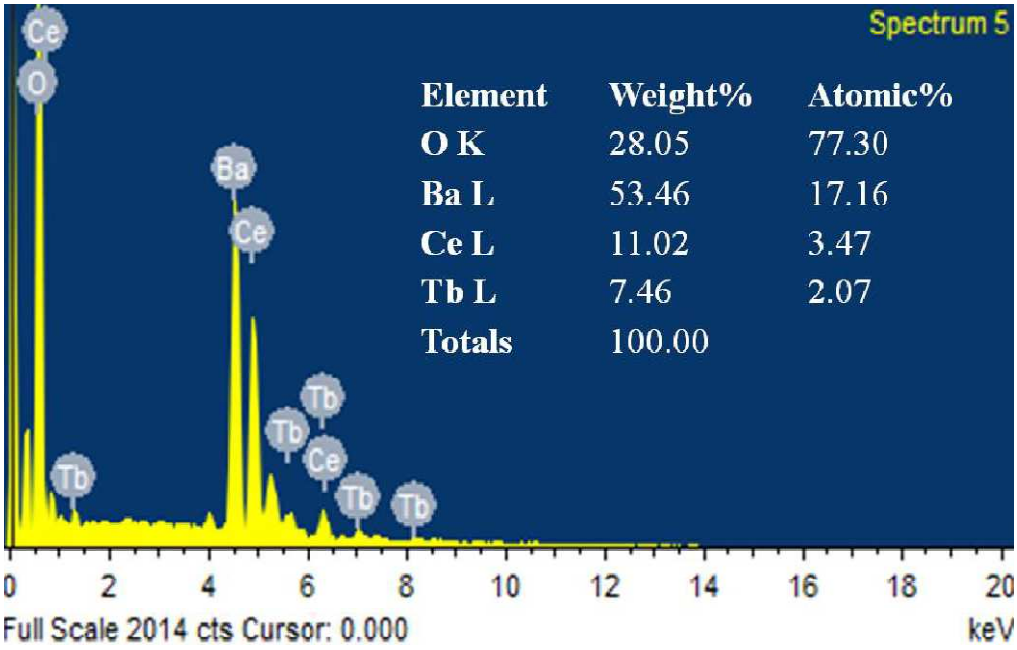

Fig. 6.21 EDS spectra of $Ba_2Ce_{0.6}Tb_{0.4}O_4$ red pigment.

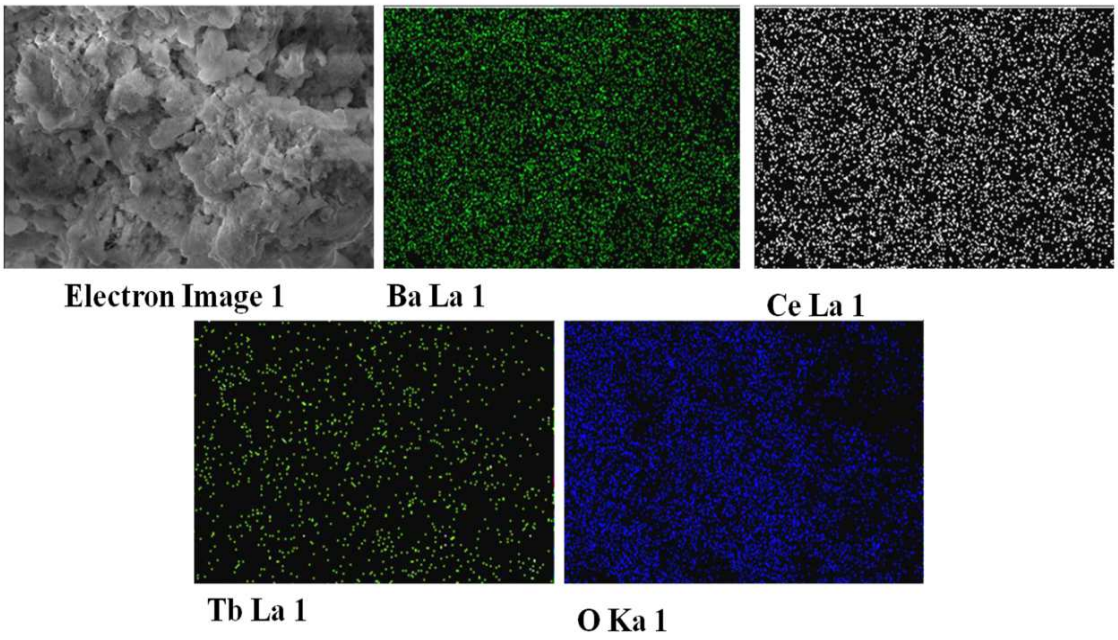

Fig. 6.22 Elemental dot mapping of $Ba_2Ce_{0.4}Tb_{0.6}O_4$ red pigment.

6.3.3.4 UV-visible Studies

UV–vis absorption spectra of the $Ba_2Ce_{1-x}Tb_xO_4$ (x = 0, 0.20, 0.40, 0.60, 0.80 and 1.0) pigments are shown in Fig. 6.23. Ba_2CeO_4 have a strong absorption band around 410 nm which can be attributed to the charge-transfer transition of hybrid orbitals consisting of O(2p) – Ce(4f). By Tb substitution, the absorption edge is drastically shifted to the longer wavelength side (red shift) i.e the 4f electrons of terbium valence shell introduce an additional electronic level of energy between the O^{2-} valence band and Ce^{4+} conduction band and red shift in the absorption edge (reduction in band gap from 3.16 eV to 1.86 eV) is observed and the variation of band gap with increasing terbium doping is tabulated in Table 6.7. It was observed that there is a decreasing trend of band gap upto x = 0.60, further there is a slight increase. Similar results have also been observed in the terbium doped Sr_2CeO_4 systems which may be due to the structural transition.

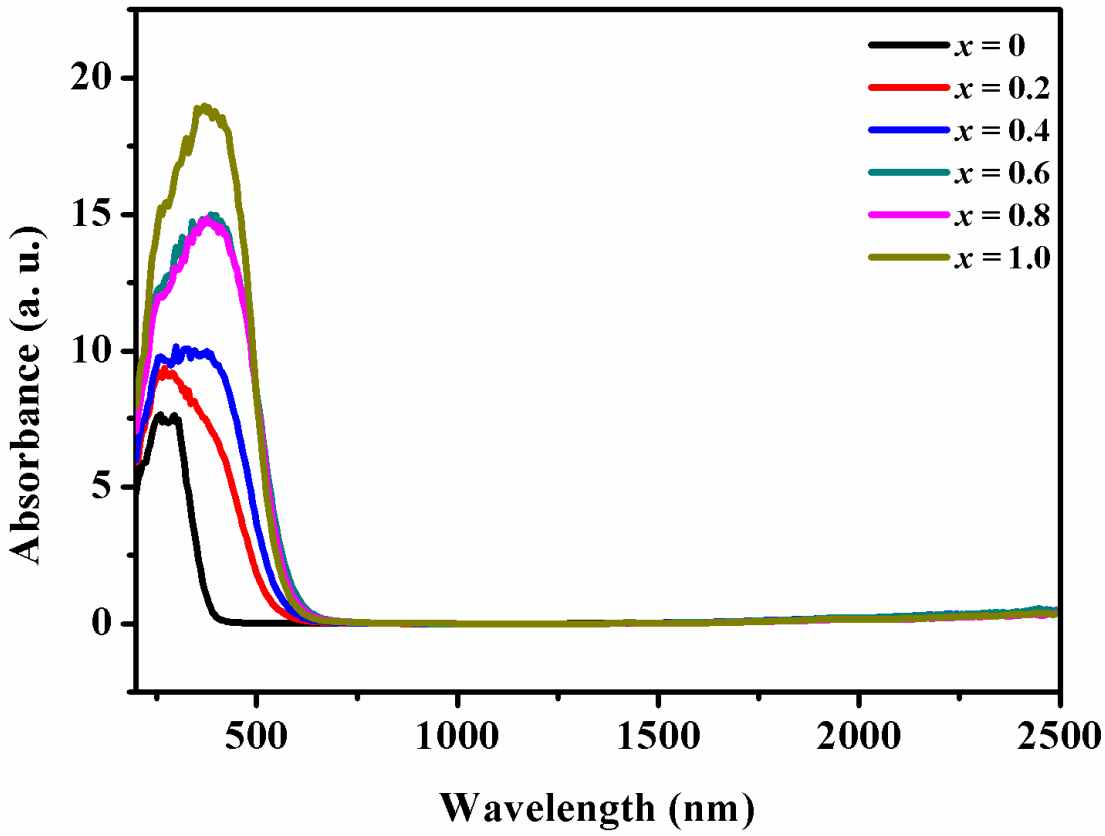

Fig. 6.23 Absorption spectra of $Ba_2Ce_{1-x}Tb_xO_4$ (x = 0, 0.20, 0.40, 0.60, 0.80 and 1.0) pigments.

Table 6.7 Color coordinates, band gap NIR reflectance and solar reflectance values of the $Ba_2Ce_{1-x}Tb_xO_4$ (x = 0, 0.20, 0.40, 0.60, 0.80 and 1.0) pigments.

	L^*	a^*	b^*	C_{ab}	$h°$	E_g (eV)	R (%)	R' (%)
x = 0	91.44	-1.12	5.71	5.82	101.05	3.16	87	85
x = 0.20	67.24	19.03	50.22	53.7	69.24	2.15	89	86
x = 0.40	58.82	28.92	48.6	55.06	61.96	2.08	88	87
x = 0.60	45.76	30.09	39.53	49.68	52.72	1.86	89	86
x = 0.80	48.09	31.48	43.39	53.61	54.03	2.01	88	84
x = 1.0	50.70	32.47	51.52	60.89	57.77	2.13	88	85

6.3.3.5 Color performance

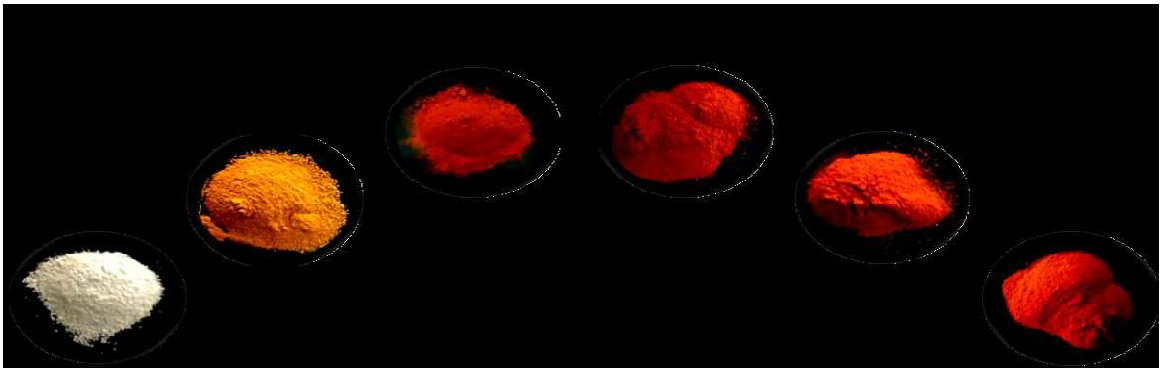

Fig. 6.24 Photographs of the $Ba_2Ce_{1-x}Tb_xO_4$ (x = 0, 0.20, 0.40, 0.60, 0.80 and 1.0) pigments.

The chromatic properties of the $Ba_2Ce_{1-x}Tb_xO_4$ (x = 0, 0.20, 0.40, 0.60, 0.80 and 1.0) pigments were evaluated by CIE 1976 L^* a^* b^* color coordinates values (Table 6.7). Doping of terbium in Ce^{4+} site results in the decrease of L^* values and a gradual increase in the a^* values from 19.03 (x = 0.20) to 32.47 (x = 0.20). The color coordinates of the typical pigment powder (Ba_2TbO_4) are significantly higher than that of the commercially available Fe_2O_3 pigment (L^* = 38.9, a^* = 28.9, b^* = 25.3) (Wendusu et al. 2014). The hue angle values reveal that the terbium doped Ba_2TbO_4 pigments lie in the reddish brown region of the cylindrical color space (h^0 = 0-35 for

red and 35-70 for orange).The photographs of the synthesized pigments are shown in Fig. 6.24.

6.3.3.6 NIR Reflectance Studies

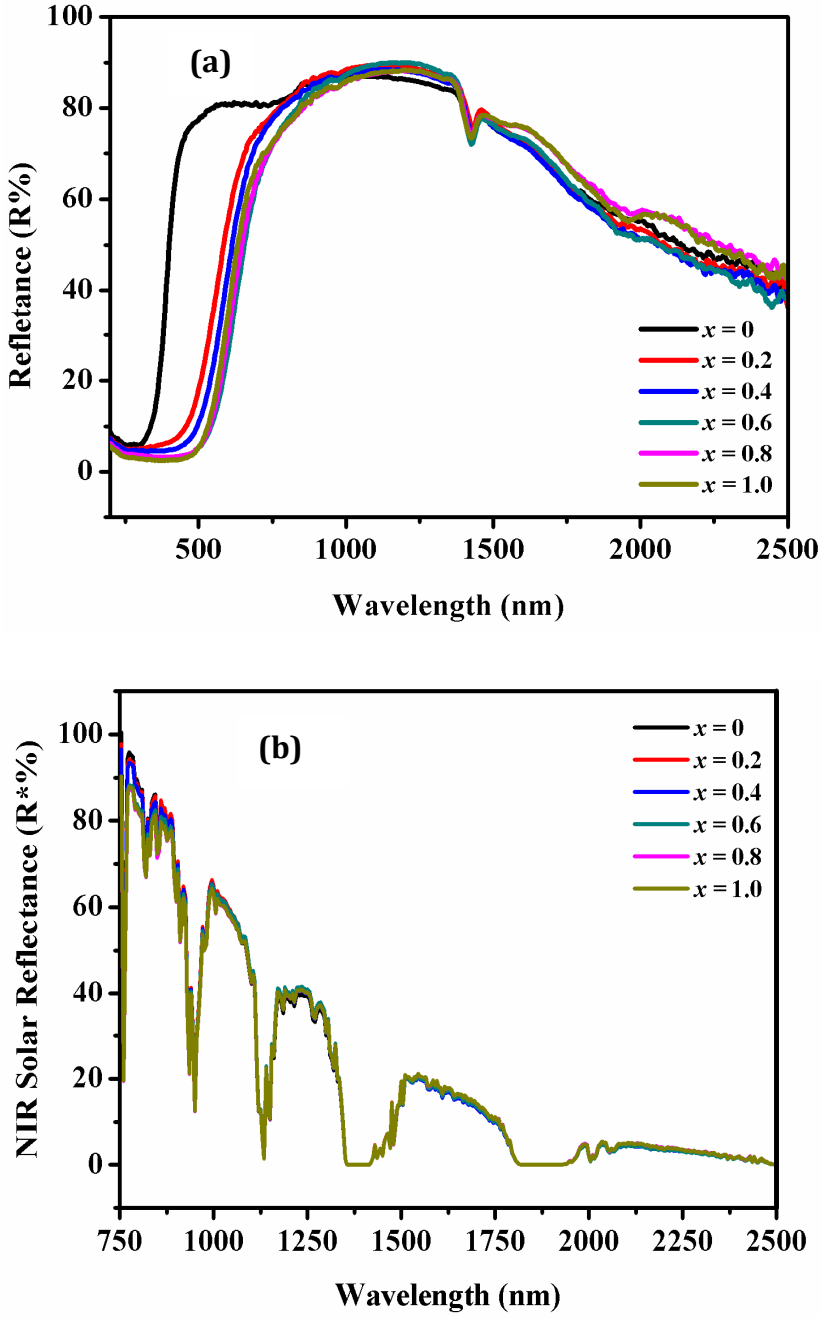

Fig. 6.25 NIR reflectance and NIR solar reflectance spectra of the $Ba_2Ce_{1-x}Tb_xO_4$ (x = 0, 0.20, 0.40, 0.60, 0.80 and 1.0) pigments.

NIR reflectance and NIR solar reflectance of the synthesized pigments are given in Fig. 6.25 a-b. It was seen that the undoped Ba_2CeO_4 sample exhibits NIR

reflectance (R) and NIR solar reflectance (R') of about 87% and 85% respectively. With the doping of Tb, the reflectance of the pigment slightly increases and all the pigments possess high NIR and solar reflectance which are higher than those of reported red pigments. Detailed information of NIR reflectance and NIR solar reflectance values are listed in Table 6.7. These values suggest that the pigments barely absorb the NIR solar energy (Huang et al. 2018). Hence, the designed pigments having high reflectance has been replacing the conventional inorganic red pigments as a way forward.

6.3.4 Acid/Alkali resistance and Thermal stability studies

Table 6.8 The color coordinates of $SrBaCe_{0.6}Tb_{0.4}O_4$ yellow and $Ba_2Ce_{0.4}Tb_{0.6}O_4$ red powder pigments after chemical resistance tests.

Composition	5% Acid/Alkali	L^*	a^*	b^*	ΔE^*_{ab}
$SrBaCe_{0.6}Tb_{0.4}O_4$	HCl	0.86	0.76	0.68	1.33
	HNO_3	0.85	0.74	0.62	1.23
	NaOH	0.76	0.59	0.65	1.16
	H_2O	0.34	0.41	0.57	0.78
$Ba_2Ce_{0.4}Tb_{0.6}O_4$	HCl	0.89	0.77	0.70	1.37
	HNO_3	0.73	0.79	0.77	1.32
	NaOH	0.68	0.72	0.68	1.20
	H_2O	0.49	0.53	0.44	0.85

The chemical stability in acid and alkaline media is essential in order to make the pigments useful in substrate due to the accumulation of acidic pollutants in the atmosphere that leads to the tarnishing of the substrates. Here, we have taken the typical pigments that exhibited better chromatic properties as well as reflectance; $SrBaCe_{0.6}Tb_{0.4}O_4$ yellow and $Ba_2Ce_{0.4}Tb_{0.6}O_4$ red pigment. The selected pigments were soaked in 5% HCl, HNO_3, NaOH and H_2O solution. The color coordinates of the soaked pigment samples are measured and compared with the untreated original

powder. The total color difference (ΔE^*_{ab}) was calculated and listed in Table 6.8 in the supporting information. The small values of ΔE^*_{ab} indicate that the designed pigments are chemically stable in the acid/alkali/H_2O media. Thermal stability of the typical pigments were investigated by thermo-gravimetric analysis in the range 50 - 1000˚C and the results clearly indicate that there is an insignificant weight loss ($SrBaCe_{0.6}Tb_{0.4}O_4$ = 0.19%; $Ba_2Ce_{0.4}Tb_{0.6}O_4$ = 0.27%) of the pigment in the above temperature range (Fig. 6.26 and 6.27).

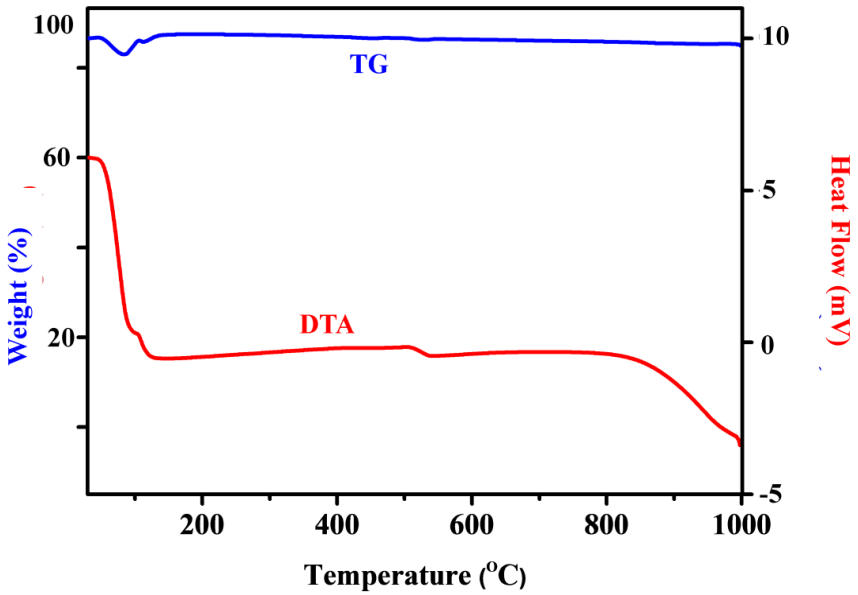

Fig. 6.26 TG-DTA of powdered $SrBaCe_{0.6}Tb_{0.4}O_4$ yellow pigment.

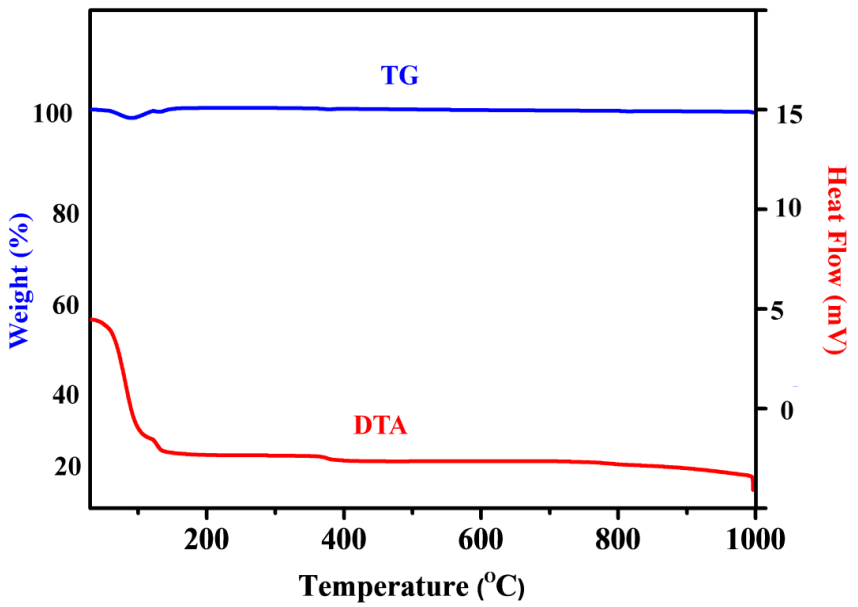

Fig. 6.27 TG-DTA of powdered $Ba_2Ce_{0.4}Tb_{0.6}O_4$ red pigment.

6.3.5 Application Studies

To evaluate the suitability of the developed pigments for energy saving applications, their performance was tested on a plastic material and building roofing material, concrete cement. For the coloration of plastics, 10 wt% $SrBaCe_{0.6}Tb_{0.4}O_4$ yellow and $Ba_2Ce_{0.4}Tb_{0.6}O_4$ red pigment powder was dispersed in Poly(methyl methacrylate) (PMMA) and compressed to a cylindrical disc and is shown in Fig. 6.28. The intensity of the color of plastics will depend on the concentration of the pigment used. The color coordinates of the polymer plastic were measured at different locations on the surface using portable spectrophotometer Miniscan EZ4000S (Hunter Lab USA) and the $L^*a^*b^*$ values obtained were more or less the same revealing the uniform distribution of the pigment particles in the polymer matrix. Thus the designed pigments may find potential application in the coloration of plastic materials.

Fig. 6.28 Photograph of 10 wt% $SrBaCe_{0.6}Tb_{0.4}O_4$ + PMMA and $Ba_2Ce_{0.4}Tb_{0.6}O_4$ + PMMA. The polymer matrix exhibit uniform distribution of pigment particles in the substrate.

Pigments coatings that absorb less NIR radiation other than the visible region can provide high solar reflectance along with pleasing color than that of conventional roofing materials and to keep objects cooler than they would be. To analyse the performance of the designed pigments as cool colorants for reducing the heat build-up, the typical pigments were coating on the concrete cement with and without TiO_2 base coat. The NIR solar reflectance spectra of the $SrBaCe_{0.6}Tb_{0.4}O_4$ yellow and $Ba_2Ce_{0.4}Tb_{0.6}O_4$ red pigment coated are shown in Fig. 6.29. The

photographs of the coating materials are displayed in Fig. 6.30 and the reflectance values of the coatings are depicted in Table 6.8. It is very interesting to note that the NIR reflectance and the corresponding solar reflectance of both yellow and red pigment coated substrates are higher than that of the bare concrete. Thus these non-white coatings (yellow and red coatings) can reduce the surface temperature of the building roofs and lead to energy savings.

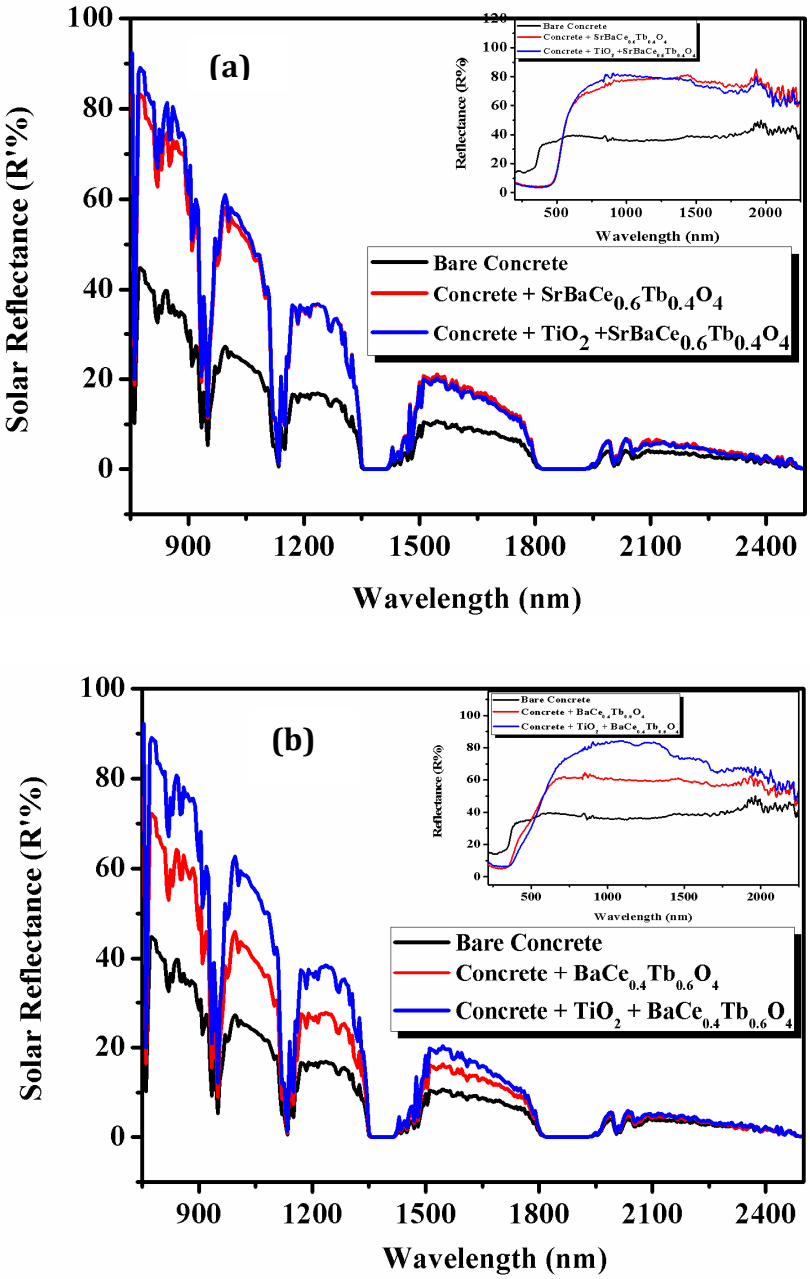

Fig. 6.29 NIR solar reflectance spectra of pigments a) $SrBaCe_{0.6}Tb_{0.4}O_4$ yellow and b) $Ba_2Ce_{0.4}Tb_{0.6}O_4$ red coated concrete cement with and without TiO_2 base coat (NIR reflectance in the inset)

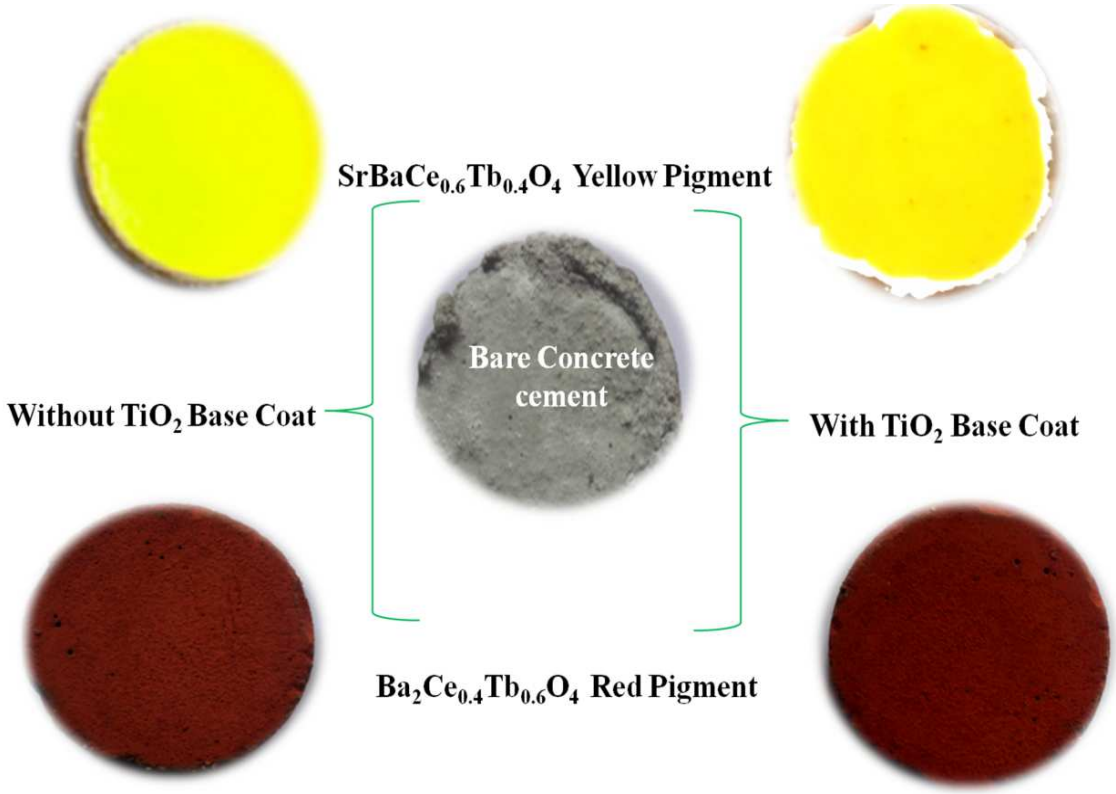

Fig. 6.30 Photographs of bare cement slab, $SrBaCe_{0.6}Tb_{0.4}O_4$ yellow and $Ba_2Ce_{0.4}Tb_{0.6}O_4$ red pigment coated cement slab without and with TiO_2 base coat.

Table 6.9 NIR reflectance and the solar reflectance data of $SrBaCe_{0.6}Tb_{0.4}O_4$ yellow and $Ba_2Ce_{0.4}Tb_{0.6}O_4$ red pigment coated on concrete cement.

Coatings	$SrBaCe_{0.6}Tb_{0.4}O_4$		$Ba_2Ce_{0.4}Tb_{0.6}O_4$	
	NIR reflectance (%)	NIR reflectance (%)	NIR Solar reflectance (%)	NIR Solar reflectance (%)
Bare Concrete	35.63	33.49	35.63	33.49
Concrete + Pigment	78.34	76.25	60.10	56.45
Concrete + TiO_2 + Pigment	80.38	79.08	84.27	82.89

6.4 Conclusions

A series of cerium based inorganic pigments with the formulae: $Sr_2Ce_{1-x}Tb_xO_4$ (x = 0, 0.20, 0.40, 0.60, 0.80 and 1.0), $Sr_{2-x}Ba_xCe_{0.6}Tb_{0.4}O_4$ (x = 0.25, 0.50, 0.75, 1.0, 1.25, 1.50 and 2.0) and $Ba_2Ce_{1-x}Tb_xO_4$ (x = 0, 0.20, 0.40, 0.60, 0.80 and 1.0) have been successfully developed via conventional solid-state reaction route. Terbium substitution in Sr_2CeO_4 exhibit various yellow colors by fine tuning of the band gap from 3.03 (white) to 2.52 eV (reddish-greenish yellow). The doping of Ba^{2+} in $Sr_2Ce_{0.6}Tb_{0.4}O_4$ changes the color from bright yellow to red. Terbium oxidation states play the key role in the band gap tuning. The pigments $SrBaCe_{0.6}Tb_{0.4}O_4$ (yellow; L^* = 77.34, a^* = 18.09, b^* = 75.36, R = 91%) and $Ba_2Ce_{0.4}Tb_{0.6}O_4$ (red; L^* = 45.76, a^* = 30.09, b^* = 39.53, R = 89%) exhibits brilliant coloristic and reflectance properties. All the pigments are thermally and chemically stable. The investigations on the optical and color characteristics of these pigments suggest that these pigments have the potential to be used as environmentally benign yellow pigments for plastic coloring and cool roof applications.

Chapter 7

Pigmentary colors from yellow to red in $Bi_2Ce_2O_7$ by rare earth ion substitutions as possible high NIR reflecting pigments

A new series of high near-infrared (NIR) reflecting pigments with colors ranging from yellow to red by tuning the $Bi_2Ce_2O_7$ with rare earth ion substitutions on both A and B sites were synthesized by a solid state reaction method. The absorption edge is gradiently red shifted on substitution from Y to Tb resulting colors yellow to red. A brilliant yellow hue was obtained for $Bi_{1.75}Y_{0.25}Ce_2O_7$ (b^*= 51.4), whereas $Bi_2Ce_{1.50}Tb_{0.50}O_7$ (a^*=15.0) exhibited a red color. High NIR solar reflectance of 93% and 88% were obtained for $Bi_{0.5}Y_{1.5}Ce_2O_7$ yellow and $Bi_2Ce_{1.50}Tb_{0.50}O_7$ red pigments respectively. The application study of these selected pigments was investigated in the polymer matrix which demonstrates their coloring performance for various potential applications. These results demonstrate the synthesized pigments as potential near infrared reflective candidates for cool roof applications.

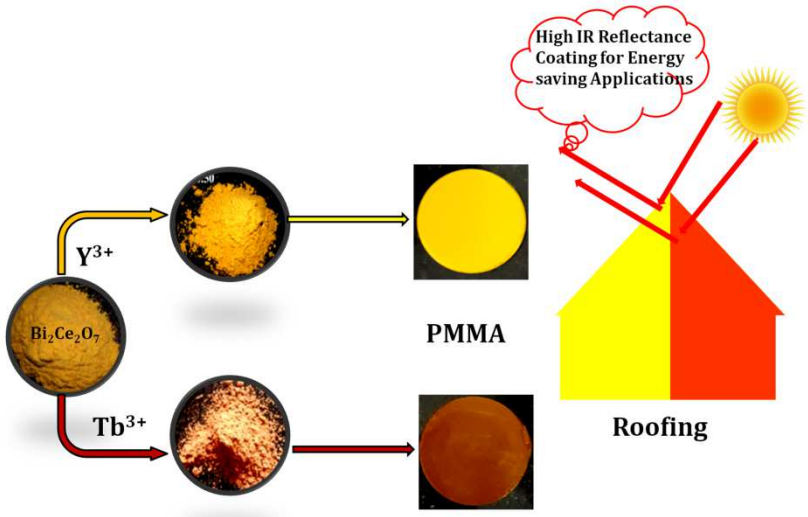

Athira et al. ***Dyes Pigm.,*** *160,* ***2019****, 177-187.*

7.1 Introduction

Inorganic pigments, which have been widely used from the prehistoric times which include naturally occurring substances prepared from minerals or their combustion products as well as synthetic compounds produced from appropriate raw materials and also by hybrid pigment types derived from organic dyes and selected mineral supports (Jesionowski et al. 2013). The majority of the inorganic pigments are suitable for use in a variety of applications such as paints and lacquers, plastics, inks, construction materials, paper, glass, and ceramics. The global consumption of pigments for 2012 (TiO_2: 50%, Colored inorganic pigment: 15%, Carbon black: 25% and Colored organic pigment: 10%) confirms the greater importance of inorganic pigments compared to organic pigments [Garo et al. 2010]. There is a necessity for developing stable and reproducible inorganic pigments with more intense shades and of low toxicity which favour the use of lanthanide oxides, which can substitute the conventional pigments (Kumari et al. 2008; Athira et al. 2017).

Recently, a series of lanthanide based inorganic pigments have been proposed as the possible substitutes for the traditional toxic pigments (Stranska et al. 2013; Grazenaite et al. 2018; Lin et al. 2018). These possess excellent chemical and thermal stabilities, low toxicity and color diversities which are the appropriate raw materials for the preparation of pigments (Honda et al. 2013). Among the lanthanide oxides, cerium oxide and its related materials have been studied and used as a pigment base because of its opacity, low toxicity and high temperature stability (Vishnu et al. 2009; Imanaka et al. 2008; Sulcova et al. 2002). Among the cerium based pigments, complex metal oxides of Sr_2CeO_4 (Athira et al. 2014), $Y_2Ce_2O_7$ (Athira et al. 2015; Vishnu et al. 2011; Zhao et al. 2013), $Sm_2Ce_2O_7$ (Vishnu et al. 2010) and $La_2Ce_2O_7$ (Bin et al. 2017) were extensively studied as yellow and red inorganic pigments with high NIR reflectance, which were potential as a replacement for traditional industrialized toxic pigments.

Another important oxide which has a potential in the field of pigment application is bismuth oxide and it seems to be interesting because they provide various color hues from yellow to orange (Tesitelova et al. 2017; Kumari et al. 2011). Most research is based on bismuth oxide (Bi_2O_3), which exhibits polymorphism with four different crystallographic forms (α, β, γ and δ-Bi_2O_3) (Steele et al. 2014). Among

the four polymorphs, the most stable form of the room temperature variety in Bi_2O_3 is the α-monoclinic polymorph (Darche et al. 2007). Many works have been reported in developing various hues of only Bi_2O_3 by various Ln ions substitutions into the host lattice of Bi_2O_3 (Sulcova et al. 2012). Recently $Bi_2Ce_2O_7$ which is considered as a promising optical material with a band gap of 2.3 eV has been investigated for inorganic pigment and solar photocatalytic activity materials (Sha et al. 2012). The low band gap systems allow easily to fine tune the band gap producing various colorants. Also, the system constitutes less toxic elements like Bi and Ce would make them eco-friendly host material. However, the studies about synthesis optimization and pigmenting properties of $Bi_2Ce_2O_7$ are still lacking, since most of the research concerning this system is focused on catalytic or redox properties. However, the coloristic performance is not adequate and their NIR reflectance has not been investigated. Hence developing novel colored pigments with high NIR reflectance become an important challenge in the current scenario.

In this context, we synthesized a cerium oxide based host lattice with the general formula $Bi_2Ce_2O_7$ and yttrium was substituted in Bi^{3+} site and terbium was substituted in Ce^{4+} site via a conventional solid state method to give the compositions $Bi_{2-x}Y_xCe_2O_7$ and $Bi_2Ce_{2-x}Tb_xO_7$ (x = 0.25, 0.50, 0,75, 1.0, 1.25 and 1.50) in order to probe the influence of substitutions on the structure and coloristic properties to obtain a new class of yellow and red, less-toxic pigments possessing high NIR reflectance. The properties of these pigments to confer high color hue as well as high NIR reflectance have also been evaluated in this article. The structure, morphology, optical and coloristic properties of the prepared powders were characterized by powder X-ray diffractometer (XRD), scanning electron microscope (SEM) with energy dispersive spectrometry (EDS), X-ray photoelectron spectroscopy (XPS), UV–vis NIR Spectroscopy and CIE 1976 $L^*a^*b^*$ color scales.

7.2 Experimental

7.2.1 Materials and Methods

The cerium-based pigments with the general formula $Bi_{2-x}Y_xCe_2O_7$ and $Bi_2Ce_{2-x}Tb_xO_7$ (x = 0.25, 0.50, 0,75, 1.0, 1.25 and 1.50) were synthesized by the conventional solid-state route. The raw materials, Bi_2O_3, CeO_2, Y_2O_3 and Tb_4O_7 (Sigma-Aldrich, 99.99% purity) were weighed in the stoichiometric ratio and homogenized by wet

mixing with acetone in an agate mortar until the fine slurry was obtained. The slurry was dried by placing it in an air oven at a temperature of 100°C. The mixing and drying were repeated three times to obtain a homogenous mixture. The mixed product was then calcined in a platinum crucible in an electric furnace at 1000 °C for 6 h. The temperature of the furnace is programmed with an initial heating rate of 10°C/min up to 700°C followed by a heating rate of 5°C/min to attain 1000°C.

7.2.2 Characterization

The crystalline structure of the calcined powders was characterized using X-ray powder diffraction (XRD) using a Ni-filtered Cu-Kα radiation with a PANalytical X'pert Pro diffractometer operated at 45 kV and 30 mA. Data were collected from 10 to 90° 2θ range with a step size of 0.016°. XPS of the samples were undertaken to establish the oxidation states and variations of the binding energies of the constituent elements using PHI 5000 Versa probe II having Al Kα monochromatic source. Particle morphological analysis of the powder was performed using a JEOL scanning electron microscope (model JSM-5600 LV) with an acceleration voltage of 15 kV. The X-ray microchemical analysis and elemental mapping of the samples were carried out using a Silicon Drift Detector–X-MaxN attached with a Carl Zeiss EVO SEM. The UV–vis NIR spectra of the pigments were recorded by a Shimadzu, UV-3600 spectrometer through diffuse reflectance technique using polytetrafluoroethylene (PTFE) as a reference. The optical band gap (Eg) of the synthesized samples was calculated using tauc plot. The NIR solar reflectance was determined from ASTM Standard G173-03. The color parameters of the pigment powders were determined by UVPC color analysis software coupled to the UV-3600 spectrophotometer at the measurement conditions kept as an illuminant D65, 10° complementary observer and measuring geometry d/8°. The thermal stability of the typical pigment was checked in the temperature range of 50–1000 °C by SII Nanotechnology Inc., thermogravimetric/differential thermal analysis (TG/DTA) 6200 in the air atmosphere at a heating rate of 10°C/min.

7.2.2 Application studies

Chemical resistance tests using acid/base solutions and water were also performed. A pre-weighed amount of the typical pigments: $Bi_{1.75}Y_{0.25}Ce_2O_7$, $Bi_2Ce_{1.50}Tb_{0.50}O_7$ with the best coloristic property was treated with 5% HCl, HNO_3,

NaOH, and H_2O and soaked for 1 h with continuous stirring using a magnetic stirrer. The pigment powder was then filtered, washed with deionized water, dried, and weighed. The CIE color coordinates were measured, and the color difference (ΔE^*_{ab}) was calculated from the following equation.

$$\Delta E^*_{ab} = \sqrt{(\Delta L^*)^2 + (\Delta a^*)^2 + (\Delta b^*)^2} \quad (7.1)$$

To test the capacity of the pigment samples to impart the yellow and red hues, the selected pigments were incorporated into a polymer substrate like Poly (methyl methacrylate) (PMMA) which is a well known water soluble polymeric material extensively used for cold extrusion of many inorganic oxides such as alumina and zirconia. A viscous solution of PMMA (90 wt%) was made using a conventional electric coil heater and 10 wt% of the pigment was slowly added with stirring and converted to a thick paste. The paste was then transferred into a mould and compressed into a cylindrical disc.

7.3 Results and discussion

7.3.1 Structural analysis of $Bi_{2-x}Y_xCe_2O_7$ and $Bi_2Ce_{2-x}Tb_xO_7$ systems

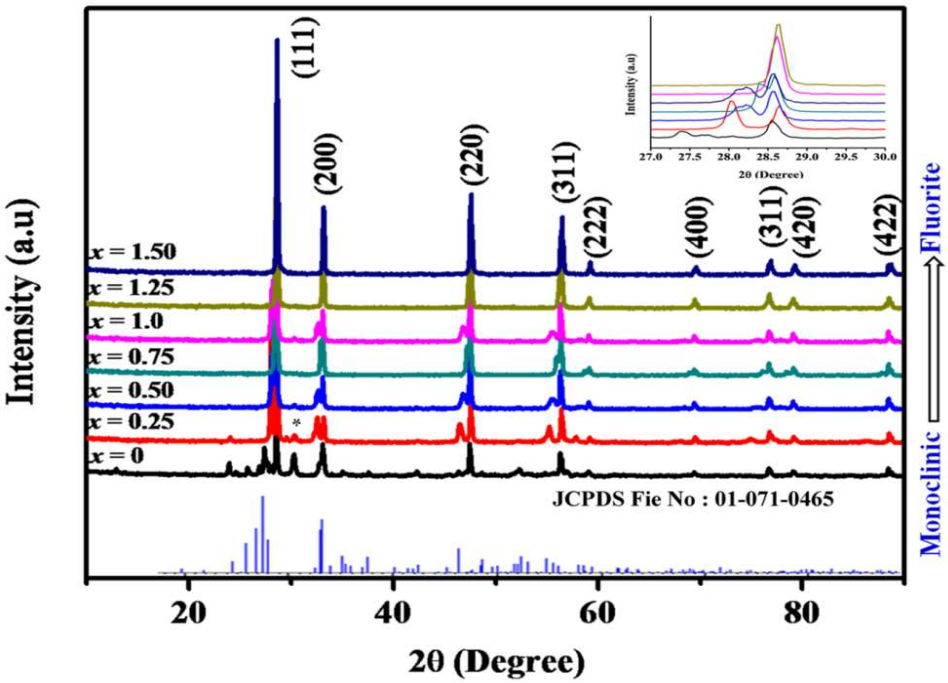

Fig. 7.1 Powder X-ray diffraction patterns of $Bi_{2-x}Y_xCe_2O_7$ (x = 0, 0.25, 0.5, 0.75, 1.0, 1.25, 1.5) pigments. The substitution of Y^{3+} in Bi^{3+} induces a structural transition from monoclinic to cubic fluorite. Additional Bi_4O_7 peaks are denoted by *.

Figs. 7.1 and 7.2 present the powder XRD patterns of the samples, $Bi_{2-x}Y_xCe_2O_7$ and $Bi_2Ce_{2-x}Tb_xO_7$ (x = 0, 0.25, 0.5, 0.75, 1.0, 1.25, 1.5) with different concentrations of yttrium and terbium. The sharp and intense peaks indicate the crystalline nature of the samples. The substitution of rare earths in Bi^{3+} and Ce^{4+} sites in $Bi_2Ce_2O_7$ induces a structural transition from a monoclinic to a cubic fluorite type structure. The parent compound: $Bi_2Ce_2O_7$ crystallizes in the monoclinic structure having the space group $P21/c$ and the XRD patterns are in accordance with the JCPDS File No. 01-071-0465. The substitution of rare earths progressively transforms it into a cubic fluorite type structure (*Fm3m*) and it well matches with the JCPDS File No. 03-065-5923. The monoclinic to fluorite type phase transition is made evident in the powder diffraction pattern. The introduction of Y^{3+}/Tb^{4+} into $Bi_2Ce_2O_7$ slightly shifts the peaks to higher 2θ angle (Inset of Figs. 7.1 and 7.2) evidencing the substitution of the ions in the lattice with contraction as expected because the ionic radius of Y^{3+} (r=0.101 nm CN=8) is smaller than that of the Bi^{3+} (r=0.118 nm, CN=8) and the ionic size of Tb^{4+} (0.088 nm, CN=8) is smaller than that of Ce^{4+} (0.097 nm, CN=8). Further, a minor secondary phase of Bi_4O_7 (marked as * in Figs. 7.1 and 7.2) is observed with a lower concentration of rare earth substitution.

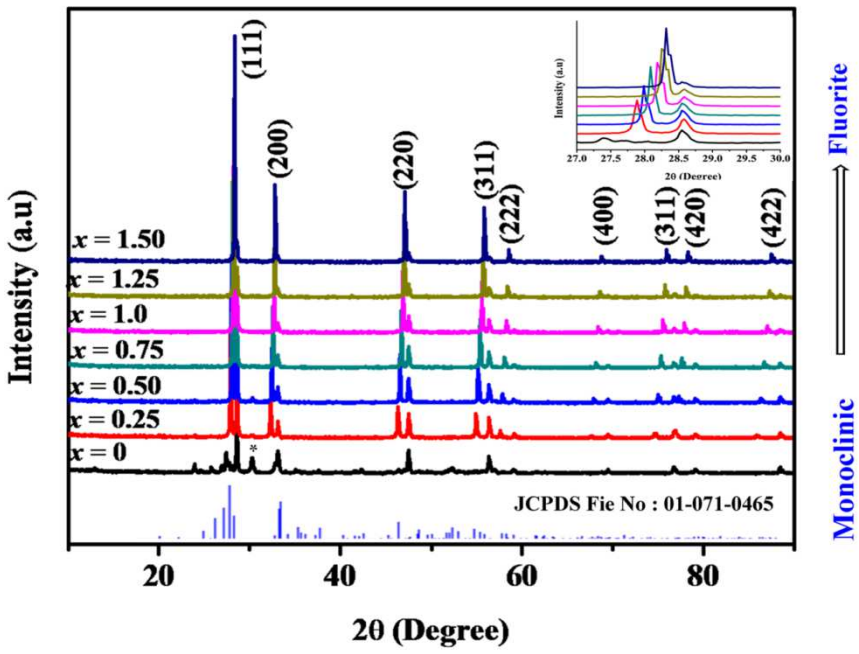

Fig. 7.2 Powder X-ray diffraction patterns of $Bi_2Ce_{2-x}Tb_xO_7$ (x = 0, 0.25, 0.5, 0.75, 1.0, 1.25 and 1.5) pigments. The substitution of Tb^{4+} in Ce^{4+} site induces a structural transition from monoclinic to cubic fluorite. Additional Bi_4O_7 peaks are denoted by *.

The crystallite size was calculated from Debye Scherrer formula

$$D=0.9\lambda/\beta\cos\theta \quad (7.2)$$

where D is the crystallite size, λ is the wavelength of X-ray used, β and θ are the half width of X-ray diffraction lines and half diffraction angle of 2θ. The calculated crystallite size varies from 85 to 126 nm in the case of Y and 85 to127 nm in the case of Tb. It is also seen that the crystallite size value shows a marked difference between $Bi_2Ce_2O_7$ and rare earth doped $Bi_2Ce_2O_7$ compounds ($x \geq 0.50$), which also suggests the structural transition by rare earth doping

7.3.2 Morphological studies of $Bi_{2-x}Y_xCe_2O_7$ and $Bi_2Ce_{2-x}Tb_xO_7$ systems

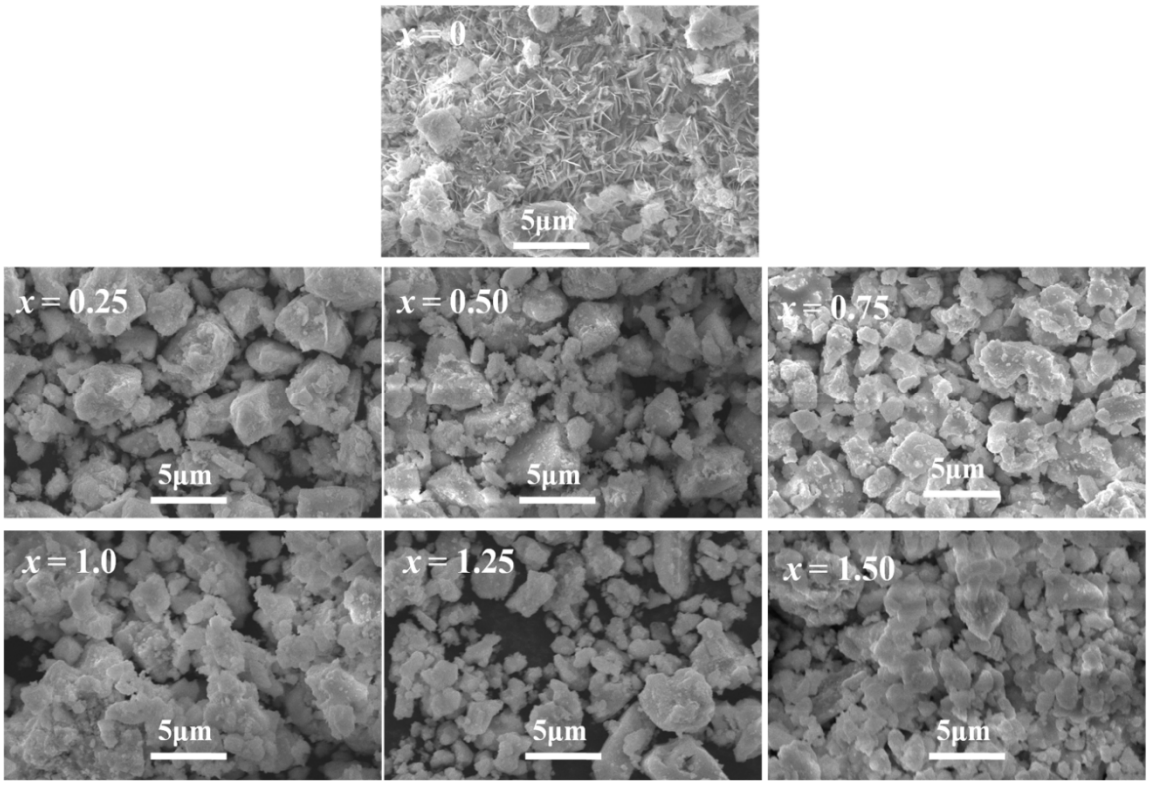

Fig. 7.3. Typical SEM images of $Bi_{2-x}Y_xCe_2O_7$ (x = 0, 0.25, 0.50, 0.75, 1.0, 1.25 and 1.50) pigments.

Figs. 7.3 and 7.4 show the SEM micrographs of yttrium and terbium doped $Bi_2Ce_2O_7$ samples for different doping concentrations. It is seen that the particles are slightly bigger for Tb doped $Bi_2Ce_2O_7$ compared to Y substituted one and shows an increasing trend in particle size with substitution. The micrographs show highly agglomerated particles in the size range 1–3 µm. The rare earth doping in both the

systems made vivid changes in the particle size and morphology of the parent compound. These changes may be attributed to the variation in the crystallization due to the structural differences from the parent compound. The compositions of all the samples were checked by energy dispersive spectrometer (EDS) analysis attached with SEM. EDS micro-chemical analysis of the typical samples $Bi_2Ce_2O_7$, $Bi_{1.75}Y_{0.25}Ce_2O_7$ yellow pigment and $Bi_2Ce_{1.5}Tb_{0.50}O_7$ red pigment are shown in Fig. 7.5, which identifies the presence of all the expected elements in the sample. The stoichiometry obtained from the EDS analysis is in close agreement with the theoretical formulae.

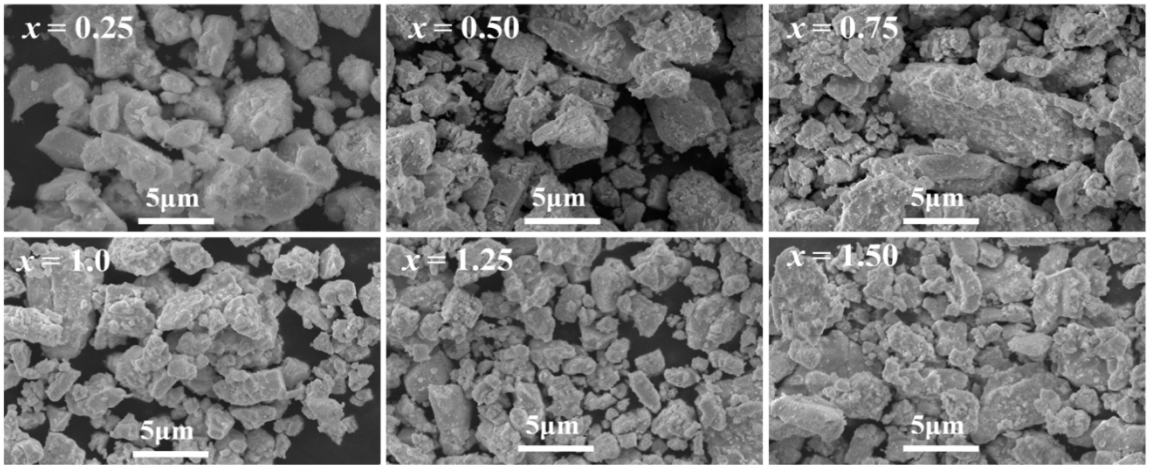

Fig. 7.4 Typical SEM images of $Bi_2Ce_{2-x}Tb_xO_7$ (x = 0.25, 0.50, 0.75, 1.0, 1.25 and 1.50) pigments.

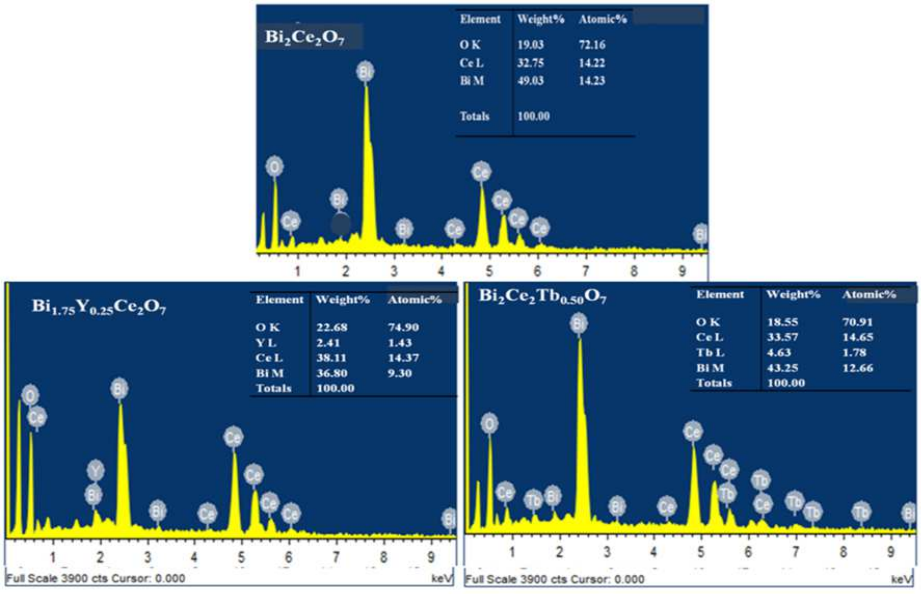

Fig. 7.5 EDS spectra of $Bi_2Ce_2O_7$, $Bi_{1.75}Y_{0.25}Ce_2O_7$ and $Bi_2Ce_{1.50}Tb_{0.50}O_7$ samples which identifies the presence of all expected elements.

Elemental X-ray dot mapping analysis of the synthesized $Bi_{1.75}Y_{0.25}Ce_2O_7$ yellow pigment and $Bi_2Ce_{1.5}$ $Tb_{0.50}O_7$ red pigment are shown in Figs. 7.6 and 7.7 respectively. This mapping shows that all the elements are uniformly distributed in the sample.

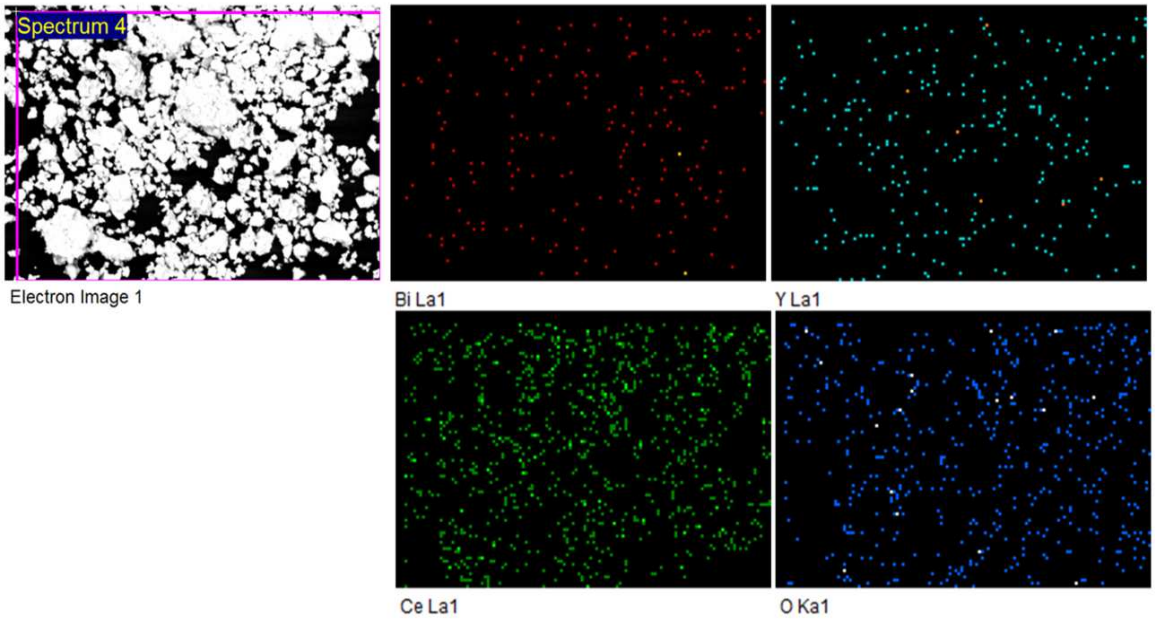

Fig. 7.6 Elemental mapping of the typical $Bi_{1.75}Y_{0.25}Ce_2O_7$ yellow pigment and it confirms that all the elements are uniformly distributed in the sample.

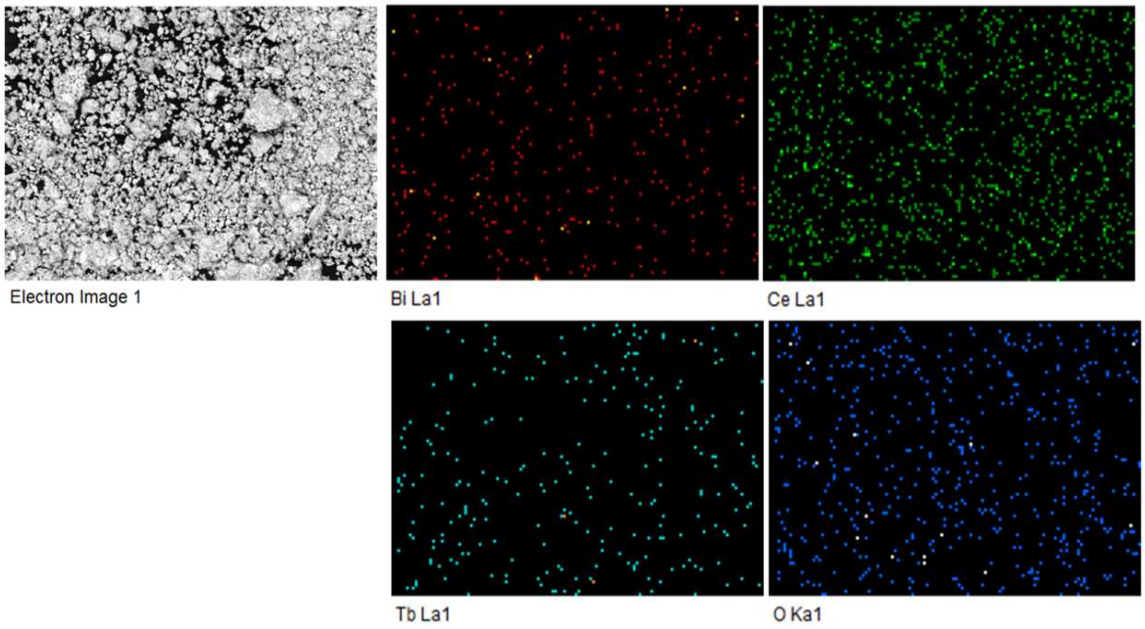

Fig. 7.7 Elemental mapping of the typical $Bi_2Ce_{1.50}Tb_{0.50}O_7$ red pigment and it confirms that all the elements are uniformly distributed in the sample.

7.3.3 XPS studies of $Bi_{2-x}Y_xCe_2O_7$ and $Bi_2Ce_{2-x}Tb_xO_7$ systems

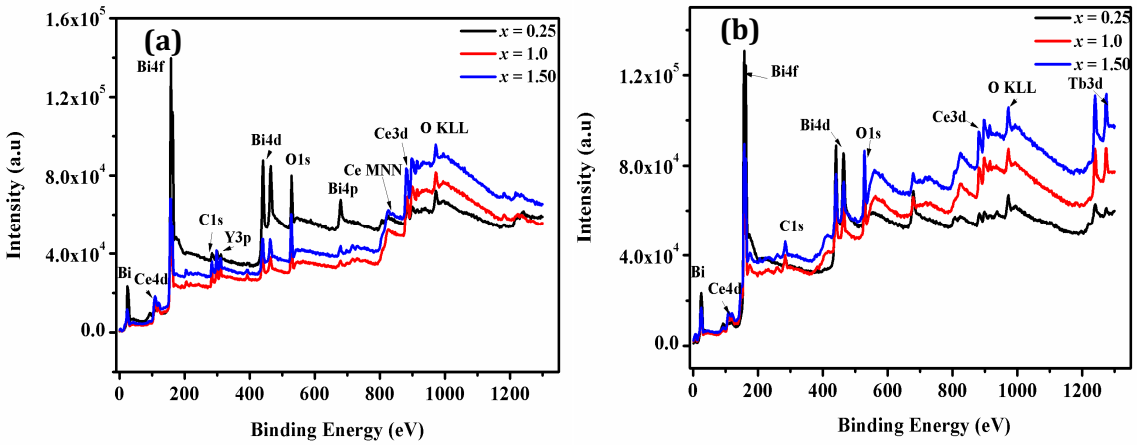

Fig. 7.8 XPS survey spectra of a) $Bi_{2-x}Y_xCe_2O_7$ and b) $Bi_2Ce_{2-x}Tb_xO_7$ (x = 0.25, 1.0 and 1.50) pigments

A wide survey scan X-ray photoelectron spectra of the $Bi_{2-x}Y_xCe_2O_7$ and $Bi_2Ce_{2-x}Tb_xO_7$ (x= 0.25, 1.0 and 1.5) pigments in the range 0–1300 eV are shown in Fig. 7.8. The recorded XPS spectra were charge-corrected with respect to an adventitious C 1s signal at 284.6 eV. A series of peaks from Bi 4d, Ce 3d, Y 3p, Tb 3d, C 1s and O 1s are clearly observed.

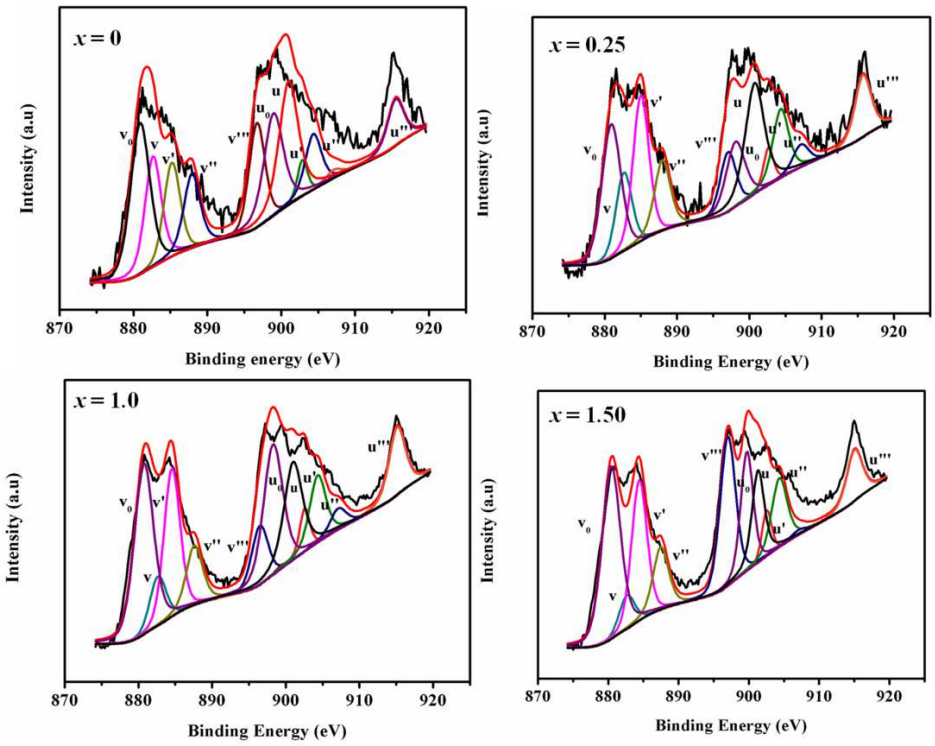

Fig. 7.9 Deconvoluted XPS spectra of Ce(3d) core levels of $Bi_{2-x}Y_xCe_2O_7$ (x = 0, 0.25, 1.0 and 1.50) pigments.

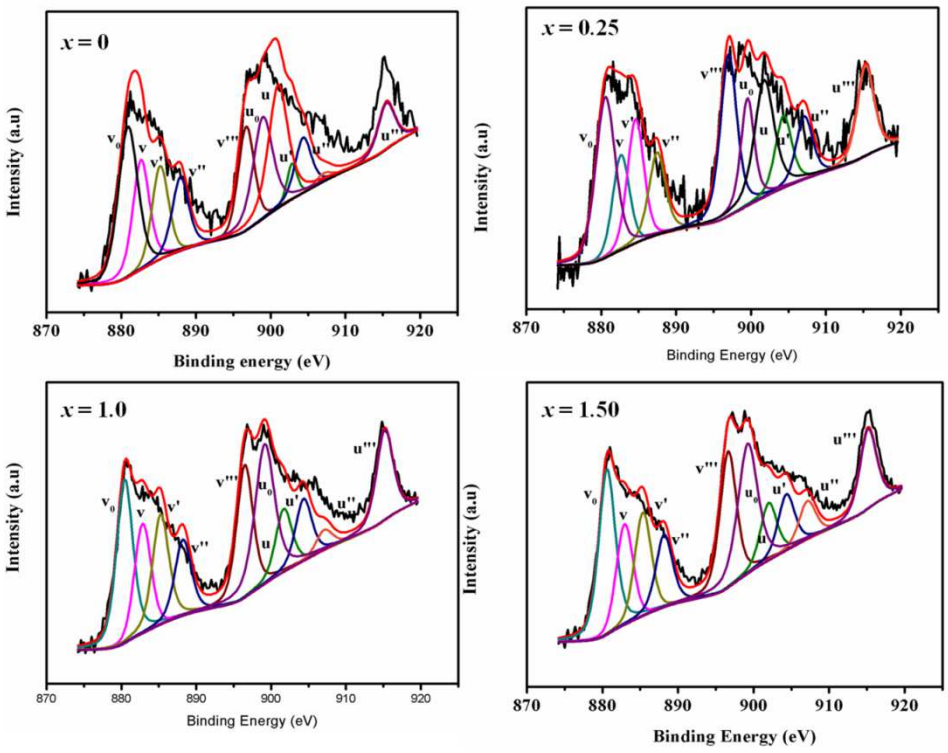

Fig. 7.10 Deconvoluted XPS spectra of Ce(3d) core levels of $Bi_2Ce_{2-x}Tb_xO7$ (x = 0, 0.25, 1.0 and 1.50) pigments.

The deconvoluted XPS of Ce 3d core levels spectra for the yttrium and terbium doped $Bi_2Ce_2O_7$ samples are shown in Figs. 7.9 and 7.10. It can be seen that the Ce 3d electron core level XPS spectra are composed of 10 peaks related to five different spin–orbit doublets due to two multiplets 3/2 and 5/2 along with 3 + and 4 + oxidation states of Ce (Kumar et al. 2009). The multiplicity of these states arises from different Ce 4f level occupancies in the final state. According to this result, tetravalent Ce^{4+} and trivalent Ce^{3+} species are considered to coexist on the surface of all the samples ie. *v/u, v"/u",* and *v"'/u"'* are attributed to tetravalent Ce^{4+}; *v/u* and *v"/u"* that are due to a mixture of $3d^94f^2O^2p^4$ and $3d^94f^1O^2p^5$ configurations, and *v"'/u"'* is a $3d^94f^0O^2p^6$ final state, while, v_0/u_0 and *v'/u'* are attributed to trivalent Ce^{3+}, are due to $3d^94f^1O^2p^6$ and $3d^94f^2O^2p^5$ final state (Ramana et al. 2016). To evaluate the Ce^{3+} concentration, we measured the surface relative molar ratio of $Ce^{3+}/(Ce^{3+} + Ce^{4+})$ from the peak areas of Ce^{3+} and Ce^{4+} in Ce 3d spectrum and the values are listed in Table 7.1. When Y^{3+}/Tb^{4+} was doped into $Bi_2Ce_2O_7$, the Ce 3d XPS shows that the peaks of Ce^{4+} 3d3/2 and Ce^{4+} 3d5/2 become stronger than the undoped $Bi_2Ce_2O_7$ sample indicating the decrease of Ce^{3+} concentration in the

sample with respect to the increase in dopant concentration. It was found that the concentration of Ce^{3+} is relatively less for Tb^{4+} substitution compared to that for Y^{3+}.

The deconvoluted spectrum of Tb 3d is shown in Fig. 7.11. The XPS spectrum (Fig. 7.12a) shows the presence of Tb^{3+} and Tb^{4+} ions in the samples. The characteristic peaks of Tb 3d region were generally centred at around 1242.41and 1275.79 eV, corresponding to Tb $3d_{5/2}$ and $3d_{3/2}$, respectively (Li et al. 2016). From the deconvoluted spectrum (Fig. 7.11), we clearly see the separated doublets for Tb^{3+} (1239.09 and 1274.94 eV) and Tb^{4+} (1242.59 and 1276.28 eV), respectively. The deconvoluted peak areas of XPS spectra were calculated to estimate the concentration of the corresponding valence states ions and the values are listed in Table 7.1. These results demonstrated that the mixed valence states of the terbium species (+3 and +4) in the system and Tb^{3+} is more dominant in the synthesized system.

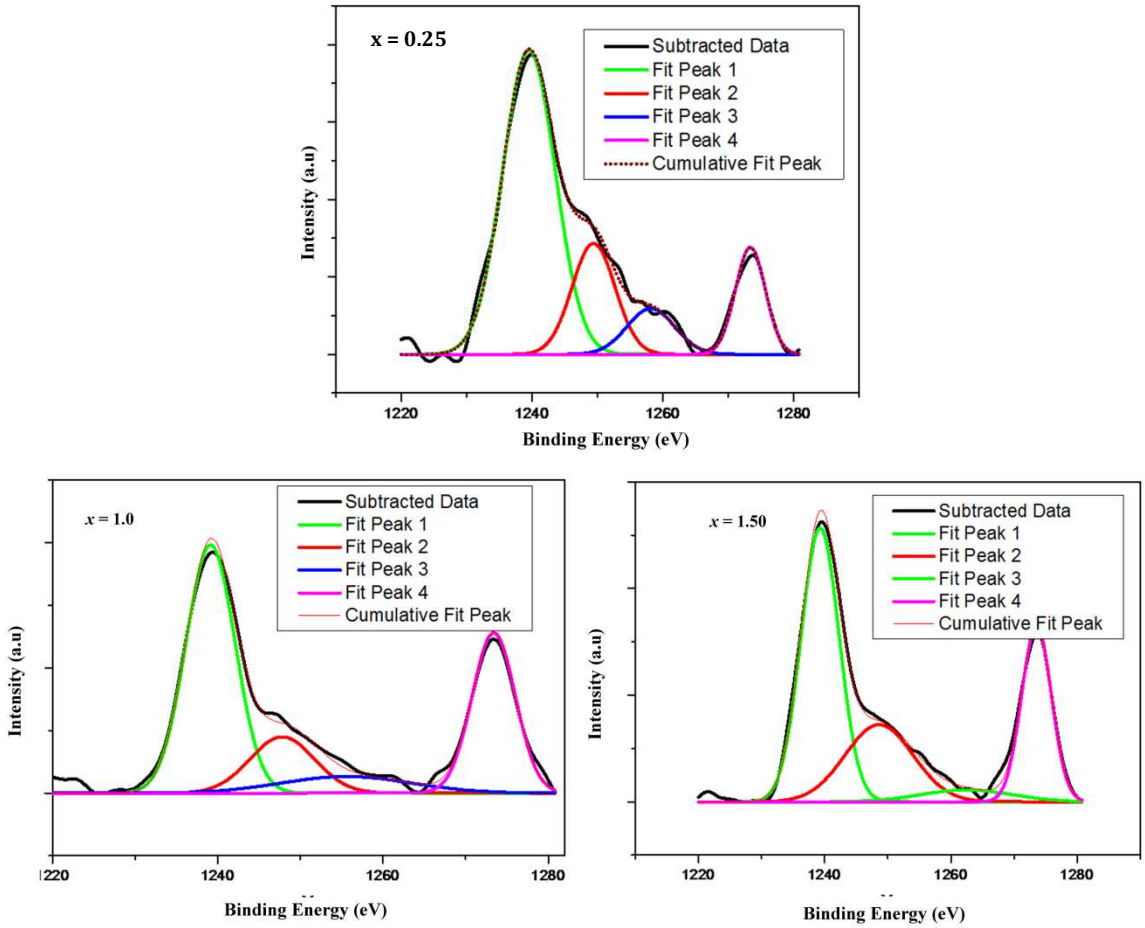

Fig. 7.11 Deconvoluted XPS spectra of Tb (3d) of $Bi_2Ce_{2-x}Tb_xO_7$ (x = 0, 0.25, 1.0 and 1.50) pigments

Table 7.1 Ce^{3+} concentration values of $Bi_{2-x}Y_xCe_2O_7$ and $Bi_2Ce_{2-x}Tb_xO_7$ (x = 0, 0.25, 0.50, 0.74, 1.0, 1.25 and 1. 50) pigments and Tb^{3+} concentration values of $Bi_2Ce_{2-x}Tb_xO_7$ (x = 0.25, 1.0, 1.25 and 1. 50) pigments calculated from XPS analysis.

	[Ce^{3+}]%		[Tb^{3+}]%
	Y	Tb	Tb
x = 0	28.93		
x = 0.25	21.19	18.62	50.53
x = 1.00	20.11	12.37	53.03
x = 1.50	21.60	12.30	52.02

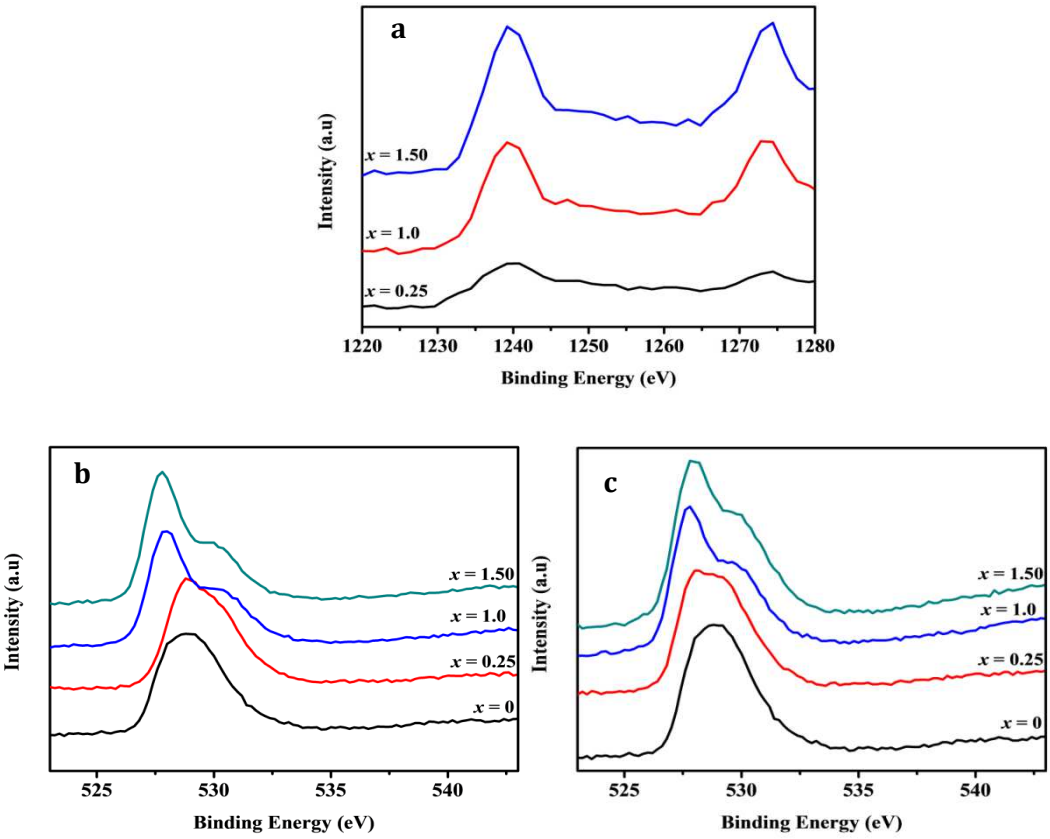

Fig. 7.12 XPS spectra of a) Tb(3d) core levels of $Bi_2Ce_{2-x}Tb_xO_7$ (x = 0.25, 1.0 and 1.50); b) O(1s) core levels of $Bi_{2-x}Y_xCe_2O_7$ and c) O(1s) core levels of $Bi_2Ce_{2-x}Tb_xO_7$ (x = 0, 0.25, 1.0 and 1.50) pigments.

Fig. 12b–c gives the XPS of O 1s core levels of $Bi_{2-x}Y_xCe_2O_7$ and $Bi_2Ce_{2-x}Tb_xO_7$ (x=0, 0.25, 1.0 and 1.50) pigments. For pure $Bi_2Ce_2O_7$, only one peak at 528.8 eV is noticeable which is contributed to the lattice oxygen of the host. However, by Y^{3+}/Tb^{4+} doping, another peak at 530.2 eV appears and the peak intensity gradually increases with the increase in Y^{3+}/Tb^{4+} concentration which may attribute to the increase in oxygen vacancies in the lattice. This is obvious in the present case of structural transition to fluorite structure.

7.3.4 UV–vis NIR spectroscopic studies of $Bi_{2-x}Y_xCe_2O_7$ and $Bi_2Ce_{2-x}Tb_xO_7$ systems

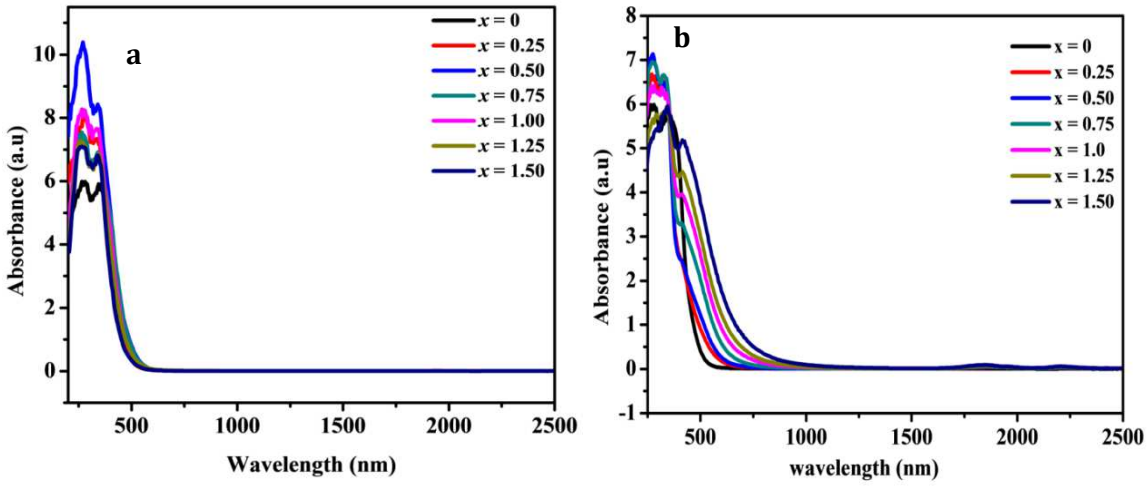

Fig. 7.13 Absorption spectra of a) $Bi_{2-x}Y_xCe_2O_7$ and b) $Bi_2Ce_{2-x}Tb_xO_7$ (x = 0, 0.25, 0.50, 0.75, 1.0, 1.25 and 1.50) pigments

The absorption spectra of the $Bi_{2-x}Y_xCe_2O_7$ and $Bi_2Ce_{2-x}Tb_xO_7$ (x=0, 0.25, 0.5, 0.75, 1.0, 1.25 and 1.50) pigments in the UV–vis–NIR region are displayed in Fig. 13a–b. The absorption spectra of the $Bi_{2-x}Y_xCe_2O_7$ pigments is characterized by a broad absorption band due to charge transfer transition from the valence band consisting of the O (2p) orbitals to the conduction band derived from the Y (3d) orbitals and the secondary Bi(6p) orbitals. Strong visible absorption in the blue region (complimentary of yellow) is observed and the absorption edge is gently shifted to the longer wavelength side (red shifting) by the Y^{3+} substitution. The tauc plot method was employed to estimate band gap energies (Eg) of the synthesized samples from the absorption spectra and the variation of the band gap is listed in Table 7.2. Consequently, the prepared pigments exhibit various yellow colors by fine tuning the band gap from 2.49 eV to 2.19 eV. As indicated by the XPS analysis, the Y^{3+}

substitution in the Bi^{3+} site increases the Ce^{4+} concentrations enabling the charge transfer energy to a lower level. Thus the decrease in band gap can be explained on the basis of the shift of charge transfer band to higher wavelengths due to a reduction in the CTB energy by Y^{3+} doping. Therefore the Y^{3+} substitution allows fine tuning of the band gap displaying various yellow hues.

Table 7.2 Color coordinates and band gap values of the $Bi_{2-x}Y_xCe_2O_7$ (x = 0, 0.25, 0.50, 0.74, 1.0, 1.25 and 1.05) yellow pigments.

	L^*	a^*	b^*	C_{ab}	$h°$	E_g (eV)
x = 0	82.91	5.44	48.76	49.06	83.63	2.49
x = 0.25	83.36	3.52	51.36	51.48	86.07	2.38
x = 0.50	76.85	13.33	47.97	49.79	74.47	2.35
x = 0.75	77.14	11.32	48.63	49.92	76.89	2.31
x = 1.00	79.82	8.17	46.70	47.41	80.07	2.28
x = 1.25	78.61	8.18	45.18	43.95	79.26	2.19
x = 1.50	83.15	5.49	43.78	44.95	82.33	2.17

In the case of $Bi_2Ce_{2-x}Tb_xO_7$ (x=0, 0.25, 0.5, 0.75, 1.0, 1.25 and1.50) pigments, the coloring mechanism is based on the shift of the charge transfer band of O (2p) - Ce (4f) to higher wavelengths i.e. red shifting along with introducing an additional electronic level by doping terbium. The band gap energy is related to the valence band consisting of filled O (2p) orbitals and the conduction band derived from the empty 4f orbitals of Ce^{4+} ions. The band gap between the anionic band and cationic band of $Bi_2Ce_2O_7$ is 2.49 eV. By doping $Bi_2Ce_2O_7$ with Tb ions, the 4f electrons of terbium valence shell introduce an additional electronic level of energy between the O^{2-} valence band and Ce^{4+} conduction band and a large reduction in band gap is

observed from 2.49 eV to 1.49 eV and the variation of band gap with increasing terbium doping is tabulated in Table 7.3.

Table 7.3 Color coordinates and band gap values of the $BiCe_{2-x}Tb_xO_7$ (x = 0, 0.25, 0.50, 0.74, 1.0, 1.25 and 1. 05) red pigments.

Composition	L^*	a^*	b^*	C_{ab}	$h°$	E_g (eV)
x = 0	82.91	5.44	48.76	49.06	83.63	2.49
x = 0.25	70.75	12.11	32.49	34.67	69.54	1.93
x = 0.50	62.26	15.01	32.07	35.4	64.91	1.82
x = 0.75	55.66	14.36	26.62	30.24	61.65	1.80
x = 1.00	50.37	13.08	22.98	26.44	60.34	1.74
x = 1.25	46.09	11.23	18.61	21.73	58.88	1.69
x = 1.50	42.01	10.37	15.83	18.92	56.77	1.49

7.3.5. Color performance of $Bi_{2-x}Y_xCe_2O_7$ and $Bi_2Ce_{2-x}Tb_xO_7$ systems

The chromatic properties of the synthesized pigments can be numerically expressed in terms of color co-ordinates from their *CIE 1976* color coordinate values and are listed in Tables 7.2 and 7.3. The substitution of Y^{3+}/Tb^{4+} for Bi^{3+}/Ce^{4+} in $Bi_2Ce_2O_7$ tune the color from yellow to red. In the $Bi_{2-x}Y_xCe_2O_7$ pigments, lightness (L^*) of all the samples are almost similar and a slightly decreasing trend is found with Bi^{3+} substitution. The b^* value corresponding to yellow chromaticity depends on the identity of the Bi^{3+} doping and its values are slightly decreasing with doping. The red hue of the pigment as denoted by the color coordinate, a^* shows a sudden increase up to 50 mol% of Bi^{3+} and decreases after that. The richest yellow hue (b^*=51.48) was obtained for $Bi_{1.75}Y_{0.25}Ce_2O_7$ sample. The hue angles of the samples lie in the yellow region of the cylindrical color space (h°=70–105 for yellow). The chromatic properties of the typical $Bi_{1.75}Y_{0.25}Ce_2O_7$ yellow pigment powder, especially the b^* value, is comparable with a number of reported pigments such as

lanthanide doped pyrochlore inorganic pigments calcined at 1300°C and 1400°C, $Er_2Ce_{2-x}Mo_xO_7$ ($b^* \leq 50.55$) (Stranska et al. 2012), (Cr, Sb)-co-doped rutile pigments ($b^* \leq 36.27$) (Zou et al. 2014) and V-containing ZrO_2 inorganic yellow ($b^* \leq 47.99$) (Jose et al. 2017).

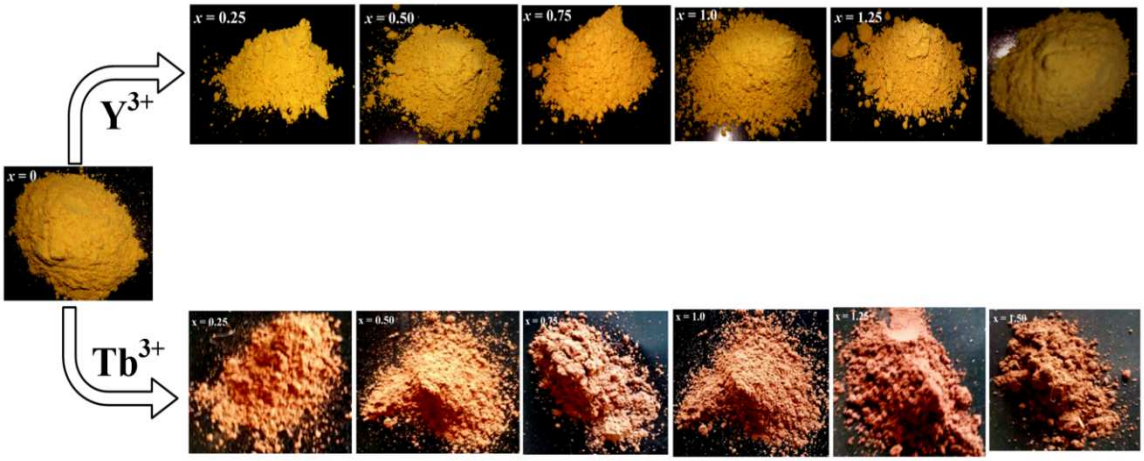

Fig. 7.14 Photographs of $Bi_{2-x}Y_xCe_2O_7$ and $Bi_2Ce_{2-x}Tb_xO_7$ (x = 0, 0.25, 0.5, 0.75, 1.0, 1.25 and 1.50) pigments.

In the $Bi_2Ce_{2-x}Tb_xO_7$ pigments, the lightness (L^*) of the samples decreases with increase in terbium concentration. The doping of terbium (x=0.50) results in an increase in the red component (a^*) to 15.01 and yellow component (b^*) to 32.07. A further increase in dopant concentration (up to x=1.50) brings about a slight decrease in the red and yellow hues, as denoted by the chromatic coordinates $a^*$and b^*, consequently the color changes to dark-brown. The photographs of the synthesized pigments are shown in Fig. 7.14. The hue angle values reveal that the terbium doped $Bi_2Ce_2O_7$ pigments lie in the reddish brown region of the cylindrical color space (h°=0–35 for red and 35–70 for orange). The color coordinates of the typical pigment powder ($Bi_2Ce_{1.5}Tb_{0.5}O_7$) are significantly higher than that of the recently reported ones i.e. in lanthanide–cerianite solid solutions (a^*=8.5) (Garcia et al. 2001), tungsten co-doped lanthanum cerium oxide (a^*=8.79) (Chen et al. 2018) and commercially available brown pigment (BR 300), (a^*=11.38) of Kawamura Chemicals Co. Ltd. Japan. The tuning of color from yellow to red can be obtained by the introduction of rare earths into the $Bi_2Ce_2O_7$ makes them in the class of non toxic (heavy metal free) inorganic yellow and red pigments for coloring applications.

7.3.6. NIR reflectance analysis of $Bi_{2-x}Y_xCe_2O_7$ and $Bi_2Ce_{2-x}Tb_xO_7$ systems

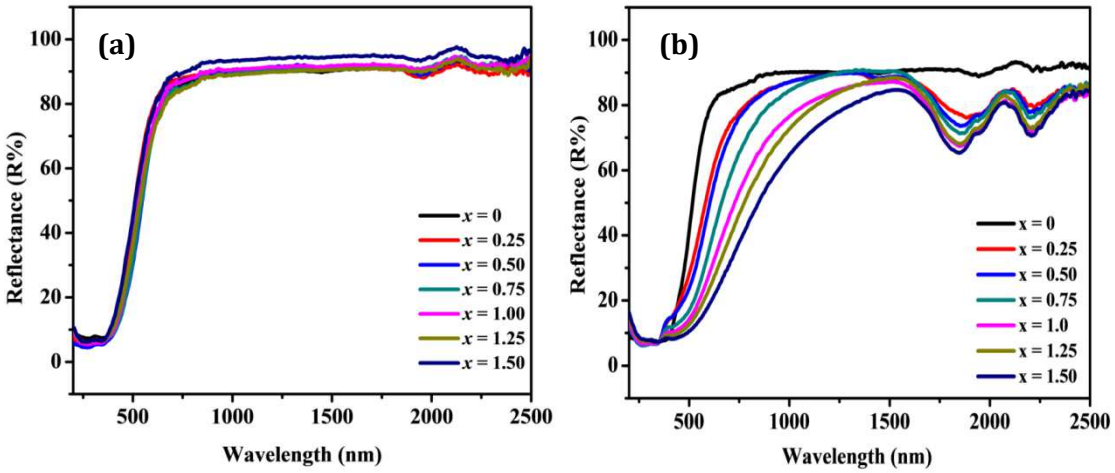

Fig. 7.15 NIR Reflectance spectra of $Bi_{2-x}Y_xCe_2O_7$ and $Bi_2Ce_{2-x}Tb_xO_7$ (x = 0, 0.25, 0.50, 0.74, 1.0 and 1.25) pigments.

NIR reflectance spectra of the new pigments $Bi_{2-x}Y_xCe_2O_7$ and $Bi_2Ce_{2-x}Tb_xO_7$ (x=0, 0.25, 0.5, 0.75, 1.0, 1.25 and 1.50) recorded in the range from 200 to 2500 nm by using PTFE as reference, are depicted in Fig. 7.15a–b. The new pigments show high NIR reflectivity over the whole range except some weak rare earth absorption bands at lower energies. In the $Bi_{2-x}Y_xCe_2O_7$ and $Bi_2Ce_{2-x}Tb_xO_7$ spectra, the compounds display a remarkable reflectance in the range 90–94%, 70–88% respectively for the yellow and red pigments which is high to reflect almost all the sun radiation energy in the NIR region and can be used as NIR reflecting pigments. Table 7.4 presents the NIR reflectance and solar reflectance of the pigment powdered samples. The NIR solar reflectance spectra determined in accordance with ASTM standard G173-03 of powdered yellow and red pigments are presented in Fig. 7.16. The high NIR and Solar reflectance displayed by all the newly designed yellow and red colored pigments encourage them as interesting colorants for the cool roof and surface coating applications.

Table 7.4 The values of NIR reflectance and the solar reflectance of $Bi_{2-x}Y_xCe_2O_7$ and $Bi_2Ce_{2-x}Tb_xO_7$ (x = 0, 0.25, 0.50, 0.74, 1.0, 1.25 and 1. 05) pigments.

Pigment composition (x)		0	0.25	0.50	0.75	1.0	1.25	1.50
NIR reflectance of the pigments (%)	Y	90.2	91.6	91.9	89.8	90.9	89.4	93.6
	Tb	90.2	86.8	87.7	84.2	80.8	75.1	70.3
Solar NIR reflectance of the pigments (%)	Y	89.5	90.2	90.2	89.4	90.6	88.8	93.2
	Tb	89.5	87.8	87.9	83.8	81.5	74.2	69.6

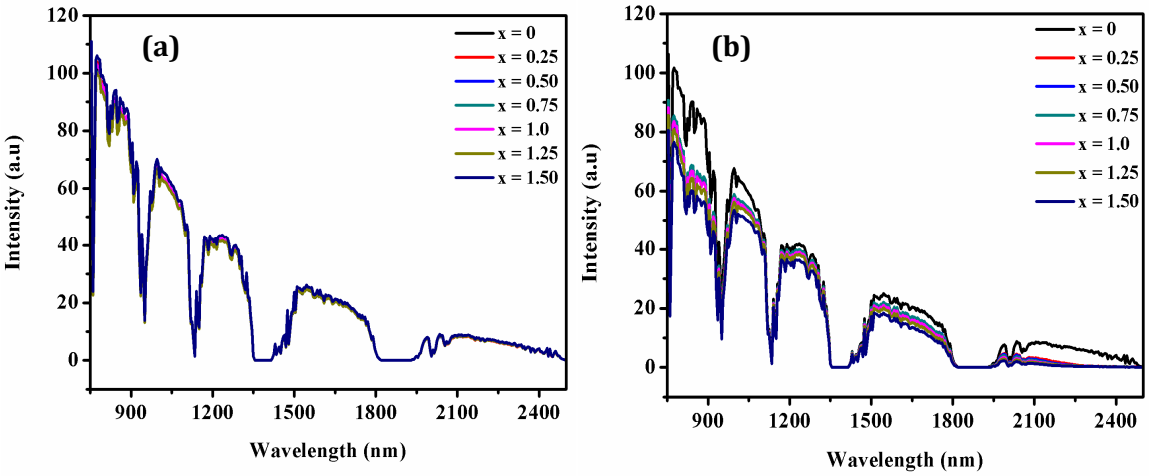

Fig. 7.16 Solar NIR Reflectance spectra of $Bi_{2-x}Y_xCe_2O_7$ and $Bi_2Ce_{2-x}Tb_xO_7$ (x = 0, 0.25, 0.50, 0.74, 1.0 and 1.25) pigments.

7.3.7 Chemical resistance and thermal stability studies of $Bi_{1.75}Y_{0.25}Ce_2O_7$ and $Bi_2Ce_{1.5}Tb_{0.5}O_7$ pigments

The day by day growth of industrialisation leads to the accumulation of acidic pollutants in the atmosphere which in turn stick to the different substrate surface that leads to the tarnishing of the surfaces. Therefore chemical resistance of the pigment needs to be established for its possible utility in any substrate. The evaluation was done by acid/alkali/water resistance of the typical pigments: $Bi_{1.75}Y_{0.25}Ce_2O_7$ and $Bi_2Ce_{1.5}Tb_{0.5}O_7$ were carried out in 5% of HCl, HNO_3, NaOH and

H_2O. There is no noticeable weight loss of the pigment for the acid, alkali, and water test. The color coordinates of the pigment samples which are subjected to the tests are measured and compared with the untreated sample. From this, the total color difference (ΔE^*_{ab}) was calculated and tabulated in Table 7.5. The small values of ΔE^*_{ab} reveal that the pigments are chemically stable in the acid/alkali/H_2O. Thermo-gravimetric analysis of the typical samples were investigated with a view to find out its thermal stability in the range 50–1000°C and the results clearly indicate that there is an insignificant weight loss ($Bi_{1.75}Y_{0.25}Ce_2O_7$=0.35%; $Bi_2Ce_{1.5}Tb_{0.5}O_7$=0.10%) of the pigment in the above temperature range (Fig. 7.17 and 7.18).

Table 7.5 The color coordinates of $Bi_{1.75}Y_{0.25}Ce_2O_7$ and $Bi_2Ce_{1.5}Tb_{0.5}O_7$ powder pigments after chemical resistance tests.

Composition	5% Acid/Alkali	L^*	a^*	b^*	ΔE^*_{ab}
$Bi_{1.75}Y_{0.25}Ce_2O_7$	HCl	0.90	0.66	0.84	1.34
	HNO_3	0.76	0.54	0.60	1.11
	NaOH	0.82	0.62	0.71	1.25
	H_2O	0.10	0.20	0.60	0.64
$Bi_2Ce_{1.5}Tb_{0.5}O_7$	HCl	0.73	0.58	0.78	1.22
	HNO_3	0.59	0.60	0.63	1.05
	NaOH	0.65	0.62	0.58	1.07
	H_2O	0.30	0.43	0.51	1.16

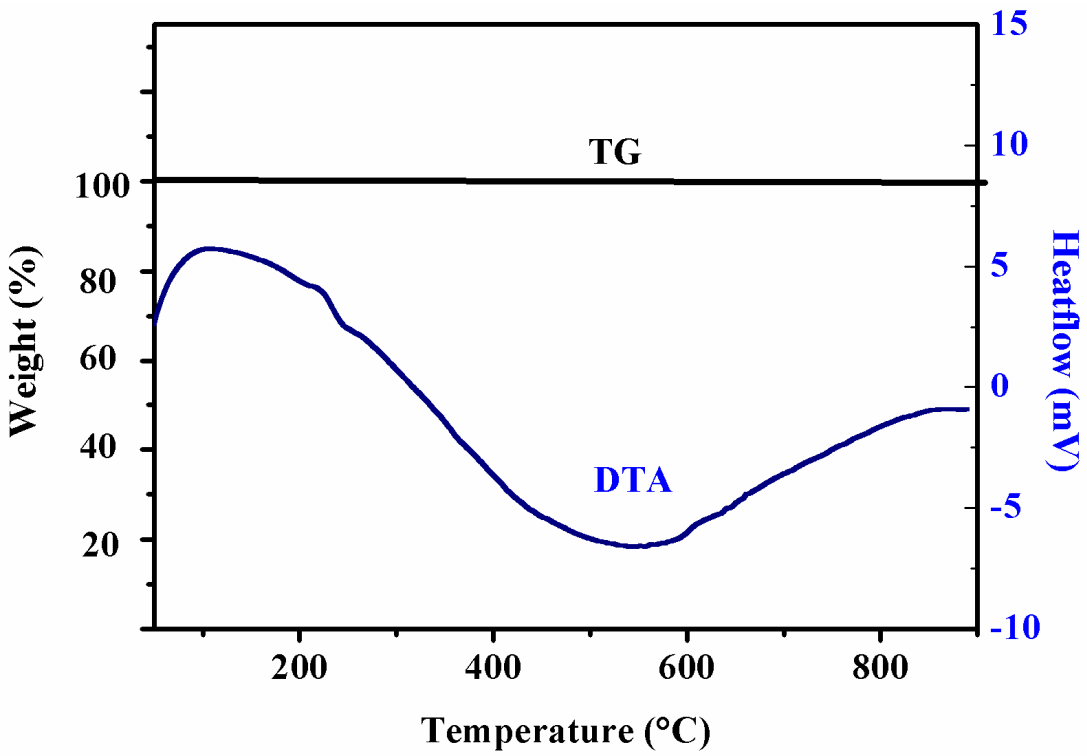

Fig. 7.17 TG-DTA of powdered $Bi_{1.75}Y_{0.25}Ce_2O_7$ pigment sample.

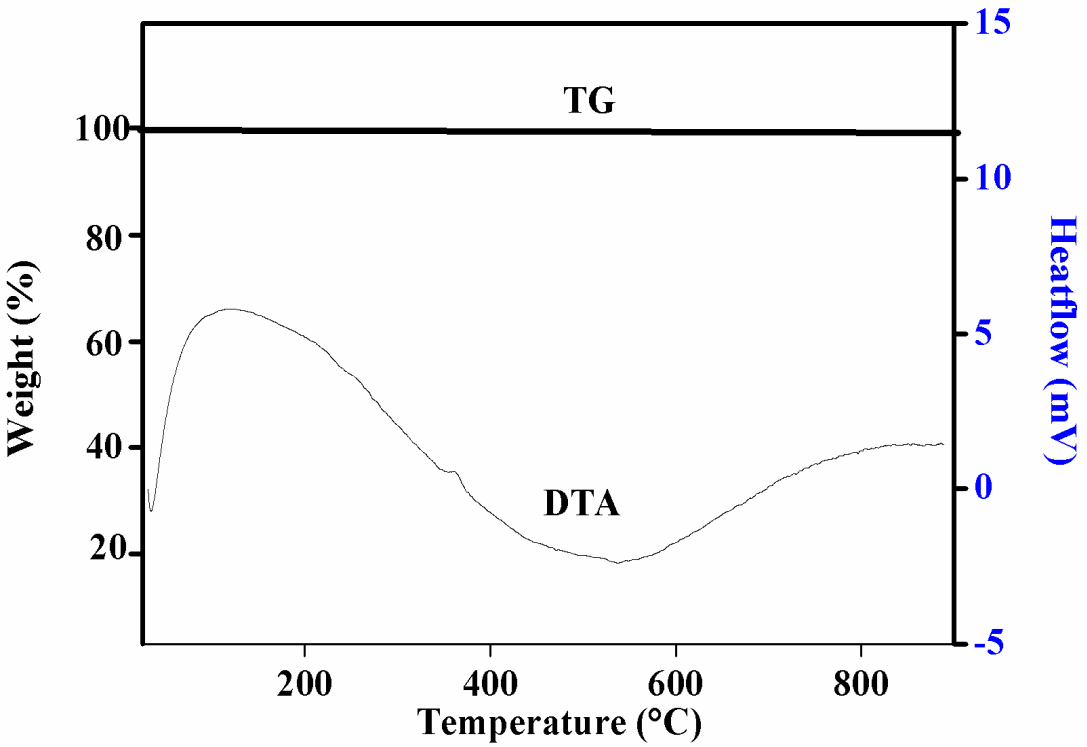

Fig. 7.18 TG-DTA of powdered $Bi_2Ce_{1.5}Tb_{0.5}O_7$ pigment sample.

7.3.8 Application study

The pigments having the best chromatic properties, $Bi_{1.75}Y_{0.25}Ce_2O_7$ and $Bi_2Ce_{1.5}Tb_{0.50}O_7$ were evaluated for its coloring performance by incorporating it into a polymer substrate such as poly (methyl methacrylate) (PMMA). Typically, 10 wt% of the pigment sample was dispersed in PMMA and compressed into a cylindrical disk (Fig. 7.19). The intensity of the color of plastics will depend on the concentration of the pigment. The color coordinates of the test pieces were measured at different locations of the polymer surface using a portable spectrophotometer Miniscan EZ4000S (Hunter Lab USA). The L^*, a^* and b^* values obtained were more or less the same, indicating the uniform distribution of the pigment particles in the polymer matrix. Thus, the developed pigments may find potential application in the coloring of various plastic materials.

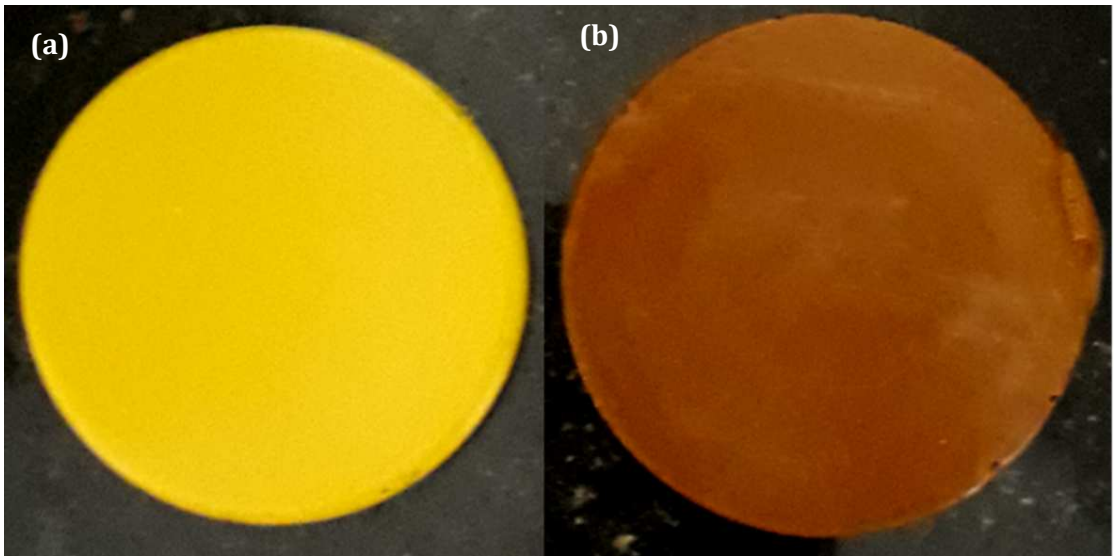

Fig. 7.19 Photographs of a) $Bi_{1.75}Y_{0.25}Ce_2O_7$ + PMMA b) $Bi_2Ce_{1.5}Tb_{0.50}O_7$ + PMMA (10 wt%).

7.4 Conclusions

A new series of cerium based yellow and red pigments: $Bi_{2-x}Y_xCe_2O_7$ and $Bi_2Ce_{2-x}Tb_xO_7$ (x = 0, 0.25, 0.5, 0.75, 1.0, 1.25 and 1.50) with high NIR solar reflectance have been prepared successfully via a conventional solid-state route. The small concentrations of Y and Tb in the $Bi_2Ce_2O_7$ matrix produces intense yellow and red colors by fine tuning the band gap. Also, these colorants are reproducible as well as thermally and chemically stable having very high NIR and solar reflectance in the range 70–95% at 1100 nm. Further, these pigments constitute less toxic elements which makes them as possible alternatives to the existing toxic chrome yellow and cadmium red. The developed yellow pigments are economically viable in comparison with the Pr and Tb based yellows. Thus these pigments have the potential to be used as environmentally friendly yellow and red pigments for plastic coloring and cool roof applications as energy saving products.

Chapter 8

CONCLUSIONS AND FUTURE ASPECTS

This chapter reviews the significant conclusions, relevance derived from the work of europium and terbium doped cerium based oxides for phosphor and pigment applications. The conclusions drawn from the studies can serve as a guideline for the designing of new cerium based optical materials (phosphor and pigment) with improved properties. The future scope of the present work is also discussed.

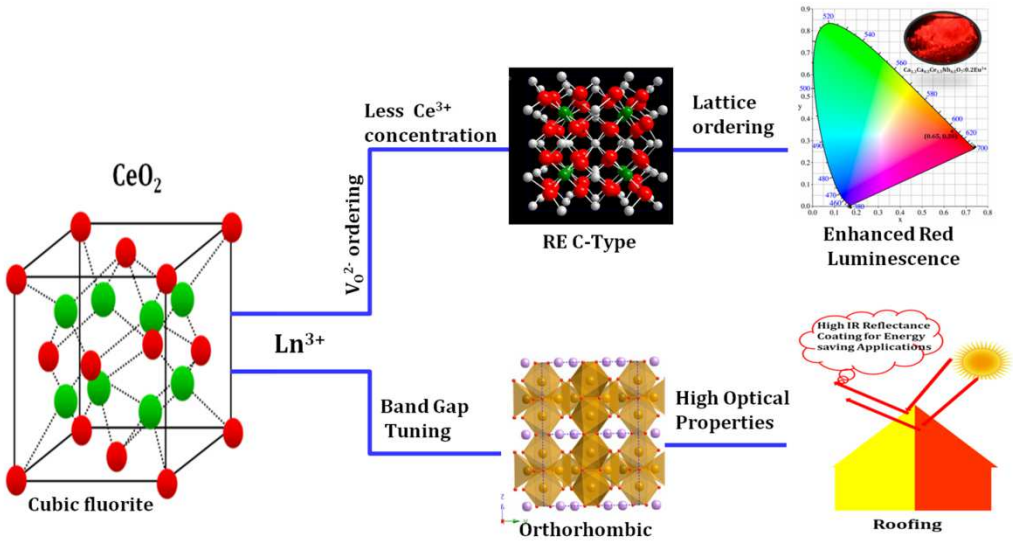

8.1 Conclusions

Several series of europium and terbium doped cerium based red phosphors and inorganic red & yellow pigments were synthesised using solid state reaction route and their optical properties were characterized. The present studies primarily investigated the photoluminescence properties for lighting applications and further focuses on the development of high NIR reflecting eco-friendly inorganic pigments for energy saving applications. The results presented in the previous chapters decipher the correlation between the fundamental understanding of the distribution and local structure of trivalent rare earth dopants and their role with respect to ionic radius, rare-earth concentration, oxygen vacancies and Ce^{3+} concentrations and how these factors control optical properties of ceria based phosphors and pigments. Some of the major conclusions derived from the research work are as follows.

- The co-substitution of contrasting rare earth ions (L and Y) in $Ce_{0.9}O_2$:$0.1Eu^{3+}$ elucidated the influence of local environment of Eu^{3+} ions on its photoluminescence behaviour and also has a distinct effect on local structure, absorption, and lifetimes.
- The defect formation of Ce^{3+} concentration was found to be a function of ionic radii of rare earths.
- The smaller lanthanide ion (Y^{3+}) substitution in the CeO_2 system inhibited defect formation, resulting in strong luminescence with more efficiency, while the bigger lanthanide ion (La^{3+}) substitution yielded poor luminescence due to increased defect formation.
- The co-substitution of contrasting rare earth metals with Eu^{3+} allow the understanding of local structure and a smaller ion like Y^{3+} greatly functionalizes CeO_2:Eu^{3+} phosphor.
- Influence of various lanthanide ion (La, Y, and Gd) substitutions on the Eu^{3+} photoluminescence properties in $A_2Ce_2O_7$ host structures was also studied.
- The difference in red emission intensities with different lanthanide ions demonstrated the influence of the degree of ordering in the crystal lattice, the Ce^{3+} concentration etc.

- Studies revealed that the gadolinium sample showed better luminescence properties in terms of f-f emission intensity, the asymmetric ratio and quantum efficiency.
- Luminescence properties with varying the Eu^{3+} concentration was studied in $Gd_{2-x}Ce_2O_7$:*x*Eu^{3+} system
- More ordering in the host lattice and more uniform distribution of Eu^{3+} ions resulting in the increased emission properties were observed in gadolinium system.
- Photoluminescence properties were further improved in $Gd_{1.8}Ce_2O_7$:*0.2*Eu^{3+} phosphors by the incorporation of Ca^{2+} and Nb^{5+} ions in Gd^{3+} and Ce^{4+} sites.
- The influence of the substitution of Eu^{3+} at the isovalent and aliovalent site of $Y_2Ce_2O_7$ on the photoluminescent properties was studied.
- The substitution of Eu^{3+} at the Ce^{4+} site induces a structural transition from a defect fluorite to a C-type structure, which increases the oxygen vacancy ordering and the distortion of the Eu^{3+} environment, and decreases the formation of Ce^{3+} states.
- Isovalent substitution at the Y^{3+} site exhibit the biphasic nature of defect fluorite and a C-type structure, thereby increasing the number of Ce^{3+} oxidation states which adversely affect the luminescence properties.
- The photoluminescent properties of $Y_2Ce_{2-x}O_7$:$_xEu^{3+}$ were studied at different Eu^{3+} concentrations under excitation with blue light.
- The cation ordering linked to the oxygen vacancy ordering led to the uniform distribution of Eu^{3+} ions in the lattice, thus allowing higher doping concentrations without quenching.
- Some of the prepared samples exhibited higher emission intensities than the standard Y_2O_3: Eu^{3+} red phosphors.
- Influence of various lanthanide ion (La, Sm, Gd and Y) substitutions on the Tb pigmentary properties in $A_2Ce_2O_7$ host structures was studied.
- The Tb substitution extends the absorption edge to longer wavelengths by introducing an additional electronic level between the valence band and conduction band leading to various red colors by fine tuning the band gap.

- The terbium doped $Y_2Ce_2O_7$ displayed intense red color (a^* = 26) with high near infrared reflectance (80%).
- Novel yellow/red inorganic pigments $A_2Ce_{1-x}Tb_xO_4$ (A = Sr and Ba) were also synthesized.
- The prepared pigments exhibit various colors by fine tuning of the band gap from 3.03 (white) to 2.37 (yellow) to 1.86 eV (red).
- Doping of Tb into Sr_2/Ba_2CeO_4 enhances the NIR reflectance at 1100nm from 87% to 91%.
- Another new series of high near-infrared (NIR) reflecting pigments with colors ranging from yellow to red by tuning the $Bi_2Ce_2O_7$ with rare earth ion substitutions on both A and B sites were synthesized successfully.
- A brilliant yellow hue was obtained for $Bi_{1.75}Y_{0.25}Ce_2O_7$ (b^*= 51.4), whereas $Bi_2Ce_{1.50}Tb_{0.50}O_7$ (a^*=15.0) exhibited a red color.
- The pigments are found to exhibit good light fastness and chemical stability.
- The applicability studies of all these synthesized typical pigments were studied in polymer matrix (poly methyl methacrylate), cement slab, asbestos sheet and ceramic glazes, which exhibited good coloring performance with high near infrared reflectance.
- Further, these pigments constitute less toxic elements which makes them as possible alternatives to the existing toxic chrome yellow and cadmium red.
- The developed yellow pigments are economically viable in comparison with the Pr and Tb based yellows and commercially available pigments.
- Thus these pigments have the potential to be used as environmentally friendly yellow and red pigments for plastic coloring, automotives and cool roof applications as energy saving products.

Thus, the synthesized CeO_2 based phosphors and pigments are found to be interesting alternatives to existing red phosphor and toxic inorganic yellow and red pigments for energy saving applications. The general conclusions drawn from the thesis work contribute to basic science, technological applications and leads to ideas that could be adopting for other cerium based oxides for different optical studies.

8.2 Future scope

This thesis explains the correlation between the fundamental understanding of the distribution and local structure of trivalent rare earth dopants and their role with respect to ionic radius, rare-earth concentration, oxygen vacancies and Ce^{3+} concentrations and how these factors control optical properties of ceria compounds that promises future scope of work and applications. A further enhancement in the Optical properties and efficiency of the cerium based oxides can be expected by different cationic modifications, different co-doping techniques, alternate synthesis routes, alteration in the morphology of the particles, etc. Thermal stability of luminescence behavior of developed red phosphors and its optimization is required. Incorporation of the developed phosphor powders to UV chip. Since the prepared cerium based pigments exhibit photochromic behaviour, the photochromic study of the developed pigments can be conducted. Study the energy savings of developed pigments for cool roof applications. The study of the output characteristics could be a future prospect of this work.

REFERENCES

Abrashev M. V., Todorov N. D., Geshev J., "Raman spectra of R_2O_3 (*R*—rare earth) sesquioxides with C-type bixbyite crystal structure: A comparative study", *J. App. Phys.,* 116 **(2014)** 103508 1-7.

Ahn K., Yoo D. S., Prasad D. H., Lee H. W., Chung Y. C., Lee J. H., "Role of Multivalent Pr in the Formation and Migration of Oxygen Vacancy in Pr-Doped Ceria: Experimental and First-Principles Investigations", *Chem. Mater.,* 24 **(2012)** 4261-4267.

Alammar T., Noei H., Wang Y., Grunert W., Mudring A. V., "Ionic liquid-assisted sonochemical preparation of CeO_2 nanoparticles for CO oxidation", *ACS Sust. Chem. Eng.,* 3 **(2015)** 42-54.

Alan M., "Phosphors development for LED lighting", *III-Vs Review The Advanced Semiconductor Magazine.,* 18 **(2005)** 32-34.

Alexander B., Leonid M. G., Oksana V. S., Joachim S., "Synthesis of luminescent ZrO_2:Eu^{3+} nanoparticles and their holographic sub-micrometer pattering in poymer composites", *Adv. Funct. Mater.* 19 **(2009)** 1819-1825.

Aruna S. T., Ghosh S., Patil K. C., "Combustion synthesis and properties of $Ce_{1-x}Pr_xO_{2-\delta}$ red ceramic pigments", *Int. J. Inorg. Mater.*, 3 **(2001)** 387-392.

Athira K. V. Raj., Rao P. P., Sreena T. S., Sameera S., Vineetha J., Renju U. A., "Remarkable changes in the photoluminescent properties of $Y_2Ce_2O_7$:Eu^{3+} red phosphors through modification of the cerium oxidation states and oxygen vacancy ordering", *Phys. Chem. Chem. Phys.,* 16 **(2014)** 23699-23710.

Athira. K. V. R., Rao P. P., Divya S., Ajuthara T. R., "Terbium doped Sr_2MO_4 [M= Sn and Zr] yellow pigments with high infrared reflectance for energy saving applications", *Powder. Technol.*, 311 **(2017)** 52-58.

Athira K. V. R., Rao P. P., Sameera S., James V., Divya S., "Synthesis of Novel Nontoxic Yellow Pigments: $Sr_2Ce_{1-x}Tb_xO_4$", *Chem. Lett.,* 43 **(2014)** 985–987.

Athira K. V. R., Rao P. P., Sameera S., S. Divya S., "Pigments based on terbium-doped yttrium cerate with high NIR reflectance for cool roof and surface coating applications", *Dyes Pigm*., 122 **(2015)** 116-125.

Avram D., Dominguez M. S., Cojocaru B., Florea M., Parvulescu V., Tiseanu C., "Toward a Unified Description of Luminescence–Local Structure Correlation in Ln Doped CeO_2 Nanoparticles: Roles of Ln Ionic Radius, Ln Concentration, and Oxygen Vacancies", *J. Phys. Chem. C., 119* (**2015)** 16303-16313.

Avram D., Gheorghe C., Rotaru C., Cojocaru B., Florea M., Parvulescu V., Tiseanu C., "Lanthanide–lanthanide and lanthanide–defect interactions in co-doped ceria revealed by luminescence spectroscopy", *J. Alloys Comp.,* 616 (**2014)** 535-541.

Babu S., Schulte A., Seal S., "Defects and symmetry influence on visible emission of Eu doped nanoceria", *Appl. Phys. Lett*. 92 **(2008)** 123112.

Balducci G., Islam M. S., Kaspar J., Fornasicro P., Graziani M., "Bulk reduction and oxygen migration in the ceria-based oxides", *Chem. Mater.,* 12 *(***2000)** 677-681.

Balestrieri M., Colis S., Gallart M., Schmerber G., Ziegler M., Gilliot P., Dinia A., "Photoluminescence properties of rare earth (Nd, Yb, Sm, Pr)-doped CeO_2 pellets prepared by solid-state reaction", *J. Mater. Chem. C.*, 3 (2015) 7014-7021.

Bao H., Chen X., Fang J., Jiang Z., Huang W., "Structure-activity Relation of Fe_2O_3–CeO_2 Composite Catalysts in CO Oxidation", *Catal. Lett*., 125 (2008)160-167.

Barreca D., Bruno G, Gasparotto A., Losurdo M., Tondello E., "Nanostructure and optical properties of CeO_2 thin films obtained by plasma-enhanced chemical vapour deposition", *Mater. Sci. Eng. C.,* 23 **(2003)** 1013-1016.

Barton D. G, Shtein M., Wilson R. D., Soled S. L, Iglesia E. J., "Structure and electronic properties of solid acids based on tungsten oxide nanostructures", *J. Phys. Chem. B.,* 103 **(1999)** 630-640.

Beche E., Charvin P., Perarnau D., Abanades S., Flamant G., "Ce 3d XPS investigation of cerium oxides and mixed cerium oxide ($Ce_xTi_yO_z$)", *Sur. Interface Anal.,* 40 **(2008)**264-267.

Bendiganavale A. K., Malshe V. C., "Infrared reflective Inorganic pigments", *Recent patents on Chemical engineering*, 1 **(2008)** 67-79.

Bhim, A., Gopalakrishnan, J., Natarajan, S., "Exploring the corundum structure as a host for colored compounds – synthesis, structures and optical studies of $(MM')_3TeO_6$ (M = Mg, Mn, Co, Ni, Zn; M' = Mg, Mn, Co, Ni, Cu)", *Eur. J. Inorg. Chem*., **(2018)** 2277.

Bhosale A. K., Shinde P. S., Tarwal N. L., Pawar R. C., Kadam P. M., Patil P.S., "Synthesis and characterization of highly stable optically passive CeO_2–ZrO_2 counter electrode" *Electrochim. Acta.,* 55 **(2010)** 1900-1906.

Bin H., Yu X., Chao H., Chen J., Sun X., "Environment-friendly pigments based on praseodymium and terbium doped $La_2Ce_2O_7$ with high near-infrared reflectance: Synthesis and characterization", *Dyes Pigm*., 147 **(2017)** 225-233.

Blasse G.., "On the Eu^{3+} Fluorescence of Mixed Metal Oxides (IV): The Photoluminescent Efficiency of Eu^{3+} Activated Oxides", *J. Chem. Phys.,* 45 **(1966)** 2350-2356.

Blasse, G., "Handbook on Physics and Chemistry of Rare earths", *North Holland Publishing Company, Netherlands.,* **(1979)**.

Blasse G., "Scintillator materials", *Chem. Mater*., 6 **(1994)** 1465-1475.

Bondioli F., Ferrari A. M., Lusvargi L., Manfredini T., Nannerone S., Pasquali L., Selvaggi G., "Synthesis and characterization of praseodymium-doped ceria powders by a microwave-assisted hydrothermal route", *J. Mater. Chem*., 15 **(2005)** 1061-1066.

Borchert H., Frolova Y. V., Kaichev V. V., Prosvirin I. P., Alikina G. M., Lukashevich A. I., Zaikovskii V. I., Moroz E. M., Trukhan S. N., Ivanov V. P., Paukshtis E. A., Bukhtiyarov V. I., Sadykov V. A., "Electronic and chemical properties of nanostructured cerium dioxide doped with praseodymium", *J. Phys. Chem. B*., 109 (**2005)** 5728-5738.

Bunzil J. C., Choppin G. R., *Elsevier, Amsterdam*, **1989**.

Burroughs P., Hamnett A., Orchard A. F., Thornton G., "Satellite structure in the X-ray photoelectron spectra of some binary and mixed oxides of lanthanum and cerium", *J. Chem. Soc. Dalton Trans*., **1976**, 1686-1698.

Buxbaum G., "Industrial Inorganic Pigments", 2nded., Wiley-Vch, Weinheim, Germany, 1997.

Cao R., Quan G., Shi Z., Chen T., Luo Z., Zheng G., Hu Z., "Synthesis and luminescence properties of $La_2Zr_2O_7$:R (R = Sm^{3+}, Bi^{3+}, Sm^{3+}/ Bi^{3+}) phosphor", *J. Phys. Chem. Solids*., 118 **(2018)** 109-113.

Carvalho L. G. A., Rocha L. A., Buarque J. M. M, Gonçalves R. R., Nascimento C. S., Schiavona M. A., Ribeirod S. J. L., Ferrari J. L., "Color tunability in green, red and infra-red upconversion emission in $Tm^{3+}/Yb^{3+}/Ho^{3+}$ co-doped CeO_2 with potential application for improvement of efficiency in solar cells", *J. Lumin.,* 159 (**2015)** 223-228.

Cerro, S., Gargori, C., Llusar, M., Monros, S., "Orthorhombic (Fe_2TiO_5)-monoclinic (Cr_2TiO_5) solid solution series: Synthesis by gel routes, coloring and NIR reflectivity evaluation", *Ceram. Int*. 44 **(2018)** 13349-13359.

Chavan S. V., Mathews M. D., Tyagi A. K., "Phase Relations and Thermal Expansion Studies in the Ceria Yttria System", J. Am. Ceram. Soc., 87 (**2004)** 1977-1980.

Chavan S. V., Tyagi A. K., "Phase relations and lattice thermal expansion studies in the $Ce_{0.50}$ $RE_{0.50}$ $O_{1.75}$ (RE= rare-earths)", *Mater. Sci. Eng. A*., 404 (**2005)** 57-63.

Chen M. Y., Zu X. T., Xiang X., Zhang H. L., "Effects of ion irradiation and annealing on optical and structural properties of CeO_2 films on sapphire", *Physica B*., 389 (**2007)** 263–268.

Chen, X. Yu, H. Bin, X. Sun, "Sustainable cool pigments based on iron and tungsten co-doped lanthanum cerium oxide with high NIR reflectance for energy saving", *Dyes Pigm.,* 154 **(2018)** 1-7.

Cho, J. H., Bass M., Babu S., Dowding J. M., Self T. W., Seal S., "Up conversion luminescence of Yb^{3+}–Er^{3+} codoped CeO_2 nano crystals with imaging applications", *J. Lumi.,* 132 (**2012)** 743-749.

Christie R. M., "Color Chemistry", *Royal Society of Chemistry Publishing,* **(2001)**.

Coduri M., Scavini M., Allieta M., Brunelli M., Ferrero C., "Defect structure of Y-doped ceria on different length scales", *Chem. Mater.,* 25 (**2013)** 4278-4289.

Culubrk S., Antic Z., Cincovic M. M., Ahrenkiel P. S., Dramicanin M. D., "Synthesis and luminescent properties of rare earth (Sm^{3+} and Eu^{3+}) doped $Gd_2Ti_2O_7$ pyrochlore nanopowders", *Opt. Mater*., 37 **(2014)** 598-606.

Dai P., Zhang X., Zhou M., Li X., Yang J., Sun P., Xu C., Liu Y., "Thermally stable pyrochlore $Y_2Ti_2O_7$:Eu^{3+} orange-red emitting phosphors", *J. Am. Ceram. Soc.,*95 **(2012)** 658-662.

Denning J. H., Ross S. D., "The vibrational spectra and structures of rare earth oxides in the A modification", *J. Phys. C: Solid State Phys*., 5 (**1972)** 1123-1133.

Devaiah D., Reddy L. H., Kuntaiah K., Reddy B. M., "Design of novel ceria-based nano-oxides for CO oxidation and other catalytic applications", *Indian J. Chem.,* 51 **(2012)** 186-195.

Dilawar N., Mehrotra S., Varandani D., Kumaraswamy B. V., Haldar S. K., Bandyopadhyay A. K., "A Raman spectroscopic study of C-type rare earth sesquioxides", *Mater. Charact.,* 59 (**2008)** 462-467.

Drache M., Roussel P., Wignacourt J. P., "Structure and oxide mobility in Bi-Ln-O materials: heritage of Bi_2O_3", *Chem. Rev*., 107 **(2007)** 80-96.

Du F., Zhu R., Huang Y., Tao Y., Seo H. J., "Luminescence and microstructures of Eu^{3+} - doped $Ca_9LiGd_{2/3}(PO_4)_7$", *Dalton Trans*., 40 **(2011)** 11433-11440.

Dutta P. S., Khanna A., "Eu^{3+} activated molybdate and tungstate based red phosphors with charge transfer band in blue region", *ECS J. Solid State Sci. Technol*., 2 **(2013)** R3153 - R3167.

Emeline A. V., Kuzmin G. N., Purevdorj D., Ryabchuk V. K., Serpone N., "Spectral dependencies of the quantum yield of photochemical processes on the surface of wide band gap solids gas/solid systems", *J Phys. Chem. B.,* 104 **(2000)** 2989-2899.

Eppler R., Eppler D., "Which Colors Can and Cannot Be Produced in Ceramic Glazes", *Ceram. Eng. Sci. Proc*., 15 **(1994)** 281-288.

Fan Z., Chang P. C., Lu J. G., Walter E. C., Penner R. M., Lin C. H., Lee H. P., "Photoluminescence and polarized photodetection of single ZnO nanowires", *Appl. Phys. Lett*. 85 **(2004)** 6128.

Fan Z., Chao C. C., Babaei F. H., Prinz F. B., "Improving solid oxide fuel cells with yttria-doped ceria interlayers by atomic layer deposition", *J. Mater. Chem.,* 21 (**2011)** 10903-10906.

Feldmann C., Justel T., Ronda C. R., Schmidt P. J., "Inorganic luminescent materials: 100 years of research and application"**,** *Adv. Funct. Mater*., 13 **(2003)** 511-516.

Francis M. P., Mastelaro V. R., "Activity and Characterization by XPS, HR-TEM, Raman Spectroscopy, and BET Surface Area of CuO/CeO_2-TiO_2 Catalysts", *J Phys. Chem. B*., 105 **(2001)**10515-10522.

Fu Y. P, "Preparation and characterization of Y_2O_3: Eu phosphors by combustion process", *J. Mater Sci*., 42 **(2007)** 5165-5169.

Fujihara S., Oikawa M., "Structure and luminescent properties of CeO_2: rare earth (RE = Eu^{3+} and Sm^{3+}) thin films", *J Appl. Phys.,* 95 (**2004)** 8002-8006.

Garcia A., Llusar M., Calbo J., Tena M. A., Monros G., "Low-toxicity red ceramic pigments for porcelainised stoneware from lanthanide-cerianite solid solutions", *Green. Chem.*, 3 **(2001)** 238-242.

Garo D., "Pigments – a growth market", *Eur. Coat. J.,* 1 **(2012)** 10–13.

Glerup M., Nielsen O. F., Poulsen F. W., "The Structural Transformation from the Pyrochlore Structure, A2B2O7, to the Fluorite Structure, AO2, Studied by Raman Spectroscopy and Defect Chemistry Modeling", *J. Solid State Chem. ,* 160 **(2001)** 25-32.

Gnanam S., Rajendran V.," Influence of Various Surfactants on Size, Morphology, and Optical Properties of CeO_2 Nanostructures via Facile Hydrothermal Route" *J. Nanopart.,* **(2013)** 839391- 6.

Grazenaite E., Jasulaitiene V., Rimantas R., Kareiva A., "Sol-gel synthesis, characterization and application of lanthanide-doped cobalt chromates ($CoCr_{2-x}Ln_xO_4$; Ln = Tm^{3+} and Yb^{3+})", *J. Eur. Ceram. Soc.,* 38 **(2018)** 3361-3368.

Guo M., Lu J., Wu Y., Wang Y., Luo M., "UV and visible Raman studies of oxygen vacancies in rare-earth-doped ceria*", Langmiur.,* 27 (**2011)** 3872-3877.

Guoa H., Yanmin Q., "Preparation, structural and photoluminescent properties of CeO_2:Eu^{3+} films derived by Pechini sol–gel process", *Appl. Surf. Sci.,* 254 **(2008)** 1961-1965.

Hagiwara T., Kyo Z., Manabe A., Yamamura H., Nomura K., "Formation of C-type rare earth structures in the $Ce_{1-x}Nd_xO_{2-\delta}$ system: a factor in the decrease in oxide-ion conductivity", *J. Ceram. Soc. Jap.,* 117 (**2009)** 1306-1310.

Hardy E. A., "The performance of color-television picture tube phosphor screens", *IEEE Trans. Broadcast Telev. Receivers*., 11 **(1965)** 33-37.

Ho C., Yu J. C., Kwong T., Mark A. C., Lai S., "Morphology-Controllable Synthesis of Mesoporous CeO_2 Nano- and Microstructures", *Chem. Mater.,* 17 **(2005)** 4514-4522.

Honda T., Masui T., Imanaka N., "Novel environmentally friendly inorganic blue pigments based on calcium scandium silicate garnet", *Chem. Lett*., 42 **(2013)** 1562-1564.

Hongsong Z., Jianguo L., Gang L., Zheng Z., Xinli W., "Investigation about thermophysical properties of $Ln_2Ce_2O_7$ (Ln = Sm, Er and Yb) oxides for thermal barrier coatings", *Mater. Res. Bull*., 47 **(2012)** 4181-4186.

Hongsong Z., Zhengying W., Yongde Z., Gang L., Zhenjum L., "Preparation, characterization of $A_2Ce_2O_7$ (A = La and Gd) and their photo-catalytic activity properties", *Energy Environ. Focus*., 4 **(2015)** 324-329

Horlait D., Claparede L., Clavier N., Szenknect S., Dacheux N., Ravaux J., Podor R., "Stability and Structural Evolution of $Ce^{IV}_{1-x}Ln^{III}_{x}O_{2-x/2}$ Solid Solutions: A Coupled μ-Raman/XRD Approach", *Inorg. Chem.,* 50 (**2011)** 7150-7161.

Ikuma Y., Nagasawa S., Hayasshi N., Kamiya M., "Crystal structure of the CeO_2-$YO_{1.5}$ System", *J. Jpn. Soc. Powder Powder Metall.,* 52 **(2005)**599-602.

Imagawa H., Suda A., Yamamura K., Sun S., "Monodisperse CeO_2 nanoparticles and their oxygen storage and release properties", *J. Phys. Chem. C.,* 115 **(2011)** 1740-1745.

Imanaka N., Masui T., Furukawa S., "Novel nontoxic and environment-friendly inorganic yellow pigment", *Chem. Lett*., 37 **(2008)** 104-105.

Jansen M., Letschert H. P., "Inorganic yellow-red pigments without toxic metals", *Nature.,* 404 **(2000)** 980-982.

Jeevanandam P., Mulukutla R. S., Philips M., Chaudari S., Erickson L. E., Klabunde K. J., "Near infrared reflectance properties of Metal oxide nanoparticles", *J. Phys. Chem.*, 111 **(2007)** 1912-1918.

Jehng J. M., I. E. Wachs, "Structural chemistry and Raman spectra of Niobium oxides", *Chem. Mater*., 3 **(1991)** 100-107.

Jesionowski T., Ciesielczyk F., "Pigment Inorganic" *Encyclopedia of Color Science and Technology*, (2013) https://doi.org.10.1007/978-3-642-27851-8_180-1.

Ji P., Zhang J., Chen F., Anpo M., "Ordered mesoporous CeO_2 synthesized by nanocasting from cubic Ia3d mesoporous MCM-48 silica: formation, characterization and photocatalytic activity", *J. Phys. Chem. C.,* 112 (**2008**) 17809–17813.

Jiang H., You W., Liu X., Liao J., Wang P., Yang B., "Yb^{3+} and Er^{3+} co-doped $Y_2Ce_2O_7$ nanoparticles: synthesis and spectroscopic properties", *Bull. Mater. Sci*., 36 **(2013)** 1147-1151.

Jiang L., Yao M., Liu B., Li Q., Liu R., Hang L., Lu S., Gong C., Zou B., Cui T., Liu B., "Controlled synthesis of CeO_2/Graphene Nanocomposites with highly enhanced optical and catalytic properties", *J. Phys. Chem. C*., 116 (2012) 11741-11745.

Jianlan C., Gregory A. H., "Raman and Fluorescence Spectroscopy of CeO_2, Er_2O_3, Nd_2O_3, Tm_2O_3, Yb_2O_3, La_2O_3, and Tb_4O_7", *J. Spectrosc.,* (**2015)** 940172 1-8.

Johnston R. M. In., Putton T. C. (Ed.), "Pigment Handbook, 3", *Wiley- Interscience Publication.*, New York, **(1973)** 229.

Jose M. C., Javier A., "V-containing ZrO_2 inorganic yellow nano-pigments prepared by hydrothermal approach", *Dye Pigm*., 146 **(2017)** 178-188.

Joubert M.F., "Photon avalanche upconversion in rare earth laser materials", *Opt. Mater.*, 11 **(1999)** 181-203.

Judd B. R., "Optical absorption intensities of rare-earth ions", *Phys. Rev*., 127 (**1962**) 750-761.

Kalland L. E., Norberg S. T., Kyrklund J., Hull S., Eriksson S. G., Norby T., Mohn C. E., Knee C. S., "C-type related order in the defective fluorites $La_2Ce_2O_7$ and $Nd_2Ce_2O_7$ studied by neutron scattering and ab initio MD simulations", *Phys. Chem. Chem. Phys*., 18 **(2016)** 24070-24080

Keramidas V. G., White W. B, "Raman spectra of oxides with the fluorite structure", *J. Chem. Phys.,* 59 **(1973)**1561-1562.

Khan M. M., Ansari S. A., Pradhan D., Han D. H., Lee J., Cho M. H., "Defect-induced band gap narrowed CeO_2 nanostructures for visible light activities", *Ind. Eng. Chem. Res*., 53 (2**014)** 9754-9763.

Kilbourn B.T., in: "Cerium and Cerium Compounds", *Ullmann's encyclopedia,* Vol. 5, p. 728.

Kortum G., "Reflectance Spectroscopy Principles, Methods, Applications", *Springer,* New York, **1969**.

Kosacki I., Petrovsky V., Anderson H. U., "Raman Spectroscopy of Nanocrystalline Ceria and Zirconia Thin Films", *J. Am. Ceram. Soc.,*85 **(2002)**2646-2650.

Krupa J. C., "High-energy optical absorption in f-compounds", *J. Solid State Chem*., 17 **(2005)** 483-488.

Kubelka P., Munk F., "Ein Beitragzur Optik der Farbanstriche", *Zeitshrift fuer Technischr Physik*., 12 **(1931)** 593-601.

Kumar A., Karakoti A. S., Schuile A., Seal S., "Luminescence properties of Europium-doped cerium oxide nanoparticles:Role of oxygen vacancy and oxidation state", *Langmuir.,* 25 **(2009)** 10998-11007.

Kumari L. S., Rao P. P., Reddy M. L. P., "Environment-friendly red pigments from CeO_2-Fe_2O_3-Pr_6O_{11} solid solutions", *J. Alloys Comp.,* 461 **(2008)** 509-515.

Kumari L. S., Gayathri T. H., Sameera S. F., Rao P. P., "Y-doped Bi_2MoO_6 as environmentally Friendly Yellow Pigments", *J. Am. Ceram. Soc*., 94 **(2011)** 320-323.

Kumari L. S., Rao P. P., Sameera S., Koshy P., "Synthesis and optical properties of $Ce_{0.95}Pr_{0.05-x}M_xO_2$ (M = Mn, Si) as potential ecological red pigments for coloration of plastics", *Ceram. Int.,* 38 **(2012)** 4009-4016.

Kunimi S., Fujihara S., "Synthesis and luminescent properties of CeO_2 : Pr^{3+}, Eu^{3+} Red Pigments", *ECS J. Solid. State. Sci. Tech.,* 1 **(2012)** R32-R36.

Kuo Y. F., Tseng T. Y., "Structure-related optical properties of rapid thermally annealed $Ba_{0.7}Sr_{0.3}TiO_3$ thin films", *Mater. Chem. Phys.,* 61 **(1999)** 244-250.

Larsson P. O., Andersson A., "Complete Oxidation of CO, Ethanol, and Ethyl Acetate over Copper Oxide Supported on Titania and Ceria Modified Titania", *J. Catal.,* 179 **(1988)** 72-89.

Laversenne L., Guyot Y., Adad M. C., Boulon G., "Optimization of spectroscopic properties of Yb^{3+}-doped refractory sesquioxides: cubic Y_2O_3, Lu_2O_3 and monoclinic Gd_2O_3", *Opt. Mater.* 16 (2**001)** 475-483.

Lawrence N. J., Brewer J. R., Wang L., Wu T. S., Wells-Kingsbury J., Ihrig M. M., Wang G., Soo Y. L., Mei W. N., Cheung C. L., "Defect engineering in cubic cerium oxide nanostructures for catalytic oxidation", *Nano. Lett.*, 11 **(2011)** 2666-2671.

Lee H. Y., Kim S., Hong Y. P., Lee Y. C., Park Y. H., Ko K. H., "Controlling the texture of CeO_2 films by room temperature RF magnetron sputtering", *Surf. Coat. Technol.,* 173 **(2003)** 224-228.

Lenka S., Sulcova P., Jitka M.,"Study of ceramic pigments based on $Er_2Ce_{2-x}Mo_xO_7$", *J. Therm. Anal. Calorim.,* 109 **(2012)** 643–648.

Levinson, R., Berdahl, P., Akbari, H., "Solar spectral optical properties of pigments-Part II: Survey of common colorants". *Sol. Energy Mater. Sol. Cells.,* 89 **(2005)** 351-
.

Li H., Li W., Gu S., Wang F., Zhou H., "In-built Tb^{4+}/Tb^{3+} redox centers in terbium-doped bismuth molybdate nanograss for enhanced photocatalytic activity", *Catal. Sci. Technol.*, 6 **(2016)** 3510-3519.

Li H. L., Xie R. J., Hirosaki N., Takeda T., Zhou G.H., "Synthesis and luminescence properties of orange-red-emitting $M_2Si_5N_8:Eu^{2+}$ (M = Ca, Sr, Ba) light-emitting diode conversion phosphors by a simple nitridation of MSi_2", *Int. J. Appl. Ceram. Tec.,* 6 **(2009)** 459-464.

Li Y. Q., Mei S. G., Byon, Y. J., Wang J. L., Zhang G. L., "Highly solar radiation reflective Cr2O3-3TiO2 orange nanopigment prepared by a polymer-pyrolysis method", *ACS Sustainable Chem. Eng*., 2 **(2014)** 318-.

Liao C., Cao R., Ma Z., Li Y., Dong G., Sharafudeen K. N., "Synthesis of K_2SiF_6:Mn^{4+} phosphor from SiO_2 powders via Redox Reaction in HF/$KMnO_4$ solution and their application in warm-white LED", J. Qiu, *J. Am. Ceram. Soc*., 96 **(2013)** 3552-3556.

Liao J., Nie L., Wang Q., Liu S., Fu J., Wen H. R., "Microwave hydrothermal methoand photoluminescence properties of $Gd_2Sn_2O_7$:Eu^{3+} reddish orange phosphors", *J. Lumin*., 183 **(2017)** 377-382.

Lim W. F., Cheong K. Y., "Oxygen vacancy formation and annihilation in lanthanum cerium oxide as a metal reactive oxide on 4H-silicon carbide", *Phys. Chem. Chem. Phys.,* 16 **(2014)** 7015-7022.

Lin Y., Han A., Ye M., Chen X., Yao L., Ding C., "Synthesis and characterization of environmentally begin inorganic pigments with high NIR reflectance; Lanthanum-doped $BiFeO_3$", *Dyes Pigm*., 148 **(2018)** 137-146.

Linda F. T., Rao P. P., Mariyam T., Mahesh S. K., Reshmi V. R., "Effect of Zr^{4+} and Si^{4+} substitution on the luminescence properties of $CaMoO_4$:Eu^{3+} red phosphors", *J. Mater Sci. Mater Electron.*, 25 **(2014)** 2387-2393.

Linda F. T., Rao P. P., Mahesh S. K., Sreena T. S., and Parvathi S. B., "Effect of host structure on the photoluminescence properties of Ln_3TaO_7:Eu^{3+} red phosphors", *Optical Mater*., 52 **(2016)** 134-143.

Liu L., Han A., Ye M., Zhao M., "Synthesis and characterization of Al^{3+} doped $LaFeO_3$ compounds:A novel inorganic pigments with high near-infrared reflectance", *Sol. Energy Mater. Sol. Cells*., 132 **(2015)** 377-384.

Liu X., Chen S., Wang X., "Synthesis and photoluminescence of CeO_2:Eu^{3+} phosphor powders", *J. Lumi.* 127 (**2007)** 650-654.

Llusar M., Calbo J., Badeness J. A., Tena M. A., Monros G., "Synthesis of iron zircon coral by coprecipitation routes", *J. Mater. Sci.,* 36 **(2001)** 153-163.

Llusar M., Vitaskova L., Sulcova P., Tena M. A., Badenes J. A., Monros G., "Red ceramic pigments of terbium-doped ceria prepared through classical and non-conventional coprecipitation routes", *J. Europ. Ceram. Soc*., 30 **(2010)** 37-52.

Logothetis E. M., "12th State of-the-Art symposium on Ceramics in Service of Men, Washington, DC", **1976**.

Luo X., Cao W., Xing M., "Preparation of nano Y_2O_2S:Eu phosphor by ethanol assisted combustion synthesis method", *J. Rare Earth*., 24 **(2006)** 20-24.

Mahesh S. K., Rao P. P., Thomas M., Francis T. L., Koshy P., "Influence of cation substitution and activator site exchange on the photoluminescence properties of Eu^{3+} -doped quaternary pyrochlore oxides", *Inorg. Chem*., 52 **(2013)** 13304-13313.

Maksimchuk P. O., Masalov A. A., Malyukin Y. V., "Spectroscopically detected formation of oxygen vacancies in nano-crystalline CeO_{2-x}", *J. Nano- Electron. Phys*., 5 **(2013)** 01004 1-4.

Malathi M., Sreenu K., Ravi G., Kumar P. V., Reddy C. H., Guje R., Velchuri R., Vithal M., "Low temperature synthesis of fluorite-type Ce-based oxides of composition $Ln_2Ce_2O_7$ (Ln = Pr, Nd and Eu): photodegradation and luminescence studies", *J. Chem. Sci.*, 129 **(2017)** 1193-1203

Mandal B. P., Grover V., Roy M., Tyagi A. K., "X-Ray Diffraction and Raman Spectroscopic Investigation on the Phase Relations in Yb_2O_3- and Tm_2O_3-Substituted CeO_2", *J. Am. Ceram. Soc.,* 90 **(2007)** 2961-2965.

Mariyam T., Rao P. P., Deepa M., Chandran M. R., Koshy P., "Novel powellite-based red-emitting phosphors: $CaLa_{1-x}NbMoO_8:xEu^{3+}$ for white light emitting diodes", *J. Solid State Chem.,* 182 **(2009)** 203-207.

Mariyam T., Rao P. P., Mahesh S. K., Reshmi V. R., Linda F. T., Koshy P., "Improvement of Morphology and Luminescence Properties of Powellite Type Red Phosphors $CaGd_{1-x}NbMoO_8:xEu^{3+}$ Synthesized via Citrate Gel Route", *J. Am. Ceram. Soc.,* 95 **(2012)** 2260-2265.

Marrocchelli D., Bishop S. R., Kilner J., "Chemical expansion and its dependence on the host cation radius", *J. Mater. Chem. A.,*1 (**2013)** 7673-7680.

Masui T., Peng Y., Machida K. I., Adachi G. Y., "Reduction Behavior of CeO_2– ZrO_2 Solid Solution Prepared from Cerium Zirconyl Oxalate", *Chem. Mater.,* 10 **(1998)** 4005-4009.

Melchionna M., Fornasiero P., "The role of ceria-based nanostructured materials in energy applications", *Mater. Today.,* 17 **(2014)** 349-357.

McBride J. R., Hass K. C., Poindexter B. D., Weber W. H., "Raman and X-ray studies of $Ce_{1-x}RE_xO_{2-y}$, where RE= La, Pr, Nd, Eu, Gd, and Tb*", J. Appl. Phys.,* 76 **(1994)** 2435-2441.

Min B. H., Lee J. C., Jung K. Y., Kim D. S., Choi B. K, Kang W., "Aerosol synthesized $CeO_2:Eu^{3+}/Na^+$ red nanophosphor with enhanced photoluminescence", *RSC Adv.*, 6 **(2016)** 81203-81210.

Nakajima A., Yoshihara A., Ishigame M., "Defect-induced Raman spectra in doped $Ce0_2$", *Phys. Rev. B.,* 50 **(1994)** 13297-13307.

Nakamura A., "New defect-crystal-chemical approach to non-Vegardianity and complex defect structure of fluorite-based MO_2–$LnO_{1.5}$ solid solutions (M^{4+} = Ce,

Th; Ln^{3+} = lanthanide) part I: Model description and lattice-parameter data analysis", *Solid State Ionic.,* 181 **(2010)** 1543-1564.

Nakayama M., Martin M., "First-principles study on defect chemistry and migration of oxide ions in ceria doped with rare-earth cations", *Phys. Chem. Chem. Phys.,* 11 **(2009)** 3241-3249.

Nahum M., Hector B., Raquel M., Beartriz J., Juan B. C., Purificacion E., "Optimization of Praseodymium –doped cerium pigment synthesis temperature", *J. Am. Chem. Soc.,* 86 **(2003)** 425-430.

Nazarov M., Noh D. Y., "New Generation of Europium and Terbium Activated Phosphors: From Syntheses to applications", *Pan Stanford Publishing, Pte. Ltd., Singapore* **(2011)**.

Neeraj S., Kijima N., Cheetham A. K., "Novel red phosphors for solid state lighting; the system $Bi_xLn_{1-x}VO_4$; Eu^{3+}/Sm^{3+} (Ln = Y, Gd)", *Solid State Commun*., 131 **(2004)** 65-69.

Netterfield R. P., Sainty W. G., Martin P. J., Sie S. H.," Properties of CeO_2 thin films prepared by oxygen-ion-assisted deposition", *Appl. Opt.,* 24 **(1985)** 2267-2272.

Nishida T., Ban T., Kobayashi N., "High-color-rendering light sources consisting of a 350-nm ultraviolet light-emitting diode and three-basal-color phosphors", *Appl. Phys. Lett.*, 82 **(2003)** 3817-3819.

Nishino H., Yamamura H., Arai T., Kakinuma K., Nomura K., "Effect of Cation Radius Ratio and Unit Cell Free Volume on Oxide-Ion conductivity in Oxide Systems with Pyrochlore-Type Composition", *J. Ceram. Soc. Japan.,* 112 **(2004)** 541-546.

Nolan M., "Charge Compensation and Ce^{3+} Formation in Trivalent Doping of the CeO_2 (110) Surface: The Key Role of Dopant Ionic Radius", *J. Phys. Chem. C.,* 115 (**2011**) 6671-6681.

Normand F. L., Hilaire L., Kili K., Krill G., Maire G., "Oxidation State of Cerium in Cerium-Based Catalysts Investigated by Spectroscopic Probes", *J. Phys. Chem.,* 92 **(1988)** 2561-2568.

Ofelt G. S., "Intensities of crystal spectra of rare-earth ions." *J. Chem. Phys.*, 37 (**1962**) 511-520.

Olegario R. C., Souza E. C. F., Borges J. F. M., Cunha J. B. M, Andrade A. V. C., Antunes S. R. M., Antunes A. C., "Synthesis and characterization of Fe^{3+} doped cerium praseodymium oxide pigments", *Dyes Pigm.,* 97 **(2013)** 113-117.

Ou D. R., Mori T., Ye F., Kobayashi T., "Oxygen vacancy ordering in heavily rare-earth-doped ceria", *Appl. Phys. Lett.,* 89 (**2006)** 171911 1-3.

Pavlov R. S., Castello J. C., Marza V. B., Hohembergerger J. M., "New Red-Shade Ceramic pigments based on $Y_2Sn_{2-x}Cr_xO_{7-\delta}$ ", *J. Am. Ceram. Soc.,* 85 **(2002)** 1197-1202.

Patsalas P., Logothetidis S., Metaxa C., "Optical performance of nanocrystalline transparent ceria films", *Appl. Phys. Lett.,* 81 **(2002)** 466-468.

Patil S., Seal S., Guo Y., Schulte A., "Norwood, Role of trivalent La and Nd dopants in lattice distortion and oxygen vacancy generation in Cerium oxide nanoparticles", J. *App. Phys. Lett,.* 88 (**2006**) 243110 1-3.

Peiterson L., Soverna s., Meijerink A., "On the nature of the luminescence of Sr_2CeO_4", J. Electrochem. Soc., 147 **(2000)** 4688-4691.

Piao X., Machida K., Horikawa T., Hanzawa H., Yasuo S., Naoto K., "Preparation of CaAlSiN3:Eu2+ phosphors by the self-propagating high-temperature synthesis and their luminescent properties", *Chem. Mater*., 19 **(2007)** 4592-4599.

Primus P. A., Ritschel T., Siguenza P. Y., Cauqui M. A., Garrido J. C. H., Kumke M. U., "High-Resolution Spectroscopy of Europium-Doped Ceria as a Tool To Correlate Structure and Catalytic Activity", *J. Phys. Chem. C,.* 118 **(2014)** 23349-23360.

Radhakrishnan A. N., Rao P. P., Sibi K. S., Deepa M., Koshy P., "Order-disorder phase transformations in quaternary pyrochlore oxide system: Investigated by X-ray diffraction, transition electron microscopy and Rman spectroscopic techniques", *J. Solid State Chem.,* 182 **(2009)** 2312-2318.

Rahaman M. N., Zhou Y. C., "Effect of solid solution additives on the sintering of ultra-fine CeO_2 powders", *J. Europ. Ceram. Soc.* 15 **(1995)** 939-950.

Ramana S., Rao B. G., Venkataswamy P., Rangaswamy A., Reddy B. M., "Nanostructured Mn-doped ceria solid solutions for efficient oxidation of vanillyl alcohol", *J. Mol. Catal. A Chem*. 415 **(2016)** 113–121.

Ratinen H., "X-ray-excited optical fluorescence from pure and rare-earth-doped magnesium and calcium oxides", *Phys. Status Solidi A.*, 12 **(1972)** 175-180.

Reddy B. M., Bharali P., Saikia P., Park S. E., van den Berg M. W. E., Muhler M., Grunert W., "Structural characterization and catalytic activity of nanosized $Ce_xM_{1-x}O_2$ (M = Zr and Hf) mixed oxides", *J. Phys. Chem. C*., 112 **(2008)** 11729-11737.

Reddy B. M., Katta L., Thrimurthulu G.. "Novel Nanocrystalline $Ce_{1-x}La_xO_{2-\delta}$ (x= 0.2) Solid Solutions: Structural Characteristics and Catalytic Performance", *Chem. Mater.,* 22 (**2010)** 467-475.

Repelin Y., Proust C., Husson E., Benny J. M., "Vibrational spectroscopy of the C-form of yttrium sesquioxide", *J. Solid State Chem.,* 118 **(1995**) 163-169.

Rhone P., French Patent 1.257.078, **1960**.

Richards B.S., "Enhancing the performance of silicon solar cells via the application of passive luminescence conversion layers", *Sol. Energy Mater. Sol. Cells.,* 90 **(2006)** 2329-2337.

Ridwan M., Tamarany R., Han J., Nam S. W., Kim J. K., Choi S. H., Jang S. C., Yoon C. W., "Atomically dispersed Cu on $Ce_{1-x}RE_xO_{2-\delta}$ nanocubes (RE = La and Pr) for water gas shift: influence of OSC on catalysis", *RSC Adv.* 5 **(2015)** 89478-89481.

Roh J., Hwang S. H., Jang J., "Dual-Functional CeO_2:Eu^{3+} Nanocrystals for Performance-Enhanced Dye-Sensitized Solar Cells", *ACS Appl. Mater. Interfaces.,* 6 **(2014)** 19825–19832.

Romeo M., Bak K., Fallah J. E., Normand F. L., Hilaire L., "XPS study of the reduction of cerium dioxide*", Surf. Interface Anal.* 20 **(1993)** 508-512.

Rossell H. J., Scott H. G., "Ordering in fluorite-related oxide systems", *J. De Physique.,* 38 **(1977)** C7 28-31.

Sameera S., Rao P. P., James V., Divya S., Raj A. K. V., "Influence of $(LiLa)_{1/2}MoO_4$ substitution on the pigmentary properties of $BiVO_4$", *Dyes Pigm*., 104 **(2014)** 41-47.

Setlur A. A., Heward W. J., Gao Y., Srivastava A. M., Gopi R. C, Shankar M. V., "Crystal chemistry and luminescence of Ce^{3+} -doped $Lu_2CaMg_2(Si,Ge)_3O_{12}$ and its use in LED based lighting", *Chem. Mater*., 18 **(2006)** 3314-3322.

Sha D., Giridhar M., Row T. N. G., "Synthesis and structure of $Bi_2Ce_2O_7$: a new compound exhibiting high solar photocatalytic activity", *Dalton. Trans*., 41 **(2012)** 9598-9600.

Shalav A., Richards B. S., Green M. A., "Luminescent layers for enhanced silicon solar cell performance: Up-conversion", *Sol. Energy Mater. Sol. Cells*., 91 **(2007)** 829-842.

Sharma A., Varshney M., Park J., Ha T. K., Chae K. H., Shin H., "Bifunctional $Ce_{1-x}Eu_xO_2$($0 \leq x \leq 0.3$) nanoparticles for photoluminescence and photocatalyst applications: an X-ray absorption spectroscopy study", *J. Phys. Chem. Chem. Phys.,* 17 (**2015)** 30065-30075.

Shi S., Hossu M., Hall R., Chen W., "Solution combustion synthesis, photoluminescence and X-ray luminescence of Eu-doped nanoceria CeO_2:Eu", *J. Mater. Chem.* 22 **(2012)** 23461-23467.

Shi S., He L., Geng L., Jiang L., Wang S., Zhang J., Zhou J., "Solution combustion synthesis and enhanced luminescence of Eu^{3+} -activated $Y_2Ce_2O_7$ phosphor nanopowders", *Ceram. Int*. 41 **(2015)** 11960-11965.

Shi S., Li K., Wang S., Zong R., Zhang G., "Structural characterization and enhanced luminescence of Eu-doped $2CeO_2$–$0.5La_2O_3$ composite phosphor powders by a facile solution combustion synthesis", *J. Mater. Chem. C*., 5 **(2017)** 4302-4309.

Shukla R., Gupta S. K., Grover V., Natarajan V., Tyagi A. K., "The role of reaction conditions in the polymorphic control of Eu^{3+} doped $YInO_3$: structure and size sensitive luminescence", *Dalton. Trans.,* 44 (**2015)** 10628-10635.

Shyu J. Z., Weber W. H., Gandhi H. S., "Surface Characterization of Alumina-Supported Ceria", *J. Phys. Chem.,* 92 **(1988)** 4964-4970.

Silversmith A. J., Boye D. M., Brewer K. S., Gillespie C. E., Lu Y., Campbell D. L.,"$^5D_3$-^7F_J emission in terbium-doped sol–gel glasses", *J. Lumin.,* 121 **(2006)** 14-20.

Som S., Dutta S., Vijay K., Vinod K., Swart H. C., Sharma S. K., " Swift heavy ion irradiation induced modification in structural, optical and luminescence properties of Y_2O_3:Tb^{3+} nanophosphor", *J. Lumi.,* 146 **(2014)**, 162-173.

Som S., Kunti A. K., Vinod K., Vijay K., Dutta S., Chowdhury M., Sharma S. K., Terblans J. J., Swart H. C., "Defect correlated fluorescent quenching and electron phonon

coupling in the spectral transition of Eu^{3+} in $CaTiO_3$ for red emission in display application", *J. Appl. Phys.* 115 **(2014)** 193101-14.

Som S., Mitra P., Vijay K., Vinod K., Terblas J. J., Swart H. C., Sharma S. K., "The energy transfer phenomena and colour tenability in $Y_2O_2S:Eu^{3+}/Dy^{3+}$ micro-fibers for white emission in solid state lighting applications", *Dalton Trans.,* 43 **(2014)** 9860-9871.

Sorbello C., Barja B. C., Jobbagy M., "Monodispersed Ce (IV)–Gd(III)–Eu(III) oxide phosphors for enhanced red emission under visible excitation", *J. Mater. Chem. C.,* 2 (**2014)** 1010-1017.

Sreeram K. J., Aby C. P., Nair B. U., "Synthesis and characterization of doped rare earth oxides for environmentally benign non-toxic reddish –yellow pigments", *Chem. Lett.* 37 **(2008)** 902-903.

Sreena T. S., Rao P. P., Raj A. K. V., Babu P. S., "Influence of Structural Disorder on the Photoluminescence Properties of Eu^{3+} Doped Red Phosphors: $Ca_2Y_{3-x}Nb_3O_{14}$: xEu^{3+}," *Chem. Select*., 1 (**2016)** 3413 -3422.

Srinivasan R., Chandra Bose A., "Structural and optical properties of Eu^{3+} doped cerium oxide nanophosphors", *Funct. Mater. Lett.,* 4 (**2011)** 13-16.

Steele J. A., Lewis R. A., "In situ micro-Raman studies of laser-induced bismuth oxidation reveals metastability of β-Bi_2O_3 microislands", *Opt. Mater. Express*., 4 **(2014)** 2133–2142.

Stranska L., Sulcova P., Milan V., "Synthesis and properties of inorganic pigments based on pyrochlore compounds with different lanthanides", *J. Therm Anal. Calorim*., 113 **(2013)** 127-135.

Sudarsan V., "Optical materials: Fundamentals and applications", *Functional Materials Preparation, Processing and Applications*., **(2012**) 285-322.

Sulcova P., "The synthesis and analysis of $Ce_{0.95-y}Pr_{0.05}Gd_yO_{2-y/2}$ pigments", *Dyes Pigm.,* 52 **(2002)** 89-93.

Sulcova P., Trojan M., "Study of $Ce_{1-x}Pr_xO_2$ pigments", *Thermochim. Acta*., 395 **(2002)** 251-255.

Sulcová P., Vitaskova L., Vondrasek M., Trojan M., "Synthesis and characterization of the $Ce_{0.9}Tb_{0.1}O_2$", *Ceram. Mater*., 60 **(2008)** 136-138.

Sulcová P., Vitaskova L., Trojan M., "Thermal analysis of the $Ce_{1-x}Tb_xO_2$ pigments", *J. Therm. Anal. Calorim.* 99 **(2010)** 409-413.

Sulcova P., "Thermal stability and color properties of new pigments based on $BiREO_3$", *J. Therm Anal Calorim*., 109 **(2012)** 639-42.

Tesitelova K., Sulcova P., "Synthesis and study of mixed oxide inorganic pigment from Bi_2O_3-ZnO-CeO_2 system", *J. Therm. Anal Calorim*., 130 **(2017)** 57-62.

Thomas R., Dube D. C., "Optical Properties of Sol–Gel Processed Amorphous and Crystalline $SrTiO_3$ Thin Films", *Jpn. J. Appl. Phys.,* 39 **(2000)** 1771-1775.

Thomas R., Due D. C., Kamalasanan M. N., Chandra S., "Optical and electrical Properties of $BaTiO_3$ Thin Films prepared by chemical solution deposition", *Thin Solid Films.*, 346 **(1999)** 212-225.

Thorat A. V., Ghoshal T., Carolan P., Holmes J. D., Morris M. A., "Defect chemistry and vacancy concentration of luminescent europium doped ceria nanoparticles by the solvothermal method", *J. Phys. Chem. C.,* 118 (**2014)** 10700-10710.

Tick P.A., "Transparent glass ceramics for 1300 nm amplifier applications", *J. Appl. Phys.,* 78 **(1995)** 6367-6374.

Tiseanu C., Cojocaru B., Avaram D., Parvulescu V. I., Vela-Gonzalez A. V, Dominguez S. M., "Isolated centers versus defect associates in Sm^{3+} -doped CeO_2: a spectroscopic investigation", *J. Phys. D: Appl. Phys*., 46 **(2013)** 275302 1-8.

Tiseanu C., Parvulescu V. I., Boutonnet M., Cojocaru B., Primus P. A., Teodorescu C. M., Solans C., Dominguez M. S., "Surface versus volume effects in luminescent ceria nanocrystals synthesized by an oil-in-water microemulsion method", *Phys. Chem. Chem. Phys.* 13 (**2011)** 17135-17145.

Trovarelli A., de Leitenburg C., Dolcetti G., "Design Better Cerium–based Oxidation Catalysts", *Chem. Tech*., 27 **(1997)** 32-40.

Vimal G., Mani K P., Biju P. R., Joseph C., Unnikrishnan N. V., Ittyachen M. A., "Structural studies and luminescence properties of CeO_2:Eu^{3+} nanophosphors synthesized by oxalate precursor method", *Appl. Nanosci.,* 5 **(2015)** 837-846.

Vinod K., Vijay K., Som S., Duvenhage M. M., Ntwaeaborwa O. M., Swart H. C., "Effect of Eu doping on the photoluminescence properties of ZnO nanophosphors for red emission applications", *Appl. Surf. Sci*., 308 **(2014)** 419-430.

Vishnu V. S., George G., Divya V., Reddy M. L. P., "Synthesis and characterization of new environmentally benign tantalum – doped $Ce_{0.8}Zr_{0.2}O_2$ yellow pigments: applications in coloring of plastics", *Dyes Pigm.,* 82 **(2009)** 53-57.

Vishnu V. S., George G., Reddy M. L. P., "Effect of molybdenum and praseodymium dopants on the optical properties of $Sm_2Ce_2O_7$: Tuning of band gaps to realize various color hues", *Dyes Pigm*., 85 **(2010)** 117-123.

Vishnu V. S., Reddy M. L. P., "Near-infrared reflecting inorganic pigments based on molybdenum and praseodymium doped yttrium cerate: synthesis, characterization and optical properties". *Sol. Energy. Mater. Sol. Cells*., 95 **(2011)** 2685-2692.

Veronica M. G. P, Hofmann A., Sauer J., "Oxygen vacancies in transition metal and rare earth oxides: Current state of understanding and remaining challenges", *Surf. Sci. Rep.* 62 **(2007)** 219-270.

Walrand C. G., Binnemans K., "Rationalization of Crystal-Field Parametrization, in Handbook on the Physics and Chemistry of Rare Earths", ed. K. A. Gschneidner Jr. and L. Eyring, *North-Holland, Amsterdam*., 23 **(1996)**.

Wang J., Cheng Y., Huang Y., Cai P., Kim S., Seo H. J.,"Structural and luminescent properties of red-emitting Eu^{3+}-doped ternary rare earth antimonates R_3SbO_7 (R = La, Gd, Y)", *J. Mater. Chem. C.*, 2 **(2014)** 5559-5569.

Wang Z. L., Li G. R., Ou Y. N., Feng Z. P., Qu D. L., Tong Y. X., "Electrochemical Deposition of Eu^{3+}-Doped CeO_2 Nanobelts with Enhanced Optical Properties", *J. Phys. Chem. C.,* 115 (**2011)** 351-356.

Wang Z., Quan Z., Lin J., "Remarkable changes in the optical properties of CeO2 nanocrystals induced by lanthanide ions doping", *Inorg. Chem.,* 46 (**2007)** 5237-5242.

Weber W. H., Hss K. C., McBride J. R., "Raman study of CeO_2: second-order scattering, lattice dynamics, and particle-size effects", *Phys. Rev. B.,* 48 (**1993)** 178-185.

Wei Xi., Pan W., Cheng L., Li B., "Atomistic calculation of association energy in doped ceria", *Solid. State. Ionics*., 180 (**2009)** 13-17.

Wu J., Shi S., Wang X., Li J., Zong R., Chen W., "Controlled synthesis and optimum luminescence of Sm^{3+}-activated nano/submicroscale ceria particles by a facile approach", *J. Mater. Chem. C*., 2 (**2014)** 2786-2792.

Wu X. D., Dye C. R., Muenchausen R. E., Foltyn S. R., Maley M., Rollett A. D., Garcia A. R., Nogar N. S., "Epitaxial CeO_2 films as buffer layers for high-temperature superconducting thin films", *Appl. Phys. Lett.,* 58 **(1991)** 2165-2167.

Xie R. J., Li Y. Q., Yamamoto H., Hirosaki N., "Nitride phosphors and solid state lighting", *CRC Press*, (**2011**).

Yabe S., Sato T., "Cerium oxide for sunscreen cosmetics", *J Solid. Stat. Chem.,* 171 **(2003)** 7-11.

Yashima M., Tomoya T. J.*,* "Atomic displacement parameters of ceria doped with rare-earth oxide $Ce_{0.8}R_{0.2}O_{1.9}$ (R= La, Nd, Sm, Gd, Y, and Yb) and correlation with oxide-ion conductivity*", Phys. Chem. C.,* 114 (**2010)** 10670.

Yuan Q., Duan H. H., Li L. L., Sun L. D., Zhang Y. W., Yan C. H., "Controlled synthesis and assembly of ceria-based nanomaterials", *J. Colloid. Inter. Sci.,* 2 **(2009)** 151-167.

Yu M., Lin J., Zhou Y. H., Wang S. B., "Citrate–gel synthesis and luminescent properties of $ZnGa_2O_4$ doped with Mn^{2+} and Eu^{3+}", *Mater. Lett.,* 56 **(2002)** 1007-1013.

Yu Y., Chen D., Huang P., Lin H., Yang A., Wang Y., "Sensitization and protection of Eu^{3+} luminescence by CeO_2 in nano-composite", *J. Alloys Compd*., 513 **(2012)** 626-629.

Zhang F., Chan S. W., Spanier J. E., Apak E., Jin Q., "Cerium oxide nanoparticles: Size-selective formation and structure analysis", *Appl. Phys. Lett.,* 80 **(2002)** 127-129.

Zhang H., Yang Q., Zhang B., Lu S., "Raman spectroscopic investigation of lanthana-doped neodymium-yttria transparent ceramics", *J. Raman Spectrosc.,* 42 (**2011)** 1384-1387.

Zhan Z., Barnett S. A.," An Octane-Fueled Solid Oxide Fuel Cell", *Science.,* 308 **(2005)** 844-847.

Zhao M., Han A., Ye M., Wu T., "Preparation and characterization of Fe^{3+} doped $Y_2Ce_2O_7$ pigments with high near-infrared reflectance", *Sol. Energy*., 97 **(2013)** 350-355.

Zou J., Zhang P., Liu C., Peng Y., "Highly dispersed (Cr, Sb)-co-doped rutile pigments of cool color with high near-infrared reflectance", *Dye Pigm.,* 109 **(2014)** 113-119.

LIST OF PUBLICATIONS

1. **Athira K. V. Raj**, P. Prabhakar Rao and Sreena T. S, "Color Tunable Pigments with High NIR Reflectance in Terbium Doped Cerate Systems for Sustainable Energy Saving Applications", ***ACS Sustainable Chemistry and Engineering***, 7, **2019**, 8804–8815.

2. **Athira K. V. Raj**, P. Prabhakar Rao, Sreena T. S, Aju Thara T. R, "Pigmentary Colors from yellow to red in $Bi_2Ce_2O_7$ by rare earth ion substitutions as possible high NIR reflecting pigments", ***Dyes and Pigments***, 160, **2019**, 177-187.

3. **Athira K. V. Raj**, P. Prabhakar Rao, Sreena T. S, Aju Thara T. R, "Broad greenish-yellow luminescence in $CaMoO_4$ by Si^{4+} acceptor doping as potential phosphors for white light emitting diode applications", ***Journal of Materials Science: Materials in Electron***, **2018**, https://doi.org/10.1007/s10854-018-9757-x.

4. **Athira K. V. Raj**, P. Prabhakar Rao, Sreena T. S, Aju Thara T. R, "Influence of local structure on photoluminescence properties of Eu^{3+} doped CeO_2 red phosphors through induced oxygen vacancies by contrasting rare earth substitutions", ***Physical Chemistry Chemical Physics***, 19, **2017**, 20110-20120.

5. **Athira K. V. Raj**, P. Prabhakar Rao, Divya S, Aju Thara T. R, "Terbium doped Sr_2MO_4 [M = Sn and Zr] yellow pigments with high infrared reflectance for energy saving applications", ***Powder Technology,*** 311, **2017,** 52-58.

6. **Athira K. V. Raj**, P. Prabhakar Rao, Sameera S, Divya S, Ajithara T. R, Sreena T. S and Aiswarya K, "High IR Reflecting Yellow Colorants in Yttrium-doped $MgBi_{2-x}O_4$ Solid Solutions", ***Chemistry Letters,*** 45, **2016,** 928-930.

7. **Athira K. V. Raj**, P. Prabhakar Rao, Sameera S and Divya S, "Pigments Based on Terbium-doped Yttrium Cerate with high NIR Reflectance for Cool Roof and Surface Coating Applications", ***Dyes and Pigments,*** 122, **2015,** 116-125.

8. **Athira K. V. Raj**, P. Prabhakar Rao, T. S. Sreena, S. Sameera, Vineetha James and U. A. Renju, "Remarkable changes in the photoluminescent properties of $Y_2Ce_2O_7:Eu^{3+}$ red phosphors through modification of the cerium oxidation states and oxygen vacancy ordering", ***Physical Chemistry Chemical Physics,*** 16, **2014,** 23699-23710.

9. **Athira K. V. Raj**, P. Prabhakar Rao, S. Sameera, Vineetha James, and S. Divya, "Synthesis of Novel Nontoxic Yellow Pigments: $Sr_2Ce_{1-x}Tb_xO_4$", ***Chemistry Letters,*** 43, **2014,** 985-987.

10. Aju Thara T. R, P. Prabhakar Rao, **Athira K. V. Raj** and Sreena T. S, "New series of brilliant yellow colorants in rare earth doped scheelite type oxides, $(LiRE)_{1/2}WO_4$- $BiVO_4$ for cool roof applications", ***Solar Energy Materials and Solar Cells***, 200, **2019**, 110015 1-8.

11. Sreena T. S, P. Prabhakar Rao, **Athira K. V. Raj** and T. R. Aju Thara, "Exploitation of Eu^{3+} red luminescence through order-disorder structural transition in lanthanide stannate pyrochlore for warm white LED applications", ***Physical Chemistry Chemical Physics,*** 20, **2018,** 24287-24299.

12. Sreena T. S, P. Prabhakar Rao, **Athira K. V. Raj** and Ajuthara T R, "Narrow-band red-emitting phosphors, $Gd_3Zn_2Nb_3O_{14}$:Eu^{3+} with high color purity for phosphor-converted white light emitting diodes", ***Journal of Alloys and Compounds,*** 751, **2018**, 148-158

13. Sreena T. S, P. Prabhakar Rao, Ajmal K. N and **Athira K. V. Raj, "**Influence of morphology on luminescence properties of xenotime type phosphors $NaYP_2O_7:Eu^{3+}$ synthesized via solid state and citrategel routes", ***Journal of Materials Science: Materials in Electronics***, 29, **2018**, 7458-7467.

14. Divya S, P. Prabhakar Rao, **Athira K. V. Raj** and Ajuthara T. R, "Intense Blue Colors in Wolframite-Type Co^{2+}:$MgWO_4$ Oxides through distortion in Co^{2+} octahedra", ***Chemistry Select***, 3, **2018**, 410-417.

15. Sameera S, P. Prabhakar Rao, Divya S, **Athira K.V. Raj** and Ajuthara T. R, **"**High IR reflecting $BiVO_4$-$CaMoO_4$ based yellow pigments for cool roof applications", ***Energy and Buildings,*** 154, **2017**, 491-498.

16. Reshmi V R, P. Prabhakar Rao, **Athira K. V. Raj** and Sreena T. S, "Novel molybdenum based pyrochlore type red phosphors, $NaGd_{1-x}SnMoO_7$: $x$$Eu^{3+}$ under near UV and blue excitation", ***Journal of Luminescence*** 190, **2017**, 6–9.

17. Aju Thara T. R, P. Prabhakar Rao, Divya S, **Athira K. V. Raj** and Sreena T. S, "Enhanced NIR Reflectance with Brilliant Yellow Hues in Scheelite type Solid Solutions, $(LiLaZn)_{1/3}MoO_4$ - $BiVO_4$ for Energy Saving Products", ***ACS Sustainable Chemistry and Engineering,*** 5, **2017**, 5118–5126.

18. Divya S, P. Prabhakar Rao, **Athira K. V. Raj** and Ajuthara T. R, "Enhanced pigmentary properties of rare earth germanates of the type $La_2CuGe_2O_8$ through CuO_6 octahedron distortion", ***Dyes and Pigments***, 142, **2017,** 472-480.

19. Divya S, P. Prabhakar Rao, Sameera S and **Athira K. V. Raj, "**Influence of aliovalent cation substitutions on the optical properties of $In_2Cu_2O_5$ system", ***Dyes and Pigments***, 134, **2016,** 506-515.

20. Sreena T S, P. Prabhakar Rao, Linda Francis, **Athira K. V. Raj**, "Influence of Structural Disorder on the Photoluminescence Properties of Eu^{3+} Doped Red Phosphors: $Ca_2Y_{3-x}Nb_3O_{14}$: $x$$Eu^{3+}$", ***Chemistry Select,*** 13, **2016,** 3413-3422.

21. Sameera S, P. Prabhakar Rao, Divya S, **Athira K. V. Raj,** "Brilliant IR Reflecting Yellow Colorants in Rare Earth Double Molybdate Substituted $BiVO_4$ Solid

Solutions for Energy Saving Applications", ***ACS Sustainable Chemistry & Engineering,*** 3, **2015,** 1227−1233.

22. Sreena T. S, P. Prabhakar Rao, Linda Francis, **Athira K. V. Raj**, Parvathi S Babu, "Structural and Photoluminescence Properties of Stannate based Displaced Pyrochlore-type Red Phosphors: $Ca_{3-x}Sn_3Nb_2O_{14}$: xEu^{3+}", ***Dalton Transactions,*** 44, **2015,** 8718-8728.

23. Divya S, P. Prabhakar Rao, Sameera S, Vineetha James, **Athira K. V. Raj**, "Monoclinic $LaGa_{1-x}Mn_xGe_2O_7$: A New Blue Chromophore Based on Mn^{3+} in Trigonal Bipyramidal Coordination with Longer Apical Bond Lengths", ***RSC Advances,*** 5, **2015,** 27278-27281.

24. Sameera Saithathul Fathimah, Padala Prabhakar Rao**,** Vineetha James**, Athira K. V. Raj,** G. R. Chitradevi and Sandhyakumari Leela, "Probing structural variation and multifunctionality in niobium doped bismuth vanadate materials", ***Dalton Transactions,*** 43, **2014,** 15851-15860.

25. S. Sameera, P. Prabhakar Rao, Vineetha James, S. Divya, **Athira K. V. Raj**, "Influence of $(LiLa)_{1/2}MoO_4$ substitution on the pigmentary properties of $BiVO_4$" , ***Dyes and Pigments***, 104, **2014,** 41-47.

List of Conference Papers

1. **Athira K V Raj**, P Prabhakar Rao, Sreena T. S and Ajuthara T R, "Enhanced photoluminescence properties of Eu^{3+} doped $A_2Ce_2O_7$ (A = La, Y and Gd) red phosphor", International Conference on Science, Technology and Applications of Rare Earths (ICSTAR) 2018. **(Best Poster Presentation Award)**

2. **Athira K V Raj**, P Prabhakar Rao, Sreena T. S, Ajuthara T R and Bradha M, "Influence of local structure on photoluminescence properties of Eu^{3+} doped CeO_2 red phosphors through induced oxygen vacancies", *National Conference on Luminescence and its Applications (NCLA)* 2018.

3. **Athira K. V. Raj**, P. Prabhakar Rao, T. S. Sreena, "Local Structure Correlation in Eu^{3+} Doped $Ln_2Ce_2O_7$ (Ln = La, Gd, Y and Lu) Red Phosphors and the Role of Ln Ionic Radius, Eu^{3+}Concentration and Oxygen Vacancies", *National Conference on Luminescence and Applications (NCLA)* 2016. **(Best Oral Presentation Award)**

4. **Athira K. V. Raj**, P. Prabhakar Rao, Mahesh S K, Linda Francis, Sreena T S and Parvathi S Babu, "Enhanced photoluminescence in $Y_2Ce_2O_7$ through oxygen vacancy ordering and the modification in cerium oxidation states", *National Seminar on Photonics and its Applications (NSPA)* 2015. **(Best Oral Presentation Award)**

5. **Athira K. V. Raj**, P. Prabhakar Rao, S. Sameera and Divya S, "Synthesis of Terbium doped yttrium cerate red pigments with high NIR reflectance for cool roof and surface coating applications", *International Conference on science, Technology and Applications of Rare Earths (ICSTAR)* 2015.

6. **Athira K. V. Raj**, P. Prabhakar Rao, Mahesh S K, Linda Francis, Sreena T S and Parvathi S Babu, "Enhanced photoluminescence in CeO_2 by Y_2O_3 addition through oxygen vacancy ordering and the modification in cerium oxidation", *International Conference on Luminescence and its Applications (ICLA)* 2015.

7. **Athira K. V. Raj**, P. Prabhakar Rao, S. Sameera, Sreena T S**,** Vineetha James and S. Divya, "Synthesis of $Sr_2M_{0.6}Tb_{0.4}O_4$ (M = Ce, Zr, Sn and Si) as yellow pigments for coloration of plastics", *(ISAS)* 2014 .

8. **Athira K. V. Raj**, P. Prabhakar Rao, Mahesh S K, Linda Francis, Reshmi V R and Sreena T S, "Effect of Si substitution on the luminescence properties of $Ce_{0.85}O_2$:0.15Eu^{3+} phosphors prepared by citrate method", *International Conference on Advanced Functional Materials (ICAFM)* 2014**.**

"Set your heart upon your work but never its reward", Radheykrishna.

……